

UNIVERSITY OF SOUTHAMPTON

FACULTY OF PHYSICAL SCIENCES AND ENGINEERING

Optoelectronics Research Centre

**Characterisation of Hollow-Core Photonic Bandgap Fibres  
and Other Multimode Fibres for Optical Communications**

by

**Nicholas Heng Loong WONG**

A thesis submitted for the degree of  
Doctor of Philosophy

June 2017



UNIVERSITY OF SOUTHAMPTON

ABSTRACT

FACULTY OF PHYSICAL SCIENCES AND ENGINEERING

Optoelectronics Research Centre

Doctor of Philosophy

CHARACTERISATION OF HOLLOW-CORE PHOTONIC BANDGAP FIBRES  
AND OTHER MULTIMODE FIBRES FOR OPTICAL COMMUNICATIONS

by Nicholas Heng Loong WONG

Progress in multimode fibre technology has opened diverse opportunities in science and technology, one of which is pushing data capacities beyond the fundamental limits of conventional single-mode fibre, so as to avert network gridlock precipitated by exponentially growing global traffic demands. Hollow-core photonic bandgap fibres (HC-PBGFs), where light propagates in air rather than glass, have been considered as a potential candidate for high-capacity telecommunications applications, while offering superior performance over solid-core fibres in terms of low loss, low latency, and ultralow nonlinearity.

This thesis presents research conducted as part of the efforts of the EU FP7 project MODE-GAP to pioneer developments in HC-PBGF and related space-division multiplexing technologies. This work is involved with the characterisation of primarily HC-PBGFs and also solid-core multimode fibres, recently and respectively fabricated through the facilities of the Optoelectronics Research Centre and other project partners. A time-of-flight method is applied to make extensive measurements on these fibres to study their modal properties, including mode coupling and differential modal delay, in order to assess their capabilities for single-mode as well as mode-division multiplexed data transmission. In support of the fibre design process, this work has aided the full characterisation of the first ever fabricated 37-cell HC-PBGFs and enabled subsequent mode-division multiplexing trials at a record capacity of 73.7 Tbit/s. Characterisation of multi-kilometre record-length HC-PBGFs is also performed, and has supported the demonstration of these fibres in metro network environments.

To further understand the modal processes and facilitate fibre improvement, a simulation environment is constructed based on a power coupling propagation model. This has enhanced interpretations of experimental time-of-flight data, as well as validated a proposed theory relating mode coupling and loss in HC-PBGFs.

Finally, an experimental technique is introduced to inspect longitudinal defects in solid- and hollow-core fibres, by applying time-of-flight principles.



# Contents

<b>Declaration of Authorship</b>	<b>xv</b>
<b>Acknowledgements</b>	<b>xvii</b>
<b>Nomenclature</b>	<b>xxiii</b>
<b>1 Introduction</b>	<b>1</b>
1.1 Motivation . . . . .	2
1.2 Research Focus and Aims . . . . .	5
1.3 Thesis Outline . . . . .	6
1.3.1 Preamble on Nomenclature and Conventions . . . . .	7
<b>2 Background</b>	<b>9</b>
2.1 Recent Developments . . . . .	9
2.2 Fibre Optics Theory . . . . .	10
2.2.1 Total Internal Reflection Guidance . . . . .	10
2.2.2 Modes in an Optical Fibre . . . . .	11
2.2.3 Discrete and Distributed Coupling . . . . .	15
2.2.4 Power Coupling . . . . .	17
2.3 The Hollow-Core Photonic Bandgap Fibre . . . . .	18
2.3.1 Photonic Bandgap Guidance . . . . .	18
2.3.2 HC-PBGF Structure and Fabrication . . . . .	19
2.3.3 Guided Modes in HC-PBGFs . . . . .	21
2.3.4 Features of HC-PBGFs . . . . .	21
2.3.5 Recent ORC Work and Achievements . . . . .	23
2.3.5.1 The 19-cell HC-PBGF . . . . .	23
2.3.5.2 The 37-cell HC-PBGF . . . . .	24
2.3.5.3 Theoretical and Computational Studies . . . . .	24
2.3.5.4 Other Experimental and Characterisation Work . . . . .	25
2.4 Summary . . . . .	26
<b>3 A Tool for Modal Characterisation</b>	<b>27</b>
3.1 Time-of-Flight Operating Principle . . . . .	28
3.2 Experimental Set-Up and Procedure . . . . .	31
3.2.1 Excitation . . . . .	31
3.2.2 Detection . . . . .	33
3.3 Experimental Proof of Concept . . . . .	34
3.3.1 2-mode Step-Index Fibre . . . . .	34

3.3.2	4-Mode Step-Index Fibre . . . . .	36
3.3.2.1	Discrete Mode Coupling . . . . .	36
3.3.2.2	Distributed Mode Coupling . . . . .	38
3.3.2.3	Summary of Observations . . . . .	40
3.4	Characterisation of a Novel 9-Mode Fibre . . . . .	40
3.4.1	Mode Excitation and DMD . . . . .	41
3.4.2	Mode-Dependent Loss Characterisation . . . . .	43
3.5	Comparing ToF and $S^2$ Methods . . . . .	45
3.6	Summary and Future Work . . . . .	46
<b>4</b>	<b>Characterisation of HC-PBGFs</b> . . . . .	<b>49</b>
4.1	ToF Measurements on HC-PBGFs . . . . .	50
4.1.1	Extinction Ratio and Distributed Coupling Measurements After Selective Mode Excitation . . . . .	51
4.1.2	Vector Modes . . . . .	56
4.1.3	Differential Group Delay . . . . .	57
4.1.4	Summary . . . . .	60
4.2	Data Transmission in HC-PBGFs . . . . .	60
4.2.1	Experimental Transmission Set-Up . . . . .	61
4.2.2	Single-Mode Transmission Over HC-PBGF . . . . .	63
4.2.3	The First Data Transmission Through a 37c HC-PBGF . . . . .	64
4.2.4	MDM Data Transmission Over HOMs Using Direct Detection . . . . .	66
4.2.5	Other Trials . . . . .	67
4.3	Diagnosing HC-PBGF Performance Using ToF . . . . .	68
4.3.1	Initial ToF Diagnostics . . . . .	69
4.3.2	Effects of Respooling . . . . .	72
4.3.3	Aftermath . . . . .	76
4.4	2 $\mu$ m Waveband ToF Measurements . . . . .	76
4.4.1	2 $\mu$ m-Wavelength Measurement Set-Up . . . . .	76
4.4.2	Characterisation of a HC-PBGF in the 2 $\mu$ m-Wavelength Region . . . . .	77
4.5	Concluding Remarks . . . . .	78
<b>5</b>	<b>Modelling the Propagation of Modes</b> . . . . .	<b>81</b>
5.1	Mathematical Model . . . . .	82
5.1.1	Formulation . . . . .	82
5.1.2	Initialisation . . . . .	84
5.1.3	Propagation Solver Implementation . . . . .	86
5.1.3.1	Iterative Stepping Method (ISM) . . . . .	86
5.1.3.2	Split-Step Fourier Method (SSFM) . . . . .	87
5.1.3.3	Comparison of Propagation Methods . . . . .	89
5.2	Analysis of Propagation . . . . .	91
5.2.1	Evolution of Power . . . . .	91
5.2.2	Effects of Varying Coefficients . . . . .	96
5.3	Fitting with Experimental Data . . . . .	100
5.3.1	Determination of Coupling Coefficients Through Fitting . . . . .	101
5.3.2	Comparing Calculated and Measured ToF . . . . .	104
5.4	Conclusions and Future Work . . . . .	106

<b>6</b>	<b>Inspection of Fibre Defects</b>	<b>109</b>
6.1	Defect-Induced Mode Coupling . . . . .	110
6.1.1	Concept . . . . .	110
6.1.2	Simulation . . . . .	111
6.1.3	Experimental Verification . . . . .	113
6.1.4	A More Realistic Example . . . . .	115
6.2	Defect Inspection Experimental Set-Up and Method . . . . .	117
6.2.1	Mode-Selective OTDR . . . . .	117
6.2.2	Infrared Side-Scattering . . . . .	118
6.2.3	Time-of-Flight . . . . .	120
6.3	Inspection of Defects in HC-PBGFs . . . . .	121
6.4	Conclusions and Future Work . . . . .	125
<b>7</b>	<b>Conclusions</b>	<b>127</b>
7.1	Summary of Main Chapters . . . . .	127
7.2	Future Work . . . . .	129
7.3	Concluding Remarks . . . . .	130
<b>A</b>	<b>Calculation of Focal Lengths For Free-Space Set-Up</b>	<b>131</b>
<b>B</b>	<b>MATLAB Code For Pulse Propagation With Mode Coupling</b>	<b>133</b>
B.1	Main Program: <code>Coupling.m</code> . . . . .	133
B.2	Parameter Initialisations: <code>SetParameter_4MF.m</code> . . . . .	138
B.3	Propagation Solver Function Using ISM: <code>powerCouplingISM.m</code> . . . . .	140
B.4	Propagation Solver Function Using SSFM: <code>powerCouplingSSFM.m</code> . . . . .	142
<b>C</b>	<b>Derivation of Fourier Transform Representation of The Derivative</b>	<b>145</b>
<b>D</b>	<b>Other Collaborative Work</b>	<b>147</b>
D.1	Enabling Fibre Measurements Through ToF . . . . .	147
D.1.1	Accurate Mode-Dependent Loss Measurements on HC-PBGFs . . . . .	147
D.1.2	Low Crosstalk Splicing of HC-PBGF with SMF . . . . .	148
D.2	Enabling Amplifier Development Through ToF – Cladding Pumped Few- Moded EDFA . . . . .	149
D.3	Spatial Mode Switchable Erbium-doped Fibre Laser . . . . .	150
	<b>List of Publications</b>	<b>151</b>
	<b>Other Artistic Creations</b>	<b>157</b>
	<b>References</b>	<b>161</b>



# List of Figures

1.1	Attenuation spectrum of SSMF. . . . .	2
1.2	Physical dimensions available in optical fibre communications. . . . .	4
2.1	Simplified cross-section of an SCF. . . . .	11
2.2	Various modes propagating in a multimode fibre. . . . .	12
2.3	Time-of-flight of discrete and distributed coupling after an $LP_{11}$ mode-selective launch in a multimode fibre. . . . .	16
2.4	Simplified cross-section of a HC-PBGF. . . . .	18
2.5	Hexagonal TLH tessellation for HC-PBGF transverse geometry. . . . .	20
2.6	SEM of a 37-cell HC-PBGF. . . . .	20
2.7	Plot of effective index versus wavelength in a fictional HC-PBGF, showing the bandgap. . . . .	21
2.8	Plot of fibre roughness spectral density against deformation spatial frequency. . . . .	22
3.1	Pulse propagation through a 4MF. . . . .	28
3.2	Example of a ToF trace for an optimised $LP_{11}$ launch showing key features. . . . .	30
3.3	Time-of-flight experimental set-up. . . . .	31
3.4	Spectrum of output signals from PFL and OBPF. . . . .	32
3.5	Layouts of various phase plate geometries showing phase regions. . . . .	33
3.6	Pulse propagation through a 2MF. . . . .	35
3.7	ToF measurements for a 2MSIF. . . . .	35
3.8	Pulse propagation through a 4MF. . . . .	36
3.9	ToF measurements for a 4MSIF. . . . .	37
3.10	$S^2$ measurement for the 4MSIF. . . . .	38
3.11	ToF measurements for the 9MGRINF. . . . .	41
3.12	ToF measurements for the 9MGRINF after selective launching. . . . .	42
3.13	$S^2$ measurements for the 9MGRINF. . . . .	43
3.14	Optical Time-domain Reflectometry experimental set-up. . . . .	44
3.15	OTDR measurements on the 9MGRINF. . . . .	44
4.1	SEM cross-sections of various HC-PBGFs. . . . .	51
4.2	ToF measurements showing the selectively excited $LP_{01}$ and $LP_{11a/b}$ modes in fibre 19c1. . . . .	52
4.3	ToF measurements for $LP_{01}$ , $LP_{11}$ , and $LP_{21}$ selective launches in fibre 19c2. . . . .	53
4.4	ToF measurements for $LP_{01}$ , $LP_{11}$ , and $LP_{21}$ selective launches in fibre 37c1. . . . .	54

4.5	ToF measurements for $LP_{01}$ , $LP_{11}$ , and $LP_{21}$ selective launches in fibre 37c2. . . . .	55
4.6	ToF set-up for DGD measurements. . . . .	58
4.7	DGD measurements of the $LP_{01}$ and $LP_{11}$ modes in fibres 37c1 and 19c2. . . . .	59
4.8	Example of an open eye in an eye diagram. . . . .	61
4.9	10 Gbit/s data transmission set-up. . . . .	62
4.10	Eye diagrams for data transmission through various 19c HC-PBGFs. . . . .	63
4.11	Eye diagrams for data transmission through fibre 37c1. . . . .	64
4.12	BER measurements for data transmission through fibre 37c1. . . . .	65
4.13	Eye diagrams for data transmission through fibre 37c2, using direct detection on HOMs. . . . .	66
4.14	Eye diagrams for data transmission through a 19c HC-PBGF used for data centre experiments. . . . .	67
4.15	SEM cross-section of the record-length 19c HC-PBGF. . . . .	68
4.16	Eye diagrams for transmission through sectioned bands of the long-length 19c HC-PBGF. . . . .	69
4.17	ToF experimental set-up for long-length fibre diagnostics. . . . .	70
4.18	ToF for band A of the long-length HC-PBGF. . . . .	71
4.19	ToF for band A of the long-length HC-PBGF, with mandrel wrapping. . . . .	72
4.20	ToF for various bands of the long-length HC-PBGF. . . . .	73
4.21	ToF for bands A and B of the long-length HC-PBGF, with dispersion compensation. . . . .	73
4.22	ToF for band A of the long-length HC-PBGF, after respooling. . . . .	74
4.23	Eye diagrams for transmission through respooled sectioned bands of the long-length 19c HC-PBGF. . . . .	75
4.24	ToF for band C of the long-length HC-PBGF, after the second respooling. . . . .	75
4.25	ToF experimental set-up for 2 $\mu$ m-wavelength measurements. . . . .	77
4.26	SEM cross-section of a 19c HC-PBGF designed for operation in the 2 $\mu$ m-wavelength region. . . . .	77
4.27	ToF for a 3.8 km-long 19c HC-PBGF operating in the 2 $\mu$ m-wavelength region. . . . .	78
5.1	Various simulation time-domains for pulse propagation in a fibre. . . . .	83
5.2	Visualisation of the 3D matrix $\mathbf{P}$ . . . . .	84
5.3	Schematic of the SSFM. . . . .	88
5.4	Numerical stability comparison of ISM and SSFM. . . . .	90
5.5	Superimposed comparison of numerical stability of ISM and SSFM. . . . .	90
5.6	Comparison of computation time growths for ISM and SSFM. . . . .	91
5.7	Simulated power evolution in a 4MF with $\mathcal{C}_{01 \leftrightarrow 11}$ coupling, after $LP_{01}$ selective launch. . . . .	92
5.8	Modal delay spread in a 4MF with $\mathcal{C}_{01 \leftrightarrow 11}$ coupling. . . . .	93
5.9	Total and decomposed ToF traces in a 4MF with $\mathcal{C}_{01 \leftrightarrow 11}$ coupling. . . . .	94
5.10	Total power evolution of modes in a 4MF with $\mathcal{C}_{01 \leftrightarrow 11}$ . . . . .	95
5.11	Simulated power evolution in a 4MF with $\mathcal{C}_{01 \leftrightarrow 11}$ coupling, after $LP_{11}$ selective launch. . . . .	96
5.12	Simulated ToF with varying $\alpha_{01}$ in a 4MF with $\mathcal{C}_{01 \leftrightarrow 11}$ coupling. . . . .	97
5.13	Total and decomposed ToF traces in a 4MF with $\mathcal{C}_{01 \leftrightarrow 11}$ coupling, with $\alpha_{01} > \alpha_{11}$ . . . . .	98

5.14	Simulated ToF with varying $\alpha_{11}$ in a 4MF with $\mathcal{C}_{01 \leftrightarrow 11}$ coupling. . . . .	98
5.15	Simulated ToF with varying $\mathcal{C}$ scalings in a 4MF with $\mathcal{C}_{01 \leftrightarrow 11}$ coupling. . .	99
5.16	Total power evolution of $LP_{01}$ and $LP_{11}$ in a 4MF, for different $\mathcal{C}$ scaling cases. . . . .	100
5.17	Measured and fitted ToF traces of a 4MSIF. . . . .	102
5.18	Coupling coefficients resulting from fitting ToF results of a 4MSIF. . . . .	104
5.19	Measured and fitted ToF traces of a 19c HC-PBGF. . . . .	105
5.20	Measured and fitted ToF traces of the 37c HC-PBGF. . . . .	106
6.1	Pulse propagation and discrete mode coupling in a composite two-segment 2MF. . . . .	111
6.2	Mode component transit map in a simulated two-segment 2MF. . . . .	112
6.3	Simulated ToF for a two-segment 2MF. . . . .	113
6.4	Two fibre spools concatenated by a fusion splicer. . . . .	114
6.5	ToF measurements for a 2MGRINF butt coupled via splicer to a 2MSIF. .	115
6.6	Simulated ToF for a HC-PBGF with a longitudinal defect. . . . .	116
6.7	Infrared side-scattering (IRSS) capture set-up. . . . .	119
6.8	IR defect spot detection. . . . .	119
6.9	Photograph of IRSS laboratory equipment. . . . .	120
6.10	SEM cross-section of the 19c HC-PBGF used in defect analysis. . . . .	121
6.11	Mode-selective OTDR for a 19c HC-PBGF with longitudinal defects. . . .	122
6.12	Snapshots of IR-illuminated bright spots at defects in the 19c HC-PBGF. .	123
6.13	OTDR and ToF measurements on the defective 19c HC-PBGF. . . . .	124
A.1	Free-space lens setup used in ToF experiments. . . . .	131
D.1	Cutback loss measurements for 37c1. . . . .	148
D.2	ToF measurement showing low crosstalk in a 19c HC-PBGF spliced at the input with SMF. . . . .	149



# List of Tables

2.1	The first few guided modes of a circular step-index fibre. . . . .	14
3.1	Simulated mode intensity profiles in a multimode fibre. . . . .	29
3.2	DMDs of the 4MSIF. . . . .	37
3.3	DMDs of the 9MGRINF. . . . .	42
3.4	Modal attenuation of the 9MGRINF. . . . .	44
4.1	List of HC-PBGFs used in experiments. . . . .	50
4.2	Discrete mode peak extinction ratios for fibre 19c1. . . . .	52
4.3	Discrete mode peak extinction ratios for fibre 19c2. . . . .	53
4.4	Discrete mode peak extinction ratios for fibre 37c1. . . . .	55
4.5	Discrete mode peak extinction ratios for fibre 37c2. . . . .	55
4.6	Measured DGDs of HC-PBGFs from ToF. . . . .	58
5.1	User-specified coefficients for mode propagation simulation. . . . .	85
6.1	DMDs of each segment in an example composite two-segment 2MF. . . . .	112



## Declaration of Authorship

I, **Nicholas Heng Loong WONG**, declare that the thesis entitled *Characterisation of Hollow-Core Photonic Bandgap Fibres and Other Multimode Fibres for Optical Communications* and the work presented in the thesis are both my own, and have been generated by me as the result of my own original research. I confirm that:

- this work was done wholly or mainly while in candidature for a research degree at this University;
- where any part of this thesis has previously been submitted for a degree or any other qualification at this University or any other institution, this has been clearly stated;
- where I have consulted the published work of others, this is always clearly attributed;
- where I have quoted from the work of others, the source is always given. With the exception of such quotations, this thesis is entirely my own work;
- I have acknowledged all main sources of help;
- where the thesis is based on work done by myself jointly with others, I have made clear exactly what was done by others and what I have contributed myself;
- parts of this work have been published in the [List of Publications](#) at the end of the thesis.

Signed:.....

Date:.....



## Acknowledgements

I wish to convey my deepest gratitude to my supervisor Prof. David Richardson for taking me on as his student, and providing guidance, advice, and various research opportunities. His calm disposition always has an uncanny way of making me feel confident about myself, even during the most trying of times. Thanks go to my co-supervisors Prof. Periklis Petropoulos and Dr Shaif-ul Alam, who guided me along the way and taught me a few laboratory tricks. I want to express my sincere appreciation to Dr Yongmin Jung, who has patiently taught and mentored me since the start of the programme. I am grateful to him for being a true friend, and particularly for answering the many questions I would raise, even after office hours.

I wish to thank everyone in the MODE-GAP and COSIGN projects, especially those based at the *Optoelectronics Research Centre (ORC)*, for ongoing collaborations that has led to state of the art research and numerous first demonstrations. Additionally, I want to thank the staff and students in the *pulsed fibre lasers*, *microstructured optical fibres*, and *optical fibre communications* groups for individually and collectively affording their kindest help, technical assistance, and advice. There are a great number of individuals at the *ORC* who gave me academic, technical, and experimental support to facilitate my progress.

A word of thanks go to my friends and colleagues in our student-led *University of Southampton Optics and Photonics Society (OPSoc)*, especially to Matthew Posner, whose friendship I will cherish for years to come.


This work could not have been done without the love and support of my family, relatives, and friends. I am especially indebted to my parents, who raised me, facilitated my education, and continue to be there for me, and to Jeremy and Angie, for putting up with a largely absent brother over the last few years.

Finally, I want to thank the person without whom I would have taken a lot longer to get through the final stages of my thesis, Amy. She has been a source of love, strength, motivation, hope, and comfort, and she never gave up on me.

*The work in this thesis has been supported by the European Commission 7th Framework Programme under grant agreements 258033 (MODE-GAP) and 619572 (COSIGN), as well as the UK Engineering and Physical Sciences Research Council (EPSRC) through grants EP/I01196X/1 (The Photonic Hyper-highway) and EP/H02607X/1 (Centre for Innovative Manufacturing in Photonics).*



*“All our dreams can come true,  
if we have the courage to pursue them.”*

WALTER E. DISNEY 



*To my parents.*



# Nomenclature

## Technical Abbreviations

16QAM	16-ary Quadrature Amplitude Modulation
19c	19-cell
2MF	2-mode Fibre
2MGRINF	2-Mode Graded-Index Fibre
2MSIF	2-mode Step-Index Fibre
32QAM	32-ary Quadrature Amplitude Modulation
37c	37-cell
3D	3-Dimensional
4MF	4-Mode Fibre
4MSIF	4-Mode Step-Index Fibre
9MGRINF	9-Mode Graded-Index Fibre
A.U.	Arbitrary Units
B2B	Back-To-Back
BPG	Bit Pattern Generator
CCD	Charge-Coupled Device
clk	Clock Signal
CWL	Continuous Wave Laser
DCA	Digital Communications Analyser
DCF	Dispersion-Compensating Fibre

DGD	Differential Group Delay
DMD	Differential Mode Delay
DP	Dual-Polarisation
DSP	Digital Signal Processing
DWDM	Dense Wavelength-Division Multiplexing
EA	Error Analyser
EDFA	Erbium-Doped Fibre Amplifier
EH	Hybrid (mode)
EoP	End of Pull
ER	Extinction Ratio, denoted by $r_{\text{ex}}$
FFT	Fast Fourier Transform
FMF	Few-Mode Fibre
FUT	Fibre Under Test
FWHM	Full Width at Half Maximum
HC-PBGF	Hollow-Core Photonic Bandgap Fibre
HE	Hybrid (mode)
HOM	Higher-Order Mode
ICT	Information and Communications Technology
IR	Infrared
IRSS	Infrared Side-Scattering
ISM	Iterative Stepping Method
ISM	Iterative Stepping Method
LD	Laser Diode
LHS	Left-Hand-Side
LP	Linearly Polarised
MCF	Multicore Fibre
MDL	Mode-Dependent Loss

---

MDM	Mode-Division Multiplexing
MFD	Mode Field Diameter
MIMO	Multiple-Input-Multiple-Output
MMF	Multimode Fibre
MPI	Multipath Interference
MSEM	MicroStructure Element Method
MUT	Mode Under Test
MUX	Multiplexing
MZM	Mach-Zehnder modulator
NLSE	Nonlinear Schrödinger Equation
NRZ	Non-Return-To-Zero
OBPF	Optical Bandpass Filter
ODE	Ordinary Differential Equation
OM	Other Mode
OOK	On-off Keying
OSA	Optical Spectrum Analyser; can also refer to <i>The Optical Society</i> (see <b>Other Abbreviations</b> below)
OSSR	Optical Side Scattering Radiometry
OTDR	Optical Time-Domain Reflectometry or Optical Time-Domain Reflectometer
PC	Polarisation Controller
PD	Photodetector
PDE	Partial Differential Equation
PDM	Polarisation-Division Multiplexing
PFL	Pulsed Fibre Laser
PG	Pulse Generator
PM	Power Meter
PP	Phase Plate

PRBS	Pseudorandom Binary Sequence
PSD	Power Spectral Density
PSK	Phase-Shift Keying
QAM	Quadrature Amplitude Modulation
QPSK	Quadrature Phase-Shift Keying
RFA	Radio-Frequency Amplifier
RHS	Right-Hand-Side
Rx	Receiver
$S^2$	Spatially and Spectrally Resolved Imaging
SCF	Solid-Core Fibre
Scope	Oscilloscope
SDM	Space-Division Multiplexing
SEM	Scanning Electron Microscope
SG	Signal Generator
SMF	Single-Mode Fibre
SoP	Start of Pull
SSFM	Split-Step Fourier Method
SSMF	Standard Single-Mode Fibre
TDFA	Thulium-Doped Fibre Amplifier
TE	Transverse Electric
TEDI	Time-of-Flight Enabled Defect Inspection
TIR	Total Internal Reflection
TLH	Triangular Lattice of Holes
TLS	Tunable Laser Source
TM	Transverse Magnetic
ToF	Time-of-Flight
Trig	Trigger Signal

Tx	Transmitter
VOA	Variable Optical Attenuator
WDM	Wavelength-Division Multiplexing

### Other Abbreviations

#	Number
CERN	European Organization for Nuclear Research; French: <i>Organisation européenne pour la recherche nucléaire</i>
CLEO	Conference on Lasers and Electro-Optics
CLEO-PR	Conference on Lasers and Electro-Optics Pacific Rim
COSIGN	Combining Optics and SDN In next Generation data centre Networks
E.g.	For example; Latin: <i>Exempli gratia</i>
ECOC	European Conference and Exhibition/Exposition on Optical Communications
EPSRC	Engineering and Physical Sciences Research Council
Et al.	And others; Latin: <i>Et alia</i>
Etc.	Et cetera
ETOP	Education and Training in Optics and Photonics Conference
FP7	European Commission 7th Framework Programme
I.e.	That is; Latin: <i>Id est</i>
ICTON	International Conference on Transparent Optical Networks
IEE	Institution of Electrical Engineers
IEEE	Institute of Electrical and Electronics Engineers
ITU	International Telecommunication Union
IYL 2015	International Year of Light and Light-based Technologies
MODE-GAP	Multi-mode capacity enhancement with PBG fibre
MOFG	Microstructured Optical Fibres Group
NFOEC	National Fiber Optic Engineers Conference

---

NSN	Nokia Siemens Networks (now Coriant)
Nº	Number of
OECC	Opto-Electronics and Communications Conference
OFC	Optical Fiber Communication Conference and Exposition
OFCG	Optical Fibre Communications Group
OPSoc	University of Southampton Optics and Photonics Society
ORC	Optoelectronics Research Centre
OSA	The Optical Society; can also refer to <i>Optical Spectrum Analyser</i> (see <b>Technical Abbreviations</b> above)
PFLG	Pulsed Fibre Lasers Group
PGC	Photonics Global Conference
PhD	Doctor of Philosophy
QELS	Conference on Quantum Electronics and Laser Science
SIAM	Society for Industrial and Applied Mathematics
SUM	IEEE Photonics Society Summer Topical Meeting Series
W.r.t.	With respect to
WSOF	Workshop on Specialty Optical Fibers and their Applications

### Mathematical Notation

$\approx$	Approximation
$\bar{x}$	Mean of $x$ , $\bar{x} = \frac{1}{N} \sum_{i=1}^N x_i$
$\mathcal{O}(\cdot)$	Algorithmic complexity
$:=$	Definition
$\cos(\cdot)$	Cosine function
$\text{diag}(\cdot)$	Conversion of a vector to a diagonal matrix
$\exp(\cdot)$	Exponential function, $\exp x = e^x$
$\mathcal{F}\{\cdot\}$	Fourier transform, $\hat{f}(\omega) = \mathcal{F}\{f(t)\} := \int_{-\infty}^{\infty} f(t) e^{-j\omega t} dt$
$\in$	Set membership

$\mathcal{F}^{-1}\{.\}$	Inverse Fourier transform, $f(t) = \mathcal{F}^{-1}\{\hat{f}(\omega)\} := \frac{1}{2\pi} \int_{-\infty}^{\infty} \hat{f}(\omega) e^{j\omega t} d\omega$
$(.)^{op}$	Element-wise exponentiation of vector or matrix to $p$ th power, Hadamard power
$(.)^T$	Matrix transpose
$\log(.)$	Base-10 logarithm function
$\log_2(.)$	Base-2 logarithm function
$\mathbb{N}$	Set of natural numbers
$\mathbf{1}$	Column vector of 1s
$\mathbf{A} \circ \mathbf{B}$	Element-wise product of matrices $\mathbf{A}$ and $\mathbf{B}$ , Hadamard product
$\frac{d^p}{dx^p}(\cdot)$	Ordinary $p$ th derivative with respect to $x$
$\frac{\partial}{\partial x}(\cdot)$	Partial derivative with respect to $x$
$\propto$	Proportionality
$\Pr(\cdot)$	Probability operator
$\sin(\cdot)$	Sine function
$\sum(\cdot)$	Summation
$\tan(\cdot)$	Tangent function
${}^N C_p$	$\aleph$ $p$ -combinations from a set of $N$ elements, ${}^N C_p = \frac{N!}{p!(N-p)!}$

### Roman Symbols and Units

$A_{pu}$	Optical pulse amplitude
$A$	Coupling strength [ $\text{m}^{-9}$ ]
$\mathcal{A}_{pu}$	Optical pulse envelope
$B$	Bandwidth [Hz]
BER	Bit error rate
$C$	Data capacity [bit/s]
$\mathbf{C}$	Mode coupling and loss coefficient matrix
$c$	Coupling coefficient [ $\text{m}^{-1}$ ]

---

$\mathbf{c}$	Coupling coefficient matrix [ $\text{m}^{-1}$ ]
$\check{D}$	DMD operator in coupled power equation
$d$	Diameter [m]
$e$	Euler's number, $e = \lim_{x \rightarrow \infty} \left(1 + \frac{1}{x}\right)^x = 2.71828 \dots$
$f$	Focal length [m]
$i$	Index
$j$	Imaginary unit, $j = \sqrt{-1}$
$l$	Azimuthal index of a mode
$\ell$	Length [m]
$\mathcal{M}$	Magnification
$m$	Radial index of a mode; also, mode index
$N$	Integer
$N_l$	Highest azimuthal mode index
$N_m$	Highest radial mode index; also, highest mode index
$N_t$	Highest time index
$N_z$	Highest distance index
$n_{\text{cl}}$	Refractive index of fibre cladding
$n_{\text{co}}$	Refractive index of fibre core
$n$	Number of omitted cells in a HC-PBGF
$P$	Power [W or dBm for absolute; also, dB for relative or normalised]
$P_{\text{in}}$	Input power [W or dB]
$P_{\text{pu}}$	Optical pulse power [W]
$P_{\text{rec}}$	Received power [dBm]
$P_{\text{pk}}$	Peak power [W]
$\mathbf{P}_{\text{in}}$	Input power vector [W]
$\mathbf{P}_{\text{pu}}$	Optical pulse power vector [W]
$\mathbf{P}_z$	$N_t \times N_m$ optical power matrix at distance step $z$ [W]

---




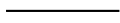
$P_d$	Discrete power scaling factor [%]
$P_r$	Power redistribution factor [%]
$\mathbf{P}_d$	Vector of discrete power scaling factors [%]
$p$	Integer
$q$	Mode index
$R_b$	Bit rate [bit/s]
$\mathcal{R}$	Temporal resolution [s]
$r_{\text{ex}}$	Extinction ratio [dB]
SNR	Signal-to-noise ratio [dB]
$t$	Time or absolute temporal delay [s]
$\mathbf{t}$	Time vector [s]
$v$	Mode group velocity [m/s]
$w$	Beam waist radius [m]
$z$	Distance [m]

### Greek Symbols and Units

$\alpha$	Attenuation or loss per unit length [dB/m; commonly dB/km]
$\boldsymbol{\alpha}$	Vector of attenuation or loss per unit length [dB/m; commonly dB/km]
$\beta$	Propagation constant [ $\text{m}^{-1}$ ]
$\Delta n_{\text{eff}}$	Relative effective refractive index
$\Delta t$	Relative time delay [s]
$\Delta$	Optical fibre core/cladding refractive index difference
$\Delta\tau$	Relative time delay per unit length, DGD, DMD [s/m]
$\boldsymbol{\Delta\tau}$	Vector of relative time delay per unit length, DGD, DMD [s/m]
$\delta t$	Time-step [s]
$\delta z$	Space-step [m]
$\theta$	Angle [rad or °]

$\tilde{\theta}_c$	Complement of the critical angle for TIR [rad or °]
$\kappa$	PBGF deformation spatial frequency [ $\mu\text{m}^{-1}$ ]
$\Lambda$	Spatial period or pitch [m]
$\lambda$	Wavelength [m]
$\pi$	Ratio of a circle's circumference to its diameter; $\pi = 3.14159\dots$
$\tau$	Absolute time delay per unit length [s/m]
$\tau_w$	Optical pulse temporal FWHM [s]
$\boldsymbol{\tau}$	Vector of absolute time delay per unit length [s/m]
$\omega$	Angular frequency [rad/s]
$\boldsymbol{\omega}$	Angular frequency vector [rad/s]

### Schematic Legend

	Optical beam
	FUT
	SSMF
	Electrical cable

# Chapter 1

## Introduction

Fibre optics has revolutionised the way and speed at which we communicate information, since the idea of using dielectric-fibre waveguides for telecommunications was first proposed by Kao and Hockman in 1966 [1]. Today, networks of optical fibres form the backbone of the internet, consisting of thousands of kilometres of submarine and terrestrial communications cables. Compared to other media such as coaxial copper cables and satellite communication links, not only do optical fibres perform superiorly in terms of reach and capacity [2], but they are also immune to impairments like electromagnetic interference [3]. Fibre cables are also about an order of magnitude thinner and two orders of magnitude lighter than their coaxial counterparts, thus making them easier to install and in longer sections [4]. In 1988, the first transatlantic undersea optical fibre system called TAT-8 (Transatlantic No. 8) was deployed, linking Tuckerton, New Jersey; Lands End, UK; and Penmarch, France; delivering an effective capacity of about 560 Mbit/s [5]. Since 1975, much research has been devoted to reducing loss, increasing capacity, and enhancing the bit rate-distance product [6]. Some enabling advances include the erbium-doped fibre amplifier (EDFA) in 1987 [7], and multiplexing techniques such as wavelength-division multiplexing (WDM). More recently, significant research effort has been directed towards space-division multiplexing (SDM), which promises further dramatic increases in capacity.

Following this, the focus of this doctoral thesis is on the hollow-core photonic bandgap fibre (HC-PBGF); a recent development and potential candidate to improve upon the limitations of conventional solid-core standard single-mode fibres (SSMFs). As described later in Chapter 2.1, HC-PBGFs guide light in a way very different from conventional solid-core fibres (SCFs); most of the light propagates in air rather than glass [8]. As such, they offer several predicted improvements over conventional fibres, namely, lower loss [9, 10], lower nonlinearity [11, 12], and lower latency [8, 12, 13]. HC-PBGFs also generally have larger cores and can support a multitude of guided modes [11], presenting the opportunity for high-capacity mode-division multiplexing (MDM) based data transmission [12]. These attributes make HC-PBGFs extremely attractive.

This introductory chapter describes the motivation for the work in Section 1.1, the scope of the research and its aims in Section 1.2, and the outline of the thesis in Section 1.3.

## 1.1 Motivation

The demand for ever more internet bandwidth is on a steady rise and recent studies project the annual growth in global average internet traffic to be about 40-60% [15–17]. This has come about with the advent of new services such as cloud computing, social networking, and online 3-dimensional (3D) and high-definition video streaming [16]. Meanwhile, as economies prosper and socio-politics evolve, more and more people are gaining access to information and communications technology (ICT) [18]. As the so-called “digital divide” is gradually narrowed, bandwidth demands on the worldwide communications infrastructure are set to increase. Previously, the capacity of the global communications network was considered to be practically infinite, but innovations such as the aforementioned WDM have enabled large system bandwidth to be exploited to the point where we are approaching channel capacity [16]. This theoretical upper bound on the rate at which information can be transmitted cleanly over a physical communications channel was formulated by Claude Shannon in 1948 [19] and states that the maximum capacity is

$$C = B \log_2 (1 + \text{SNR}), \quad (1.1)$$

where  $B$  is the channel bandwidth and SNR is the signal-to-noise ratio. Although it may seem feasible to boundlessly increase the capacity by perpetually increasing either or both of these quantities, this is not the case in reality because of practical limitations. Firstly, the bandwidth of a fibre is limited by its low-loss transmission window as displayed in Figure 1.1; this is about 50 THz for SSMF, covering the 1260 nm to 1625 nm waveband [4]. Secondly, the SNR is bounded by the nonlinearity present in optical fibres, which serves to restrict useful signal powers and thereby place a physical limit to

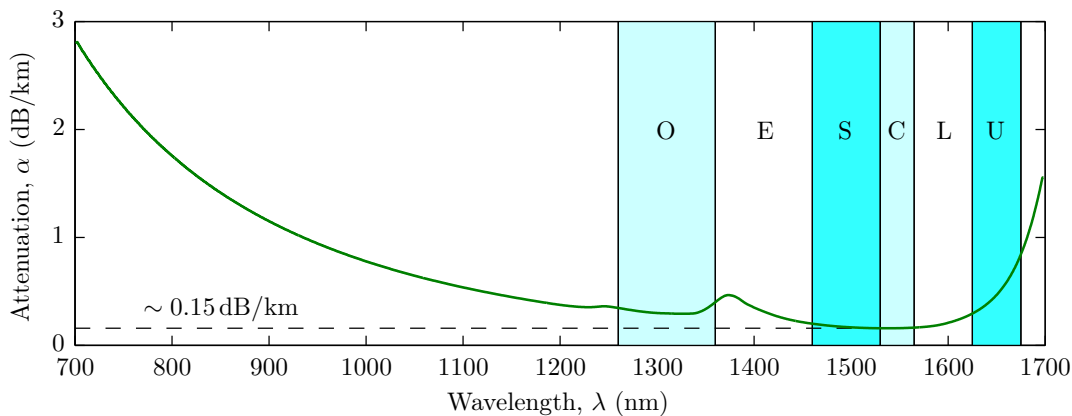


FIGURE 1.1: Attenuation spectrum of SSMF. Alphabets indicate traditionally used wavebands: original (O), extended (E), short (S), conventional (C), long (L), and ultralong (U). *Adapted from [14].*

the Shannon capacity [16, 20]. The inevitable convergence towards this limit, a phenomenon known as the “capacity crunch”, and that which has been predicted to occur within the next ten or so years, can only be averted through radical improvements to the underlying fibre network infrastructure [16, 21, 22]. In addition to this issue being widely acknowledged by the optics academic community, it has also recently been gaining awareness in more public and non-specialist spheres thanks to various university-based *public engagement with research* efforts [23–26] as well as cross-disciplinary networking forums [27].

In the effort to increase capacity in SSMF, various physical dimensions, as shown in Figure 1.2, have been exploited, namely,

- **Time.** In *time-division multiplexing*, the temporal dimension  $t$  is divided into a series of time frames, each containing a set of consecutive time slots, within each of which a data symbol from a particular signal is transmitted. Different signals are identified by their ordered positions within each frame [14].
- **Quadrature.** The electromagnetic carrier wave onto which data is modulated has two orthogonal quadratures arising from the sine and cosine (or real and imaginary) components. Utilising both of these results in a two-dimensional symbol alphabet [28], which allows for *high-order modulation formats* such as quadrature amplitude modulation (QAM), e.g. 16QAM and 32QAM, and phase-shift keying (PSK), e.g. 8PSK. Figure 1.2 illustrates the constellation diagrams of these formats.
- **Frequency.** Multiple signals are transmitted in parallel by using each to modulate a carrier of a different frequency [28]. In optical communications, carriers are identified by their wavelengths and so this is known as *wavelength-division multiplexing* (WDM).
- **Polarisation.** *Polarisation-division multiplexing* involves the transmission of independent signals on each of two orthogonal polarisations [29]. This doubles the capacity relative to a single-polarisation system [28].

Through rapid technological advances, especially that of recent WDM systems, total capacities of  $\sim 20$  Tbit/s have been achieved [30], which is at a factor of only four to seven from the nonlinear Shannon limit [4]. Additional improvements are expected to only provide diminishing returns with limited scalability, leading the communications community to acknowledge that the capacity of SSMF is nearing exhaustion [4, 16, 22, 28]. As depicted in Figure 1.2, the only remaining dimension available for exploration, and the only one that can offer multiple orders of magnitude in capacity scalability, is **space** [4, 28, 31]. Two approaches that aim to realise this are to use fibres with multiple cores, namely, multicore fibres (MCFs) [32], and fibres whose core is enlarged to allow the propagation of multiple waveguide modes, namely, multimode fibres (MMFs) or few-mode fibres (FMFs). This necessarily requires going beyond conventional SSMF and is

what drives research into novel types of optical fibres that could potentially provide an urgently required solution.

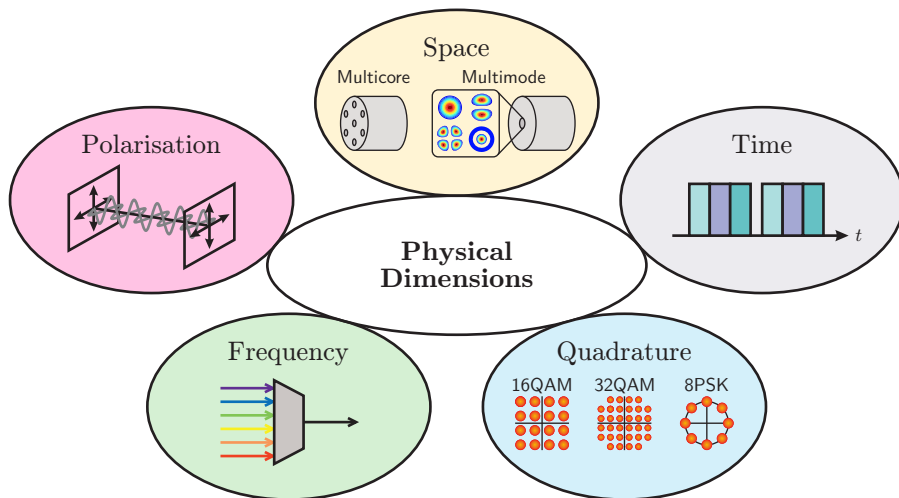


FIGURE 1.2: Physical dimensions available in optical fibre communications [28].

Solid-core FMFs have been explored to address the capacity problem by encoding data onto multiple simultaneously propagating modes in the same fibre [33]. However, their ultimate loss, nonlinearity, and latency limits remain approximately the same as for SSMF, and the more complex transceiver and fibre drawing technology requirements bring their competitiveness over the cost of deploying an equivalent number of channels' worth of SSMFs into question [34]. With their benefits over conventional fibres mentioned above, HC-PBGFs are strong contenders for improving the global fibre infrastructure. However, they are a recent endeavour and there is much to be understood about them in order to fully exploit their capabilities. Such properties that hinder their potential are loss (attenuation) and mode coupling. Although the minimum predicted loss for HC-PBGF is 0.13 dB/km, to date, the lowest loss reported experimentally is 1.2 dB/km [10], which is still an order of magnitude larger than the record for SSMF ( $\sim 0.15$  dB/km [35]). Fabrication efforts are seeking to push that number down as fibre drawing methods improve. Mode coupling is detrimental to both single-mode data transmission as energy is coupled away from the fundamental mode to higher-order modes (HOMs), and to high-capacity mode-division multiplexed transmission as it induces crosstalk and renders modes no longer independent. The properties of PBGFs also make coupling and loss inter-related [36], though experimental treatments in this regard are sparse. An extensive study of the modal characteristics in HC-PBGFs, as well as general solid-core multimode fibres, is thus the goal of the project.

## 1.2 Research Focus and Aims

In October 2010, the *Optoelectronics Research Centre (ORC)* at the *University of Southampton* began a collaboration with eight other industrial, research, and academic partners from around the world on a European Commission funded Seventh Framework Programme (FP7) project called “Multi-mode capacity enhancement with PBG fibre” or *MODE-GAP*. The goal of this project was to realise a 100-fold enhancement of the total data transmission capacity of broadband core networks in order to avert grid-lock within the internet due to the rapidly approaching capacity limit of current networks spurred by the exponential increase in data traffic [37]. This would be achieved through the development of ultralow-loss, ultralow-nonlinearity HC-PBGFs as well as the relevant SDM techniques to harness the multiple spatial mode channels in these fibres [38]. The *ORC* was tasked specifically with the former.

To demonstrate low-loss, high-capacity HC-PBGFs requires extensive theoretical and experimental analyses of these fibres, with the goals of understanding their intricate optical properties and gradually improving their design so as to enable them to realistically match and surpass the performance of conventional solid-core, single-mode fibres. The work in this thesis focusses on exploring the modal and data transmission properties of HC-PBGFs and directly contributed to the fibre development efforts in *MODE-GAP*.

The technical scope of this thesis includes the careful study of HC-PBGFs to assess the following:

- mode extinction and group delays, which affect their
  - capability for single-mode data transmission, and
  - capability for multimode data transmission (MDM) using either digital signal processing algorithms or direct detection
- mode coupling properties, that are related to
  - efforts to reduce loss, and which also determine
  - effectiveness for MDM applications
- actual data transmission performance, that prove their
  - aforementioned potential in the single-mode and MDM regimes, and
  - capability over kilometre lengths, i.e. potential for long-haul communications
- longitudinal defects, in relation to
  - detecting and locating them, and
  - inspecting any induced discrete mode coupling

These are addressed on three fronts. Firstly, characterisation measurements are performed on these fibres with particular emphasis on the time-of-flight (ToF) method. Apart from studying the fibre properties, ToF itself is also shown to be a versatile tool to obtain certain information about the modal properties in HC-PBGFs as well as conventional SCFs, highlighting several advantages it has over other methods. On the systems level, data transmission is carried out on these fibres to assess their actual communications performance. Secondly, a model is implemented to simulate the mode coupling actions in FMFs and HC-PBGFs. By matching simulated and experimental data, it is possible to gather information such as coupling strength, and working with the fabrication team, to also verify predictions based on other models about the origins of mode coupling. Thirdly, to address the question of fibre defects, a method using ToF is developed to detect defects and study possible mode coupling behaviour therein.

Accomplishing these objectives has required collaboration with researchers in the Pulsed Fibre Lasers (PFLG), Microstructured Optical Fibres (MOFG), and Optical Fibre Communications (OFCG) groups at the *ORC*. Their contributions to the work presented in this thesis is explicitly acknowledged where appropriate.

### 1.3 Thesis Outline

The thesis proceeds with a background in Chapter 2, where some theoretical concepts are treated and the HC-PBGF is properly introduced and compared with conventional SCFs. The relevant prior art and recent achievements pertaining to HC-PBGFs is also reviewed.

Chapter 3 introduces the time-of-flight characterisation technique and outlines its principle of operation and experimental set-up. The concept is demonstrated through progressive measurements on 2-mode and 4-mode step-index fibres, where the processes of discrete and distributed mode coupling are explained. The chapter ends with results of characterisation on a novel 9-mode fibre as part of MODE-GAP collaborative work.

Chapter 4 presents characterisation results on HC-PBGFs, including the first ever 37-cell PBGF, and discusses the observations of the modal behaviour. Part of the purpose for these measurements is to determine suitability for single-mode and MDM data transmission. These transmission trials are also included in the chapter. An systematic investigation into diagnosing unexpected performance of a record-length PBGF is detailed. The chapter ends with a brief account of supportive work in ToF characterisation on PBGFs at the 2  $\mu\text{m}$  wavelength region.

Next, a simulation model to study the behaviour of mode propagation and coupling in fibres is described in Chapter 5. The simulation requires the solution of a partial differential equation, and two solver schemes are considered and compared. A study on

how various physical parameters affect mode propagation is presented, with implications on interpreting ToF measurements. The utility of the model to quantify mode coupling, as well as to verify predictions about the origins of the coupling, is then demonstrated.

Penultimately, Chapter 6 describes a method, enabled by ToF, to detect longitudinal defects in fibres and to reveal any defect-induced discrete mode coupling. The principle of the technique is explained, and the method is utilised to inspect a defective HC-PBGF.

Lastly, Chapter 7 concludes the thesis by summarising the main chapters, offering a few possibilities for future work, and making some final remarks. Appendix D describes some work I was involved with in a supporting role.

### 1.3.1 Preamble on Nomenclature and Conventions

Throughout the thesis, where otherwise specified, ‘modes’ and ‘mode groups’ refer to linearly polarised (LP) modes. At times, the acronym for “hollow-core photonic band fibre”, “HC-PBGF”, is written in shorthand as “PBGF”. The terms are synonymous in this thesis.

Equations are referenced by their numbers in parentheses, e.g. (5.1).



## Chapter 2

# Background

This chapter includes some background information as well as relevant theory. Section 2.1 reviews advances in SDM technology. Some fibre optics fundamentals, including modal theory, are covered in Section 2.2. Section 2.3 explains the guidance principle in HC-PBGFs and reviews recent achievements of the *ORC* in PBGF technology, followed by a brief summary in Section 2.4.

### 2.1 Recent Developments

There has been much work on trying to increase capacity in optical fibres. The SDM regime, which has gained much interest, seeks to exploit the spatial domain to make use of multiple channels within a single fibre. As mentioned in Section 1.1, two possible approaches are to use multicore fibres (MCFs) or multimode fibres/few-mode fibres (MMFs/FMFs). In 2012, a record capacity of 1.01 Pbit/s was achieved with SDM applied to 52 km of MCF (12 single-mode cores) [39]. This record was later pushed to 1.05 Pbit/s over a combination of MCF (3 km) and FMF [40]. With regards to MMFs, the technique of encoding independent signals on separate modes is known as mode-division multiplexing (MDM). Experimental proofs of concept have been shown using 2-mode [41–43], 3-mode [41, 44], and 6-mode [45] arrangements. Recently, a system utilising a combination of dense WDM (DWDM), MDM, polarisation-division multiplexing (PDM) in conjunction with the 16-ary QAM format to give DP-16QAM, and a multimode EDFA (another recent development [46–49]) was able to transmit data at a rate of 73.7 Tbit/s over 119 km of FMF [50]. This, and other recent MDM attempts [45, 51], rely on digital signal processing (DSP) at the receiver that uses multiple-input-multiple-output (MIMO) algorithms to undo the effects of mode coupling and thereby recover the signals. While this has been shown to be highly effective when few modes are concerned, the complexity of the DSP systems increases as more modes are used, owing to the larger differential group delays involved [12, 52]. Thus far, all the systems mentioned have operated with

SCFs. The HC-PBGF described in the following sections attempts to make use of some of these developments, as well as provide imperative improvements over conventional SCFs.

## 2.2 Fibre Optics Theory

### 2.2.1 Total Internal Reflection Guidance

The conventional means by which light propagates in an optical fibre is *total internal reflection* (TIR). Light travels through a dielectric core of refractive index  $n_{\text{co}}$  and diameter  $d$ , that is surrounded by a dielectric cladding of refractive index  $n_{\text{cl}} < n_{\text{co}}$ , as shown in Figure 2.1. In the ray optics paradigm, a ray incident upon the interface between the two dielectrics at an angle  $\theta$  from the interface axis that is smaller than the complementary critical angle  $\tilde{\theta}_c$ , will be (theoretically) completely reflected. Starting from Snell's law of refraction, TIR guidance is achieved when

$$n_{\text{cl}} < n_{\text{co}} \cos \theta < n_{\text{co}}. \quad (2.1)$$

In the wave optics paradigm, the propagating light wave is represented, in Cartesian coordinates, as a **wavevector**  $\mathbf{k} = (k_x, k_y, k_z)$  whose component in the direction of propagation ( $z$ ) is the **propagation constant**  $\beta \equiv k_z$ . The wave has a **wavenumber**  $k_o = 2\pi/\lambda_o$ , where  $\lambda_o$  is the wavelength and the subscript  $_o$  denotes quantities in free-space. Within the fibre core, the propagation constant is given by

$$\beta = n_{\text{co}} k_o \cos \theta, \quad (2.2)$$

where the factor of  $n_{\text{co}}$  embodies the scaling of free-space wavenumber by the core medium [14]. The TIR requirement (2.1) can thus be expressed as [53]

$$n_{\text{cl}} k_o < \beta < n_{\text{co}} k_o. \quad (2.3)$$

If  $\beta > n_{\text{co}} k_o$ , then  $\theta$  is imaginary and the light will be evanescent, i.e. decaying exponentially into the cladding [54–56].

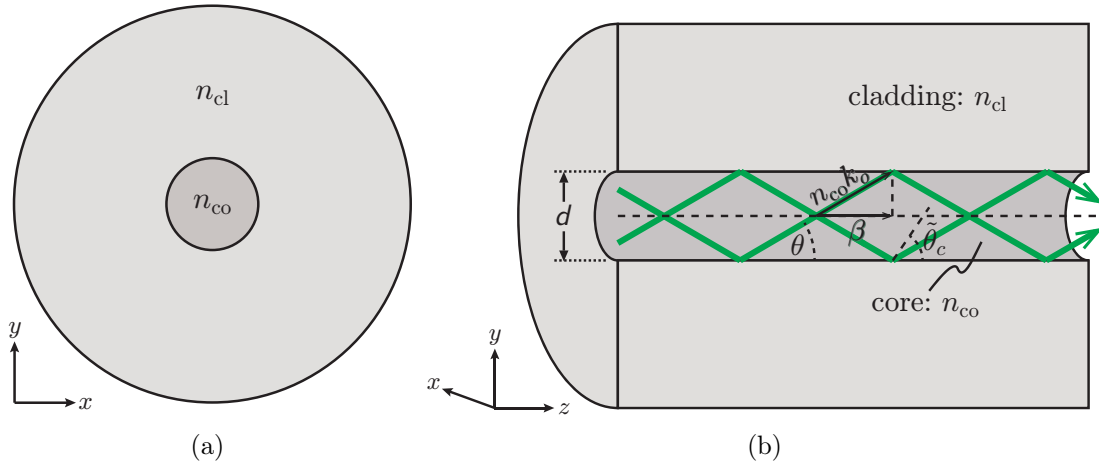


FIGURE 2.1: Simplified cross-section of an SCF in (a) the  $(x, y)$ -plane and (b) three dimensions showing TIR guidance. Green lines indicate light rays. Light grey regions are silica (cladding); dark grey regions are doped silica (core); white regions are air. Axis coordinates are inset.

### 2.2.2 Modes in an Optical Fibre

This section, as well as Sections 2.2.3 and 2.2.4 that follow, provides some theory for guided modes and modal propagation.

It is possible for light (at the same wavelength) to be guided as a variety of distinct spatial **modes** in optical fibres. Modes (as formally defined later in Definition 2.2) are distinguished by their propagation constant and (2.3) gives the range of propagation constants allowed for guidance. However, the set of guided modes in a fibre is discrete rather than continuous. This is because of the *self-consistency condition* [14] necessary for guided modes:

**Definition 2.1 (Self-Consistency Condition).** *In one round trip, a wave that reflects twice off the core/cladding interface of an optical fibre accumulates a path distance lag of  $2d \sin \theta$  behind the original wave, as well as an additional phase after each reflection. The **self-consistency condition** states that the total phase shift between the two waves must be a multiple of  $2\pi$ .*

This condition prescribes the allowed bounce angles  $\theta_m$ ,  $m = 0, 1, 2, \dots$ , for a given wavelength  $\lambda$ , core diameter  $d$ , and core/cladding index difference (captured by  $\tilde{\theta}_c$ ). The  $\theta_m$  in turn determine the propagation constants of the guided modes [14]

$$\beta_m = n_{co} k_o \cos \theta_m, \quad 0 \leq \theta_m \leq \tilde{\theta}_c. \quad (2.4)$$

Only a discrete set of modes, corresponding to a discrete set of bounce angles and propagation constants, are guided. Figure 2.2 gives an example of the trajectories of three

modes propagating in an optical fibre, with blue, orange, and green<sup>1</sup> representing modes of increasing order and bounce angles.

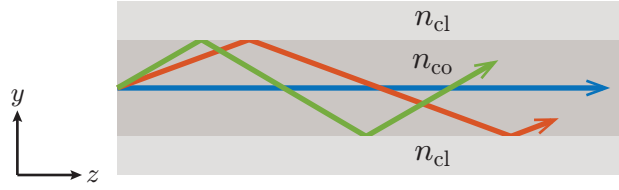


FIGURE 2.2: Various modes, distinguished by coloured rays, propagating in a multi-mode fibre. The positions of the arrowheads show how far each mode has travelled in  $z$  at one snapshot of time.

In the electromagnetic optics paradigm, each mode has a characteristic field distribution in the transverse plane [14]. The actual modes that propagate in fibres are known as **vector modes**, since they represent the exact vector solutions to the wave equation. They are categorised into transverse electric (TE), transverse magnetic (TM), and hybrid (HE and EH) modes. Each mode has a unique propagation constant and effective refractive index, except the even and odd modes of the hybrid modes, whose only difference is their polarisation pattern, but nonetheless share the same propagation constant and so are *degenerate* in a perfectly circular fibre [57]. Modes also differ in their group velocities. As Figure 2.2 shows, the modes arrive at the fibre output at different times, with higher-order modes advancing more slowly and arriving later. This effect is known as **modal dispersion** [58], and may present a challenge for high-capacity communications by limiting the interference-free bandwidth [6, 59]. It will be seen later that modal dispersion can be exploited to enable *time-of-flight* measurements on fibres, the main measurement technique presented in this thesis.

With these principles in place, we are ready to provide a formal definition of modes in an optical fibre.

**Definition 2.2 (Fibre Mode).** *Modes in an optical fibre are fields that maintain the same transverse distribution and polarisation at all locations along the fibre axis. Each mode has a distinct propagation constant and group velocity, a characteristic transverse field distribution, and two orthogonal polarisation states [14].*

Exact vector solutions of the wave equation are generally complicated to compute and in practice, it is easier to deal with *linearly polarised* (LP) modes. These are approximate scalar solutions of the wave equation and are used in the *weakly guiding approximation*, where the core/cladding index difference is small, i.e.  $\Delta := (n_{co} - n_{cl}) / n_{cl} \ll 1$  [57, 60]. This is applicable to most SCFs and to a certain extent, HC-PBGFs. In this approximation, each mode within a family<sup>2</sup> degenerates such that their propagation constants

<sup>1</sup>Note that the colours here distinguish modes, not wavelengths. All the modes are at the same wavelength of light.

<sup>2</sup>“Family” in this context refers to groupings of vector modes whose propagation constants are close to one another.

become approximately equal. The LP modes are then linear coherent superpositions of vector modes within their respective mode group [56, 57]. Table 2.1 lists the transverse intensity spatial profiles of the first few guided LP modes and their vector mode compositions in a circular step-index fibre. The table also provides the nomenclature for the various modes, based on the conventions used in [56, 57, 60–70]:

- For an  $LP_{lm}$  mode,
  - $l$  is the azimuthal index and is the number of azimuthal nodes (i.e. lines of zero intensity) in the intensity profile. The nodal lines are oriented azimuthally at equally spaced angles between 0 rad and  $\pi$  rad.
  - $m$  is the radial index and  $(m - 1)$  is the number of radial nodes (i.e. concentric rings of zero intensity) in the intensity profile; or alternatively,  $m$  is the number of intensity maxima along radial lines from the centre and outward to  $\infty$ .
- For the  $LP_{11}$  mode group, the <sup>even</sup> and <sup>odd</sup> superscripts indicate modes whose spatial intensities are maximised along the  $x$ -axis (horizontal) and  $y$ -axis (vertical), respectively [63, 68]. For other  $l > 1$  modes, these are labels applied to the two orthogonal spatial orientations.
- The  $_x$  and  $_y$  subscripts indicate modes whose transverse electric field vector is aligned only along the  $x$ -axis and  $y$ -axis, respectively [70].

TABLE 2.1: The first few guided modes of a circular step-index fibre. LP modes are shown with their vector mode compositions. Arrows in the spatial intensity profiles indicate the directions of the electric field vector. *Adapted from [57], Fig. 1 and [56], Fig. 1.9.*

Vector Modes			LP Modes			
Group Name	Mode Name	Profile	Group Name	Mode Name	Composition	Profile
HE <sub>11</sub>	HE <sub>11x</sub>		LP <sub>01</sub>	LP <sub>01x</sub>	HE <sub>11x</sub>	
	HE <sub>11y</sub>			LP <sub>01y</sub>	HE <sub>11y</sub>	
TE <sub>01</sub>	TE <sub>01</sub>		LP <sub>11</sub>	LP <sub>11x</sub> <sup>even</sup>	HE <sub>21</sub> <sup>even</sup> + TM <sub>01</sub>	
HE <sub>21</sub>	HE <sub>21</sub> <sup>even</sup>			LP <sub>11y</sub> <sup>even</sup>	HE <sub>21</sub> <sup>odd</sup> - TE <sub>01</sub>	
	HE <sub>21</sub> <sup>odd</sup>			LP <sub>11x</sub> <sup>odd</sup>	HE <sub>21</sub> <sup>odd</sup> + TE <sub>01</sub>	
TM <sub>01</sub>	TM <sub>01</sub>			LP <sub>11y</sub> <sup>odd</sup>	HE <sub>21</sub> <sup>even</sup> - TM <sub>01</sub>	
HE <sub>31</sub>	HE <sub>31</sub> <sup>even</sup>		LP <sub>21</sub>	LP <sub>21x</sub> <sup>even</sup>	EH <sub>11</sub> <sup>even</sup> - HE <sub>31</sub> <sup>odd</sup>	
	HE <sub>31</sub> <sup>odd</sup>			LP <sub>21y</sub> <sup>even</sup>	EH <sub>11</sub> <sup>odd</sup> + HE <sub>31</sub> <sup>even</sup>	
EH <sub>11</sub>	EH <sub>11</sub> <sup>even</sup>			LP <sub>21x</sub> <sup>odd</sup>	EH <sub>11</sub> <sup>odd</sup> - HE <sub>31</sub> <sup>even</sup>	
	HE <sub>11</sub> <sup>odd</sup>			LP <sub>21y</sub> <sup>odd</sup>	EH <sub>11</sub> <sup>even</sup> - HE <sub>31</sub> <sup>odd</sup>	
HE <sub>12</sub>	HE <sub>12x</sub>		LP <sub>02</sub>	LP <sub>02x</sub>	HE <sub>12x</sub>	
	HE <sub>12y</sub>			LP <sub>02y</sub>	HE <sub>12y</sub>	

### 2.2.3 Discrete and Distributed Coupling

In MMFs, multiple supported modes can be excited to carry optical power simultaneously. In certain situations, it may be desirable for light to propagate as only one mode or a subset of the total number of guided modes in a fibre. “Coupling”, in this context, refers to light going into and propagating as one or more modes other than the intended mode, and this can occur either discretely or distributedly. With regards to telecommunications, where various modes are used as different data channels, coupling represents a form of interference, as the coupling of power across modes is akin to interchannel crosstalk when MDM is applied. In the ray optics paradigm, MDM is an analogous form of SDM, with rays of various modes taking different paths along the fibre (see Figure 2.2). Thus, this phenomenon is also known as multipath interference (MPI) [71, 72].

*Discrete coupling*<sup>3</sup> occurs at the launch or splice interfaces of optical fibres, or any point defects along their length. In practice, the incident light does not overlap 100% with the intended mode, and some proportion of power is instead transferred into one or many other (normally adjacent) modes [71]. For example, if the  $LP_{01}$  mode is intended, most of the light at the interface will excite and propagate as that mode, but some light will instead launch the  $LP_{02}$  mode, and perhaps even  $LP_{03}$ ,  $LP_{04}$ , etc. These modes will then copropagate. In real fibres, the nearest neighbour approximation [71], which posits that modes predominantly couple to their nearest adjacent azimuthal and radial neighbours, is often used. This is firstly because the coupling strength between two modes is inversely proportional to the difference between their propagation constants [52, 76, 77]. Secondly, HOMs often suffer greater losses through the fibre, and so their contribution to coupling is negligible compared to lower-order nearest neighbours. The nearest neighbour approximation, which is applicable in both the discrete and the distributed coupling regimes, can be summarised in the following cases:

- Nearest azimuthal neighbour, i.e.  $LP_{l,m}$ ,  $LP_{l\pm 1,m}$ : In the discrete regime, a perfectly central launch would theoretically not cause coupling of this type, due to mode orthogonality. Practically however, perfect central launches are difficult to achieve and there is often some slight misalignment in the launch optics. In this case, it is possible to inadvertently excite azimuthal neighbour modes.
- Nearest radial neighbour, i.e.  $LP_{l,m}$ ,  $LP_{l,m\pm 1}$ : This form of coupling occurs naturally at discrete interfaces, and has the possibility to occur even with perfect central launch conditions.

In practice, either of the above can have the dominant observable effect, depending on how strong the influence of launch misalignment is on the excitation.

---

<sup>3</sup>Some texts [71, 73–75] use the terms “discrete *scattering*” and “distributed *scattering*”, since the mode coupling here is caused by scattering effects.

On the other hand, *distributed coupling* describes the continuous coupling of power between modes, along the length of the fibre due to random imperfections such as surface roughness, core width variations, index inhomogeneities, or microbends [71, 78]. In the distributed regime, nearest azimuthal neighbour coupling is the most likely process [71].

To understand discrete and distributed coupling, consider the example of a pulse launched in a fibre whose output is recorded in the time-domain (e.g. on an oscilloscope). Figure 2.3 shows  $LP_{11}$  (orange) launched into the fibre as the intended mode or *mode under test* (MUT). Due to launch offsets, an  $LP_{01}$  (blue) component and an  $LP_{21}$  (green) component are also excited. From the launch side to the end of the fibre, these three mode components propagate at their respective distinct group velocities  $v$  (these relate to the  $\frac{\text{distance}}{\text{time}}$  gradients of the respective lines), with  $v_{21} < v_{11} < v_{01}$ , and arrive at the output, separated in time (solid peaks). At the output, the differential group delay (DGD) (also known as also known as *differential mode delay* (DMD) [79–82] in this context) between these components will be at their maximum achievable values, since all mode components will have travelled the full length of the fibre; the  $LP_{01}$  and  $LP_{21}$  peaks appear farthest away temporally from the main  $LP_{11}$  output peak. On the other hand, light that couples into the  $LP_{01}$  and  $LP_{21}$  modes, continuously or distributedly over the length of the fibre (blue and green dashed lines, respectively, branching away from the solid orange main  $LP_{11}$  line), will have DMD values that are between zero and the respective aforementioned maximums. The further along the fibre a coupling instance occurs, the shorter the distance the resultant converted component would travel after leaving the main  $LP_{11}$  component, and therefore, the smaller the DMD relative to

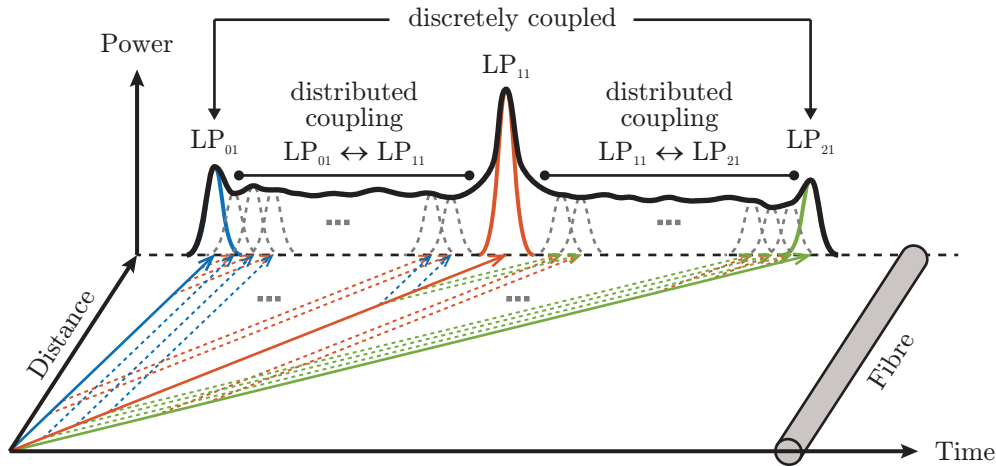


FIGURE 2.3: Time-of-flight of discrete and distributed coupling after an  $LP_{11}$  mode-selective launch in a multimode fibre. The main  $LP_{11}$  component (orange, solid) is accompanied by  $LP_{01}$  (blue) and  $LP_{21}$  (green) components that are discretely coupled at launch (solid) and distributedly coupled over the fibre length (dashed), as well as components from these two modes that are distributedly coupled back to  $LP_{11}$  (orange, dashed). Gradients of  $\frac{\text{distance}}{\text{time}}$  lines are indicative of mode group velocities. The locations along the solid discretely coupled lines from which the other dashed mode lines branch off indicate the lengthwise position along the fibre that distributed coupling events occur. The overall trace appears as the black envelope.

the final main  $LP_{11}$  peak [71]. Moreover, power from the discretely coupled  $LP_{01}$  and  $LP_{21}$  components is also coupled to  $LP_{11}$  continuously. These components, illustrated by the dashed orange lines leaving the solid blue ( $LP_{01}$ ) and green ( $LP_{21}$ ) lines, propagate at  $LP_{11}$ 's group velocity for the remainder of the fibre length. The distributedly coupled components end up as the grey peaks at the end of the fibre. These continuous processes form coupling plateaus [71] in the time-domain trace that span the respective pulse peaks produced by the launch-side discrete coupling. The black envelope in Figure 2.3 illustrates the overall trace and what would be seen in a real measurement: distributedly coupled plateaus demarcated by discretely coupled peaks. The characterisation of an MMF using this method is known as a *time-of-flight* measurement, and has been used throughout this project as a tool for assessing the potential of various fibres for MDM transmission.

### 2.2.4 Power Coupling

Discrete and distributed scattering cause mode coupling. Power is exchanged between modes as they propagate through an optical fibre, hence the specific name, *power* coupling. Coupling is an important consideration in fibres used for data transmission because it directly affects their impulse response [77].

Power coupling is modelled by the following coupled power equation [76–78, 83] for the power  $P_m$  in mode  $m$  over axial distance  $z$  and time  $t$ :

$$\frac{\partial P_m}{\partial z} + \tau_m \frac{\partial P_m}{\partial t} = -\alpha_m P_m + \sum_q \mathcal{C}_{m,q} (P_q - P_m), \quad m, q = 1, 2, \dots, \quad (2.5)$$

where  $\tau_m$  is the modal group delay per unit length,  $\alpha_m$  is the mode-specific attenuation per unit length, and  $\mathcal{C}_{m,q}$  is the coupling coefficient between modes  $m$  and  $q$ .  $\mathcal{C}_{m,q}$  is symmetric (i.e.  $\mathcal{C}_{m,q} = \mathcal{C}_{q,m}$ ) [78] and is proportional to the difference between the propagation constants  $\beta$  of modes  $m$  and  $q$  [77, 83]:

$$\mathcal{C}_{m,q} \propto \frac{A}{(\beta_m - \beta_q)^8}, \quad (2.6)$$

where  $A$  is the coupling strength that depends on the fibre structure [77]. (2.6) shows that the difference in propagation constants must be small for the coupling coefficient to be appreciable. This gives credence to the nearest neighbour approximation in Section 2.2.3. It is noted that although [77] makes the assumption that the vector modes within their LP mode groups have strong coupling due to small propagation constant differences, its applicability may only extend to certain types of solid-core MMFs. As shown in Chapter 4, in HC-PBGFs, the  $\beta$ -separation of vector modes within an LP mode group can be almost of the same order as that between adjacent LP mode groups. In Section 5.3.2

therefore, this assumption is not imposed, and instead, all vector modes are individually considered, in a fashion similar to [83].

To the best of my knowledge, this coupled power analysis has been done only with SCFs, to study their impulse response in the presence of mode coupling [77, 83]. This work seeks to apply this in a similar way to HC-PBGFs.

## 2.3 The Hollow-Core Photonic Bandgap Fibre

HC-PBGFs, also known as air-core fibres, differ from conventional step-index SCFs in both structure and guidance mechanism, in that their cores are air instead of solid dielectric material, and therefore do not guide light through TIR. While detailed studies of PBGF structures and fabrication are outside the scope of this thesis, the following subsections are included to provide some basic information. The section concludes with a brief review of recent developments from our Centre.

### 2.3.1 Photonic Bandgap Guidance

HC-PBGFs are a variant of photonic crystal fibres,<sup>4</sup> in that they contain a form of periodicity in their structure. This periodicity is an alternation between two dielectrics with different refractive indices in the transverse ( $x$  and  $y$ ) directions. The cladding is a periodic array of holes within a solid dielectric (e.g. silica) lattice, as shown in the  $x$ - $y$  plane of Figure 2.4.

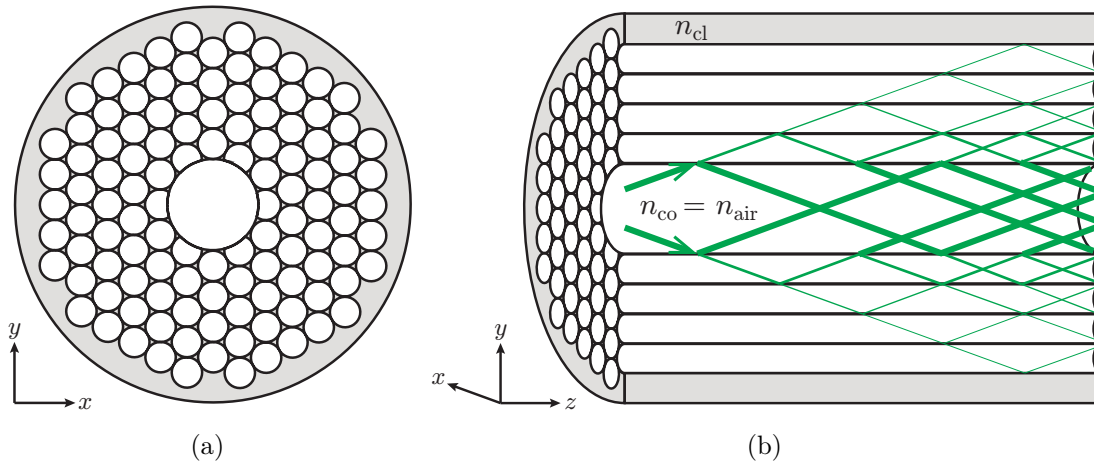


FIGURE 2.4: Simplified cross-section of a HC-PBGF in (a) the  $(x, y)$ -plane and (b) three dimensions exhibiting bandgap guidance. Green lines represent light rays, with thickness corresponding to intensity. Light grey regions are silica; white regions are air. Axis coordinates are inset.

<sup>4</sup>These are also known as microstructured optical fibres [84].

When light is incident upon the periodic crystal structure, it gets reflected and transmitted at each layer. For certain frequency (wavelength) bands, the multiple reflections interfere coherently to satisfy the Bragg condition [54, 55, 85] that prohibits light from propagating through the crystal. These forbidden bands are gaps in the photonic crystal's transmission spectra, and are hence known as **bandgaps**. This is analogous to the solid-state physics model of electronic bandgaps formed via a periodicity of atomic potentials in semiconductors [14, 55, 84–86].

If a defect is introduced into the crystal cladding that breaks its translational periodicity, then it is possible for modes of light within a particular bandgap to propagate within the defect [84, 87, 88]. Such a defect can be realised as an enlargement of a hole in the central cladding region. This, shown as the larger central region inside the cladding in Figure 2.4, is the core of the fibre; hence the name “hollow-core”. Because the bandgap effect prevents propagation transversely, light is thus confined to travel within the locality of the central core defect [11, 53], along the axial direction [89]. The core defect is essentially a cavity that is surrounded by reflecting walls [84] and as depicted in Figure 2.4b, the periodic cladding acts to reflect light such that it is concentrated (confined) within the central core channel [54, 55, 85]. This forms the PBGF guidance mechanism.

Note that for guidance along the longitudinal ( $z$ ) direction, where light travels mostly normal or “out-of-plane” with respect to the plane of periodicity ( $x, y$ ), i.e.  $\beta/k_o \approx 1$ , any index contrast between the two dielectrics (holes and lattice) will satisfy the conditions for bandgap guidance [90]. This permits the use of air holes within a silica lattice, despite the modest refractive index difference of the two media.

### 2.3.2 HC-PBGF Structure and Fabrication

The transverse structure of a HC-PBGF comprises the outer cladding, which consists of a triangular lattice of holes (TLH) [54] or **cells** of air within a silica network of interstitial struts, and a central core, which is simply a larger air hole. The TLH geometry can be described as having concentric “rings” of cells. The large core hole is an omission of one or more of such holey rings. Since the rings are layered discretely, variation of the core size is thus limited to a being of a discrete set of multiples of cells; or equivalently, the core diameter is an approximate integer multiple of the cladding pitch<sup>5</sup>  $\Lambda$  or lattice constant [11]. Cladding cells in the shape of rounded hexagons provide a better air-filling fraction<sup>6</sup> than circular ones [9, 86], and so the number of omitted cells  $n$  in the

<sup>5</sup>The terms “hole-to-hole spacing”, “inter-hole distance” [86], “centre-to-centre spacing” [90], and “spatial period” [84] are also used synonymously here.

<sup>6</sup>The air-filling fraction determines the width and position of the bandgap [9, 91] and therefore has an effect on the fibre transmission bandwidth. Generally, a high air-filling fraction is necessary for wide-bandwidth, low-loss transmission [86].

core follows the progression for a cyclic hexagon tessellation, i.e.

$$n_i = \begin{cases} 3, & i = 1, \\ 1 + 6 \sum_{x=2}^i (x - 1), & i \in \mathbb{N}, i \geq 2, \end{cases} \quad (2.7)$$

where  $i$  is the cycle index. Hence, we have fibres with 3, 7, 19, 37, etc. omitted cells for their cores, as illustrated in Figure 2.5. In PBGF parlance, fibres are identified by their core size and the naming convention follows “ $n$ -cell HC-PBGF”.

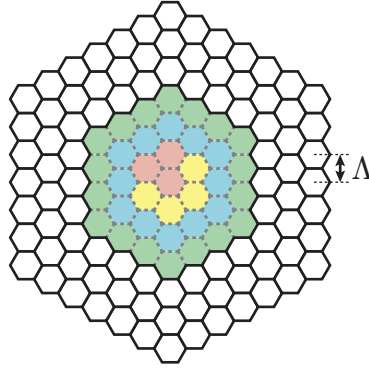


FIGURE 2.5: Hexagonal TLH tessellation for HC-PBGF transverse geometry. Dashed grey lines show omitted cells constituting the fibre core of various sizes, namely (green + (blue + (yellow + (red = 3) = 7) = 19) = 37) cells. White hexagons represent the cladding holes.  $\Lambda$  = pitch.

From a fabrication perspective, the fibre is made by applying the stack-and-draw method to a preform of stacked capillaries<sup>7</sup>. The core is made by omitting a number of capillaries (cells) in the middle of the stack [9, 11]. During the draw, differential pressures within the holey structure are accurately controlled to prevent surface tension induced collapse as well as to achieve a high air-filling fraction from substantial expansion of the holey region [92].

Figure 2.6 shows the scanning electron microscope (SEM) image of a 37-cell HC-PBGF that was fabricated in our cleanroom and presented in [93–95].

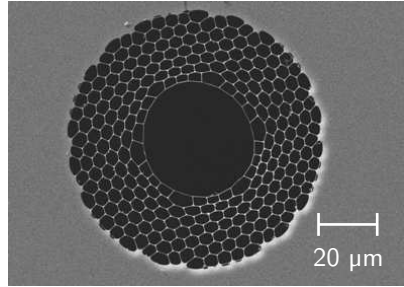


FIGURE 2.6: SEM of a 37-cell HC-PBGF. Taken from [93], Fig. 1(a). Used with permission.

<sup>7</sup>These capillaries later form the cladding hollow ‘cells’ or holes.

### 2.3.3 Guided Modes in HC-PBGFs

Figure 2.7 presents a plot of effective index against wavelength, colloquially known as a dispersion graph, of a fictional PBGF. Only modes within the bandgap, indicated by the mode curves in the dispersion graph, can be guided and propagate along the fibre. It has been shown theoretically that 19-cell PBGFs can support up to 40 guided modes [11, 86], whereas this number is doubled for 37-cell PBGFs [86, 93, 94]. The extent of the bandgap is dependent on the cladding structure. Since this is the same regardless of core size, it means that the larger number of modes guided in 37-cell fibres have effective indices and propagation constants that are closer to one another, as compared to the 19-cell case, i.e. the bandgap in the 37-cell dispersion graph is more densely populated with mode curves [11].<sup>8</sup>

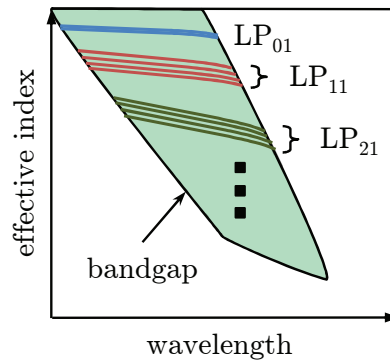


FIGURE 2.7: Plot of effective index versus wavelength in a fictional HC-PBGF, showing the bandgap.

### 2.3.4 Features of HC-PBGFs

HC-PBGFs, by virtue of their material and guidance properties, introduce a number of improvements over conventional SCFs. Firstly, HC-PBGFs exhibit low optical nonlinearity [9, 11]. This is because most (more than 99% for the fundamental mode [10]) of the light propagates in air, where there is much less nonlinearity (nearly 3 orders of magnitude lower [12]) than in silica. Experiments have also accordingly shown that HC-PBGFs with larger cores experience less field overlap with the glass core surround and therefore have lower nonlinearity [11]. Secondly, HC-PBGFs have the potential for lower loss, again since the light propagates in air as opposed to silica and thence experiences much less scattering and absorption [9, 10]. In fact, the primary loss mechanism in HC-PBGFs comes from surface roughness-induced scattering [10, 11], rather than Rayleigh scattering, and attempts have been made to minimise this by reducing the optical field overlap at the core/cladding boundary through enlarging the core size, e.g. from 19 cells to 37 cells [93]. Thirdly, air being the medium of propagation in HC-PBGFs means that

<sup>8</sup>Reference [11] shows this trend for 3-, 7-, and 19-cell PBGFs. The explanation above is an extrapolation to the 37-cell case.

signals transmitted suffer lower latency compared with SCFs, by as much as 31% [8, 96], since light travels faster in air than it does in silica. Experiments on 19-cell HC-PBGFs have confirmed this improvement [13].

Attempts have also been made to exploit the multimode nature of HC-PBGFs, and MDM was realised for the first time in 7-cell and 19-cell fibres in [97]<sup>9</sup> and [98], respectively. Recent published work has shown successful MDM on a 37-cell fibre [93], the first of its kind, though only the first two LP mode groups were used. In order to tap into the supposedly vast resource of guided modes in HC-PBGFs, detailed studies of the properties of mode coupling need to be made. Our understanding of mode coupling (crosstalk) in PBGFs is that it is related to loss. Of the energy scattered by surface roughness along the fibre core surround, some actually excites other guided modes. This is the effect of distributed coupling previously described. [10] provided a theoretical treatise on the effects of loss from surface roughness. This behaviour is shown in a reproduced plot in Figure 2.8. The deformations causing the roughness along the surface are modelled as a wave with spatial frequencies  $\kappa$ . The degree of roughness is quantified by the spectral density, and shows an inverse trend with increasing  $\kappa$ . It is predicted that the effects of mode coupling and loss come from the low and high spatial frequency regions, respectively. This means that coupling and loss are distinct but related, though the complete details of that relation are not yet fully understood. It has been suggested that as losses are pushed lower owing to better fabrication techniques, mode coupling and crosstalk should follow suit and also decrease [36]. Therefore, one of the aims of the MOFG in the *ORC*, as well as this thesis, is to model mode coupling in HC-PBGFs, in order to better comprehend its properties and dependencies on other parameters, and thereby extend the established theoretical framework.

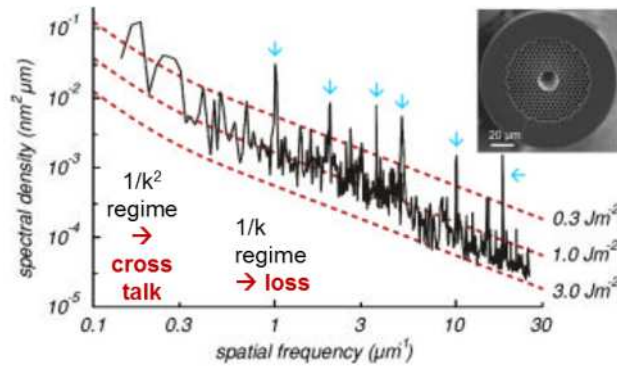


FIGURE 2.8: Plot from [10] of fibre roughness spectral density against deformation spatial frequency  $\kappa$  ( $= k$  in the plot). Adapted by F. Poletti; used with permission.

<sup>9</sup>This is also the first demonstration of MDM in a HC-PBGF.

### 2.3.5 Recent ORC Work and Achievements

The following subsections review work that has been done on 19- and 37-cell HC-PBGFs that were fabricated in our Centre's cleanroom facility. Several elements involving work presented in this thesis are noted.

#### 2.3.5.1 The 19-cell HC-PBGF

19-cell (19c) HC-PBGFs have been fabricated for potential applications in low-loss, low-latency data transmission [13]. Cutback measurements showed the fibre in [13] to have a low loss of 3.5 dB/km at a wavelength of  $\sim 1500$  nm and a wide transmission bandwidth of 160 nm. Time-of-flight measurements were performed to assess its modal characteristics and while several HOMs were present, good selective excitation results showed the possibility of single-mode operation, leading to a demonstration of 1.45 Tbit/s single-mode data transmission in [99]. Later, high capacity transmission was achieved at 24 Tbit/s using DWDM and dual-polarisation 32-ary quadrature amplitude modulation (DP-32QAM) [34]. MDM (two modes) was also demonstrated over a 19c PBGF, using an integrated mode multiplexer in [100].

As mentioned previously, experiments were also carried out to test latency. In [13], time-of-flight measurements taken at the operating wavelength of 1556 nm recorded the arrival time of pulses sent through the 19c HC-PBGF relative to the back-to-back setup. By comparing this with the case of using a standard telecommunications (solid-core) fibre, it was found that light in the hollow core indeed propagates close to the speed of light in vacuum, which is about 1.46 times faster than in SCFs. Subsequently, HC-PBGFs have been explored for a number of low-latency data communications applications. Gamma irradiation tests on a 19c PBGF in [101] showed good radiation hardness and demonstrated the potential for using HC-PBGF-based optical links in harsh radiation environments, such as the Large Hadron Collider at the *European Organization for Nuclear Research (CERN)*, for high energy physics experiments. Data centre interconnection is also considered as an application, and the use of HC-PBGF links was demonstrated in [102] and [103], with preliminary proofing data transmission trials performed by myself (see Section 4.2.5).

Operation at the 2  $\mu$ m wavelength region, which is the predicted region of lowest loss for HC-PBGFs [10], is also being studied. A 19c HC-PBGF operating at 2008 nm was fabricated, and preliminary transmission results at 8 Gbit/s, the first ever transmission in a 2  $\mu$ m PBGF, showed the potential for ultralow-loss applications [104]. Later, the first 2  $\mu$ m-waveband WDM transmission over PBFG was demonstrated on this fibre in [105], achieving a capacity of 16 Gbit/s over four channels. These experiments used a custom built thulium-doped fibre amplifier that was subsequently fully characterised and

reported in [106]. In [107], the  $\lambda^{-3}$  wavelength scaling behaviour of transmission loss in HC-PBGFs predicted in [10] was experimentally verified for the first time.

Finally, recent efforts have been made to scale the reach of HC-PBGFs for application in metropolitan networks. [108] reported a record-length 11 km (1550 nm-wavelength) 19c HC-PBGF, the longest ever single span fabricated. It was subsequently sectioned and used in a 74.8 km recirculating loop experiment at 40 Gbit/s in [109]. This particular work included my contributions to mode coupling characterisation and performance diagnostics (see Section 4.3). Macrobending effects on this fibre were studied in [110]. A long 3.8 km 2  $\mu$ m-wavelength 19c PBGF was also made and reported in [111]. 52 Gbit/s data transmission was achieved in this fibre in [112].

### 2.3.5.2 The 37-cell HC-PBGF

Attempts to reduce loss due to surface roughness scattering [10] in HC-PBGFs have spurred efforts to increase the core size from 19 cells to 37 cells. A 37-cell (37c) HC-PBGF has been fabricated, and cutback measurements by myself and others at the 1550 nm-wavelength displayed a minimum loss of 3.3 dB/km for the fundamental mode [93]. Modal characterisation as well as single-mode data transmission at 40 Gbit/s, which involved myself and fellow group members, were performed and presented in [94]. In [93] and [95], the possibility of applying MDM was validated, and by implementing a system with 3 modes and 96 DWDM channels carrying 256 Gbit/s DP-16QAM data, a total capacity record of 73.7 Tbit/s was achieved.<sup>10</sup> These works include a large component of the thesis contributions, and Chapter 4 describes the modal and data transmission experiments herein.

### 2.3.5.3 Theoretical and Computational Studies

Work from our Centre has also been carried out to model the physical behaviour and optical mechanisms within HC-PBGFs. Models have been developed to study surface roughness scattering and its contribution to loss [113, 114]; to predict in real-time the structural (e.g. air-filling fraction) and optical (e.g. transmission bandwidth) properties of drawn fibres from their preform structures [92]; to explain the origin of surface modes and techniques for suppressing them [115]; to elucidate how optical performance is affected by distortions in the fibre microstructure [116]; and to investigate the effects of microbending on intermodal coupling and loss [117]. An improved technique has been developed in [118] to overcome previous resolution limitations when digitally reconstructing actual PBGF cross-sectional geometries from SEM images of real fibres. These methods

---

<sup>10</sup>This multidimensional multiplexing scheme is the same as that for the earlier FMF trial [50] mentioned in Section 2.1, just applied to a HC-PBGF instead, hence the similar capacity figure.

have collectively enabled more accurate predictions of loss, transmission bandwidth, and surface mode properties in fabricated PBGFs.

Distributed mode coupling in HC-PBGFs has also been analysed in [36]. We were able, in part by using a mode propagation simulation routine that I developed [119] (presented in Chapter 5), to model the origin of said coupling, compare it with that in SCFs, and further explain its relationship with surface scattering induced loss.

Other efforts have been targeted towards making the fibre design process more cost efficient. A fluid dynamics model was formulated in [120] to predict the structural evolution of preforms drawn to fibres. This formed the basis of the “MicroStructure Element Method” (MSEM) in [121], which is able to simulate virtual fibre draws from arbitrary drawing parameters. This has been combined with the electromagnetics model in [116] to create a toolset that can virtually draw practically accurate HC-PBGFs and predict their structural and optical properties, thus offering a cost- and time-saving alternative in fibre design, compared to empirical trial and error based optimisation on actual fibres [122]. The MSEM has also been employed to study the impact of upscaling preform sizes to enable volume manufacturing of longer-length fibres [123].

#### 2.3.5.4 Other Experimental and Characterisation Work

On the experimental front, various characterisation methods have been advanced. In the context of modal content measurement, improvements have been made to the  $S^2$  technique [73] including decreasing the scan time to enable near real-time measurements, as well as reducing spectral leakage and sampling errors to increase the accuracy of measured MPI values. These have been respectively demonstrated theoretically in [124] and [125], and applied experimentally to HC-PBGFs in [126] and [127]. Additionally, a low-coherence interferometry method for measuring group velocity dispersion was reported in [128]. This was extended with mode-selective measurements of 3-, 7-, and 19-cell HC-PBGFs in [129].

The issue of splicing has been investigated. A new technique was developed to realise low-loss splicing of HC-PBGFs to themselves [130] and to SCFs [131], with reliable 40 Gbit/s single-mode data transmission subsequently demonstrated over 1 km of spliced PBGF spans in [132].

Methods to study longitudinal defects in HC-PBGFs have also been addressed. X-ray computed tomography was used in [133] to scan PBGFs and preforms. This allows for 3D structural visualisation of identified defects. In [134], an infrared side-scattering technique for locating fibre defects was introduced to overcome the metre-scale resolution limit of existing optical time-domain reflectometry (OTDR) measurements. By incorporating a rig on a fibre-rewinding machine in our Centre, a new “Optical Side Scattering

Radiometry” (OSSR) technique was developed which simultaneously offers centimetre-scale spatial resolution as well as a high dynamic range of up to 60 dB (compared to OTDR where a trade-off must be made). This was reported in [135], which included my contributions of bidirectional OTDR measurements for the comparative study (see Section 6.3). These measurements also form part of a separate defect inspection method that I developed in [136] to utilise mode-selective OTDR and time-of-flight to locate defects in PBGFs and investigate defect-induced mode coupling, which is the subject of Chapter 6.

## 2.4 Summary

This chapter has provided the relevant background for the thesis. Theoretical fundamentals concerning optical guidance and mode propagation in SCFs and HC-PBGFs have been covered. Reviews of some recent developments in high-capacity communications, as well as experimental and computational achievements of the *ORC* in 19c and 37c HC-PBGF technology, have been included. The chapters that follow describe the main technical work in the thesis.

## Chapter 3

# A Tool for Modal Characterisation

HC-PBGFs have the ability to guide a large number of optical modes (theoretically, up to 40 in 19c [11] and up to 80 in 37c [86, 94] fibres, both including degeneracies). In order to assess their capability of using different modes or mode groups as independent communications channels, or conversely, to determine if they can be used for single-mode operation amid the multiple modes supported, it is therefore necessary to study the modal behaviours of such fibres. Primarily, we are interested in information including extinction ratio, distributed coupling, DMD, and mode-dependent loss (MDL). There are a number of techniques available for the analysis of modal content in MMFs. These can be largely categorised into time-domain techniques and frequency-domain interferometric techniques [82]. An example of the latter is spatially and spectrally resolved imaging ( $S^2$ ) [73], where the spatial overlap of co-propagating modes produces spectral interference patterns at each transverse plane position (i.e. at each pixel) that are measured with an optical spectrum analyser (OSA). This series of traces is then Fourier transformed and summed to obtain a time-domain trace showing the relative delays and amplitudes of HOMs. In contrast, time-domain techniques such as the time-of-flight (ToF) method [82] provide similar information by temporally sampling the signal that is output from a fibre when pulsed light is launched in it. This procedure is widely adopted for measuring DMDs [79], and bears resemblance to earlier techniques for measuring chromatic dispersion [137]. A major advantage of ToF over frequency-domain techniques is that it does not need an interferometer [82], nor Fourier transform calculations, thus making it simpler to implement and faster to collect modal data. The fast response means that not only can DMD be directly measured, but the relative modal amplitudes can also be observed to vary in real-time as input launch conditions are changed. This enables a simple way of optimising selective mode launching, a feature that is not possible in  $S^2$  measurements.

ToF is versatile in its applications. Besides the relative delay, extinction, coupling, and other information provided in the time-domain traces, it can also be used as a real-time feedback aid to achieve optimised modes launches for various applications, by

checking relative mode extinctions. This is helpful as a monitoring tool when attempting experiments such as single-mode data transmission, MDM, and even optimisation of optomechanical alignment for splicing and the design of multimode amplifiers. It also affords the ability to perform other measurements on fibres, for instance, optimised-mode cutback to measure MDL.

In the following sections, I describe the ToF method and its implementation and measurement procedure in detail. The measurement principles and capabilities are illustrated, in Sections 3.1 through 3.3, through the progressive presentation of results from solid-core fibres supporting increasing numbers of modes, including a novel fibre that guides nine modes over five mode groups [138], detailed in Section 3.4. A comparison between ToF and the  $S^2$  method is then given in Section 3.5, followed by the summary and suggestions for future work in Section 3.6.

### 3.1 Time-of-Flight Operating Principle

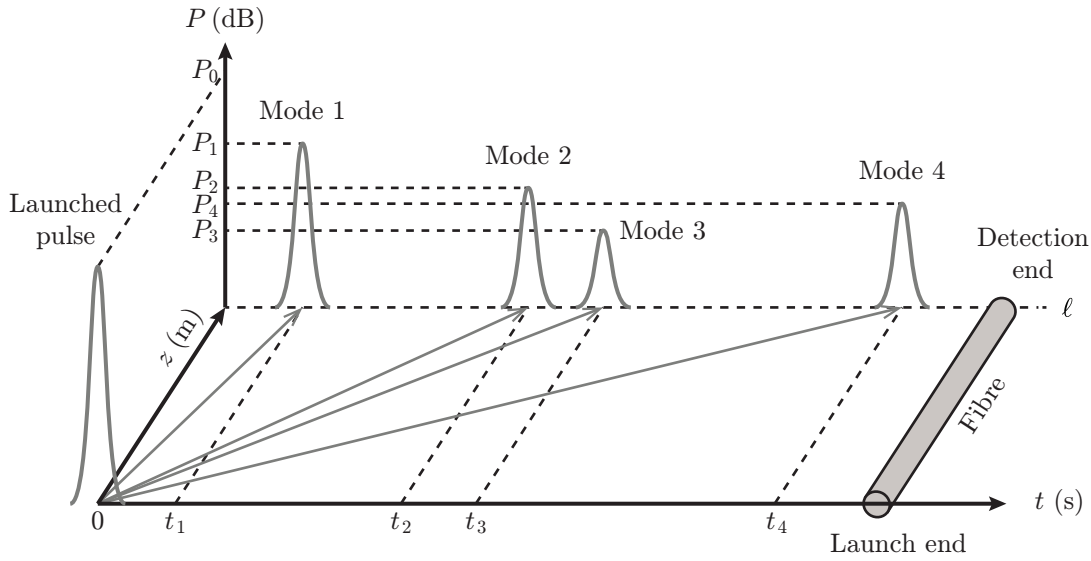


FIGURE 3.1: Pulse propagation through a 4MF of length  $\ell$ . The relative delays of different modes cause them to split into distinct pulse components after propagating through the fibre.  $t$  = time (absolute delay),  $z$  = distance,  $P$  = normalised power.

ToF measurements can be used to assess the modal content of MMFs including HC-PBGFs. This is done by exploiting modal dispersion. As various modes propagate through a fibre, they spread out in time, by virtue of the HOMs having lower group velocities than the fundamental mode, giving rise to DMD between modes [14, 80, 81]. Figure 3.1 illustrates this using an arbitrary 4-mode fibre (4MF) as an example. When a light pulse is launched into one end of the fibre, minute spatial offsets in the launching mechanism may cause the excitation of multiple modes. The total power in the original

pulse is split among these modes according to how efficiently each was respectively excited. These mode components then propagate as individual pulses at their respective group velocities, with longer grey arrowed lines in the figure indicating slower group velocities. This spreads out their arrival times  $t_m$  at the detection end of the fibre. An oscilloscope capturing this will display a series of pulse peaks corresponding to each mode component [57], with the temporal separation between peaks being determined by the difference in relative group velocity.

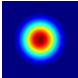
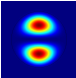
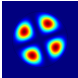
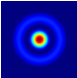
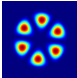
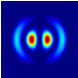
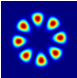
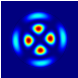
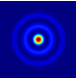
The power  $P_{\text{in}}$  (in dBm) of the original launched pulse at the fibre input evolves through the fibre as it is split among the guided modes and is also affected by loss. Neglecting contributions from non-guided modes and other discrete losses, the power composition can be approximated as

$$P_{\text{in}} = \sum_{m=1}^{N_m} (P_m + \alpha_m \ell), \quad (3.1)$$

where  $P_m$  (dBm) and  $\alpha_m$  (dB/m) are the output power and mode-dependent loss, respectively, of mode  $m$ ,  $\ell$  (m) is the fibre length, and  $N_m$  is the number of guided modes. In some fibres, e.g. solid-core fibres, the individual  $\alpha_m$  may be equal or vary negligibly, whereas in others, e.g. HC-PBGFs, they may vary considerably, with HOMs suffering higher loss based on measurements. In the latter case therefore, the output  $P_m$  are not valid indicators of the input launch efficiencies of each mode. That is, a mode that was excited to a lower power than another mode at launch might end up retaining more power at the detection end if it suffered less loss than the second mode.

The distinction in delays corresponding to individual modes is exploited to spread the arrival times of mode pulses [57] and thereby facilitate mode identification when sampled temporally on an oscilloscope.  $S^2$  analysis [74, 75, 139] provides numerical values for the DMD (per metre of fibre) that can be cross-referenced when trying to identify mode peaks as they appear on the oscilloscope during a ToF measurement. Another method for mode identification is to capture the mode image at the output of the fibre using a charge-coupled device (CCD) camera. This can be used to complement  $S^2$  measurements, or as an alternative when such numbers are unavailable. Table 3.1 shows simulated mode intensity profiles for the first nine LP modes, obtained through the COMSOL Multiphysics<sup>®</sup> modelling software ([www.comsol.com](http://www.comsol.com)) and using parameters similar to [140]. These are used as a reference for identifying mode profiles captured by a CCD.

TABLE 3.1: Simulated mode intensity profiles in a multimode fibre. The colourbar inset indicates intensity from 0 (blue) to high (red).

Mode	LP <sub>01</sub>	LP <sub>11</sub>	LP <sub>21</sub>	LP <sub>02</sub>	LP <sub>31</sub>	LP <sub>12</sub>	LP <sub>41</sub>	LP <sub>22</sub>	LP <sub>03</sub>
Intensity Profile									



A metric often employed is the extinction ratio (ER) between modes. This describes how strongly a particular mode can be received by suppressing other modes and is a measure of how distinct other modes (OMs) are in terms of received power. The ER (defined in dB for convenience) between a particular mode and an OM  $q$  is given by<sup>1</sup>

$$r_{\text{ex}} \approx -10 \log \left( \frac{P_{\text{pk},q}}{P_{\text{pk}}} \right), \quad \text{for } q = \text{LP}_{01}, \text{LP}_{11}, \text{LP}_{21}, \dots, \text{LP}_{N_l, N_m}, \quad (3.2)$$

where  $P_{\text{pk}}$  is the received peak power (in W) of the ToF pulse corresponding to the mode under test (MUT),  $P_{\text{pk},q}$  is the peak received power of the ToF pulse corresponding to OM  $q$ , and  $\text{LP}_{N_l, N_m}$  is the designation of the highest supported HOM.

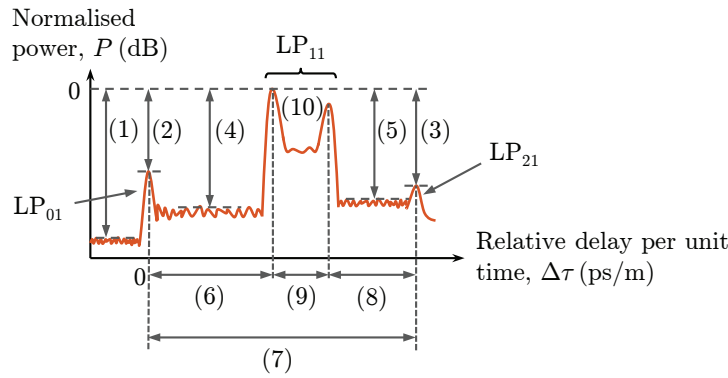


FIGURE 3.2: Example of a ToF trace for an optimised  $\text{LP}_{11}$  launch showing key features.

Figure 3.2 depicts an example ToF trace of an optimised  $\text{LP}_{11}$  launch. The main features are as follows:

- (1) Dynamic range of detector (dB); lower limit is the noise floor
- (2) ER of  $\text{LP}_{01}$  with respect to (w.r.t.)  $\text{LP}_{11}$  (dB); a measure of how much power went into  $\text{LP}_{01}$  at launch
- (3) ER of  $\text{LP}_{21}$  w.r.t.  $\text{LP}_{11}$  (dB)
- (4) Distributed coupling plateau between  $\text{LP}_{11}$  and  $\text{LP}_{01}$  (dB); indicates how much power is distributedly coupled between  $\text{LP}_{11}$  and  $\text{LP}_{01}$
- (5) Amount of distributed coupling between  $\text{LP}_{11}$  and  $\text{LP}_{21}$  (dB)
- (6) DMD between  $\text{LP}_{01}$  and  $\text{LP}_{11}$  (ps/m)
- (7) DMD between  $\text{LP}_{01}$  and  $\text{LP}_{21}$  (ps/m)
- (8) DMD between  $\text{LP}_{11}$  and  $\text{LP}_{21}$  (ps/m)

---

<sup>1</sup>Note that this definition is merely a practical estimate. Exact ERs require the calculation of the integral over all other modes.

- (9) Delay spread of vector modes within  $LP_{11}$  (ps/m)
- (10) Vector mode peaks in the  $LP_{11}$  mode group

The features in the ToF trace have implications on the fibres' data transmission abilities:

- Single-mode transmission: Higher ERs and distributed coupling plateaus indicate that less power is coupling into other modes. An ER of  $\geq 20$  dB is generally accepted as being necessary for using single modes as reliable data communications channels [13, 94].
- Using HOMs, e.g. in MDM: If higher-order mode groups spread into multiple peaks, direct detection cannot be used and DSP will be necessary to compensate for the intra-group dispersion and mode coupling, in addition to the DMD between mode groups.

In lieu of these, ToF measurements are almost always performed before any data transmission is attempted.

## 3.2 Experimental Set-Up and Procedure

### 3.2.1 Excitation

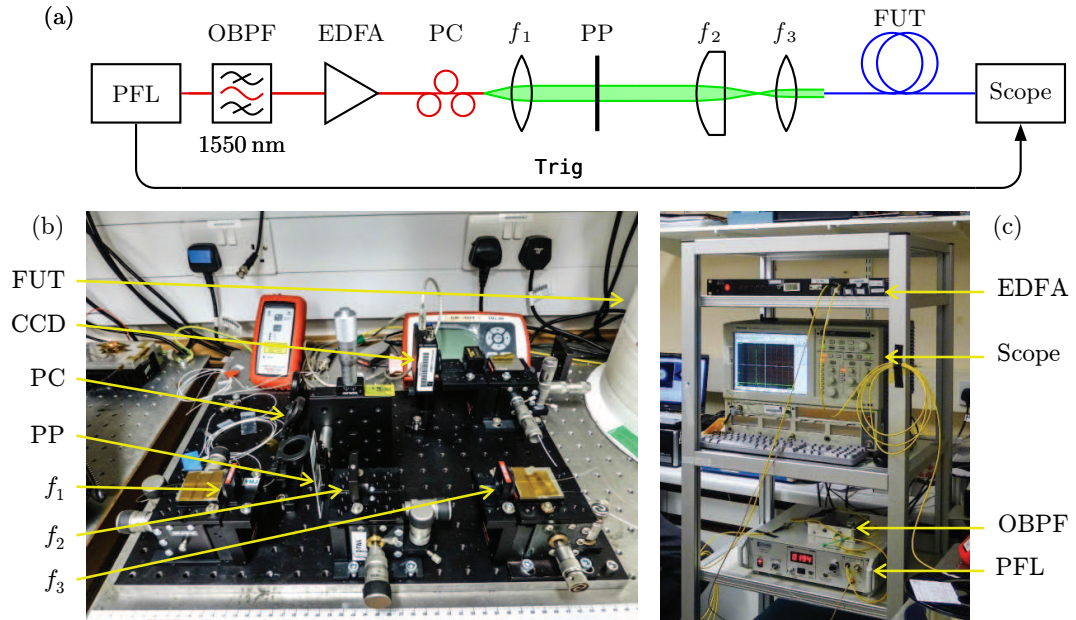


FIGURE 3.3: Time-of-flight (ToF) experimental set-up. (a) Schematic. (b-c) Equipment photographs.

The ToF set-up is as shown in Figure 3.3. A mode-locked femtosecond pulsed fibre laser (PFL), tuned at the standard telecommunications wavelength of 1550 nm, followed by an optical bandpass filter (OBPF), with a Gaussian-shaped passband bandwidth set to  $\sim 2$  nm full width at half maximum (FWHM) [13], is used to generate sub-ps optical pulses at a repetition rate of 20 MHz.<sup>2</sup> Figure 3.4 shows the spectrum of the output signal from the PFL as well as that of the filtered pulse, measured with an OSA. The purpose of limiting the bandwidth of the input pulses is to minimise chromatic dispersion [77], which causes temporal pulse broadening, so that the DGDs measured on the ToF traces can be reasonably assumed to be predominantly due to modal dispersion. In other words, the pulse bandwidth is limited to ensure that the broadening of the pulse width due to chromatic dispersion is much less than the pulse separation due to DMD, so that individual peaks can be resolved. Although this spectral narrowing brings about temporal broadening of the pulses due to the Fourier transform relation [14], the extent of the pulse widths is still within the sub-picosecond range, which is sufficiently short for the purposes of experiments of this type.

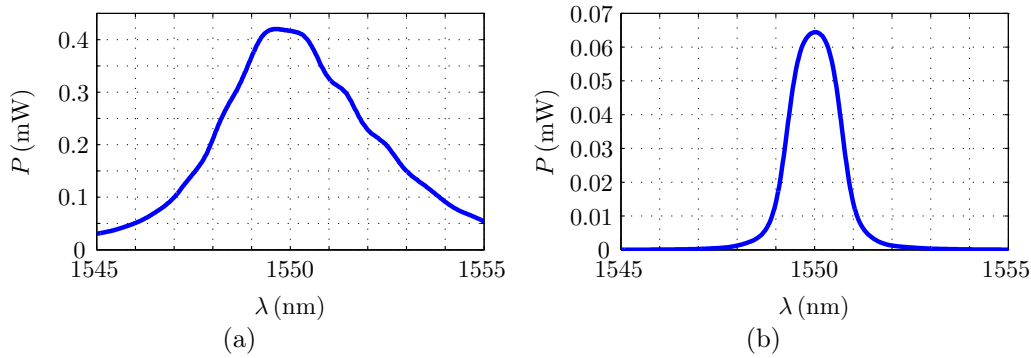


FIGURE 3.4: Spectrum of (a) output signal from PFL and (b) signal after OBPF.  $P$  = power,  $\lambda$  = wavelength.

The pulses are amplified by an EDFA and launched into the fibre under test (FUT) by means of the free-space segment. Sometimes, vector effects including polarisation dependence need to be studied. In these cases a polarisation controller (PC) is included just after the EDFA, otherwise it is omitted.<sup>3</sup> The free-space optics consists of an aspherical lens of focal length  $f_1 = 4.5$  mm or 3.1 mm to collimate the incident light at the input, a binary phase plate (PP) that can be shifted transversely to selectively excite different modes, and a telecentric imaging system [45] formed by the combination of a plano-convex lens of focal length  $f_2 = 125$  mm and another aspherical lens of focal length  $f_3 = 3.1$  mm. These values were chosen so that the demagnification achieved can

<sup>2</sup>This rate cannot be too fast. The relative delay extent of HOMs must be shorter than the pulse periodicity [82], lest intersymbol interference occurs and HOMs of adjacent cycles overlap with each other. The largest delay spread was observed to be on the order of  $\sim 10$  ns to 20 ns for km-length FUTs, and so a 20 MHz repetition rate (corresponding to a pulse period of 50 ns) is enough to accommodate this.

<sup>3</sup>Unless otherwise stated, the various ToF measurements described in this thesis have omitted the PC. It is included in the schematic in Figure 3.3 for the sake of reference.

produce a beam diameter that matches the mode field diameter (MFD) of the FUT, thus ensuring maximum coupling efficiency.<sup>4</sup> The resultant collimated beam is directly launched into the FUT.

For most experiments reported in this thesis, only modes up to  $LP_{21}$  are launched,<sup>5</sup> and therefore a 4-region PP is used in the set-up. Figure 3.5 (left) shows the phase layout of such a PP. It consists of four phase regions that shift the phase of an incident light beam, where diagonal regions shift the phase by an equal amount and adjacent regions shift the phase by a relative amount of  $\pi$  rad. This is achieved by each phase region having a different thickness introducing differences in optical path length. In the figure, the top-left region of this PP has arbitrarily been designated a phase shift of 0 rad (i.e. the reference phase shift). When a beam is incident upon the PP, its different spatial regions that pass through the different phase regions get shifted in phase by the respective relative amounts, thereby enabling the excitation of higher-order modes [141]. Because of the fact that the  $LP_{11}$  modes can be launched by passing the beam through any of the  $0|\pi$  transitions, and also that launching the  $LP_{01}$  mode does not require any phase change, the same PP can be used to launch any mode up to  $LP_{21}$  without having to switch to another PP and otherwise requiring realignment of the set-up. PPs that can excite up to  $LP_{02}$ ,  $LP_{31}$ ,  $LP_{41}$  are also shown in Figure 3.5.

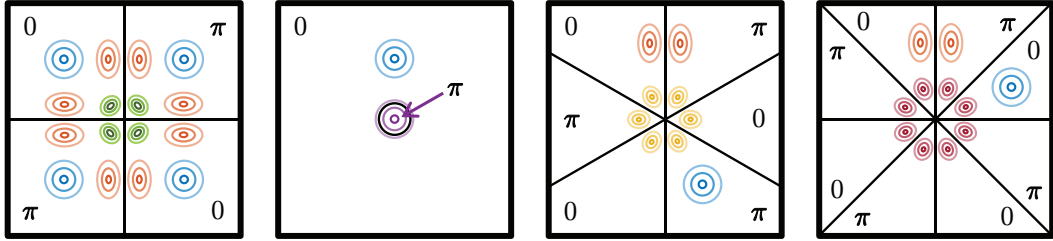


FIGURE 3.5: Layouts of various phase plate geometries showing phase regions. Thin black lines/curves demarcate  $0|\pi$  phase boundaries. Geometries are named according to the highest order mode that can be excited: (left to right)  $LP_{21}$ ,  $LP_{02}$ ,  $LP_{31}$ , and  $LP_{41}$ . Mode profiles show areas where respective modes can be excited (colour coded blue:  $LP_{01}$ , orange:  $LP_{11}$ , green:  $LP_{21}$ , purple:  $LP_{02}$ , yellow:  $LP_{31}$ , maroon:  $LP_{41}$ ). To avoid congestion, only the  $LP_{21}$  PP is shown with all excitation permutations.

### 3.2.2 Detection

After propagating through the FUT, the signals are detected by a digital serial analyser sampling oscilloscope (Scope) with an in-built 10 GHz photodetector. The FUT is mechanically mounted to the photodetector mating sleeve via a bare fibre adapter, and the scope is electrically triggered (Trig) by the PFL. The time-domain trace produced on

<sup>4</sup>See Appendix A for lens focal length calculations.

<sup>5</sup>There is a reason for this. Most FUTs are HC-PBGFs where the losses of HOMs above  $LP_{21}$  are significant enough to prevent the discrete pulse peaks from reaching the detection end with detectable remaining power.

the scope display resembles that at the detection end of Figure 3.1 with received power (in W) against time (in s). The detector has a maximum threshold of 1 mW and a noise floor of about 0.5  $\mu$ W to 1  $\mu$ W, giving a dynamic range of just over 30 dB.

A final practical consideration to note is the length of the FUT. ToF measurements require that the fibre be sufficiently long in order to spread the arrival times of mode components into distinguishable peaks [80, 81]. Apart from the fact that the relative precision of delays measured on the oscilloscope improves with fibre length [82], the photodetector's maximum resolution also influences this minimum. The 10 GHz bandwidth of the photodetector on the oscilloscope means that its maximum temporal detection resolution is 100 ps, that is, pulse peaks corresponding to adjacent modes need to be separated by at least 100 ps at the detector in order to be individually distinguished. As an example, taking the LP<sub>01</sub> mode as the reference and considering its nearest neighbour, the LP<sub>11</sub> mode, the minimum fibre length is

$$\ell_{\min} = \frac{\mathcal{R}_{\max}}{\Delta\tau}, \quad (3.3)$$

where  $\mathcal{R}_{\max}$  is the maximum resolution of the photodetector and  $\Delta\tau$  is the DMD between the LP<sub>11</sub> and LP<sub>01</sub> modes. For HC-PBGFs, the DMDs are typically  $\sim 7$  ps/m for 19c PBGFs and  $\sim 4$  ps/m for 37c PBGFs. Therefore  $\ell_{\min}$  is  $\sim 15$  m and  $\sim 25$  m for 19c and 37c fibres, respectively.

### 3.3 Experimental Proof of Concept

In order to experimentally validate the ToF set-up and demonstrate the measurement principles conceptually, experimental results are presented for measurements on a number of simple solid-core FMFs. The section starts by considering a 2-mode fibre and then moves progressively to a 4-mode fibre. The fibre samples used in each case were fabricated by our MODE-GAP collaborator, *OFS Fitel Denmark*, and had been used in early MDM trials.

With the ToF measurement principles established, Section 3.4 subsequently describes measurements on a novel 9-mode fibre, which was also fabricated by *OFS*.

#### 3.3.1 2-mode Step-Index Fibre

A 2-mode fibre (2MF) is used as the conceptual base case of multimode propagation. This fibre is able to guide LP<sub>01</sub> and LP<sub>11</sub>. Figure 3.6 depicts the propagation of both modal components from an unoptimised launch to produce the time-domain trace at the detection end.

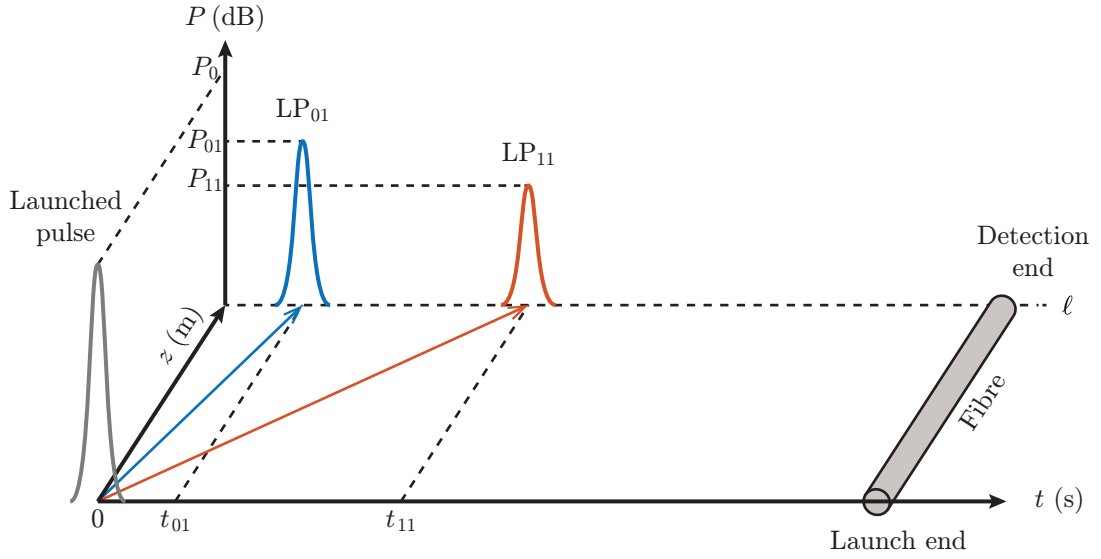


FIGURE 3.6: Pulse propagation through a 2MF of length  $\ell$  showing differences in absolute modal delay.  $t$  = time (absolute delay),  $z$  = distance,  $P$  = normalised power.

Figure 3.7 shows experimentally measured ToF traces obtained after the signals have propagated through  $\ell = 10$  km of a 2-mode step-index fibre (2MSIF), using various launch scenarios. In Figure 3.7a, the optomechanics of the free-space launch set-up are adjusted with a spatial offset to excite both  $LP_{01}$  and  $LP_{11}$  at the launch end. After propagation through the fibre, the two peaks corresponding to each mode have separated in the time-domain. The relative delay per unit length of  $LP_{11}$  compared to  $LP_{01}$  is  $\Delta\tau = (t_{11} - t_{01}) / \ell \approx 2$  ps/m. Figures 3.7b and 3.7c show the measured traces

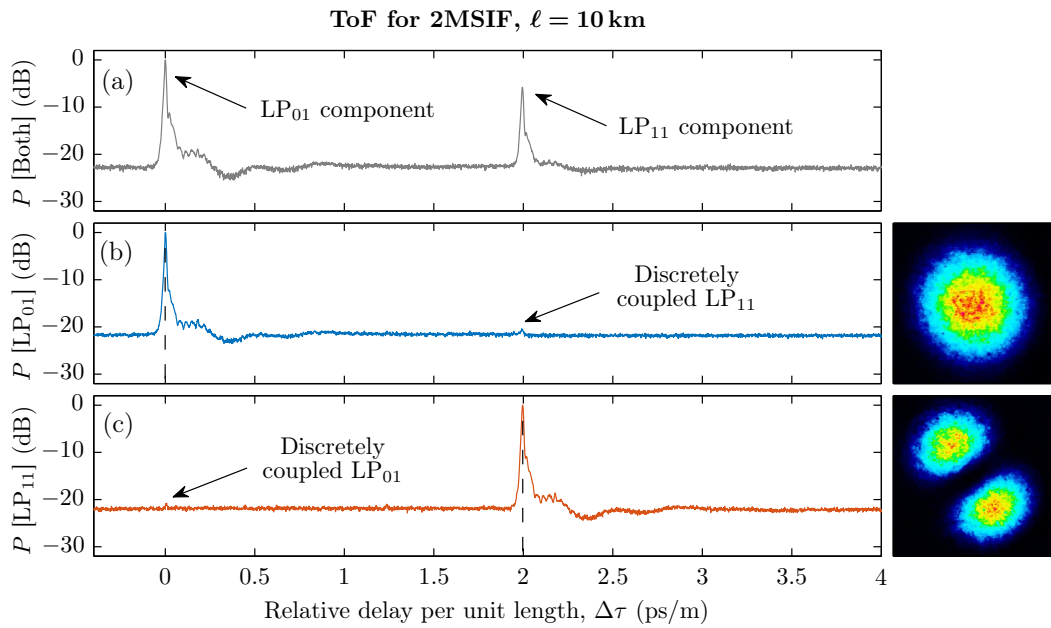


FIGURE 3.7: ToF measurements showing detected traces after (a) general offset launching and selectively launching (b)  $LP_{01}$  and (c)  $LP_{11}$  modes into a 10 km 2MSIF. CCD-captured received mode profiles are inset.  $P$  = normalised power.

for launches optimised for  $LP_{01}$  and  $LP_{11}$ , respectively. The mode intensity profile of each case is captured at the detection end of the 2MSIF by a CCD camera and is displayed next to the respective figure; each clearly shows either  $LP_{01}$  or  $LP_{11}$ . In both Figures 3.7b and 3.7c, a minute component of the other (non-intended) mode is seen at the corresponding modal delay position. These occur because a small percentage of optical power has been discretely coupled into the non-intended mode at the launch end, and has propagated at that mode's own velocity to end up in its final temporal position. This implies that the launches are nearly but not absolutely perfect. Nevertheless in both cases, the extinction ratio between the intended and non-intended modes is  $> 20$  dB. The lack of a clear plateau spanning the two mode discrete peaks also shows that there is negligible distributed mode coupling.

### 3.3.2 4-Mode Step-Index Fibre

Extending from the 2-mode case, a 4-mode fibre (4MF), which can guide  $LP_{01}$ ,  $LP_{11}$ ,  $LP_{02}$ , and  $LP_{21}$ , is considered. Figure 3.8 exemplifies the propagation of all modal components from a general pulsed launch to produce the separated pulse peaks in the time-domain trace at the detection end.

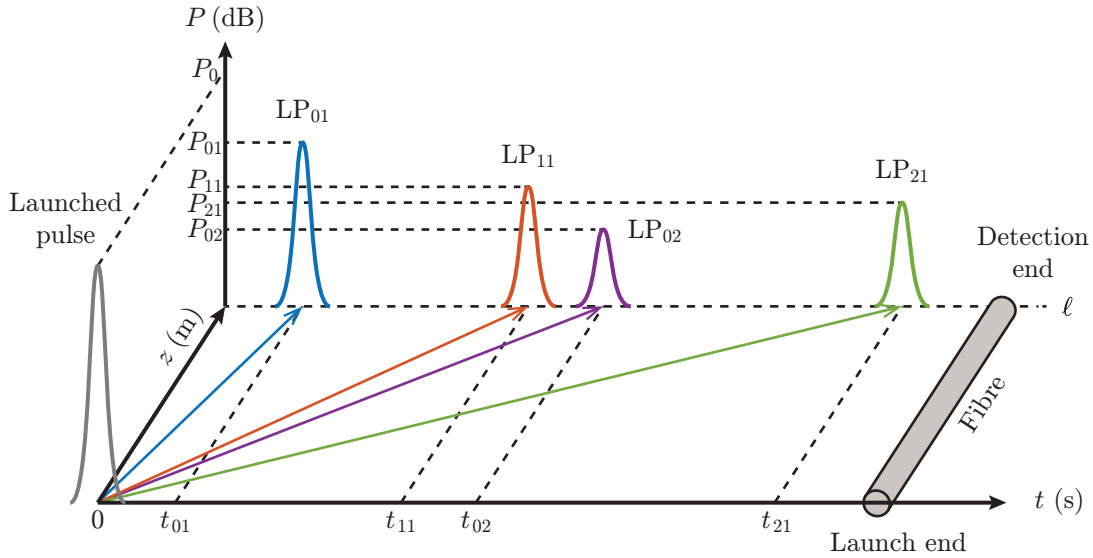


FIGURE 3.8: Pulse propagation through a 4MF of length  $\ell$  showing differences in absolute modal delay.  $t$  = time (absolute delay),  $z$  = distance,  $P$  = normalised power.

#### 3.3.2.1 Discrete Mode Coupling

An analogous output is observed in the experimentally measured ToF trace of a 4-mode step-index fibre (4MSIF) in Figure 3.9a, where, similar to Figure 3.7a, a slight launch misalignment is deliberately introduced in order to discretely excite all four modes. The

temporal positions of the modal peaks indicate their relative delays with respect to that of the  $LP_{01}$  mode, which are listed in Table 3.2.

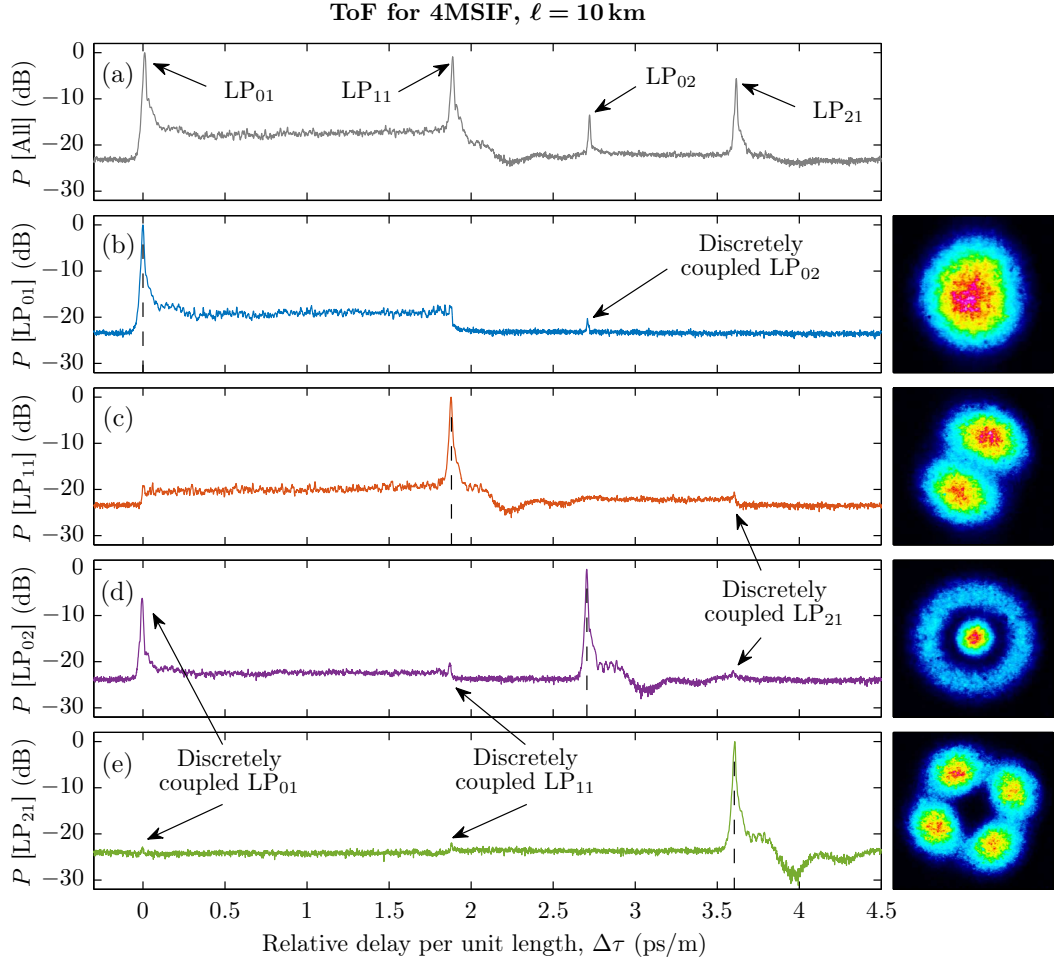


FIGURE 3.9: ToF measurements showing detected traces after (a) general offset launching and selectively launching (b–e)  $LP_{01}$ ,  $LP_{11}$ ,  $LP_{02}$ , and  $LP_{21}$  modes, respectively, into a 10 km 4MSIF. CCD-captured received mode profiles are inset.  $P$  = normalised power.

TABLE 3.2: DMDs of the 4MSIF.

Mode	$LP_{01}$	$LP_{11}$	$LP_{02}$	$LP_{21}$
$\Delta\tau$ (ps/m)	0	1.88	2.71	3.61

ToF traces for launches optimised for  $LP_{01}$ ,  $LP_{11}$ ,  $LP_{02}$ , and  $LP_{21}$  are shown in Figures 3.9b–3.9e, respectively, accompanied by the corresponding CCD camera-detected mode intensity profiles. It is important to note that these mode-specific launch results are required to be able to measure the  $\Delta\tau$  of the HOMs and thereby identify and label

the modal pulse peaks in Figure 3.9a. For comparison, Figure 3.10 displays the  $S^2$  measurement<sup>6</sup> on a 20 m sample of the fibre, showing good agreement in measured DMDs. Mode intensity profiles reconstructed from the spectral measurements are inset.

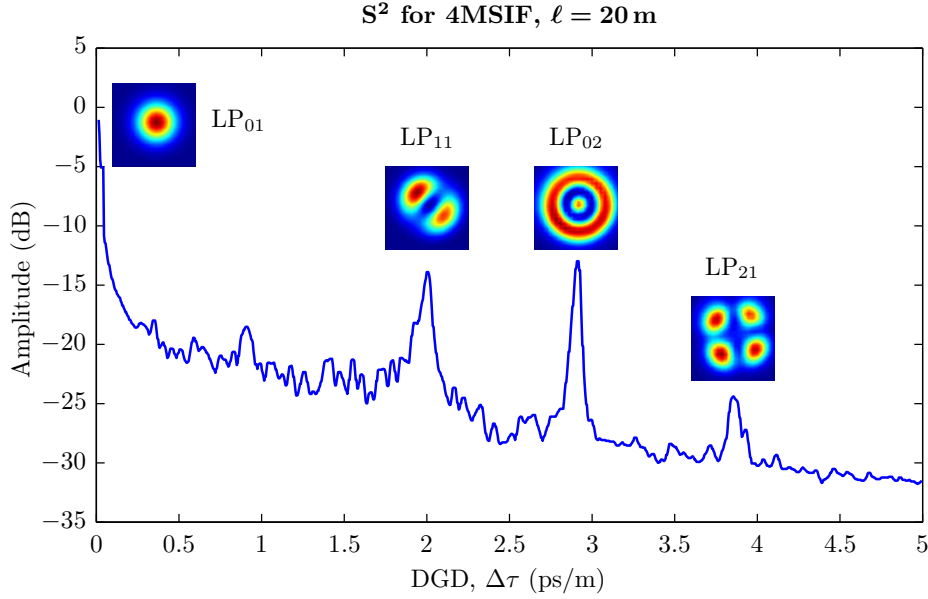


FIGURE 3.10:  $S^2$  measurement for central launching into a 20 m sample of the 4MSIF. Reconstructed mode profiles are inset. *Courtesy of MOFG.*

In the ToF results of Figure 3.9, there are small residual amounts of discrete coupling to non-intended modes in each of the optimised launch traces. For the LP<sub>02</sub>-optimised case in Figure 3.9d, there is a strong LP<sub>01</sub> component that was discretely coupled at launch. The ER between the main LP<sub>02</sub> component and this is merely 6.27 dB, despite the received mode intensity profile appearing to be predominantly LP<sub>02</sub>. This shows that it is difficult to achieve pure HOM launches in this fibre without significant components of nearest radial neighbour modes being excited as well, and corroborates the point made earlier in Section 2.2.3 that nearest radial neighbour coupling tends to occur at discrete interfaces. This is also supported by the presence of a visible LP<sub>02</sub> discrete peak in the LP<sub>01</sub> optimised launch case (Figure 3.9b). ERs of  $\geq 20$  dB are achievable in all other cases when trying to suppress the discretely coupled nearest *azimuthal* neighbour mode components.

### 3.3.2.2 Distributed Mode Coupling

Another conspicuous feature in Figure 3.9, that is seemingly absent from the 2MSIF case (Figure 3.7), is the presence of *distributed* mode coupling. Figure 3.9b shows a  $\mathcal{C}_{01 \leftrightarrow 11}$  plateau, where the notation  $\mathcal{C}_{a \leftrightarrow b}$  is used to denote coupling between modes LP<sub>a</sub> and LP<sub>b</sub>. The plateau sits at about 17.36 dB to 20.18 dB below the main LP<sub>01</sub> discrete peak. To the right-hand-side (RHS) of where  $\Delta\tau_{11}$  is supposed to be, there are no discernible

<sup>6</sup>This  $S^2$  measurement was performed by group members in the MOFG.

plateaus, implying that distributed coupling between  $LP_{01}$  and  $LP_{11}$  dominates. Note that due to the presence of the distributed  $\mathcal{C}_{01 \leftrightarrow 11}$  plateau, it cannot be conclusively said if there is also a discretely coupled  $LP_{11}$  component present and whether or not it is either at a similar ER level to the plateau, or somewhere between the plateau level and the noise floor, or simply non-existent. The only certainty is that if there is such a component, then it is no stronger than the  $\mathcal{C}_{01 \leftrightarrow 11}$  plateau. This highlights one of the tenets of ToF, that although it is rich with information, specific details can only be extracted if one is able to distinguish them from other pieces of information contained in the overall trace.

The trace in Figure 3.9c for the  $LP_{11}$  optimised launch case (which actually resembles Figure 2.3) shows that there are  $\mathcal{C}_{11 \leftrightarrow 01}$  ( $r_{\text{ex}} = 18.19 \text{ dB to } 21.44 \text{ dB}$ ) and  $\mathcal{C}_{11 \leftrightarrow 21}$  ( $r_{\text{ex}} = 21.35 \text{ dB to } 22.88 \text{ dB}$ ) distributed plateaus, with the former being more dominant. This indicates that nearest azimuthal neighbour distributed coupling can be unequal and preferential towards one of the two neighbours. Moreover, the stronger  $\mathcal{C}_{11 \leftrightarrow 01}$  plateau, despite the fact that  $(\Delta\tau_{21} - \Delta\tau_{11}) < (\Delta\tau_{11} - \Delta\tau_{01})$ , suggests that there is no arbitrary correlation between the strength of distributed coupling and differences in relative group delay; coupling can be stronger even for modes that are further spaced apart temporally. This can be attributed to the fact that it is the relative closeness of the *effective indices* of the modes that determines the strength of coupling. The group delay of a mode is not directly related to its effective index, as it has an additional dependency on the derivative of the refractive index w.r.t. wavelength [142].

The  $LP_{02}$  optimised launch case in Figure 3.9d shows a strong discretely launch-coupled  $LP_{01}$  component, as mentioned previously in Section 3.3.2.1. Because of this, as with the case of Figure 3.9b, a  $\mathcal{C}_{01 \leftrightarrow 11}$  plateau arises between  $\Delta\tau_{01}$  and  $\Delta\tau_{11}$ . What has happened in Figure 3.9d is that some launch power has gone to excite  $LP_{01}$  instead of  $LP_{02}$ , and this power has been subsequently continuously coupled to  $LP_{11}$  over the length of the fibre. This means that in a multimode fibre, it is entirely possible to have distributed coupling between two non-intended modes, and this may have implications for loss in transmission systems. Finally, a slight  $\mathcal{C}_{21 \leftrightarrow 11}$  plateau in the  $LP_{21}$  optimised launch case (Figure 3.9e) is also observed.

A point of caution must be made as to the truth of the presence of distributed coupling plateaus. As can be seen in the ToF traces (more conspicuously in Figures 3.9c, 3.9d, and 3.9e), there is some level of signal ringing immediately after the discrete peaks of the respective MUTs. This happens when the oscilloscope detector receives a large impulse and the signal oscillates before levelling off to a steady-state. The magnitude and temporal extent of the ringing ‘tail’ may be such that it could resemble a distributed coupling plateau, therefore putting into question whether or not a coupling plateau is actually present. There are two ways to resolve this. Firstly, ringing tails, being oscillations, appear more irregular and uneven than the smoother coupling plateaus. An example can be seen in Figure 3.9c, where the ToF profile between the discrete  $LP_{11}$  and

LP<sub>21</sub> peaks is made up of an uneven ringing tail followed by the real coupling plateau which is smoother. Secondly, and to give more assurance, coupling plateaus can be confirmed to exist if there is corroboration between the data of two different selective mode launch cases. For instance, it can be confirmed that the raised profile between the discrete LP<sub>01</sub> peak and where a discrete launch-coupled LP<sub>11</sub> peak would be (i.e. between 0 and 1.88 ps/m) in Figure 3.9b (blue trace) is indeed a  $\mathcal{C}_{01 \leftrightarrow 11}$  plateau because there is a corroborating  $\mathcal{C}_{01 \leftrightarrow 11}$  plateau in the orange LP<sub>11</sub> launch case trace of Figure 3.9c. The latter is trustworthy because there are no ringing effects in the left-hand-side (LHS) of the discrete LP<sub>11</sub> peak where the plateau resides. Similarly, in Figure 3.9c, the reality of the  $\mathcal{C}_{11 \leftrightarrow 21}$  plateau (between  $\Delta\tau = 1.88$  to 3.61 ps/m) is confirmed by the similar, albeit small, plateau in the green trace of the LP<sub>21</sub> launch case (Figure 3.9e). Essentially, coupling plateaus on the LHS of discretely coupled mode peaks are trustworthy, and those on the RHS can only be trusted if there is corroborating LHS evidence from the trace from the launch of the counterpart mode.

### 3.3.2.3 Summary of Observations

From these results, the following observations can be made. While there are differences between radial and azimuthal cases, the nearest neighbour theory is supported. Nearest radial neighbour coupling occurs mostly discretely, at the launch side. This is possibly due to the difficulty in practically isolating radial neighbour modes when exciting them using phase plates. On the other hand, nearest azimuthal neighbour coupling appears to occur in a predominantly distributed manner. One of the main causes of distributed coupling is continuous scattering due to surface roughness of the core/cladding interface [78]. This suggests that surface scattering has a greater influence on azimuthal as opposed to radial neighbours. It was also observed that the relative closeness of individual mode group delays, and by definition the group indices [14], has no direct correlation with the strength and relative preference of distributed mode coupling. Finally, due to the presence of detector ringing, the trustworthiness of coupling plateaus must be ascertained before they are used for analysis.

## 3.4 Characterisation of a Novel 9-Mode Fibre

Our Centre was asked by MODE-GAP project collaborators at *OFS* to characterise a novel solid-core fibre that they had fabricated, as part of the fibre development process. The fibre guides nine LP mode groups, corresponding to 15 individual spatial modes and was designed by *OFS* to have a graded-index core to minimise DMD and hence be suitable for MDM data transmission [138]. The guided modes supported are LP<sub>01</sub>, LP<sub>02</sub>, LP<sub>03</sub>, LP<sub>11</sub>, LP<sub>12</sub>, LP<sub>21</sub>, LP<sub>22</sub>, LP<sub>31</sub>, and LP<sub>41</sub>. This fibre is referred to as a 9-mode graded-index fibre (9MGRINF).

### 3.4.1 Mode Excitation and DMD

The ToF set-up was used to characterise the 9MGRINF. Figures 3.11 and 3.12 depict the ToF traces for general and mode-selective launches (using PPs as in Figure 3.5), respectively. In Figure 3.11, the measured DMDs are small as expected, much less than for the 2MSIF and 4MSIF cases (Figures 3.7 and 3.9, respectively). The DMDs between certain HOMs are so close that their individual pulse peaks have conjoined to produce only four distinguishable mode families:  $LP_{01}$ ,  $LP_{11}$ ,  $LP_{21/02}$ , and  $LP_{31/12/41/22/03}$ ; the latter appears to consist of two sub-families,  $LP_{31/12}$  and  $LP_{41/22/03}$ , as indicated by the two barely distinguishable peaks in the right-most ToF feature.

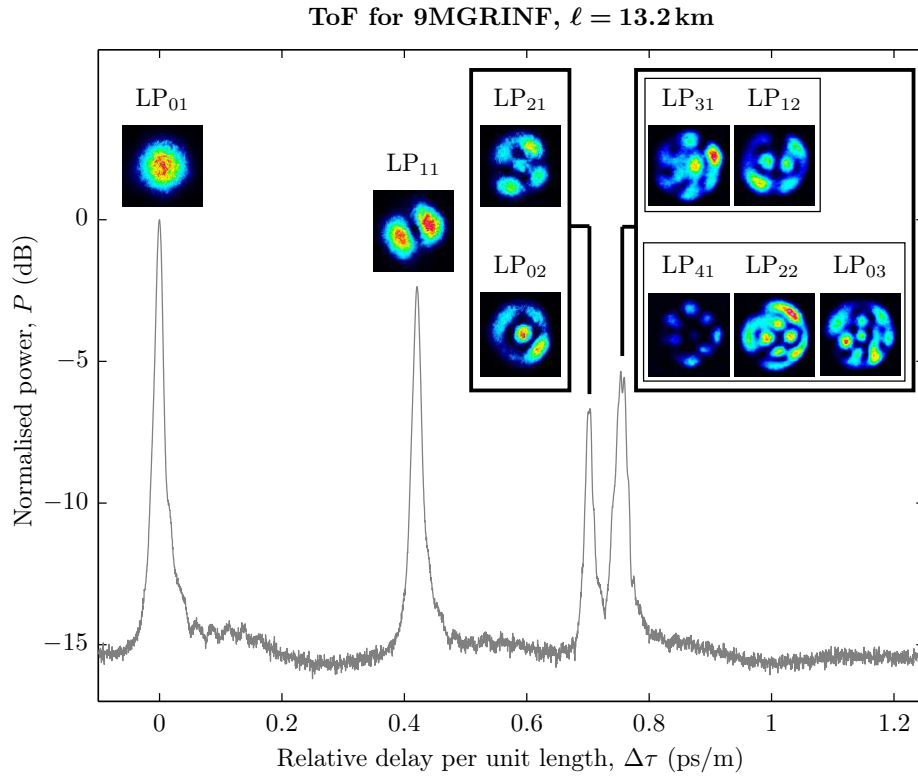


FIGURE 3.11: ToF measurements showing detected traces after general offset launching into a 13.2 km 9MGRINF. CCD-captured mode profiles are inset.

The individual mode family DMDs are obtained from Figure 3.12 and listed in Table 3.3, along with the values of each family's effective refractive index  $\Delta n_{\text{eff}}$  that were calculated in [138]. The results show that whereas the  $\Delta n_{\text{eff}}$  values are evenly spaced, the  $\Delta\tau$  values are not. This mismatch arises because the modal group delays are not directly related to their effective indices, as explained in Section 3.3.2.2. In fact, the DMD intervals seem to follow a geometric rather than linear progression, with the  $LP_{31/12}$  and  $LP_{41/22/03}$  delays occurring too close together to be accurately distinguishable. Observations from mode intensity profiles captured by the CCD camera (shown inset in Figure 3.11) confirm this. When either the  $LP_{31}$  or the  $LP_{41}$  PP was used for selective mode excitation, mode profiles from all five modes in the  $LP_{31/12}$  and  $LP_{41/22/03}$  families were observed to beat

among one another. This is similar to the behaviour observed for modes within the  $LP_{21/02}$  family;  $LP_{21}$  was seen to beat with  $LP_{02}$  when either the  $LP_{21}$  or the  $LP_{02}$  PP was used. Nevertheless, the ToF relative delay results agree well with  $S^2$  measurements performed by *OFS* [138] and displayed in Figure 3.13 which, in particular, confirm the closeness of the  $LP_{31/12}$  and  $LP_{41/22/03}$  DMDs.

TABLE 3.3: DMDs of the 9MGRINF.  $\Delta n_{\text{eff}}$  values are referenced from [138].

Mode Family	$LP_{01}$	$LP_{11}$	$LP_{21/02}$	$LP_{31/12}$	$LP_{41/22/03}$
$\Delta n_{\text{eff}} \left( \times 10^{-3} \right)$ relative to silica	10.8	8.6	6.4	4.2	2.0
$\Delta \tau$ (ps/m)	0	0.42	0.70	0.75	0.76

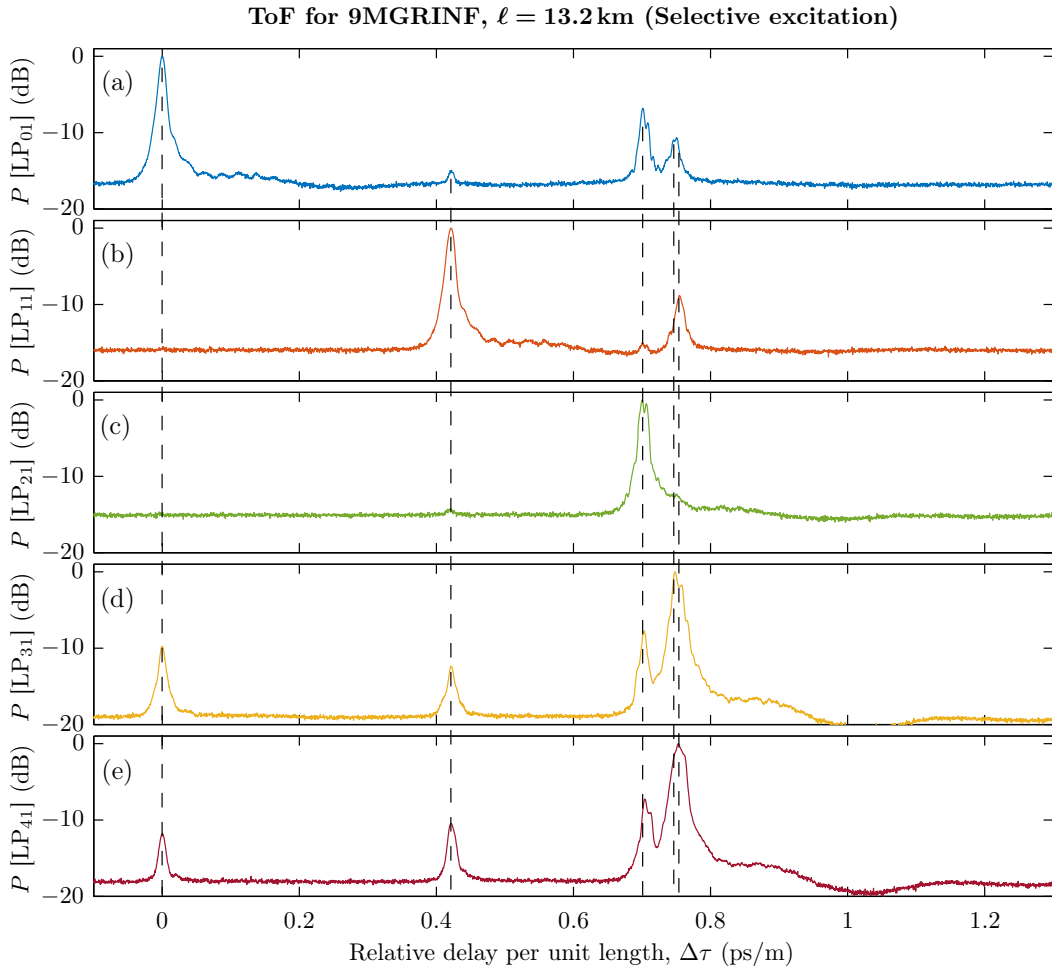


FIGURE 3.12: ToF measurements showing detected traces after selective launch through (a)  $LP_{01}$ , (b)  $LP_{11}$ , (c)  $LP_{21}$ , (d)  $LP_{31}$ , and (e)  $LP_{41}$  phase plate regions, respectively, into the 13.2 km 9MGRINF.  $P$  = normalised power.

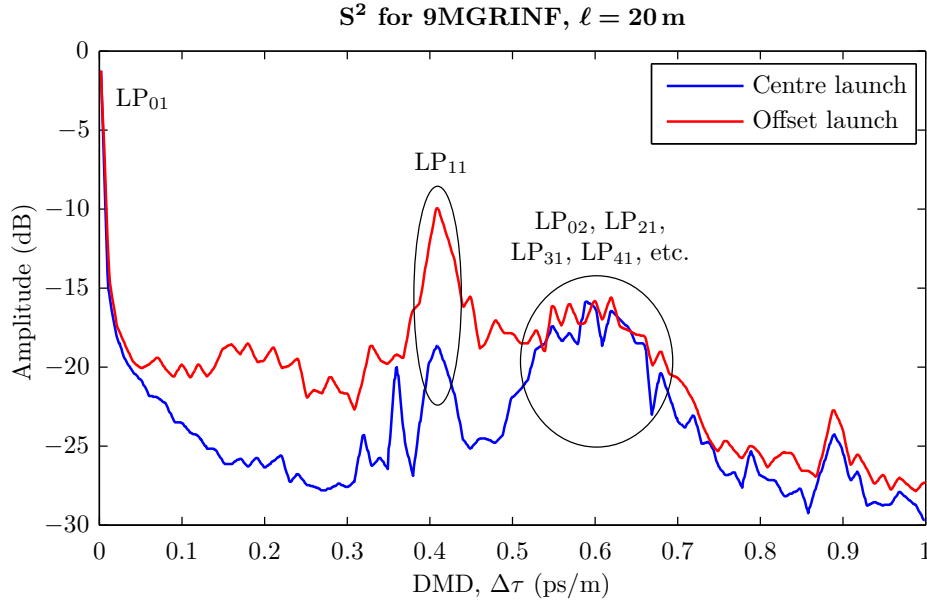


FIGURE 3.13:  $S^2$  measurements for the 9MGRINF. Measurements were taken by OFS and presented in [138].

### 3.4.2 Mode-Dependent Loss Characterisation

In order to consider this fibre for use in MDM data transmission applications, it is also important to characterise the modal loss. Optical time-domain reflectometry (OTDR) is used for this purpose. An optical time-domain reflectometer (also OTDR) launches a light pulse into the FUT. During propagation through the FUT, the pulse is attenuated and continuously scattered in all directions by means of Rayleigh scattering [143]. Some of this is backscattered and propagates towards the source, also being attenuated along the way. The OTDR measures and displays the continuous spatial distribution of backscattered optical power. At fibre interruptions, e.g. the start and end as well as defects, light is reflected by Fresnel reflection by an amount significantly larger than the Rayleigh backscattered power. An OTDR trace of a typical fibre without longitudinal defects therefore looks like a decreasing slope plotted against distance, delimited by two large peaks, each corresponding to reflections from the start and the end of the fibre [143]. In this way, the length of the fibre can be measured by the interval between the two large peaks. The attenuation of the fibre can also be calculated by the slope of the trace.

To measure the attenuation of each mode family in the 9MGRINF, the following OTDR set-up, shown in Figure 3.14, was employed, which uses the same free-space lens and PP arrangement as that in Figure 3.3. The EDFA was omitted as the OTDR's internal laser provided sufficient power. The FUT was terminated with a capped bare fibre adapter.

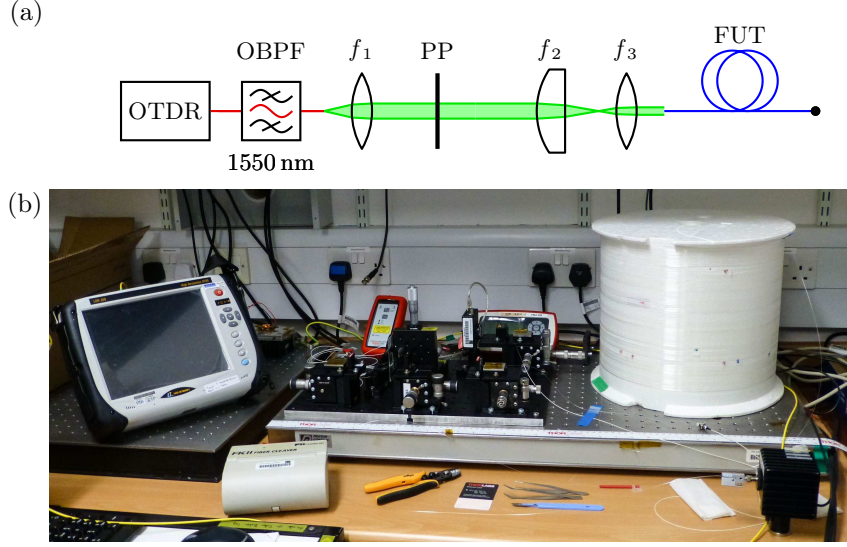


FIGURE 3.14: Optical Time-domain Reflectometry (OTDR) experimental set-up. (a) Schematic. (b) Equipment photograph showing Luciol Instruments LOR-200 OTDR.

OTDR measurements at  $\lambda = 1550$  nm were taken on the 9MGRINF while selectively exciting specific modes. The results in Figure 3.15 show that the fibre is mostly free of major longitudinal defects, except for a possible one at around  $z = 5.52$  km, which scatters light irrespective of mode. Table 3.4 lists the measured modal attenuations of this fibre and shows that while the losses are minutely larger for the HOM families, they are all comparable to the loss of SSMF [6] and hence it is possible to use this fibre for long-haul telecommunications, even using the HOMs.

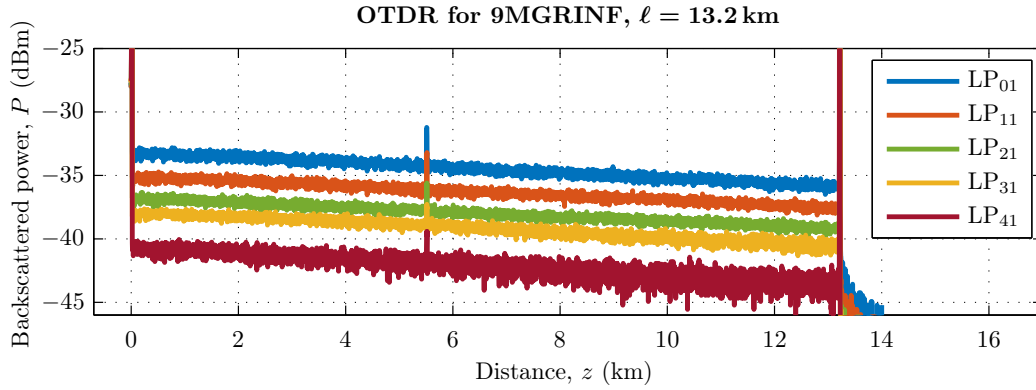


FIGURE 3.15: OTDR measurements on the 13.2 km 9MGRINF showing detected traces from selectively launching various modes.

TABLE 3.4: Modal attenuation of the 9MGRINF. All values have an uncertainty of  $\pm 0.01$  dB/km.

Mode Family	LP <sub>01</sub>	LP <sub>11</sub>	LP <sub>21/02</sub>	LP <sub>31/12</sub>	LP <sub>41/22/03</sub>
$\alpha$ (dB/km)	0.20	0.20	0.21	0.22	0.22

These measurements proved useful and the fibre design was ultimately used by *OFS* to fabricate a 22.8km MMF that supports 30 spatial and polarisation channels;  $3 \times 2$ -fold degenerate ( $LP_{01}$ ,  $LP_{02}$ ,  $LP_{03}$ ) +  $6 \times 4$ -fold degenerate ( $LP_{11}$ ,  $LP_{12}$ ,  $LP_{21}$ ,  $LP_{22}$ ,  $LP_{31}$ ,  $LP_{41}$ ) modes. The data transmission was performed by MODE-GAP project collaborators at the *Alcatel-Lucent Bell Labs* (now *Nokia Bell Labs*), and MDM was achieved using 30 Gbaud quadrature phase-shift keying (QPSK) modulation with 12 WDM channels in the C-band to obtain a spectral efficiency of 43.63 bit/(s Hz) [144].

### 3.5 Comparing ToF and $S^2$ Methods

ToF is but one of a number of modal characterisation methods that currently exist. As hinted by frequent mentions throughout the text, the  $S^2$  method is another technique that can be used for evaluating the modal behaviour in MMFs, and in the context of my groups' work on exploring multimode fibres for communications, it is often used complementarily with ToF. While both methods can provide information on aspects such as modal content and DMD, and in particular distinguish between discrete and distributed coupling [74], there are certain details uniquely provided by one or the other, as well as limitations specific to each technique. A brief comparison of the two methods was given in [75]. Here, I reiterate the main points and provide some additional comments.

As mentioned at the beginning of the chapter,  $S^2$  measurements on fibres are made by exploiting the spectral interference between modes at specific spatial beam positions, which is caused by modal group delay differences [73]. The set-up [71] requires the beam that is output from the FUT, which is illuminated by a broadband source, to be measured at every transverse position in a rastered manner. The spectrum at each position (pixel) is recorded and Fourier transformed, and the results are summed to produce an overall trace that plots amplitude against delay per unit length, and displays discrete mode peaks as well as distributed coupling plateaus, much like a ToF trace. Intensity profiles of the various modes can be constructed by integrating the measured spectrum at each pixel [73]. This provides a visual means of identifying modes and ascribing specific peaks to them. The FUT is typically of a short length ( $\sim 20$  m) to enable the capture of HOM content.

In contrast to  $S^2$ , ToF requires a long FUT length to be able to characterise modal content. This is needed in order to delay the individual propagating modes away from one another by a sufficient amount to be resolved on the oscilloscope. A PFL producing narrower input pulses (if such high-end equipment is available) might relax this requirement by some amount, but the required length scale will still be an order of magnitude greater than that in  $S^2$ . This length requirement actually has both a drawback as well as an advantage. The disadvantage is that in ToF, HOMs, which are much lossier than the fundamental mode, are likely to be attenuated severely before reaching the output

end of the FUT. This means that the traces observed from ToF typically do not contain the entirety of the modal information in the fibre. This may or may not be a problem, depending on whether such lossy HOMs are worth investigating in the first place, especially if communications applications are considered. Nevertheless, it shows that ToF can only provide a restricted level of information. Given the short FUT length,  $S^2$  is able to capture most of its modal content, and traces typically contain many more modal features than ToF. On the other hand, a long-length FUT can be useful in the sense that it provides a truer representation of the actual behaviour in a full-length fibre. ToF tests can be applied on multi-kilometre fibre samples, and so the modal processes and delay spreads actually occurring throughout the whole fibre length can be measured. Conversely, the information provided by  $S^2$  is only true to the short FUT sample, and any behaviour for full-length fibres is a prediction. Unlike  $S^2$ , ToF measurements are affected by any local defects or irregularities that occur over the long fibre length, and these can thus be detected, such as in [136].

An advantage of  $S^2$  over ToF is that it offers a larger measurement dynamic range ( $> 50$  dB reported in [71]). The dynamic range in ToF is limited by that of the detector. In our available equipment, this was limited to about 30 dB. In some cases, certain weak HOM features may become hidden under the noise floor. Efforts to amplify the signals still point to the detector as the limiting factor. Alternative detectors and measurement methods are being explored.

One key benefit unique to ToF is that measurements are done in real-time. Measurement speed is limited by the speed of the detector, and for the purposes of these experiments, a 10 GHz detector is sufficient to provide a real-time response. On the contrary, the need to raster scan the FUT output beam in  $S^2$  causes measurements to be the order of minutes [75], though recent advances have achieved reductions in scan time [126].

In general, both ToF and  $S^2$  are used to complement each other, for instance, when confirming ToF measured DMDs from  $S^2$  measurements. In most of the work in my group concerning newly fabricated fibres, they are almost always both carried out.

### 3.6 Summary and Future Work

In this chapter, the time-of-flight measurement set-up has been outlined. Measurements on 2-mode and 4-mode step-index fibres have shown the capabilities of ToF to characterise discrete and distributed coupling as well as DMD. The technique was also used to characterise a novel 9-mode fibre to assess its DMD, and combined with mode-selective OTDR measurements, the fibre was found to have low MDL and thus be suitable for MDM data transmission, a trial of which was demonstrated by other groups using the same fibre design.

A review of the ToF method compared with the  $S^2$  technique was also given. One issue that limits this ToF set-up is the dynamic range offered by the detector. Besides exploring better detectors, an alternative measurement approach has been recently considered. This technique was published in [145] and uses a vector network analyser set-up to measure the impulse response in MMFs. The reported dynamic range is about 40 dB, which prompts future investigation into adapting this technique for our own characterisation efforts, particularly for HC-PBGFs.

In the next chapter, ToF measurements on HC-PBGFs are presented. A simulation-based study of distributed mode coupling, as well as a method to inspect fibre defects using ToF, is discussed in the following chapters.



## Chapter 4

# Characterisation of HC-PBGFs

Hollow-core photonic bandgap fibres (HC-PBGFs) offer huge potential as next-generation communications fibres because of their superior performance featuring lower latency [8, 13, 96, 99], lower nonlinearity [9, 11, 96], and (predicted) lower loss [10] than conventional SCFs. The optical guidance mechanism in these fibres, as described in Section 2.3.1, necessitates large cores that inevitably support multiple guided modes. This naturally presents the opportunity [33] to harness the inherent multimodedness to increase the number of channels per fibre via mode-division multiplexing (MDM) and address the capacity crunch problem. In practice however, this is not trivial, as mode coupling due to fibre imperfections result in inter-channel crosstalk. Space-division multiplexing (SDM), the generalisation of MDM, has been standard in multiple-input-multiple-output (MIMO) radio-frequency communications, and MIMO techniques have over recent years been ported to the photonics domain, such that fibre signals suffering from crosstalk can now be recovered electronically at the receiver [146]. This is encouraging if not for the issue of scalability; systems experiencing large extents of mode coupling as well as large DMDs require commensurately complex MIMO digital signal processing (DSP) for successful crosstalk removal. To date, state-of-the-art MDM transmission trials in HC-PBGFs have been demonstrated using only the first few lowest-order modes ( $LP_{01}$  and  $LP_{11}$ ) [95, 98, 100, 147].

To fully exploit the vast capacity offered by HC-PBGFs, as well as to determine suitability for single-mode data transmission, a solid understanding of the mode propagation and coupling behaviour in these fibres is needed. Chapter 3 outlined the time-of-flight (ToF) characterisation technique and used solid-core FMFs to demonstrate its measurement principles. This chapter presents, in Section 4.1, experimental characterisation results on several 19c and 37c HC-PBGFs (which are the first 37c fibres ever fabricated), chiefly using ToF, and discusses the observations found. Section 4.2 describes data transmission experiments on these PBGFs. An account of an investigation into unexpected performance of a record-length HC-PBGF is given in Section 4.3, demonstrating

the utility of the ToF method. Section 4.4 briefly discusses ToF measurements at 2  $\mu\text{m}$ . Finally, Section 4.5 provides some concluding remarks.

The measurements in this chapter were largely made as part of the *ORC*'s HC-PBGF development programme, in support of the MODE-GAP project [37], and helped inform our understanding of the properties of HC-PBGFs for both single-mode and MDM transmission. They were the first such measurements on this form of fibre and thus scientifically useful to the programme.

## 4.1 ToF Measurements on HC-PBGFs

ToF measurements were performed, using the set-up in Figure 3.3, on various 19c and 37c HC-PBGFs. These fibres were drawn in the *ORC*'s fibre fabrication facility, by N.V. Wheeler, N.K. Baddela, and others in the MOFG. Table 4.1 lists four fibres used and outlines the nomenclature that will be referred to henceforth. The respective lengths  $\ell$ , and measured loss per unit distance<sup>1</sup>  $\alpha$  at the communications wavelength  $\lambda = 1550 \text{ nm}$ , are also given; where otherwise indicated with a selectively optimised mode number in parentheses, all loss values are for unoptimised launch conditions. While the fibres are referred to by their designations in this thesis, their actual *ORC* fibre numbers are also listed for the sake of reference. Note that 19c2 and 37c1 were presented in [13] and [93–95], respectively. The cross-sections of each fibre are displayed in the SEM images in Figure 4.1, which show the larger cores of the 37c fibres. It is worth remarking that the 37c HC-PBGFs fabricated at the *ORC* are the first and only 37c fibres ever produced. The exclusive access to these fibres makes the measurements herein unique.

TABLE 4.1: List of HC-PBGFs used in experiments.

<i>ORC</i> Fibre #	Designation	$n$ (№ cells)	$\ell$ (m)	$\alpha$ (dB/km)			
TLH-19c-08-04-BZB	19c1	19	408	6.6	—	—	—
TLH-19c-03-15-BY	19c2	19	230	4.5	—	—	—
TLH-37c-01-05-BY	37c1	37	310	4.5	3.3 (LP <sub>01</sub> )	7.4 (LP <sub>11</sub> )	—
TLH-37c-04-03-BY	37c2	37	315	4.3	3.4 (LP <sub>01</sub> )	7.5 (LP <sub>11</sub> )	—

<sup>1</sup>Loss values are from cutback measurements performed by various *ORC* MOFG fabricators.

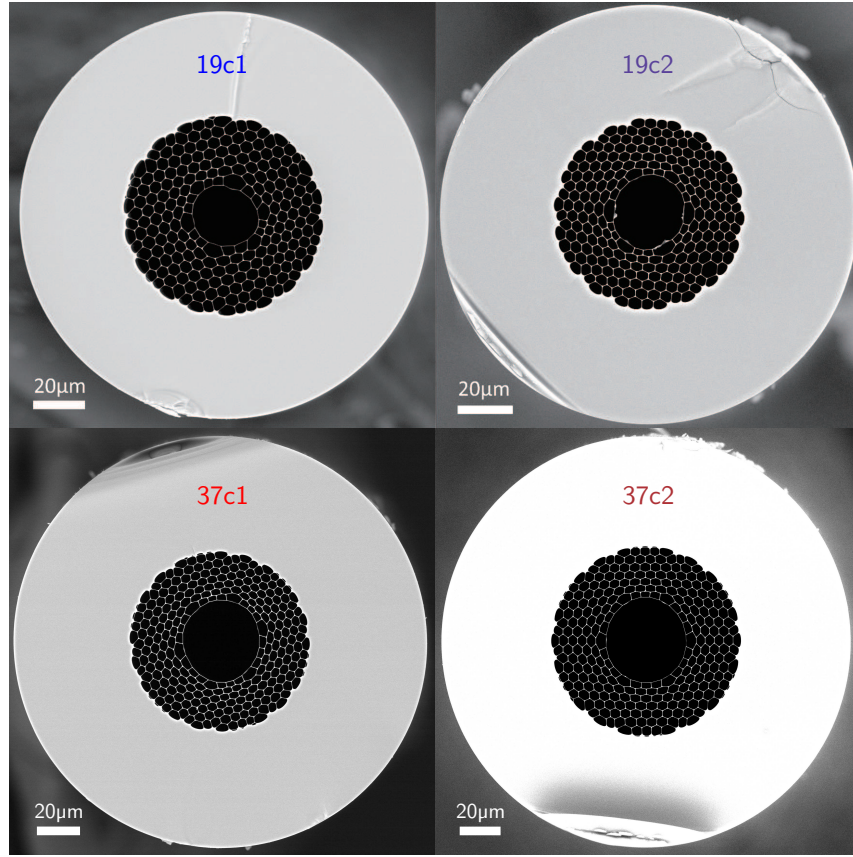


FIGURE 4.1: SEM cross-sections of various HC-PBGFs. *Courtesy of S.R. Sandoghchi and other MOFG members.*

#### 4.1.1 Extinction Ratio and Distributed Coupling Measurements After Selective Mode Excitation

Figure 4.2 shows the respective ToF traces for fibre **19c1**, where either  $LP_{01}$  or  $LP_{11a/b}$  were selectively excited (indicated in square brackets on the power axes). The  $LP_{11}$  mode was excited in two configurations; using either the horizontal or the vertical transitions in the phase plate (leftmost in Figure 3.5), these correspond to the two orthogonal odd and even spatial orientations of  $LP_{11}$ , respectively (see Table 2.1), and are designated with the subscripts <sub>a</sub> and <sub>b</sub>. The (orange and magenta) traces corresponding to these two launches are superimposed on top of each other and show minimal difference. The figure insets show the output mode profiles next to the respective ToF trace. These were captured at the output of the PBGF using a CCD camera so as to get a visual indication of which peaks correspond to which modes and thereby assist in mode identification.

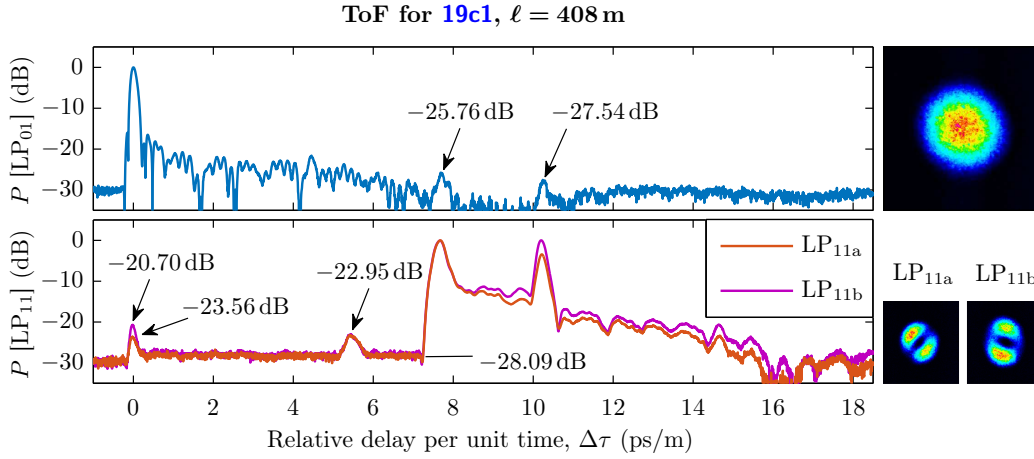


FIGURE 4.2: ToF measurements showing the selectively excited  $LP_{01}$  and  $LP_{11a/b}$  modes in fibre **19c1**. Output mode intensity profiles are inset.  $P$  = normalised power.

For each mode-selective launch, the coupling optomechanics were optimised to produce the largest extinction ratios (ERs) between the discrete peaks of the modes under test (MUTs) and the other modes (OMs). Table 4.2 lists the ERs measured for this fibre.

TABLE 4.2: Discrete mode peak extinction ratios for fibre **19c1**.

$r_{\text{ex}}$ (dB)		
w.r.t. MUT		
MUT	$LP_{01}$	$LP_{11}$
	$LP_{01}$	25.76
	$LP_{11a}$	23.56
	$LP_{11b}$	20.70

These encouragingly high ERs w.r.t. the MUTs show that for either of  $LP_{01}$  or  $LP_{11a/b}$  as the selectively launched MUT, the OM is able to be suppressed to an extent that is sufficient to enable reliable single-mode data transmission. The traces also show a  $C_{01 \leftrightarrow 11}$  distributed coupling plateau between the discrete launch-coupled  $LP_{01}$  and  $LP_{11}$  peaks at 0 ps/m and 7.7 ps/m, respectively. The magnitude of this plateau can be seen from the bottom traces for the  $LP_{11a/b}$  selective launches, and is at a relatively low level of about 28.09 dB down from the  $LP_{11}$  discrete peak. As per the caution in Section 3.3.2.2, this plateau that is on the LHS of the discrete launched-coupled  $LP_{11}$  peak is taken as the real coupling plateau, whereas the elevated ToF feature on the RHS of the discrete  $LP_{01}$  peak in the top trace (for  $LP_{01}$  selective launch) does not reflect mode coupling but rather detector ringing. This is also the case for the elevated ToF feature on the RHS of the discrete  $LP_{11}$  peak at 10.2 ps/m in the bottom traces, which cannot be assumed to be caused by mode coupling, but is instead most probably due to ringing as well. It is also observed that the  $LP_{11}$  mode group has multiple main peaks, the visible ones of which span from 7.7 ps/m to 10.2 ps/m. This has adverse implications on MDM applications and a detailed discussion is deferred to Section 4.1.2.

For the purpose of comparison, Figure 4.3 depicts the ToF traces of fibre 19c2, obtained with permission from the co-authors of [13], and also shows the trace for an optimised LP<sub>21</sub> launch. The main launched mode peaks are indicated on the respective traces, and the measured extinction ratios are shown in Table 4.3.

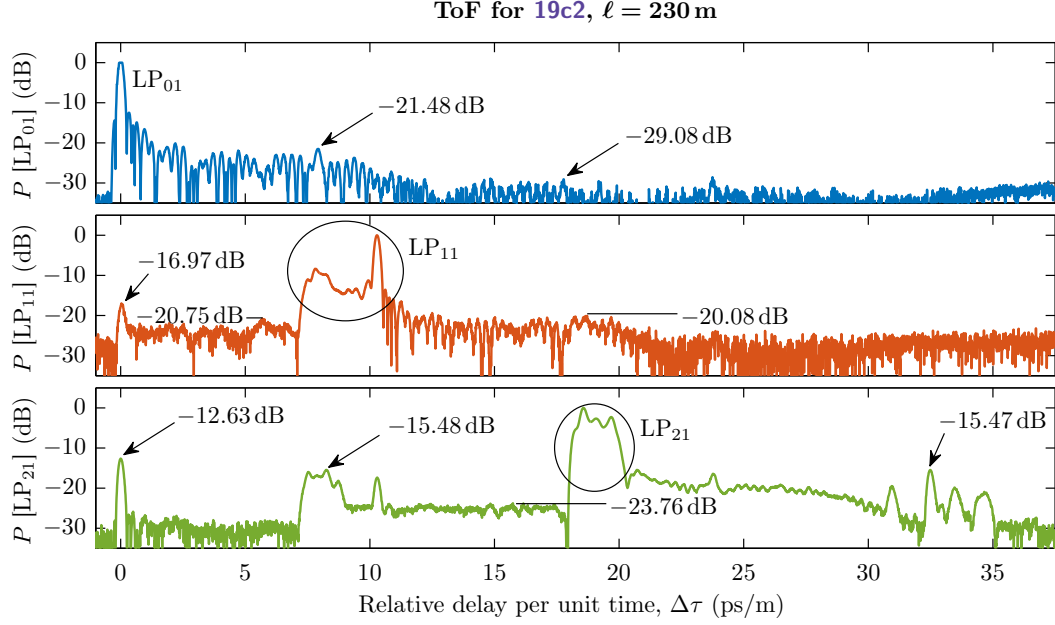


FIGURE 4.3: ToF measurements for LP<sub>01</sub>, LP<sub>11</sub>, and LP<sub>21</sub> selective launches in fibre 19c2 [13].  $P$  = normalised power.

TABLE 4.3: Discrete mode peak extinction ratios for fibre 19c2.

		$r_{\text{ex}}$ (dB) w.r.t. MUT		
		LP <sub>01</sub>	LP <sub>11</sub>	LP <sub>21</sub>
MUT	LP <sub>01</sub>		$\geq 21.48$	29.08
	LP <sub>11</sub>	16.97		$\geq 20.08$
	LP <sub>21</sub>	12.63	15.48	

Comparing this with Table 4.2, the ERs of either fibre are close for LP<sub>01</sub> as the MUT. However, the ER of LP<sub>01</sub> w.r.t. LP<sub>11</sub> as the MUT (16.97 dB) is poorer than that for fibre 19c1, suggesting that LP<sub>11</sub> in 19c2 may not perform as well as in 19c1, as a single-mode channel. It must be noted though, this assessment is subjective as the ERs are affected by the flatness of the fibre interfaces, which in turn depend on the quality of the cleaves. While repeated measurements showed similar ER levels, other tests, e.g. data transmission with eye diagrams, are needed to further confirm transmission performance. This is deferred to Section 4.2.

The green (bottom) trace in Figure 4.3 for optimised LP<sub>21</sub> launch also reveals some higher order mode peaks at 23.8 ps/m and between 30.9 ps/m and 34.7 ps/m. According to  $S^2$  measurements in [75], these coincide with the predicted DMDs of LP<sub>02</sub>, LP<sub>31</sub>, and LP<sub>12</sub>, respectively, implying that these HOMs can be guided in this fibre.

Several distributed coupling plateaus are also present. The orange (middle) trace for optimised  $LP_{11}$  launch contains a  $\mathcal{C}_{01 \leftrightarrow 11}$  plateau at about 20.75 dB down from the peak power of the main  $LP_{11}$  mode group, and the green (bottom) trace for optimised  $LP_{21}$  launch possesses a  $\mathcal{C}_{11 \leftrightarrow 21}$  plateau at about 23.76 dB below the peak power of the main  $LP_{21}$  mode group. Within the latter (green trace), the larger  $\mathcal{C}_{11 \leftrightarrow 21}$  plateau compared to the virtually absent  $\mathcal{C}_{01 \leftrightarrow 11}$  plateau indicates that the distributed mode coupling between  $LP_{11}$  and  $LP_{21}$  is stronger than that between  $LP_{01}$  and  $LP_{11}$ , a behaviour that is similar in solid-core fibres.

Comparing the measured loss of fibres 19c1 and 19c2 in Table 4.1, the latter, which has lower loss, is expected to exhibit less distributed mode coupling, based on the theory that loss and coupling are proportionally related because they both result from fibre surface roughness scattering [36]. This is however not apparent in the ToF traces. Considering  $LP_{01}$  and  $LP_{11}$  optimised launches (blue and orange/magenta traces in Figures 4.2 and 4.3), there does not seem to be a clear relation between the magnitudes of the  $\mathcal{C}_{01 \leftrightarrow 11}$  coupling plateaus and the relative difference in loss for each fibre, suggesting that ToF cannot provide conclusive information regarding loss.

ToF measurements were also performed on 37c PBGFs. Figures 4.4 and 4.5 present the measured traces for fibres 37c1 and 37c2, respectively. Tables 4.4 and 4.5 show the respective ERs.

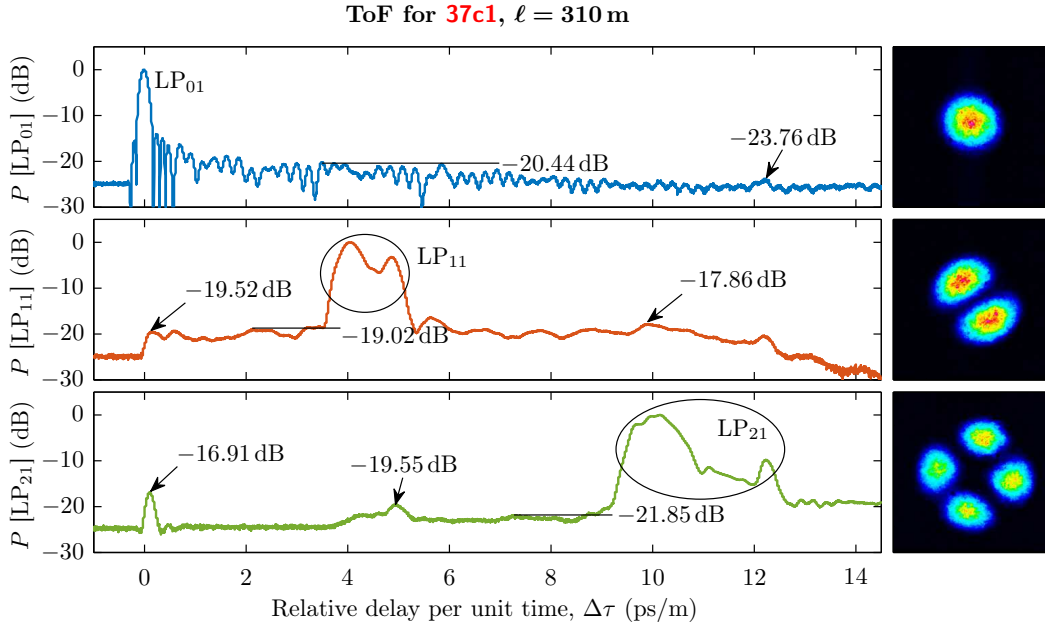


FIGURE 4.4: ToF measurements for  $LP_{01}$ ,  $LP_{11}$ , and  $LP_{21}$  selective launches in fibre 37c1. Output mode intensity profiles are inset.  $P$  = normalised power.

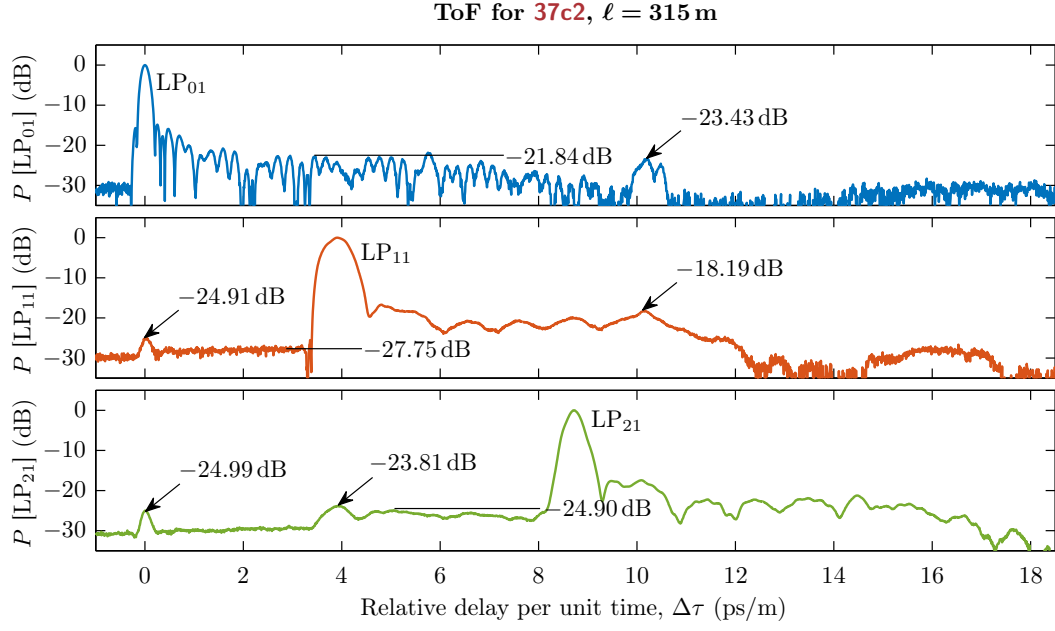


FIGURE 4.5: ToF measurements for  $LP_{01}$ ,  $LP_{11}$ , and  $LP_{21}$  selective launches in fibre **37c2**.  $P$  = normalised power.

TABLE 4.4: Discrete mode peak extinction ratios for fibre **37c1**.

		$r_{\text{ex}}$ (dB) w.r.t. MUT		
		$LP_{01}$	$LP_{11}$	$LP_{21}$
MUT	$LP_{01}$		$\geq 20.44$	23.76
	$LP_{11}$	19.52		$\geq 17.86$
	$LP_{11}$	16.91	19.55	

TABLE 4.5: Discrete mode peak extinction ratios for fibre **37c2**.

		$r_{\text{ex}}$ (dB) w.r.t. MUT		
		$LP_{01}$	$LP_{11}$	$LP_{21}$
MUT	$LP_{01}$		$\geq 21.84$	23.43
	$LP_{11}$	24.91		$\geq 18.19$
	$LP_{11}$	24.99	23.81	

These results show that  $\geq 20$  dB ERs can be attained in both fibres for  $LP_{01}$  as the MUT, indicating the possibility of reliable single-mode data transmission on this mode. This was used as the basis for single-mode transmission trials in **37c1** presented in Section 4.2 (later) and in [94]. However again, there is no apparent clear relation between the amount of distributed coupling and the measured losses.

Distributed mode coupling plateaus are visible in the ToF traces of both fibres **37c1** and **37c2**. From the orange (middle) traces for optimised  $LP_{11}$  launch in Figures 4.4 and 4.5, there is strong distributed coupling between  $LP_{01}$  and  $LP_{11}$  in fibre **37c1** (about 19.52 dB below the  $LP_{11}$  mode group peak) but much smaller similar coupling in fibre **37c2**—a cursory look at this trace might show no plateau, but there is actually a very minute

though finite slope between the  $LP_{01}$  and  $LP_{11}$  mode group discrete peaks, indicating the presence of a small plateau, at about 27.75 dB below the main  $LP_{11}$  peak.

There is also a similarity shared between the coupling behaviours of both fibres. Looking at the green (bottom) traces for optimised  $LP_{21}$  launch in both Figures 4.4 and 4.5, it can be seen that the  $\mathcal{C}_{11 \leftrightarrow 21}$  coupling plateaus (between 5 ps/m and 8 ps/m) are larger than the  $\mathcal{C}_{01 \leftrightarrow 11}$  plateaus (between 0 ps/m and 4 ps/m) for both fibres, with the former being at about 21.85 dB and 24.90 dB below the  $LP_{11}$  mode group peak power in 37c1 and 37c2, respectively. This behaviour of stronger coupling between  $LP_{11}$  and  $LP_{21}$  than between  $LP_{01}$  and  $LP_{11}$  is again similar to what was observed earlier in the 19c HC-PBGF 19c2, and reflects the general characteristic that the effective indices of HOMs are closer together than for lower-order modes [11].

As mentioned in Section 2.3.3, the mode effective indices in 37c PBGFs are more closely spaced than in 19c PBGFs. This should increase the susceptibility for crosstalk for the 37c case. However, a comparison of the distributed coupling plateaus for all four fibres shows that their levels appear to be similar. This is likely due to the fact that the larger core of 37c fibres means that there is less field overlap with the glass core surround surface [10, 12, 148], whose intrinsic roughness is the main cause of mode coupling (and loss) in the first place. Indeed, the loss measurements in Table 4.1 show the possibility of 37c PBGFs having even lower loss than their 19c counterparts, and referring the relationship between loss and coupling [36], it might also be possible to reduce crosstalk in 37c fibres as efforts are made to reduce loss.

#### 4.1.2 Vector Modes

As described in Section 2.2.2 and illustrated in Table 2.1, LP modes are made up of superpositions of pure vector modes. Each  $LP_{l,m}$  mode has two orthogonal states of polarisation ( $x$ ,  $y$ ), giving them 2-fold degeneracy in a perfectly circular fibre [57, 64]. Moreover, for each mode with azimuthal index  $l > 0$  (e.g.  $LP_{11}$ ,  $LP_{21}$ ,  $LP_{12}$ , etc.), there are additionally two orthogonal spatial orientations, (even, odd) or colloquially, (a, b) [93, 95], thus making them 4-fold degenerate [64].

In SCFs where the core/cladding refractive index contrast is low, modes of different spatial orientations within the same LP mode group have propagation constants that are close together. This means that their degeneracy is preserved, and there will be negligible delay spread between them, as observed in the ToF traces for the various SCFs in Chapter 3. Conversely, the index contrast in HC-PBGFs is typically much larger, with values possibly reaching  $\Delta > 2.2$  [91]. This breaks the degeneracy [86] and causes the vector components of the LP mode groups to propagate at different velocities and disperse in the time domain. This is evident from the ToF traces of the HC-PBGFs 19c1

(Figure 4.2), 19c2 (Figure 4.3), and 37c1 (Figure 4.4), where multiple discrete peaks are visible within the  $LP_{11}$  and  $LP_{21}$  mode groups.

On the other hand, polarisation degeneracy is broken by fibre birefringence [64]. As an example, the  $LP_{11}$  mode group is composed of different paired combinations of the  $TE_{01}$ ,  $TM_{01}$ , and degenerate  $HE_{21x/y}$  modes [57, 65, 66]. For an unpolarised launch in a perfectly circular fibre with large index contrast, one should expect to see three main peaks in the ToF trace of the mode group, since the two degenerate  $HE_{21x/y}$  polarisations have the same propagation constant [64]. It is only when the fibre does not have circular symmetry [57, 65], thereby introducing birefringence, that these two HE modes lose their mutual degeneracy, and as such, would be temporally dispersed. This seems to be the case in fibre 19c2. It is possible to make out four peaks within the discretely coupled  $LP_{11}$  mode group (between 7 ps/m and 11 ps/m) in the (green) ToF trace for optimised  $LP_{21}$  in this fibre (see Figure 4.3, bottom trace). Four peaks within the  $LP_{21}$  mode group itself can also be roughly seen in the same trace. This suggests that this fibre's transverse structure has some level of ellipticity, and that the HE polarisations are no longer degenerate. Such spreading within the LP modes imposes a difficulty in MDM applications as the dispersion needs to be compensated for if these HOMs are to be used as individual channels. This requirement relies on receiver-end DSP [95] and therefore precludes the use of direct detection systems.

On the contrary, visual inspection of the ToF traces for optimised  $LP_{11}$  and  $LP_{21}$  launches in fibre 37c2 (middle and bottom traces of Figure 4.5) shows that the vector modes within each respective mode group are not spread out as widely as in other PBGFs (for instance, compared with the same respective traces for fibre 37c1). In fact, it seems that the vector mode components in 37c2 have remained as nearly single peaks. This is promising for data transmission over HOMs using direct detection, i.e. without requiring MIMO DSP, which is the same method used to detect data sent over  $LP_{01}$ . Section 4.2 describes an attempt on such transmission using HOMs in this fibre.

### 4.1.3 Differential Group Delay

From all the ToF traces in Figures 4.2–4.5, the DGDs of the HOMs w.r.t.  $LP_{01}$  are measured and tabulated in Table 4.6. These are consistent with  $S^2$  measurements [75, 93, 94] on these fibres. We see that the DGDs are larger in the 19c PBGFs than in the 37c PBGFs. This can be expected since, as discussed in Section 2.3.3, while the size of the photonic bandgap is the same for both 19c and 37c core sizes, the latter allows more guided modes, resulting in a more densely populated bandgap with adjacent modes having more closely spaced effective indices [11]. Although the group delays of modes are not directly related to their effective indices—as mentioned in Section 3.3.2.2, they are determined by the *group indices* where there is an additional dependence on the

derivative of the refractive index w.r.t. wavelength [142]—there is still some degree of proportion between the two.

TABLE 4.6: Measured DGDs of HC-PBGFs from ToF.

Fibre	$\Delta\tau$ (ps/m)	
	LP <sub>11</sub>	LP <sub>21</sub>
19c1	7.7–10.2	—
19c2	7.8–10.3	18.6–19.7
37c1	4.1–4.9	10.1–12.3
37c2	3.9	8.7

The DGD spectrum of these fibres can also be measured. Figure 4.6 shows a modified ToF set-up which is similar to that of Figure 3.3, but with the additional use of an OSA. Instead of optimising the launch to suppress unwanted modes as for the ER measurements, the PP alignment is adjusted so that multiple modes are excited and their arrival pulses can be seen simultaneously on the oscilloscope. Here, we are interested in recording the time delays between the arrivals of OMs. For the experiment, only measurements for the LP<sub>01</sub> and LP<sub>11</sub> modes are taken.

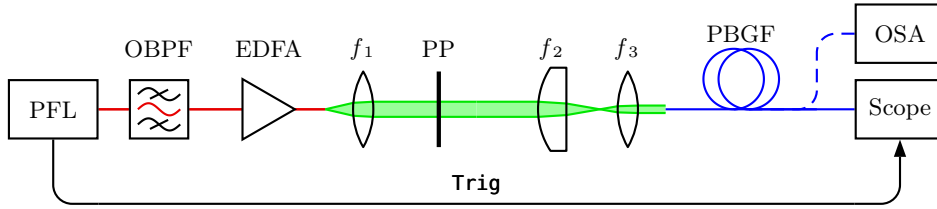


FIGURE 4.6: ToF set-up for DGD measurements.

Using the OSA to guide the tuning of the OBPF and PFL, DGD values are taken over a range of wavelengths from 1528 nm to 1562 nm, the dynamic operating range of the OBPF, which also coincides with the conventional telecommunications C-band. Note that wavelength tuning is done before DGD measurements are taken (from the oscilloscope) and the OSA is not concurrently connected to the set-up during the latter, as indicated by the dashed fibre line in the figure. That is, the fibre output is alternatively switched between the OSA and the oscilloscope detector for tuning and measurement, respectively.

DGD spectrum measurements were performed<sup>2</sup> on fibre 37c1 and Figure 4.7 displays the results. For comparative purposes, the DGD spectrum of fibre 19c2 is also reproduced with data from [13] and displayed in the same plot. The two LP<sub>11</sub> curves for each fibre (orange filled and empty triangles/circles) represent the delays of the earliest and latest

<sup>2</sup>The experiment on fibre 37c1 was jointly conducted by myself and Jung of the ORC's PFLG.

arriving distinguishable  $LP_{11}$  peaks in the ToF traces (equivalent to the orange, middle traces in Figures 4.3 and 4.4). For fibre **37c1**, the DGD between the  $LP_{11}$  and  $LP_{01}$  modes is approximately 4 to 5 ps/m (at  $\lambda = 1550$  nm), which is about 50% smaller than that for the 19-cell fibre **19c2** [8, 13, 75]. This is in good agreement with previous  $S^2$  results [93, 94], and the general prediction mentioned previously that DGD and core size are inversely related [11, 12]. In fact, the 1:2 ratio between the  $LP_{11}$  DGDs of **37c1** and **19c2** reflects the prediction that 37c PBGFs can support approximately double the number of air-guided modes than 19c PBGFs (about 80 and 40 modes, respectively) [11, 86, 93, 94]. Moreover, this double ratio is also observed to manifest in the delay spreads of the vector modes within the  $LP_{11}$  mode group itself, with the  $LP_{11}$  vector mode spread of **37c1** being approximately half that of **19c2**.

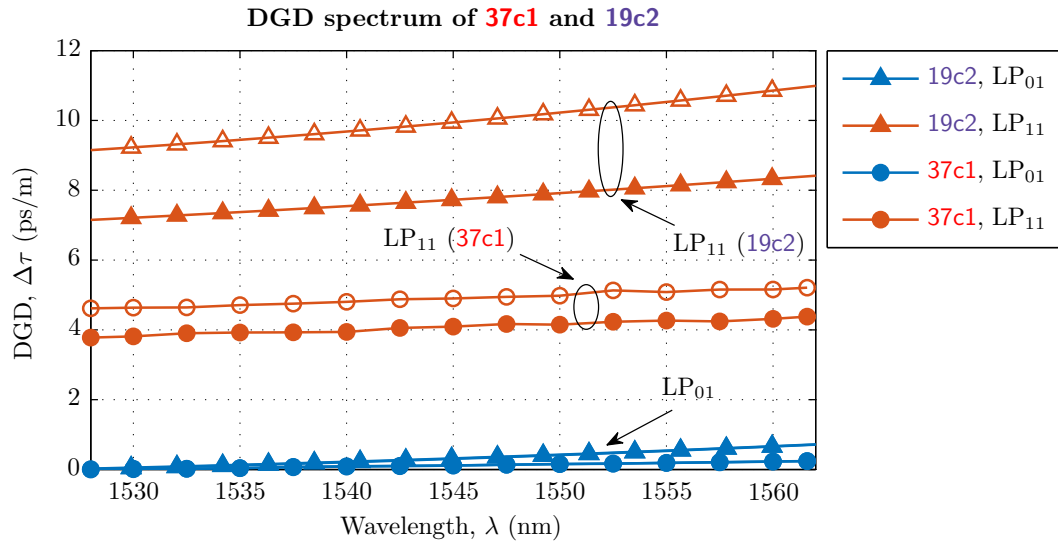


FIGURE 4.7: DGD measurements of the  $LP_{01}$  and  $LP_{11}$  modes in fibres **37c1** and **19c2**. *19c2 results courtesy of N.V. Wheeler and Y. Jung [13].*

Continuing with the analysis, it can be seen in Figure 4.7 that varying the wavelength causes the DGDs of both  $LP_{01}$  and  $LP_{11}$  to change, in both fibres. Such wavelength dependence of the DGDs suggests some chromatic dispersion in both modes in either fibre. Furthermore, the DGD variation for **19c2** is starker (i.e. the curves are steeper) than for **37c1**. This means that there is less chromatic dispersion in the latter. From the DGD curves, the dispersion, for  $LP_{01}$  and  $LP_{11}$ , respectively, is estimated to be about 21 ps/(nm km) and 46 ps/(nm km) for **19c2**, and 7 ps/(nm km) and 18 ps/(nm km) for **37c1** [93]. The latter  $LP_{01}$  dispersion is lower than the 17 ps/(nm km) typical in SSMF [6], and shows the competitive potential of HC-PBGFs.

Finally, the lack of crossings between the DGD curves implies the absence of surface modes propagating in the fibres [8, 13, 75], which concurs with the uninterrupted wide bandwidths within the C-band observed in previous broadband cutback loss measurements [13, 93].

#### 4.1.4 Summary

This section has presented ToF measurements on novel 19c and 37c HC-PBGFs. They have revealed that HOMs can be suppressed to potentially allow single-mode operation, that distributed mode coupling is present, and that temporal splitting of vector modes is common in these fibres and more significant than in SCFs. The measurements also show that the DGDs between modes are smaller for larger core sized PBGFs, experimentally confirming theoretical predictions for 37c PBGFs for the first time. Additionally, DGD spectrum measurements have provided information on chromatic dispersion of individual modes in these fibres, and also show an absence of surface mode interaction, corroborating previous transmission spectrum measurements.

Further experiments on the ability of these PBGFs to transmit data are detailed in Section 4.2. Thereafter, Section 4.3 describes the use of ToF to diagnose unexpected transmission behaviour in a long-length HC-PBGF, and is followed by Section 4.4, which briefly outlines ToF measurements in the 2  $\mu\text{m}$  waveband.

## 4.2 Data Transmission in HC-PBGFs

After having determined suitable mode extinction ratios for the HC-PBGFs under study, data is sent through them to assess their transmission capability. Two metrics commonly used for characterisation are the eye diagram and bit error rate (BER).

An eye diagram is obtained by superimposing multiple instances of a signal onto itself to produce a cumulative trace. These instances are of one or more pulse periods and it is important that the signal is sampled in synchrony with its period, necessitating reference from a clock trigger. Because of noise and interference, pulse traces are not identical to one another and so the amount of degradation from a perfect eye, arising from the superposition of these imperfect traces, is a gauge of how distorted the signal is. The eye diagram is assessed in terms of its openness and provides a convenient indication of the signal quality. If a signal is noisy and/or there is intersymbol interference, the signal levels can be pushed away from their optimum amplitude positions, resulting in the closing of the eye. Figure 4.8 depicts an example of an eye diagram for the back-to-back case in a 10 Gbit/s non-return-to-zero (NRZ) on-off keying (OOK) direct detection measurement, which shows a clean open eye. The quality of a signal determines its ability to reliably carry data, and so the eye diagram is inherently related to the BER [149].

The BER of a (binary) communications system is defined as the rate at which bit decisions are erroneously made at the receiver. This is a summed probability and can be expressed as [6]

$$\text{BER} = \Pr(1) \Pr(0|1) + \Pr(0) \Pr(1|0), \quad (4.1)$$

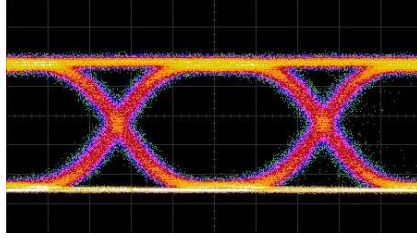


FIGURE 4.8: Example of an open eye in an eye diagram.

where  $\Pr(\mathbf{0})$  and  $\Pr(\mathbf{1})$  denote the probabilities of receiving the bits  $\mathbf{0}$  and  $\mathbf{1}$ , respectively,  $\Pr(\mathbf{1}|\mathbf{0})$  is the probability of the receiver deciding  $\mathbf{1}$  when  $\mathbf{0}$  is received, and vice versa for  $\Pr(\mathbf{0}|\mathbf{1})$ . In ideal random systems, the probabilities of receiving either  $\mathbf{0}$  or  $\mathbf{1}$  are equal and so  $\Pr(\mathbf{0}) = \Pr(\mathbf{1}) = 1/2$ . Therefore (4.1) reduces to

$$\text{BER} = \frac{1}{2} [\Pr(\mathbf{0}|\mathbf{1}) + \Pr(\mathbf{1}|\mathbf{0})]. \quad (4.2)$$

Proper characterisation usually takes BER values for a range of received optical power levels. The BER trend against received signal power is measured for both the fibre being tested and the back-to-back (B2B) case, which uses the same transmission set-up sans the FUT, i.e. the transmitter is connected directly to the receiver. A generally accepted level for reliable communications is a BER of  $10^{-9}$  [14], and any increase in the received power through a fibre channel required to achieve the same BER as the B2B case at this level is denoted as the power penalty of the channel.

Usually, a visual inspection of the eye diagram is sufficient to qualitatively assess whether or not a FUT can be used for data transmission. Only when further quantitative assessment of the transmission performance is needed are BER tests performed. All transmission experiments in this section were done at the 1550 nm telecommunications wavelength.

#### 4.2.1 Experimental Transmission Set-Up

Figure 4.9 shows the set-up for data transmission at 10 Gbit/s. The signal generator (SG) outputs a 10 GHz periodic signal that drives the bit pattern generator (BPG), which produces a  $(2^{31} - 1)$  bit-long pseudorandom binary sequence (PRBS) at a bit rate of  $R_b = 10$  Gbit/s. This is amplified by the radio-frequency amplifier (RFA) and fed to a Mach-Zehnder modulator (MZM), which uses OOK to modulate light at a wavelength of  $\lambda = 1550$  nm coming from the continuous wave laser (CWL). The components mentioned thus far make up the transmitter (Tx). The modulated light signal passes through a polarisation controller (PC), is amplified by EDFA<sub>1</sub>, and proceeds to the free-space arrangement similar to that in Figure 3.3. The light is focussed into the FUT and after propagating through it, is focussed back into an SSMF pigtail via the collimation lenses

$f_4$  and  $f_5$ , which both have focal lengths of 4.5 mm.<sup>3</sup> On the receiver end, the variable optical attenuator (VOA) is used to control the received power so as to enable taking a range of BER measurements. At this stage, the signal is split using a 50:50 coupler, with one arm being monitored by a power meter (PM) and the other continuing to the rest of the receiver. The latter starts with a second EDFA (EDFA<sub>2</sub>) acting as a pre-amplifier, followed by an OBPF that is tuned and optimised to suppress any sidebands (as seen on a separate OSA) introduced by the EDFA. The signal is split again using another 50:50 coupler, with the secondary arm this time going to a digital communications analyser (DCA)—which is triggered by the BPG—for monitoring the eye diagram. The signal in the primary arm is fed to the receiver (Rx), which detects the optical signal and converts it to an electrical one. The electrical data is inputted into the error analyser (EA), which makes BER calculations based on the reference PRBS provided by the BPG. The Rx also supplies a clock signal (Clk) to the EA for synchronisation with the Tx; this Clk is itself received from the BPG (not shown). The inclusion of the PC is to optimise the signal power through the observably polarisation sensitive PBGF FUTs. Optimisation is done by maximising the eye opening on the DCA. For comparison purposes, BER/eye diagram measurements are also taken for the B2B case (the dashed red line in the figure). This set-up includes a free-space arrangement for launching light into unconnectorised FUTs. In cases where the FUT is already connectorised with SSMF pigtailed, the free-space components can be omitted and the fibre patch cords can be connected in the same way as the B2B case. This latter method only permits single-mode transmission.

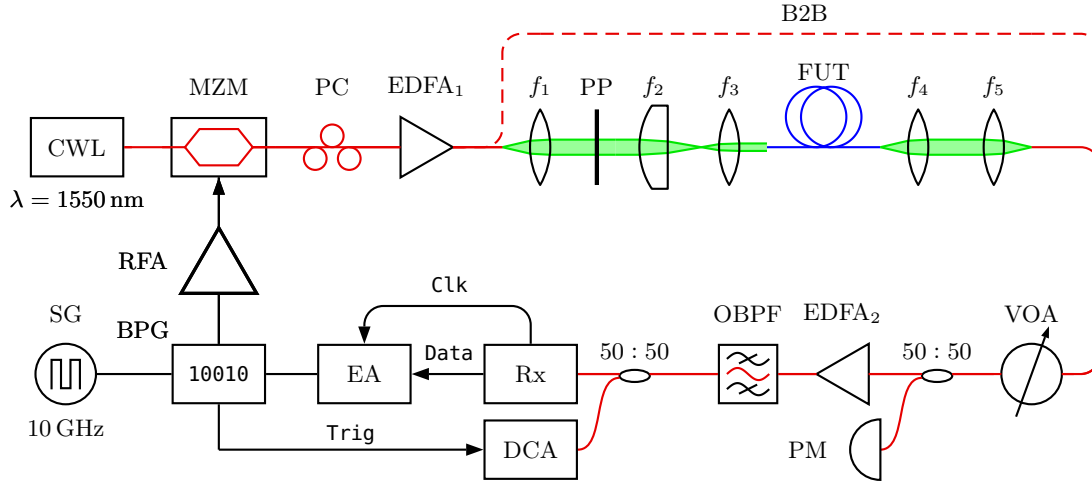


FIGURE 4.9: 10 Gbit/s data transmission set-up.

Whereas the 10 Gbit/s system is sufficient to show if FUTs can transmit data, and indeed most of the transmission tests in this thesis were performed with that set-up, the *ORC* also possesses a 40 Gbit/s system, from *SHF Communication Technologies AG*, that incorporates a built-in transmitter (Tx), among other modules. The set-up is mostly

<sup>3</sup>These focal lengths were chosen to optimise the coupling efficiency.

similar to that in Figure 4.9, with the only differences being a modularised Tx, and that the SG clocks at 40 GHz.

#### 4.2.2 Single-Mode Transmission Over HC-PBGF

Motivated by the high ERs from ToF measurements on the various PBGFs in Section 4.1.1, transmission tests were performed to experimentally assess their single-mode data transmission ability. Using the set-up in Figure 4.9, 10 Gbit/s NRZ OOK data was sent over the fundamental mode through fibres 19c1 and 19c2. The eye diagrams were taken and are displayed in Figure 4.10

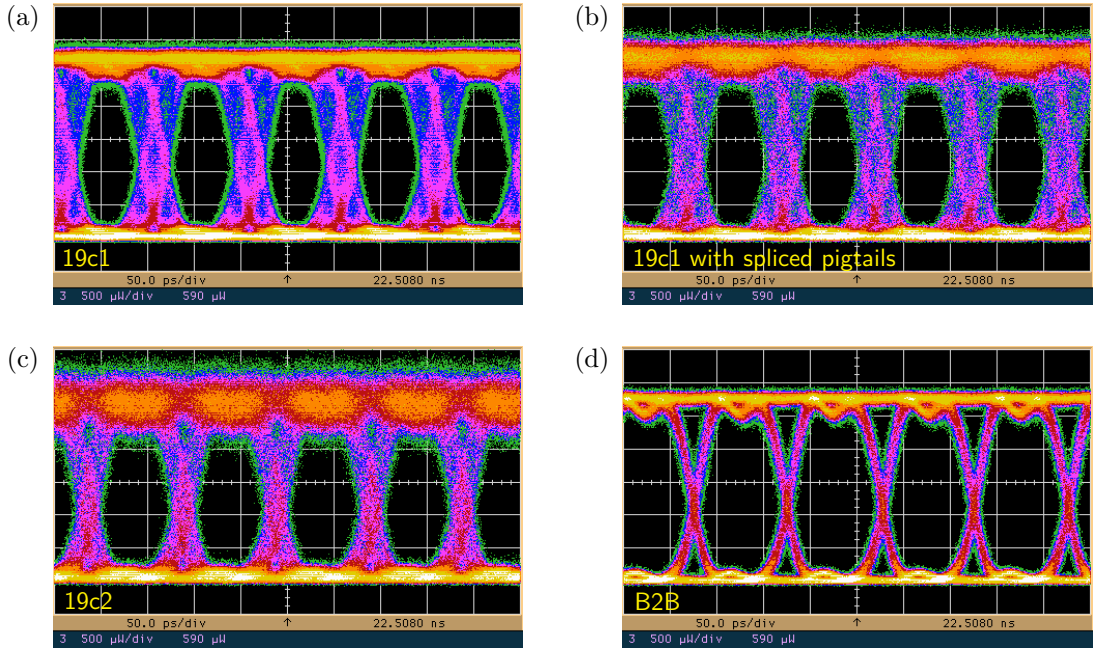


FIGURE 4.10: Eye diagrams for 10 Gbit/s NRZ OOK single-mode transmission through (a) 19c1, (b) 19c1 with spliced pigtails, and (c) 19c2. (d) B2B case.

Figures 4.10a and 4.10c show the eye diagrams for fibres 19c1 and 19c2, respectively, where the free-space arrangement was used to couple light into the PBGFs. Both eyes show some degradation from the B2B case in Figure 4.10d, but are still clearly open, indicating that both fibres can transmit single-mode data decently. The eye of 19c2 is slightly more closed than that of 19c1, suggesting poorer transmission performance. Although this is in contradiction to the comparative loss measurements for these fibres in Table 4.1, it could be that the HOMs are lossier in 19c1, and loss measurements over an optimised  $LP_{01}$  launch may possibly reveal lower attenuation than in 19c2.

Within the MODE-GAP context, fibre 19c1 was to be used by a collaborating company for low-latency trials, and its ends were spliced with SSMF pigtail connectors. Figure 4.10b depicts the transmission result for the fibre with pigtails, and the eye diagram shows small but noticeable degradation from the unconnectorised case in Figure 4.10a.

This suggests that the splices might be introducing some loss in the fibre and impairing the performance. The fibre was eventually reconnectorised and subsequently performed better,<sup>4</sup> but the result in Figure 4.10b is included to demonstrate the diagnostic ability of this transmission trial.

### 4.2.3 The First Data Transmission Through a 37c HC-PBGF

Fibre 37c1 was the first 37c HC-PBGF ever fabricated with a low 4.5 dB/km loss at 1550 nm and a wide 3-dB bandwidth of 85 nm [94]. The promising ToF characterisation results encouraged single-mode data transmission trials to be carried out, the first ever on a PBGF of this core size.

40 Gbit/s NRZ OOK was transmitted over  $LP_{01}$  through this fibre using the set-up in Figure 4.9, but with the aforementioned 40 Gbit/s modifications.<sup>5</sup> The eye diagram and BER results are shown in Figures 4.11 and 4.12, respectively.

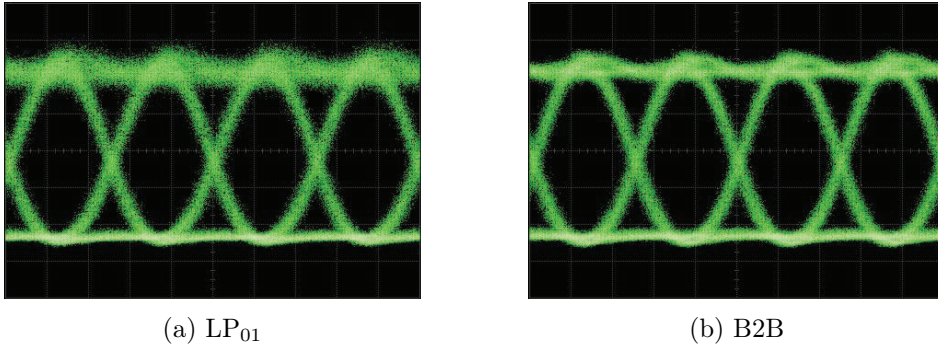


FIGURE 4.11: Eye diagrams for 40 Gbit/s NRZ OOK transmission over (a)  $LP_{01}$  through fibre 37c1 and (b) the B2B link.

Observing the two eye diagrams in Figure 4.11, there is slight degradation in the signal after propagating through the PBGF. Nevertheless, the eye in Figure 4.11a is still clearly open, indicating that the signal has not suffered much distortion. Complementing the eye diagram, the BER results in Figure 4.12 show that the fibre exerts minimal degradation on the signal, with a received power penalty of  $< 1$  dB at a BER of  $10^{-9}$ . This is very encouraging for error-free transmission and demonstrates the capability of the 37c HC-PBGF in single-mode regime communications. These results were published in [94].

In addition to predicting good single-mode transmission, the ERs and distributed coupling measured via ToF for this fibre in Section 4.1.1 suggested that while the levels of crosstalk across HOMs are not as low as for the fundamental mode, they might still be good enough for MDM transmission. The fibre was subsequently used by Sleiffer and

<sup>4</sup>These later results were unfortunately not available at the time of writing.

<sup>5</sup>These measurements were taken with the help of Y. Jung and F. Parmigiani from the *ORC*.

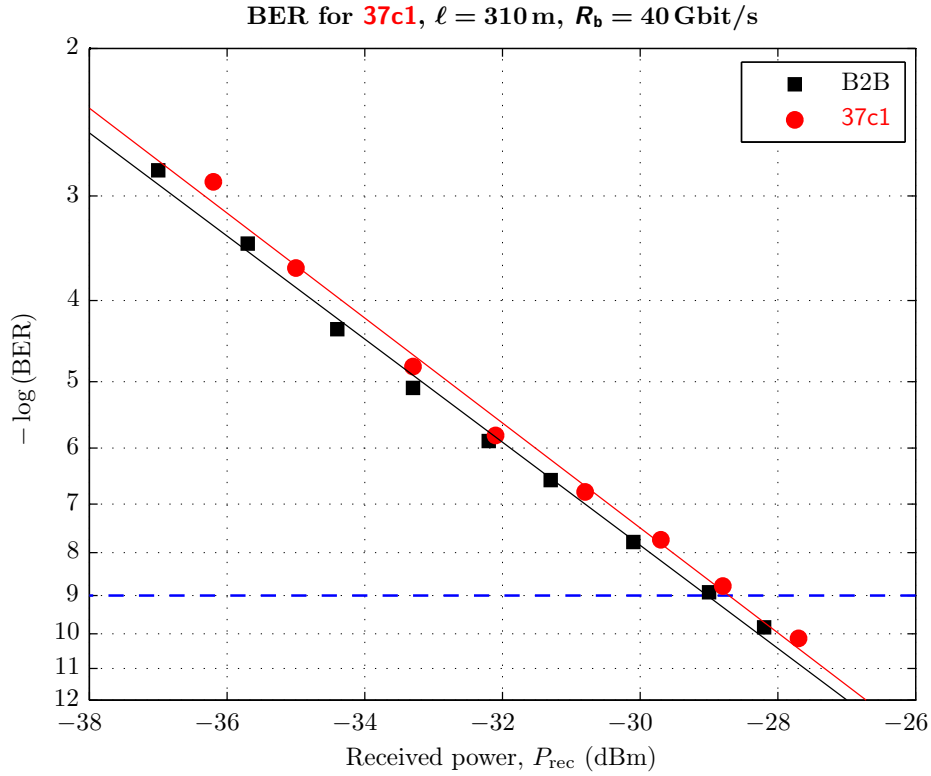


FIGURE 4.12: BER measurements for 40 Gbit/s NRZ OOK transmission over  $\text{LP}_{01}$  through fibre 37c1.

other MODE-GAP collaborators in an MDM trial with MIMO DSP employed to counter the effects of modal dispersion within the higher-order mode groups.<sup>6</sup> Three modes  $\{\text{LP}_{01}, \text{LP}_{11a}, \text{LP}_{11b}\}$  were multiplexed (MUX) using free-space optics. Each was launched with a time-delayed replica of a 96-channel WDM, 256 Gbit/s dual-polarisation, DP-16QAM signal. Selective mode excitation was done through a similar phase plate arrangement as in Figure 3.3. The modal beams were combined using beam splitters and the resulting combination was launched into fibre 37c1 via the telecentric arrangement. After transmission over the 310 m-long PBGF, the modes were demultiplexed in a manner reciprocal [51] to the MUX setup<sup>7</sup> (but without the telecentric system). Data from the three arms were collected and processed offline using MIMO DSP to decouple the signals. The BERs measured were all under the forward error correction limit, indicating that reliable communications had been achieved. In addition to this being the first demonstration of MDM transmission in a 37c HC-PBGF, the aggregate data rate was an impressive 73.7 Tbit/s, a record for HC-PBGFs. This was reported in [93] and [95].

<sup>6</sup>In this work, the modal characterisation and single-mode transmission experiments were done at the ORC and subsequently, the MDM transmission trials were carried out at then *Nokia Siemens Networks (NSN)* (now reorganised as *Coriant GmbH*) in Munich, Germany. My contributions were largely in the former, most of which has been covered in the preceding sections of this chapter. As such, the following description on MDM is kept brief.

<sup>7</sup>See [95], Fig. 2 for the complete schematic.

#### 4.2.4 MDM Data Transmission Over HOMs Using Direct Detection

The success of the MDM experiment mentioned in Section 4.2.3 relied on offline MIMO DSP, thereby increasing the complexity of the system. Direct detection removes this dependence. Prompted by the apparent single peak ToF profiles of the  $LP_{11}$  and  $LP_{21}$  modes in fibre 37c2 (see Figure 4.5 and Section 4.1.2), an MDM data transmission test using direct detection without any MIMO processing in the receiver was attempted. The set-up is similar to that in Figure 4.9, except with an additional 4-region phase plate (leftmost in Figure 3.5) between lenses  $f_4$  and  $f_5$  to enable the reception of HOMs by mapping them back to  $LP_{01}$ . NRZ OOK data was transmitted at 10 Gbit/s over the fibre in the single-mode regime using  $LP_{01}$ ,  $LP_{11}$ , and  $LP_{21}$ . Figure 4.13 shows the eye diagrams obtained.

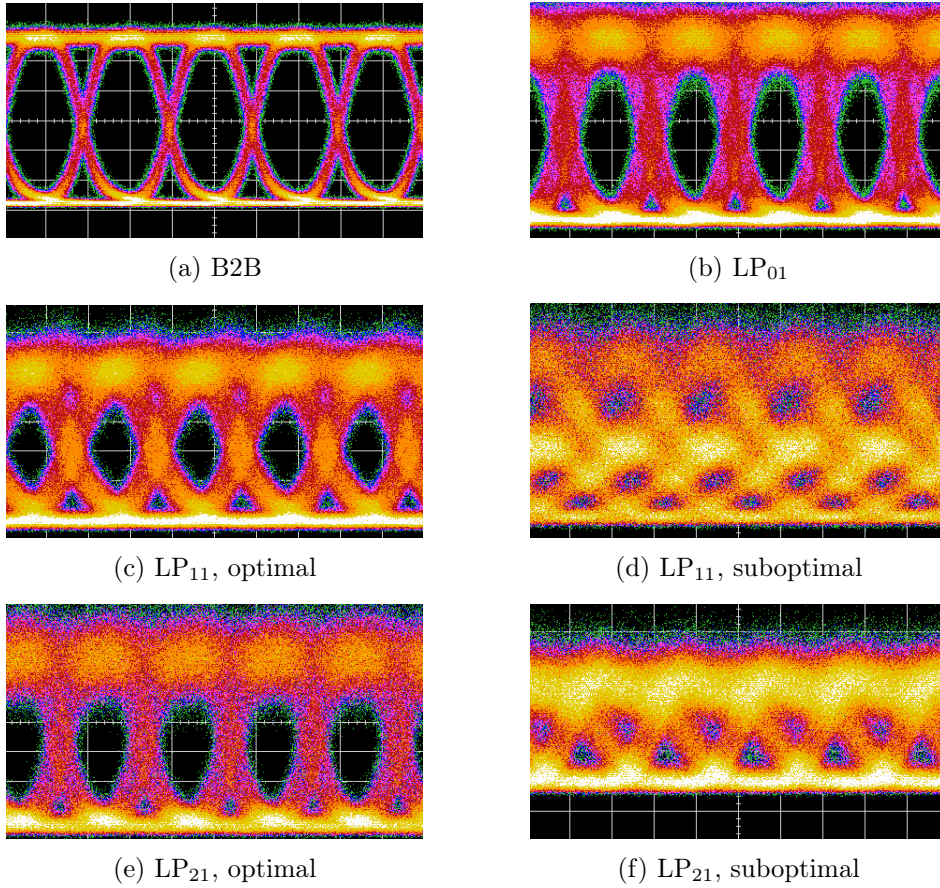


FIGURE 4.13: Eye diagrams for 10 Gbit/s NRZ OOK (a) B2B link and transmission through fibre 37c2 with direct detection using (b)  $LP_{01}$ , (c, d)  $LP_{11}$ , and (e, f)  $LP_{21}$ .

The eye openings for  $LP_{11}$  and  $LP_{21}$  are observed to be much smaller than for  $LP_{01}$ , even at optimum received power. When the received power was lowered, the  $LP_{11}$  and  $LP_{21}$  eyes closed completely, as seen in Figures 4.13d and 4.13f, suggesting that there is considerable intersymbol interference. This could imply that the intra-group modal dispersion (dispersion among the constituent vector modes) of the  $LP_{11}$  and  $LP_{21}$  mode

groups, while smaller than that in say fibre 37c1, is still large enough for direct detection not to work reliably. It was therefore decided not to continue further with BER tests. However, there is confidence in the premise that direct detection may be still successfully employed where HOMs have minimal vector spreading, and a plan has been conceived to re-attempt the experiment when a suitable HC-PBGF satisfying that property becomes available.

#### 4.2.5 Other Trials

The collaborations between the *ORC* and external partners, in projects such as MODE-GAP, have established an ecosystem where many fibres produced by the *ORC* are used in various communications experiments by our collaborators. This often requires quick pre-experiment data transmission trials, usually in the single-mode regime, to check if the fibres can indeed transmit information. A number of these tests have been performed by myself, and this subsection describes tests to check the transmission in one particular 19c HC-PBGF that was used by our partners at the *University of Bristol* for experiments in data centre networks. This partnership is part of the FP7 project called “Combining Optics and SDN In next Generation data centre Networks” or *COSIGN*, which leverages on advances in optics to build next-generation data centre architectures [150].

The fibre is a 400 m sample that was cut into  $3 \times 100$  m sections and  $6 \times 10$  m sections, to be used as low-latency fibre links in a data centre test bed. Using the set-up in Figure 4.9, 10 Gbit/s NRZ OOK single-mode transmission was carried out on the various lengths, including the full 400 m before it was chopped, and Figure 4.14 displays the resultant

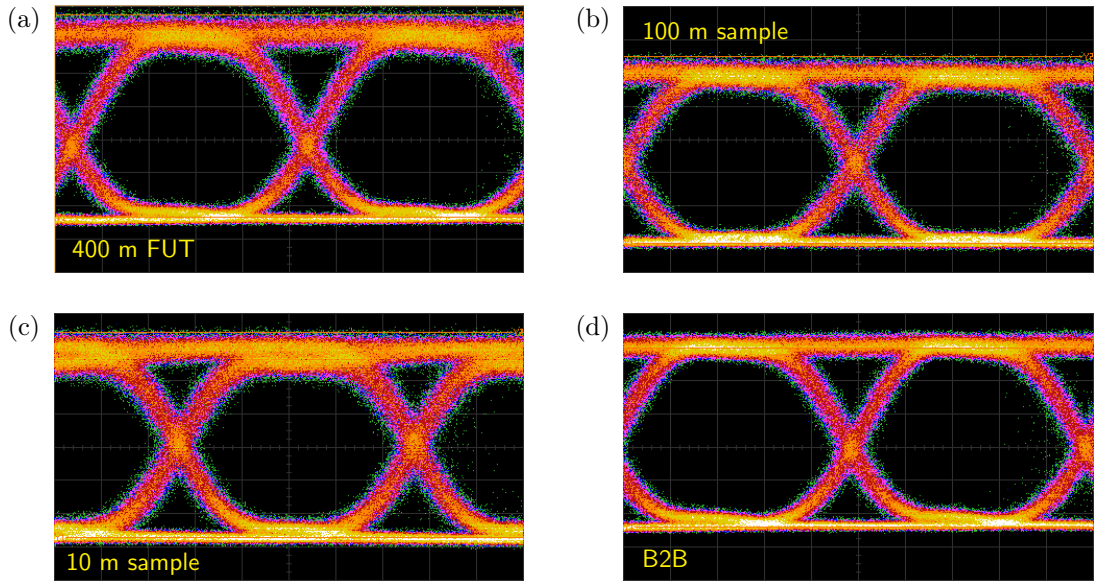


FIGURE 4.14: Eye diagrams for 10 Gbit/s NRZ OOK single-mode transmission through a 19c HC-PBGF used for data centre experiments. (a) 400 m full length, (b) 100 m sample, (c) 10 m sample, and (d) B2B case.

representative eye diagrams. Note that each sample was connectorised with SMF pigtails and no free-space launching arrangement was required.

The clearly open eyes in all cases compared to the B2B case shows that reliable data transmission has been achieved for each length sample. With this confirmation, the samples were sent to the *University of Bristol* for data centre trials, the results of which are presented in [102] and [103].

In the next section, the gears are switched back to the ToF context, where the technique is used to study a misbehaving long-length HC-PBGF.

### 4.3 Diagnosing HC-PBGF Performance Using ToF

In 2015, Chen et al. from the MOFG at the *ORC* fabricated and presented, in [108], a record-length 11 km 19c HC-PBGF, whose SEM cross-section is shown in Figure 4.15. It was the first PBGF having a continuous span of such a length, and measurements, enabled by the recently developed optical side scattering radiometry (OSSR) technique [135], showed it to have high longitudinal consistency and a modest though decent loss value of  $\sim 5$  dB/km. Data transmission trials over the C-band at 10 Gbit/s using both coherent transmission (QPSK) and direct detection (OOK) on  $LP_{01}$  measured  $\leq 2$  dB power penalty from the B2B case, demonstrating good single-mode operation [108].

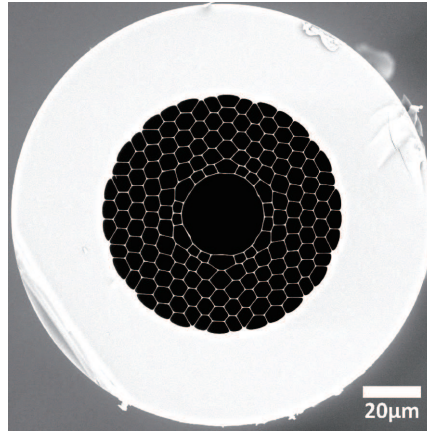


FIGURE 4.15: SEM cross-section of the record-length 19c HC-PBGF. *Courtesy of S.R. Sandoghchi [111].*

As part of our contributions to the MODE-GAP project, the fibre was chopped into three segments, Band A (3.5 km), Band B (3.5 km), and Band C (4 km), to be used in recirculating loop experiments, performed by *Coriant* and other collaborators, to demonstrate long-distance, low-latency transmission. However, quick pre-trial transmission tests after

the sectioning revealed degraded performance in some bands, as shown in the eye diagrams in Figure 4.16 for 10 Gbit/s NRZ OOK single-mode transmission.<sup>8,9,10</sup> Whereas band B transmitted cleanly with an open eye, bands A and C had eyes that were not only severely closed, but also unstable, which indicated the presence of signal distortion and interference.

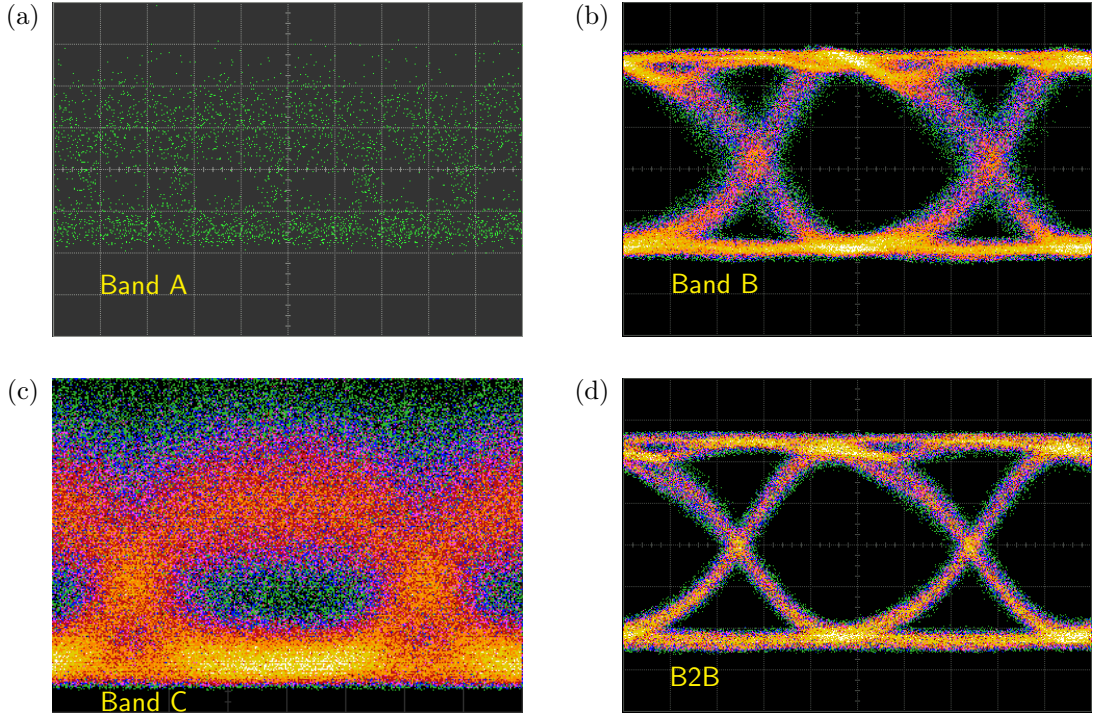


FIGURE 4.16: Eye diagrams for 10 Gbit/s NRZ OOK single-mode transmission through (a) band A (b) band B, and (c) band C of the long-length 19c HC-PBGF. (d) B2B case.

This prompted further tests, including ToF, to determine the origin of the degradation and possible remedies. The tests described in this section are my contribution to the overall investigation work that involved more than a dozen researchers from the *ORC*, each performing various tasks, e.g. OTDR, cutback measurements, connector splicing, data transmission, fibre respooling and preparation, etc.

### 4.3.1 Initial ToF Diagnostics

To determine if mode coupling or other effects were the culprit for the poor performance of the bands, ToF was measured on them using the set-up in Figure 3.3 (omitting the

<sup>8</sup>Note that all bands were connectorised with SSMF pigtails, and so no free-space launch set-up was needed.

<sup>9</sup>The results for band B as well as the B2B case were obtained from measurements that were conducted by Z. Liu of the *ORC*, with my assistance.

<sup>10</sup>Some of the eye diagrams look different because they were measured on different instruments. Nevertheless, the set-ups used were the same.

PC). At first, both the ends, SoP and EoP,<sup>11</sup> of each FUT had spliced SSMF pigtail connectors, and so the free-space launching arrangement was not used. To simulate loss, a VOA was added after the FUT, and a second EDFA, acting as a receiver pre-amplifier, was used to boost the signal after having travelled over the > km-length distance through the fibre. Figure 4.17 shows the modified experimental set-up.

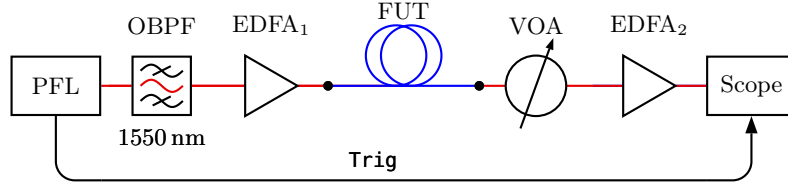


FIGURE 4.17: ToF experimental set-up for long-length fibre diagnostics.

Band A was addressed first. Measurements were taken in both directions of the fibre, and showed little difference. The pigtail connectors were then successively removed to explore their effect on the fibre behaviour. Several cases were measured. First, the pigtail at the output end (at the time, EoP) was discarded and the PBGF was reconnected to the set-up via bare fibre adapter. Next, the FUT direction was reversed and in this case, the free-space arrangement was used to launch light into the bare PBGF EoP input. Finally, the remaining connectorised end (SoP) also had its pigtail removed. The B2B case with the FUT was also measured and used as a reference. The following list enumerates these steps and defines the legend nomenclature in Figure 4.18, which summarises the measured results.

1. Back-to-back case: “B2B reference”
2. Both FUT sides connectorised, EoP to SoP direction: “Pigtail/EoP→Pigtail/SoP”
3. Both FUT sides connectorised, (reverse) SoP to EoP direction: “Pigtail/SoP→Pigtail/EoP”
4. EoP pigtail removed, (same) SoP to EoP direction: “Pigtail/SoP→Bare/EoP”
5. EoP pigtail removed, (reverse) EoP to SoP direction: “Bare/EoP→Pigtail/SoP”
6. Both SoP and EoP pigtails removed, (same) EoP to SoP direction: “Bare/EoP→Bare/SoP”<sup>12</sup>

Firstly, in deference to the technique of using ToF to detect defects (first demonstrated in [136] and described in detail in Chapter 6), the absence of discrete peaks away from

<sup>11</sup>The labels SoP and EoP refer to the sides of the fibre identified as “Start of Pull” and “End of Pull”, respectively, following fabrication nomenclature.

<sup>12</sup>Note that the case with both ends’ pigtails removed was not tested in the SoP to EoP direction, in order not to disturb the free-space alignment that was already optimised for the previous reverse direction.

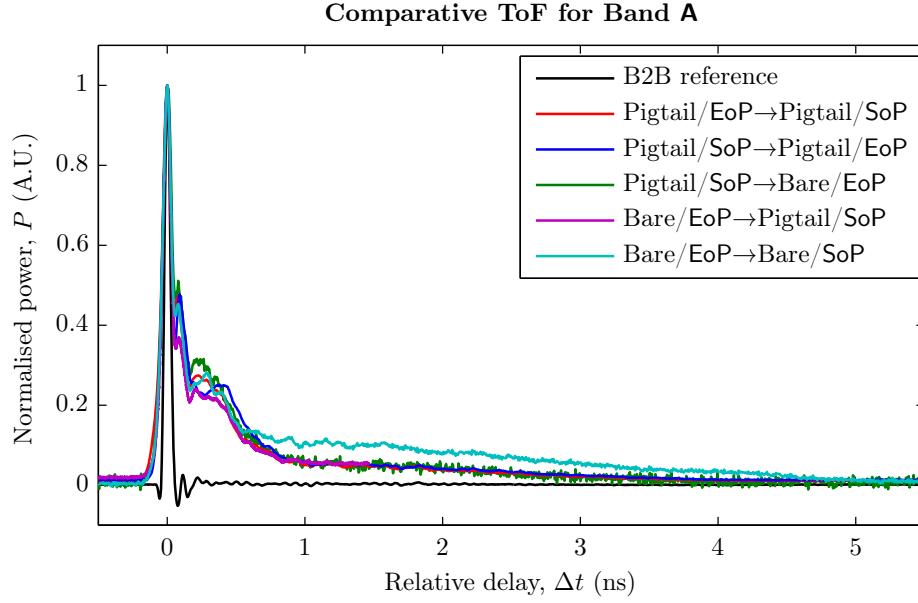


FIGURE 4.18: ToF for various connection and direction cases on band A of the long-length HC-PBGF after fundamental mode selective launch.

the main  $LP_{01}$  launched peak rules out major longitudinal defects as the cause of the degraded performance. This was confirmed by independent OTDR measurements taken by other MOFG members.

Compared to the B2B reference, the ToF results from all test cases exhibit some level of distributed mode coupling, as seen by the plateau from about 0.9 to 4.8 ns, after the main impulse. Whereas the plateau level is similar in all other cases, it is discernibly higher for the case where both SSMF pigtail connectors were removed. This implies that while there is still some remnant distributed coupling occurring when either or both FUT ends are connectorised, the SSMF pigtails do effect some suppression on the HOM content in the fibre. Without the filtering effect of the pigtails, the distributed coupling is more severe (the cyan plateau is roughly twice as high as the others). This suggests that it is the mode coupling that degrades the fibre's performance, and at the same time, absolves the pigtail connectors from blame due to any poor splices.

To further confirm that the raised plateaus in the ToF indeed result from mode coupling, the output end of the FUT was wrapped about 20 times around a  $\sim 3$  mm-diameter mandrel to strip off the HOMs. ToF measurements were taken and Figure 4.19 shows the results for two repeated wrapping cases **Wrap1** and **Wrap2**.<sup>13</sup> In both cases, there is a clear suppression of the plateau compared to the unwrapped case. The earlier ToF result when the FUT still had pigtail connectors (i.e. Pigtail/EoP→Pigtail/SoP) is also plotted for comparison, and it is observed that the distributed plateaus in the mandrel-wrapped cases have diminished to a similar level as this case. This provides validation for the fact

<sup>13</sup>The launch alignment was still preserved from earlier, and so these measurements were taken in the same EoP→SoP direction.

that mode coupling is indeed present, and also shows that mandrel wrapping can reduce the distributed coupling by a similar amount as the filtering effect of connectorised SSMF pigtails. The fact that the plateau could not be suppressed any further, even with such a tight mandrel wrap, prompted investigation into the cause of the mode coupling.

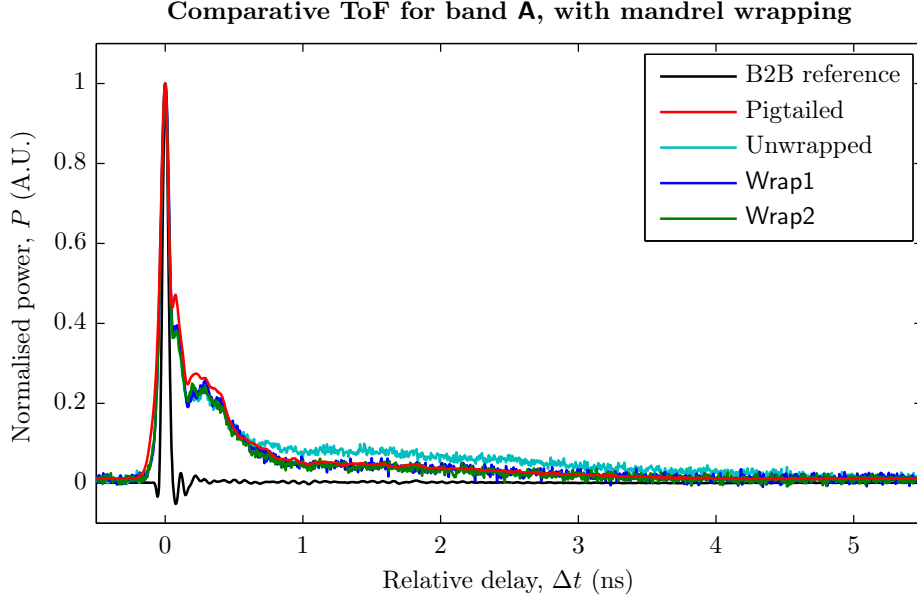


FIGURE 4.19: ToF for mandrel-wrapped band A of the long-length HC-PBGF after fundamental mode selective launch.

### 4.3.2 Effects of Respooing

It was suspected that mechanical issues pertaining to how bands A and C were spooled on their bobbins were the cause of the observed distributed mode coupling. Band C was respooled first, by MOFG members, using lower spooling speed and tension. Meanwhile, band A's pigtail connectors were respliced.

ToF measurements were taken again as depicted in Figure 4.20,<sup>14</sup> which includes the result for band B as well. The plot shows that the respooled band C has much less distributed mode coupling than band A, and its plateau is now very close to that of band B (which itself is small but finite). This confirms the suspicion that the distributed coupling in band C was caused by the way that it was originally spooled. As for band A, whose previous pigtailed and bare fibre results are also plotted for comparison, the ToF trace for the case with newly spliced pigtails closely matches that for its original pigtails, demonstrating the repeatability of the splice procedure.

Due to the long fibre lengths, pulses are broadened by dispersion, as observed in the ToF traces. To reverse this effect, a 220 m dispersion-compensating fibre (DCF) was

<sup>14</sup>This figure is plotted against the relative delay per unit length, to account for the different band lengths.

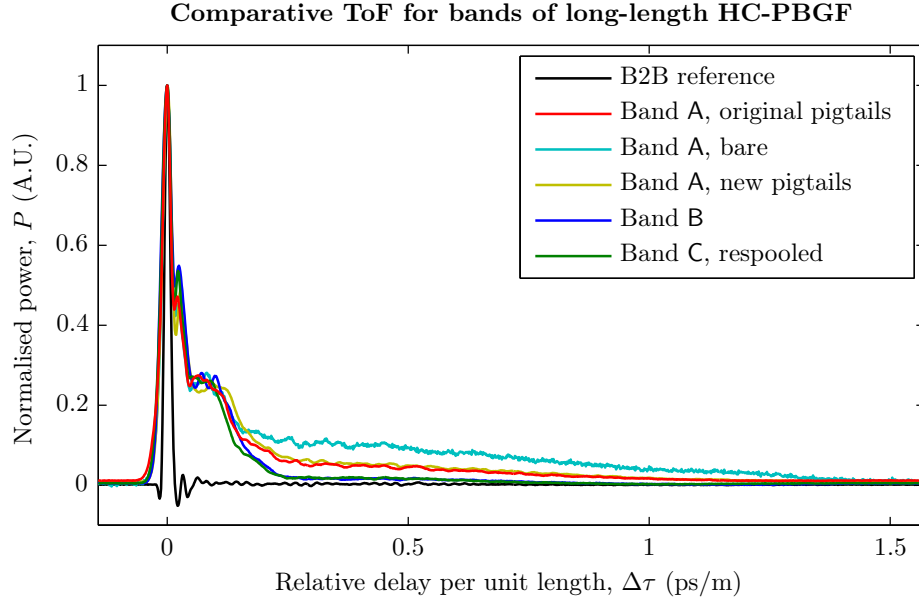


FIGURE 4.20: ToF for various bands of the long-length HC-PBGF after fundamental mode selective launch.

concatenated after the FUT. Figure 4.21 shows the corresponding reduction in dispersion-induced pulse broadening for bands A and B, after a DCF was added. Because of the narrowing of the temporal extent of the pulse, the DCF also flattens the distributed coupling plateaus for both bands.

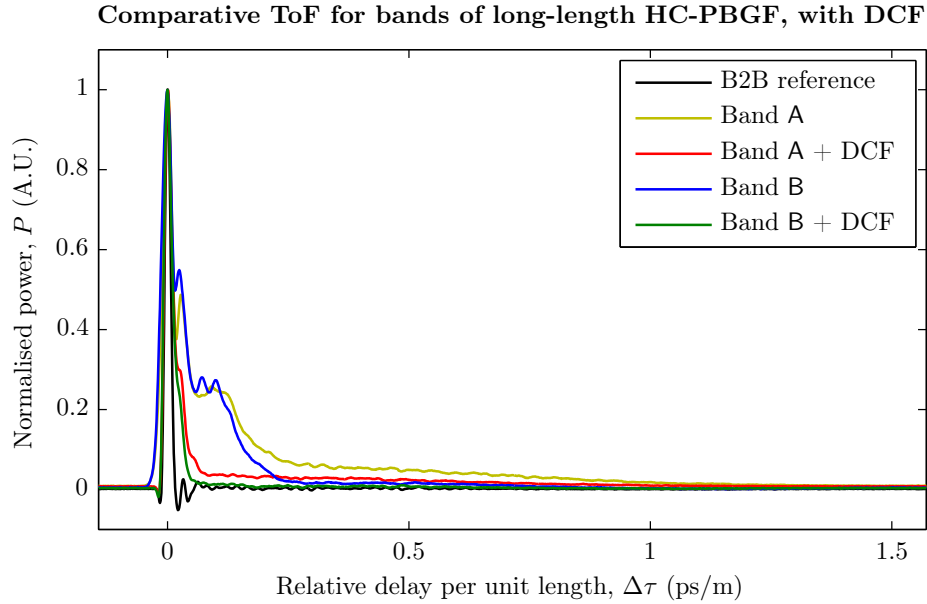


FIGURE 4.21: ToF for bands A and B of the long-length HC-PBGF after fundamental mode selective launch, with dispersion compensation.

With the results from band C showing that the spooling does affect the level of mode coupling, band A was also respooled. However during the respooling process, an 800 m

section accidentally broke off, resulting a shorter 2.7 km band, labelled A1. ToF measurements were taken again and Figure 4.22 displays the results, where the distributed coupling plateau has decreased for the respooled case, as expected.

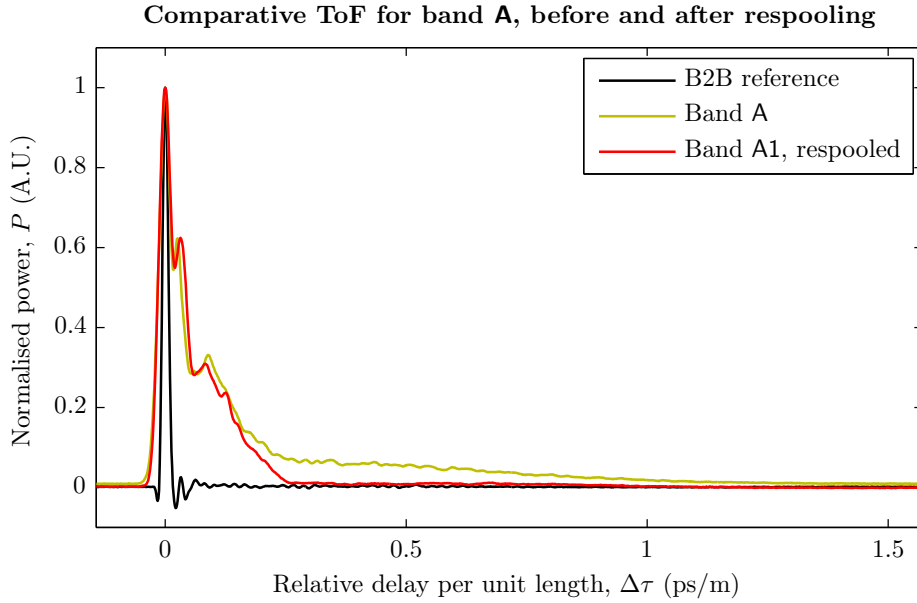


FIGURE 4.22: ToF for respooled band A1 and original band A of the long-length HC-PBGF after fundamental mode selective launch.

To verify that distributed mode coupling was causing fibres to perform poorly, data transmission tests were carried out on the respooled bands A1 and C. Figure 4.23a displays the eye diagram for band A1, showing a marked improvement over the case before the respooling (Figure 4.16a). This indicates that the distributed coupling occurring in the originally spooled band A was indeed the culprit for its previous poorer performance. Band C was also tested,<sup>15</sup> and while there was an improvement since before the respooling, its eye diagram is not as clean as that of band A1. Figure 4.23b shows the eye diagram of transmission through band C concatenated with band A1, and a comparison with Figure 4.23a confirms that the degraded eye is indeed a result of band C.

An attempt was made to improve band C's performance by respooling it a second time (done by MOFG fabricators). Figure 4.24 shows the result of ToF measurements taken following this, and includes the previous measurement for the case before the second respooling. Unfortunately, there is no observable reduction in the distributed coupling plateau between the first and second respooling; in fact the plateau for the second respooled case seems to be marginally higher than that before it. This is corroborated by additional data transmission tests<sup>16</sup> on band C, which showed a slightly more degraded

<sup>15</sup>Data was also sent through band C on its own and the eye diagram resembled Figure 4.23b. This test was conducted by Liu and the eye diagram image was not readily available at the time of writing.

<sup>16</sup>These additional tests were also conducted by Liu and the results were unavailable at the time of writing.

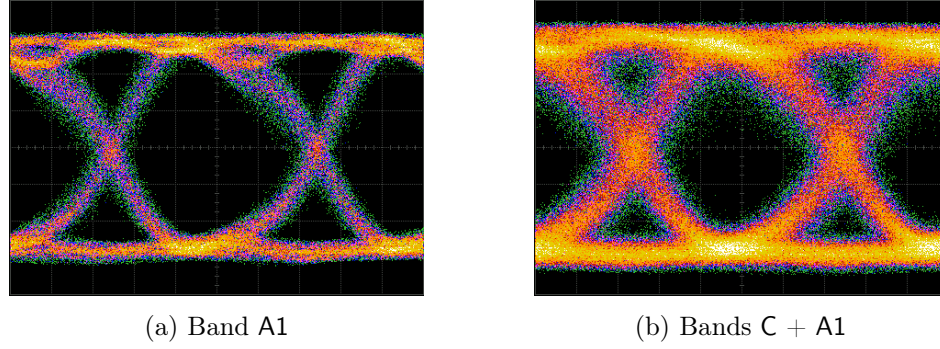


FIGURE 4.23: Eye diagrams for 10 Gbit/s NRZ OOK single-mode transmission through respoiled bands (a) A1 and (b) C of the long-length 19c HC-PBGF.

eye diagram than before the second respooling, though nevertheless improved from the original spooling case in Figure 4.16c.

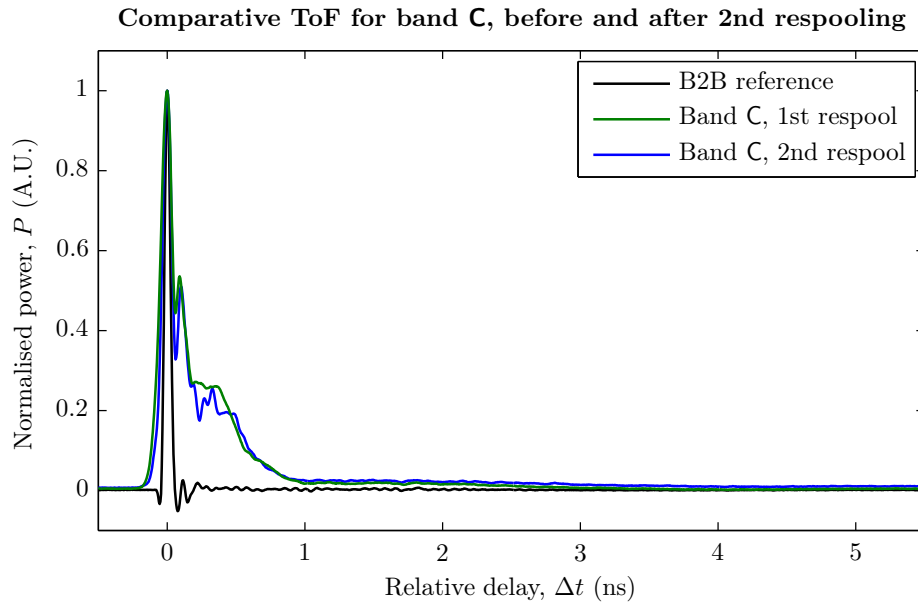


FIGURE 4.24: ToF for band C of the long-length HC-PBGF after fundamental mode selective launch, before and after the second respooling.

Whereas it is clear that mechanical aspects of spooling are responsible for the observed distributed mode coupling in the bands, the exact cause has not yet been determined. One might suppose that vector splitting due to mechanically-aggravated birefringence could have an impact. However, this is unlikely because, as discussed in Section 4.1.2, such vector effects typically manifest from discrete as opposed to distributed coupling. Any resultant features in the ToF trace would therefore more likely appear as multiple discrete peaks *within* a HOM group, rather than as a continuous plateau *between* mode groups. On the other hand, a more plausible cause might be microbending due to mechanical perturbations. From theoretical investigations [117], it is understood that microbending does have the potential to induce distributed coupling in HC-PBGFs. Further studies on this issue are currently ongoing, and at this stage, conclusions are reserved.

### 4.3.3 Aftermath

With the respooled bands performing better than their respective originally spooled cases, all three bands (including B, and with A1 and C having mandrel wraps to suppress HOMs) were sent to our MODE-GAP collaborators *Coriant*. There, bands A1 and B were eventually used in the first ever recirculating loop experiment over HC-PBGF, achieving a record reach of 74.8 km using 40 Gbit/s DP-QPSK transmission. This demonstration has paved the way for HC-PBGFs going beyond short-reach communications, and has opened up their potential for low-latency metropolitan applications, e.g. high-frequency trading networks [109].

The investigation detailed in this section has demonstrated the diagnostic ability of the ToF method in assessing the performance of fibres, especially those of multi-kilometre lengths. The next section moves away from the C-band and describes ToF measurements at the 2  $\mu$ m-wavelength region.

## 4.4 2 $\mu$ m Waveband ToF Measurements

There have been efforts to exploit the lowest-loss wavelength region of 2  $\mu$ m for data transmission in HC-PBGFs. Over 99 % of the light in PBGFs propagates in air [151], allowing them to avoid the infrared absorption losses associated with solid-core silica fibres [10]. At a predicted minimum attenuation of 0.13 dB/km, not only would PBGFs outperform conventional SSMFs [10], but they would also offer room for data capacity expansion beyond the heavily utilised C-band [28]. Early works have demonstrated transmission in the single-channel [104] as well as WDM [105] regimes. As with the 1550 nm-wavelength region, modal characterisation is critical for assessing the suitability of 2  $\mu$ m-designed PBGFs for single-mode and/or MDM applications. Again, ToF provides a useful tool. This section describes ToF measurements on a recently fabricated multi-kilometre-length 19c HC-PBGF. The work was jointly carried out between Chen of the *ORC's* MOFG, and myself, and thus the description is kept brief.

### 4.4.1 2 $\mu$ m-Wavelength Measurement Set-Up

The measurement set-up is shown in Figure 4.25. This is a modification of the set-up in Figure 3.3 to enable measurements at and around 2  $\mu$ m. A number of the components are home-built or manually assembled, due to the lack of availability of commercial versions, unlike for the 1550 nm case. In the set-up, the pulse generator (PG) electronically drives the laser diode (LD) to emit optical pulses of 1 ns duration, at a wavelength of 1988 nm,<sup>17</sup> and at a repetition rate of 1 MHz. The signal is amplified by a home-built thulium-doped

<sup>17</sup>This wavelength is within the transmission bandwidth of the fibres that were tested.

fibre amplifier (TDFA) before being launched into the FUT via the free-space lens and phase plate (PP) arrangement which is similar to that in Figure 3.3. The PP is a 2-region version designed for the  $2\mu\text{m}$  region, which can excite either  $\text{LP}_{01}$  or  $\text{LP}_{11}$ . After propagating through the FUT, the optical beam is collimated and coupled into the  $2\mu\text{m}$ -region free-space photodetector (PD)<sup>18</sup> by lens  $f_4$  (focal length =  $4.5\text{ mm}$ ).<sup>19</sup> The PD converts the detected optical signal into an electrical signal. This is amplified by the radio-frequency amplifier (RFA) and subsequently displayed on the oscilloscope, which is triggered by the PG.<sup>20</sup>

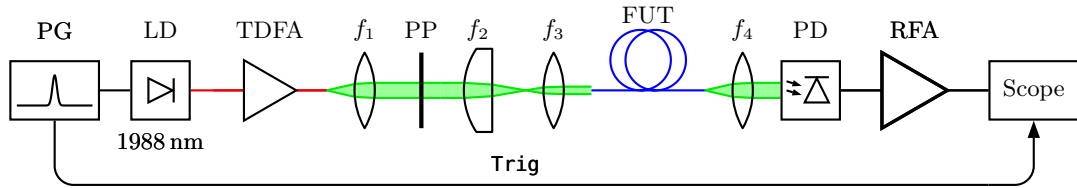


FIGURE 4.25: ToF experimental set-up for  $2\mu\text{m}$ -wavelength measurements.

#### 4.4.2 Characterisation of a HC-PBGF in the $2\mu\text{m}$ -Wavelength Region

A  $3.8\text{ km}$   $19\text{c}$  HC-PBGF was fabricated by Chen et al. in the *ORC's* MOFG for operation within the  $2\mu\text{m}$  waveband. Figure 4.26 shows the SEM cross-section.

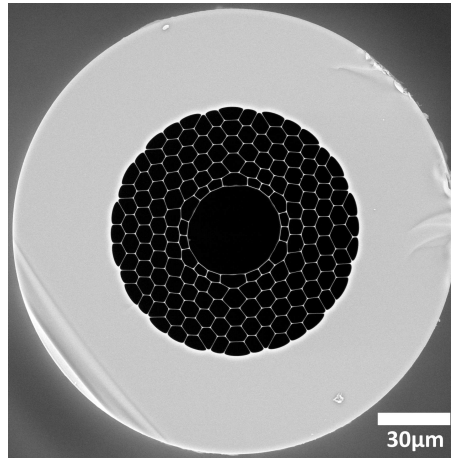


FIGURE 4.26: SEM cross-section of a  $19\text{c}$  HC-PBGF designed for operation in the  $2\mu\text{m}$ -wavelength region. *Courtesy of S.R. Sandoghchi [111].*

To determine the possibility of single-mode transmission on this fibre, ToF measurements were carried out, using the set-up in Figure 4.25. The launch optics were optimised for an  $\text{LP}_{01}$  launch and Figure 4.27a displays the resultant trace, showing good suppression

<sup>18</sup>A connectorised photodetector arrangement is also possible. A free-space version was available to us.

<sup>19</sup>This focal length was chosen to optimise the coupling efficiency.

<sup>20</sup>The experiments using this set-up were conducted by Chen and myself. The set-up itself was assembled by us, with the assistance of Jung, Slavík, and Alam of the *ORC*.

of HOMs. To show that the fibre actually does support HOMs, the PP was adjusted such that the incident beam would hit a position roughly at the binary phase interface. Figure 4.27b shows the ToF trace obtained, where HOM features can be seen, delayed from the main  $LP_{01}$  peak. In both cases, the B2B case (without the FUT) was measured and used for reference. These results indicate that it is indeed possible to operate this fibre in the single-mode regime, without strong HOM content. Its suitability for MDM applications has not yet been determined. Among other things, this necessitates achieving optimised launches of HOMs to measure extinction ratios as well as mode-dependent propagation losses, and these are possibilities for future work. Nonetheless, the principles, requirements, and limitations of realising MDM in the C-band should translate analogously to the  $2\mu\text{m}$  waveband.

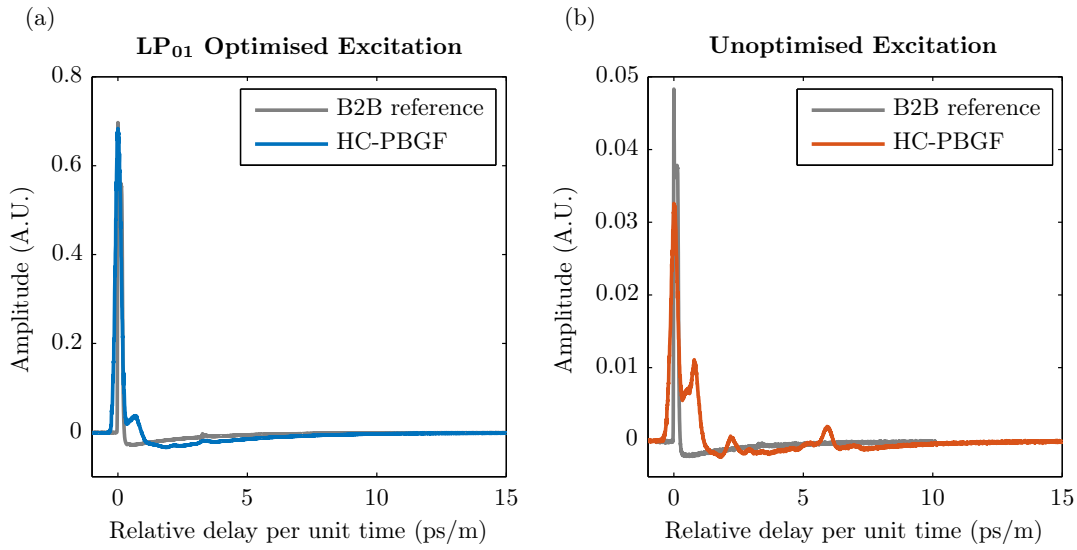


FIGURE 4.27: ToF for a 3.8 km-long 19c HC-PBGF operating in the  $2\mu\text{m}$ -wavelength region. (a)  $LP_{01}$  optimised launch. (b) Unoptimised launch attempting to excite HOMs.

This fibre was presented in [111] as an achievement of a multi-kilometre  $2\mu\text{m}$  19c HC-PBGF. Single-mode data transmission at 52 Gbit/s was also demonstrated on it and presented in [112]. This section has shown the diversity of the ToF method for characterisation beyond the C-band.

## 4.5 Concluding Remarks

This chapter has presented a collection of characterisation measurements on HC-PBGFs fabricated at the *ORC*. Through various experiments performed, predominantly using the ToF method, on 19c PBGFs and the first ever fabricated 37c PBGFs, information about the modal characteristics in these fibres has been obtained. Firstly, all attempts at optimised  $LP_{01}$  launches and a few optimised HOM launches achieved ERs in excess

of 20 dB, showing the potential for use as reliable single-mode data channels. Secondly, analysis of the peaks within LP modes suggests that the vector modes in PBGFs do not preserve spatial orientation and polarisation degeneracy to an observable extent, owing to the large core/cladding index difference and ellipticity-induced birefringence, respectively, in the fibre structures. This is a challenge for MDM transmission as complex DSP is required to compensate for the dispersion within the modes. In one 37c PBGF (37c2) though, it was found that this characteristic did not apparently manifest strongly, where the LP modes appeared as single peaks in the ToF traces, hinting at possible use in direct detection-based MDM. However, subsequent MDM tests using direct detection showed that transmission was poor over the HOMs, suggesting that the intra-group temporal spreading is still not small enough for reliable detection. Nevertheless, the prospect remains that it might still be possible to use direct detection on HOMs with even lower vector mode spreading, and these results have established an upper bound on these limits. Lastly, DGD measurements showed a decreasing trend as the core size is enlarged, in agreement with theoretical predictions. They also revealed the presence of chromatic dispersion in these PBGFs, and by showing an absence of surface mode behaviour, confirmed wide-bandwidth characteristics measured from prior broadband cutback tests.

Data transmission trials were carried out on the HC-PBGFs to assess their transmission abilities. These included comparative 10 Gbit/s tests through the various 19c PBGFs, as well as a 40 Gbit/s test on fibre 37c1, the first transmission demonstration on a 37c HC-PBGF. The fibre was subsequently used in a high-capacity MDM trial conducted by our MODE-GAP project collaborators, achieving a record 73.7 Tbit/s transmission over PBGF. Other transmission trials included the aforementioned direct-detection MDM test on fibre (37c2), as well as quick checking tests on a sectioned 19c HC-PBGF that was used by our COSIGN project partners in low-latency data centre demonstrations.

The ToF method was used to diagnose the behaviour of a sectioned 11 km record-length 19c HC-PBGF, which appeared to perform poorly in transmission checks after sectioning. Through a series of systematic measurements, it was discovered that distributed mode coupling was responsible for the poor performance, and that it was caused by how the individual sectioned bands were originally spooled. Subsequent respooling efforts by group members managed to reduce the levels of distributed coupling in the bands and improve their transmission performance. Thereafter, the bands were used, by MODE-GAP partners, to demonstrate for the first time, recirculating loop transmission over HC-PBGF, achieving a record reach of 74.8 km using 40 Gbit/s DP-QPSK, which shows the potential for HC-PBGFs beyond short-reach applications. The investigation that enabled this demonstration highlights the diagnostic ability of the ToF technique.

Finally, a brief description was given of supportive work on ToF characterisation at the 2  $\mu\text{m}$ -wavelength region, the region of predicted lowest loss in HC-PBGFs. A modified ToF measurement set-up was presented and measurements were made on a long 3.8 km

19c HC-PBGF operating in this waveband. Results showed that while the fibre supports HOMs, the fundamental mode can be selectively launched to allow for single-mode communication. Future work can be done to try to optimise the launching of HOMs, so that their individual behaviours in this fibre can be studied.

The next two chapters further develop the ToF method in terms of interpreting its results and extending its utility. Chapter 5 describes a simulation model to study the mode propagation and coupling behaviour in multimode fibres. These have direct implications on measured ToF traces. Chapter 6 presents a technique, enabled by ToF, to inspect longitudinal defects in fibres, particularly HC-PBGFs.

The usefulness of ToF in enabling other related but distinct experiments comes about as a result of its simplicity, real-time response, and direct access to temporal data. Several of such experiments are described in Appendix D.

## Chapter 5

# Modelling the Propagation of Modes

The ToF measurements in the previous two chapters provide numerous pieces of information about the modal behaviour in both solid-core and hollow-core multimode fibres, such as DMD, discrete and distributed coupling, and modal extinctions. In particular, information about mode coupling is vital to assess a fibre’s suitability for single-mode or MDM data transmission. While experimental measurements can give a qualitative sensing of the amount of mode coupling occurring in a fibre, the levels of coupling are difficult to quantify, purely based on measured data. A model that simulates the physical processes within fibres as modes propagate through them is useful to address this need.

This chapter describes the simulation of mode propagation and coupling in multimode fibres, based on modelling the physical propagation phenomena as the coupled power equation (2.5). To simulate the fibre processes requires numerically solving this equation. The formulation of the simulation is outlined in Section 5.1, which describes how each of the various physical effects are encoded. Two different solver methods are also detailed and compared. In Section 5.2, the simulation is implemented to study the how power evolves as it travels through the fibre and is affected by attenuation, mode coupling, and DMD. This gives insight into what determines the shapes of ToF output traces and aids in their interpretation. Section 5.3 describes a procedure that can be applied to fit simulated traces onto measured ToF data, in order to extract coupling coefficient values. The section also discusses how the propagation simulation model, in support of the larger MODE-GAP project, is used to validate a separate coupling coefficient model for HC-PBGFs, by showing that simulated traces using coupling coefficients, calculated from this coefficient model, match with experimentally measured ToF data. This has implications on our understanding of the relationship between loss and mode coupling in HC-PBGFs. Finally, Section 5.4 summarises the chapter and suggests some future work.

## 5.1 Mathematical Model

To better understand the underlying physical behaviour of modes propagating in optical fibres, a model is essential. The model simulates the modal loss, delay, and coupling mechanisms in a fibre and emulates the time-of-flight (ToF) experimental set-up to output results that can be directly compared to ToF measurements.

### 5.1.1 Formulation

The aim is to determine the evolution of power  $P_m$  in mode  $m$  as it propagates through the fibre and is subjected to coupling with other modes  $q$ . This involves solving the coupled power equation (2.5), which is shown again here:

$$\frac{\partial P_m}{\partial z} + \tau_m \frac{\partial P_m}{\partial t} = -\alpha_m P_m + \sum_q \mathcal{C}_{m,q} (P_q - P_m), \quad m, q = 1, 2, \dots, N_m, \quad (5.1)$$

where  $\tau_m$  is the modal group delay per unit length,  $\alpha_m$  is the modal attenuation per unit length,  $\mathcal{C}_{m,q}$  is the coupling coefficient between modes  $m$  and  $q$ , and  $N_m$  is the total number of modes being simulated. Pulse propagation in single-mode fibres (SMFs) is conventionally modelled by the nonlinear Schrödinger equation (NLSE) [142], which [152] has extended to the multimode case. While this is useful when studying chromatic dispersion and nonlinear effects, since it considers the perspective of pulse amplitudes and phases, the simpler form of (5.1) is sufficient for this study of mode coupling, which only considers pulse powers.

The solution of (5.1) requires integrating over time  $t$  and distance  $z$ . In this equation, all variables, particularly the delay  $\tau$ , are absolute. As propagation distances are at least a few hundreds of metres, the temporal scale of the absolute delay can get large (e.g. 10s of ns) compared to the scale of the relative delays between modes (which is usually on the order of a few ns). This will necessitate large amounts of memory and will slow down computation time if a sub-ns resolution (step size) is sought. Therefore, the change of variable  $t' = t - \bar{\tau}z$  is made, where  $\bar{\tau}$  is the average group delay of all the guided modes [83]. (5.1) then becomes

$$\frac{\partial P_m}{\partial z} + (\tau_m - \bar{\tau}) \frac{\partial P_m}{\partial t'} = -\alpha_m P_m + \sum_q \mathcal{C}_{m,q} (P_q - P_m). \quad (5.2)$$

This restricts the temporal (and memory) extent to remain within the confines of the largest relative delay difference, which is the region of interest anyway. Figure 5.1 contrasts simulating using absolute (left) and delay-averaged (right) temporal domains.

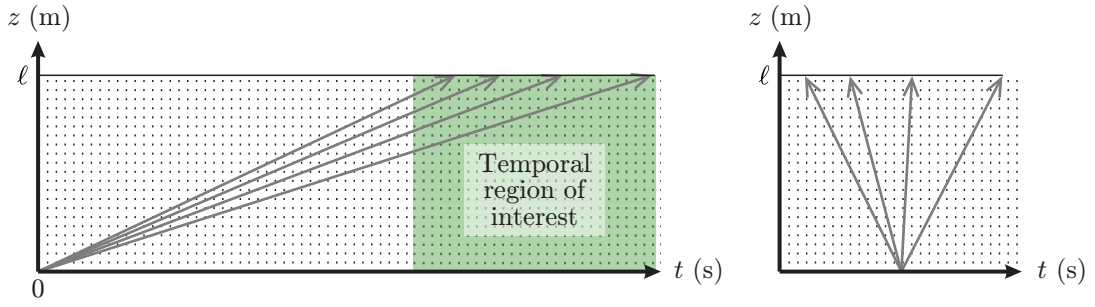



FIGURE 5.1: Simulations of pulse propagation over a fibre of length  $\ell$ , using (left) absolute and (right) delay-averaged temporal domains. Grey lines show trajectories of various modes. The sizes of the dotted square grids indicate the amount of memory required in each case.  $t$  = time,  $z$  = distance.

Although it may be theoretically possible to model this propagation problem in three dimensions using a finite element analysis based software such as COMSOL Multiphysics<sup>®</sup>, it is practically intractable to do so. The need to create a fine volumetric mesh over the whole fibre distance (which ranges from hundreds of meters to kilometers) would require long computation times—unless using supercomputer resources—and excessive amounts of memory. Modelling the problem over a single spatial dimension (distance through the fibre), capturing the fibre properties through the abovementioned coefficients, and solving numerically in a matrixised form suffices for this study. As such, the MATLAB<sup>®</sup> numerical software from  MathWorks<sup>®</sup> ([www.mathworks.com/products/matlab](http://www.mathworks.com/products/matlab)) was chosen to simulate this model, due to its excellent matrix handling capabilities. There are a number of methods available to numerically solve (5.2).

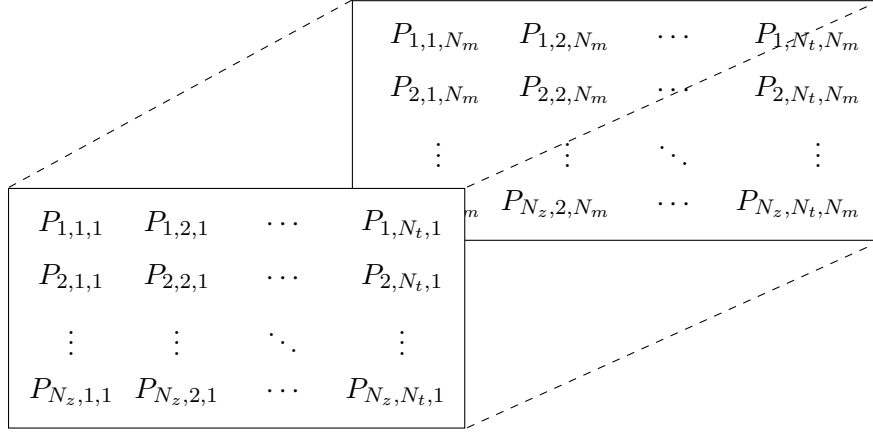
At the heart of the simulation is the numerical representation of the variable  $P$ . First, the spatial (distance over the length  $\ell$  of the fibre) and temporal domains are discretised by setting

$$z = i \cdot \delta z, \quad i = 1, 2, \dots, N_z, \quad N_z \cdot \delta z = \ell, \quad i, N_z \in \mathbb{N}, \quad (5.3a)$$

$$t' = j \cdot \delta t, \quad j = 1, 2, \dots, N_t, \quad j, N_t \in \mathbb{N}, \quad (5.3b)$$

where  $N_t$  is the last time-step index and  $[1, N_t]$  is the interval of indices<sup>1</sup> that covers the temporal domain of the simulation; it is crucial to choose the interval  $[t'_1, t'_{N_t}]$  to cover the whole span of the modal delay spread (i.e.  $t'_{N_t} - t'_1 \geq \Delta\tau_{N_m}\ell$ ) in order to avoid cyclic wrapping of the pulse envelope with propagation [153]. Then,  $P$  is represented as a 3-dimensional (3D) matrix  $\mathbf{P}$  to capture information in the time and space evolutionary dimensions, as well as the dimension over multiple modes  $m = 1, 2, \dots, N_m$ . Hence,  $P$  is discretised such that  $P_{i,j,m}$  is the power in mode  $m$  at space-step  $i$  and time-step  $j$ , as depicted in Figure 5.2.

<sup>1</sup>Note the choice to start matrix indexing from 1 rather than from 0, since MATLAB indexes matrices starting from 1, unlike many other languages.

FIGURE 5.2: Visualisation of the 3D matrix  $\mathbf{P}$ .

### 5.1.2 Initialisation

#### Input Pulsed Launch

To simulate the launching of input Gaussian pulses from the PFL, the power is initialised by creating a Gaussian envelope function  $\mathcal{A}_{\text{pu}}(t)$ :

$$P_{\text{pu}}(t) = \mathcal{A}_{\text{pu}}^2(t) = \left[ A_{\text{pu}} \exp\left(-\frac{t^2}{\tau_w^2}\right) \right]^2, \quad (5.4)$$

where  $A_{\text{pu}}$  is the input pulse amplitude and is normalised to unity, and  $\tau_w$  is the pulse temporal width (FWHM).

In MATLAB, (5.4) is executed in the vector form

$$\mathbf{P}_{\text{pu}} = \left[ A_{\text{pu}} \exp\left(-\frac{\mathbf{t}^{\circ 2}}{\tau_w^2}\right) \right]^{\circ 2}, \quad (5.5)$$

where  $\mathbf{t}$  is an  $N_t \times 1$  vector encapsulating the time dimension and the  $\mathbf{t}^{\circ 2}$  notation indicates that the individual elements of  $\mathbf{t}$  are squared.<sup>2</sup> Note that  $\mathbf{P}_{\text{pu}}$  is an  $N_t \times 1$  vector, as opposed to the  $N_z \times N_t \times N_m$  power propagation matrix  $\mathbf{P}$  in Section 5.1.1.

#### Noise Effects

The noise contributions from the PFL, EDFA, and photodetector are also included. Noise from the PFL and photodetector is in the form of shot noise and is modelled as a Gaussian random process [6]. The EDFA noise comes from amplified spontaneous emission [6, 155],

<sup>2</sup>This is known as the *Hadamard power* [154] or *element-wise exponentiation*.

and can also be modelled with Gaussian statistics [156, 157]. Hence, these noise sources are aggregated into a combined Gaussian noise contribution and added to the signal power.

### Coefficient Specification

TABLE 5.1: User-specified coefficients for mode propagation simulation. Numbered subscripts indicate mode indices.

Coefficient	Symbol	Unit	Format	MATLAB Name
Coupling coefficient	$\mathbf{C}$	1/m	$\begin{pmatrix} 0 & \mathcal{C}_{1,2} & \cdots & \mathcal{C}_{1,N_m} \\ \mathcal{C}_{2,1} & 0 & \cdots & \mathcal{C}_{2,N_m} \\ \vdots & \vdots & \ddots & \vdots \\ \mathcal{C}_{N_m,1} & \mathcal{C}_{N_m,2} & \cdots & 0 \end{pmatrix}$	<code>C</code>
Attenuation	$\alpha$	dB/m	$(\alpha_1 \ \alpha_2 \ \dots \ \alpha_{N_m})^T$	<code>alpha_dB</code>
Relative modal delay	$\Delta\tau$	s/m	$(0 \ \Delta\tau_2 \ \dots \ \Delta\tau_{N_m})^T$	<code>Delta_tau</code>
Mode power scaling factor	$\mathbf{P}_d$	%	$(P_{d1} \ P_{d2} \ \dots \ P_{dN_m})^T$	<code>P_disc</code>

Table 5.1 lists the coefficients that must be specified when initialising the simulation. The coupling coefficient is represented by the  $N_m \times N_m$  symmetric matrix  $\mathbf{C}$ ; the symmetry comes from the fact that

$$\mathcal{C}_{m,q} = \mathcal{C}_{q,m} \quad (5.6)$$

between modes  $m$  and  $q$  [78]. The central diagonal, while physically meaningless in this context, is zeroed for numerical convenience. The off-diagonal entries are populated with values either from calculating based on a coefficient equation [36, 158], or by manual fitting with experimentally obtained ToF traces.

The attenuation and modal delay factors are embodied in the  $N_m \times 1$  vectors  $\alpha$  and  $\Delta\tau$ , respectively. These values are typically acquired via experimental measurements such as cutback [93] (for attenuation) and ToF and S<sup>2</sup> [75] (for delay). Note that  $\Delta\tau_1$  is set to 0, since the delays are relative to that of the fastest propagating mode.

Lastly, since this is an initial-value problem of the propagation type [159], the amount of launch power in each mode needs to be specified. Even in a mode-selective launch, certain percentages of the total input optical power will inevitably go into one or more unintended modes, owing to the physical impossibility of a perfectly aligned launch. This *discrete coupling* at the input is encoded as an  $N_m \times 1$  power scaling vector  $\mathbf{P}_d$ , whose elements apportion the total input power among the respective modes and determine which mode(s) is dominant. The input initial condition power matrix is thereby a series

of scaled-magnitude Gaussian pulse vectors and is formed as

$$\mathbf{P}_{\text{in}} = \mathbf{P}_{\text{pu}} \mathbf{P}_d^{\text{T}}, \quad (5.7)$$

where the notation  $\mathbf{P}_d^{\text{T}}$  indicates the matrix transpose of  $\mathbf{P}_d$ .

### 5.1.3 Propagation Solver Implementation

One of the simplest means to solve (5.2) and simulate pulse propagation along the length of an optical fibre is to use a finite-difference-based iterative stepping method<sup>3</sup> and utilising MATLAB's in-built `ode23` or `ode45` solvers. This is useful for initially verifying the correctness of the model code, but has poorer computational efficiency (at least  $\mathcal{O}(N^2)$ , where  $N$  is the elemental size of the input [161]) than other schemes. Moreover, the preservation of numerical stability mandates a small step size, which is at the cost of computational time.

An alternative solving method makes use of the fast Fourier transform (FFT). This is a spectral scheme and though the implementation is not as intuitive as iterative stepping, it is more computationally efficient [152] ( $\mathcal{O}(N \log_2 N)$  [161]). As such, it is the method used in all of the main simulations in this thesis.

The next two subsections describe the implementation of each of these methods. Section 5.1.3.3 then compares their relative performance.

#### 5.1.3.1 Iterative Stepping Method (ISM)

The partial differential equation (PDE) (5.2) can be rearranged to focus on the distance differential:

$$\frac{\partial P_m}{\partial z} = (\bar{\tau} - \tau_m) \frac{\partial P_m}{\partial t'} - \alpha_m P_m + \sum_q \mathcal{C}_{m,q} (P_q - P_m). \quad (5.8)$$

Following the *method of lines* procedure [161–163], the time differential term can be discretely approximated via a centred-difference scheme [159, 160, 164]:

$$\frac{dP}{dt} \approx \frac{P(t + \delta t) - P(t - \delta t)}{2\delta t}. \quad (5.9)$$

Substituting this into (5.8), and discretising the spatial and temporal domains as per Section 5.1.1, the following is obtained:

$$\frac{dP_m}{dz} = (\bar{\tau} - \tau_m) \frac{P_{i,j+1,m} - P_{i,j-1,m}}{2\delta t} - \alpha_m P_{i,j,m} + \sum_q \mathcal{C}_{m,q} (P_{i,j,q} - P_{i,j,m}). \quad (5.10)$$

---

<sup>3</sup>This method also known as a “single-point” [159] or “one-step” [160] scheme.

The PDE (5.8) has been reformatted as a first-order ordinary differential equation (ODE) in  $z$  and can now be solved by using one of MATLAB's built-in ODE solvers. The `ode23` function is a third-order Runge-Kutta routine for solving ODEs [160]. Its ease of implementation comes from the fact that it does not necessitate the user to manually code the integration routine, and only requires as inputs the description of the ODE, the integration domain extent, and the initial conditions.

In MATLAB, (5.10) is encoded by specifying a function `powerCouplingISM` that describes the right-hand-side (RHS). It does so by looping through the time and mode dimensions and updating each element of  $\mathbf{P}$ . The solver is then implemented by a call to the `ode23` function, which takes the RHS description of (5.10) contained in `powerCouplingISM` as one of its inputs:

```
[z,P] = ode23(@powerCouplingISM,zSpan,P_in);
```

The other inputs are the spatial span `zSpan = [0,L]`, with  $L$  being the fibre length  $\ell$ , and the initial conditions as `P_in`, which is  $\mathbf{P}_{\text{in}}$  in (5.7). The `ode23` routine steps through the integration and updates the solution at each space-step until the end of the fibre is reached. The outputs are a vector `z` encapsulating the space dimension and the matrix  $\mathbf{P}$  as `P`, which now contains the complete propagation evolutionary information over space, time, and mode dimensions. This code snippet is listed in the main script `Coupling.m` which, together with the `powerCouplingISM` function, is provided in full in Appendix B.

### 5.1.3.2 Split-Step Fourier Method (SSFM)

The split-step Fourier method (SSFM) [165, 166] is a fast and efficient spectral means of numerically solving evolutionary equations and has been used extensively in many problems, including the NLSE for pulse propagation in optical fibres [152, 167].

In this case of coupled mode propagation, the PDE (5.8) can be segregated into two parts [83]:

1. A zeroth-order derivative (i.e. no derivative) part containing the attenuation (loss) and mode coupling terms, and
2. A first-order derivative part containing the delay (DMD) term.

Although in reality, the physical mechanisms within these two ‘parts’ act together simultaneously, the SSFM works by making the assumption that these effects occur independently in alternation to obtain an approximate solution to the PDE [142]. The method propagates the solution over the fibre length in successive two-part segments over distance steps of  $\delta z$ , as shown in Figure 5.3 [142, 166].

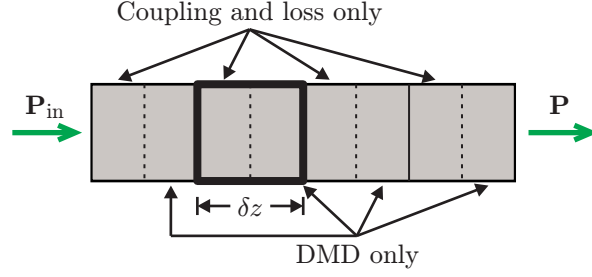


FIGURE 5.3: Schematic of the SSFM. The fibre length is divided into successive two-part segments of length  $\delta z$ . In each segment (e.g. enclosed by the thick box), the first and second parts include the effects of mode coupling and loss only, and DMD only, respectively.

### Mode Coupling and Loss

A simple ODE-solving technique such as Euler's method [159, 160, 164] is used to solve the part of (5.8) containing only coupling and loss effects (i.e. setting the DMD term to zero). In matrix form, this is

$$\mathbf{P}_{z+\delta z} = \mathbf{P}_z + \delta z \mathbf{P}_z \mathbf{C}, \quad (5.11)$$

where  $\mathbf{P}_z$  is the  $N_t \times N_m$  slice of the matrix  $\mathbf{P}$  at each  $z$ . The elements of the matrix  $\mathbf{C}$  include the effects of mode coupling and loss, and is formed as

$$\begin{aligned} \mathbf{C} &= \begin{pmatrix} -\alpha_1 - \sum_q \mathcal{C}_{1,q} & \mathcal{C}_{1,2} & \cdots & \mathcal{C}_{1,N_m} \\ \mathcal{C}_{2,1} & -\alpha_2 - \sum_q \mathcal{C}_{2,q} & \cdots & \mathcal{C}_{2,N_m} \\ \vdots & \vdots & \ddots & \vdots \\ \mathcal{C}_{N_m,1} & \mathcal{C}_{N_m,2} & \cdots & -\alpha_{N_m} - \sum_q \mathcal{C}_{N_m,q} \end{pmatrix} \\ &= \mathbf{C} - \text{diag}(\boldsymbol{\alpha} + \mathbf{C} \cdot \mathbf{1}), \end{aligned} \quad (5.12)$$

where  $\mathbf{1} = (1, \dots, 1)^T$  is an  $N_m \times 1$  column vector of 1s and the  $\text{diag}(\cdot)$  operator takes a vector and creates a square diagonal matrix with the elements of the vector along the diagonal and 0s everywhere else. It is noted that this works because of the symmetry (5.6).

### Differential Mode Delay

The part of (5.8) containing only the effect of differential mode delay (DMD) (i.e. setting the attenuation and mode coupling terms to zero) is

$$\frac{\partial P_m}{\partial z} = (\bar{\tau} - \tau_m) \frac{\partial}{\partial t'}(P_m) = \check{D}_m P_m, \quad (5.13)$$

where the operator  $\check{D}_m = (\bar{\tau} - \tau_m) \frac{\partial}{\partial t}$  accounts for the DMD. The propagation of (5.13) from  $z$  to  $z + \delta z$  is carried out by using the exponential formula [142]

$$P_m(z + \delta z) = \exp\left(\delta z \check{D}_m\right) P_m(z). \quad (5.14)$$

This can be evaluated using the Fourier transform representation of the derivative (C.4):<sup>4</sup>

$$P_m(z + \delta z) = \mathcal{F}^{-1} \left\{ \exp[\delta z (j\omega) (\bar{\tau} - \tau_m)] \mathcal{F} \{P_m(z)\} \right\}, \quad (5.15)$$

where  $\omega = 2\pi/t$  is the angular frequency,  $j = \sqrt{-1}$  is the imaginary unit, and  $\mathcal{F}\{.\}$  and  $\mathcal{F}^{-1}\{.\}$  are the Fourier transform and inverse Fourier transform, respectively, as defined in Appendix C. Turning to matrix form, this is expressed as

$$\mathbf{P}_{z+\delta z} = \mathcal{F}^{-1} \left\{ \exp \left[ \delta z (j\boldsymbol{\omega}) (\bar{\boldsymbol{\tau}} - \boldsymbol{\tau}^\top) \right] \circ \mathcal{F} \{\mathbf{P}_z\} \right\}, \quad (5.16)$$

where  $\boldsymbol{\omega}$  is an  $N_t \times 1$  vector encapsulating the angular frequency dimension,  $\boldsymbol{\tau} = \boldsymbol{\Delta}\boldsymbol{\tau} + \tau_{01}$  is an  $N_m \times 1$  vector of absolute modal delays per unit length, and the  $\circ$  notation indicates element-wise multiplication (also known as the Hadamard product).

By combining (5.11) and (5.16), the total power evolution through the fibre can be obtained. The MATLAB code for implementing this SSFM is in the `powerCouplingSSFM` function listed in Appendix B.4.

### 5.1.3.3 Comparison of Propagation Methods

#### Convergence

To assess the requirements for convergence of the ISM and SSFM schemes to an accurate solution, a *grid refinement study* [168] is performed<sup>5</sup>, where the simulations are repeated and the time-step size  $\delta t$  is halved each successive time [161]. Since the time span is fixed, this iteration is equivalent to repeatedly doubling the number of time-steps  $N_t$  in the discretisation of the time-domain. For this study, the ToF of the 4MSIF addressed in Section 3.3.2, with an LP<sub>01</sub> mode-selective launch, is simulated. Figure 5.4 plots the ToF outputs of both schemes for various values of  $N_t$ ; for reference, each result is superimposed over the fibre's experimentally measured ToF trace (in grey).

It is observed that  $N_t = 2^{11}$  steps is sufficient for the SSFM (top-right, blue) to converge, but not the ISM (top-left, purple). The large ripples near  $\Delta\tau = 0$  ps/m gradually lessen as  $N_t$  is increased to  $2^{14}$  steps (bottom-left, orange), and at  $N_t = 2^{15}$  steps (bottom-right, yellow), the trace begins to resemble the accurate solution. This means that the ISM

<sup>4</sup>The reader is referred to Appendix C for the derivation of this relation.

<sup>5</sup>The tests in this study were performed on a Microsoft<sup>®</sup> Surface<sup>™</sup> Pro 3 computer with an Intel<sup>®</sup> Core<sup>™</sup> i5-4300 CPU processor at 1.9 GHz, running the Windows<sup>®</sup> 10 Pro operating system.

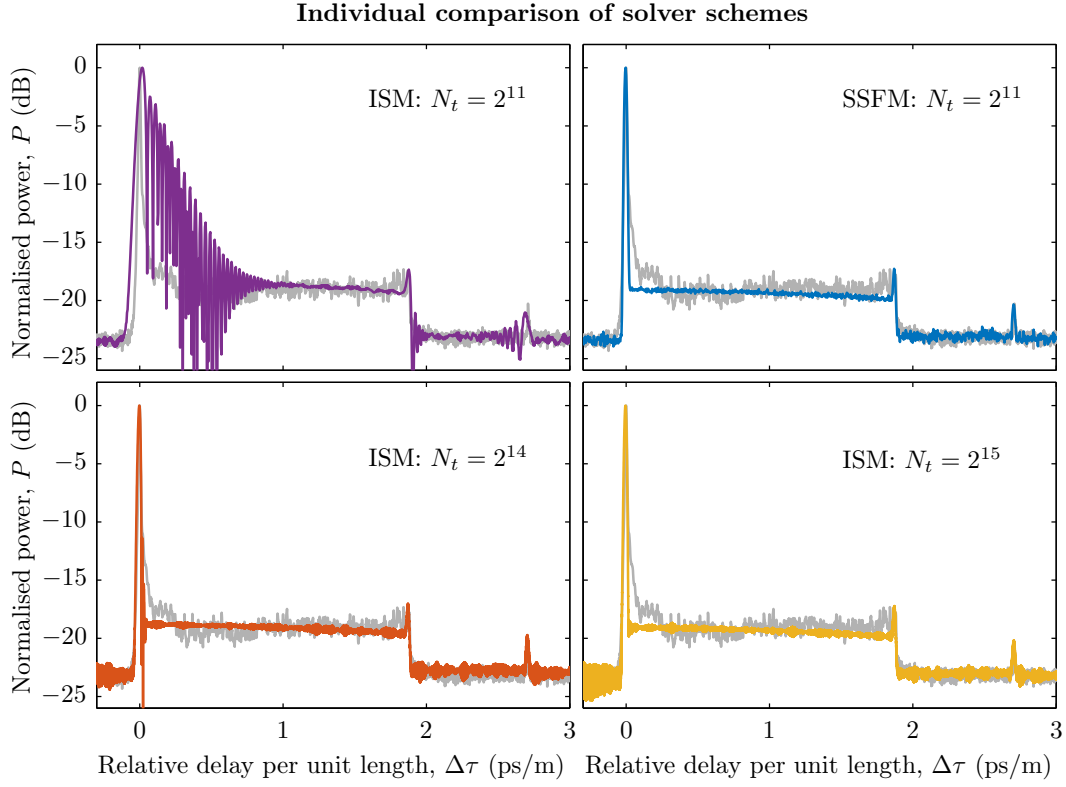


FIGURE 5.4: Numerical stability comparison of ISM and SSFM on a 4MF for various  $N_t$ . Experimentally measured ToF of the corresponding fibre is inset in grey.

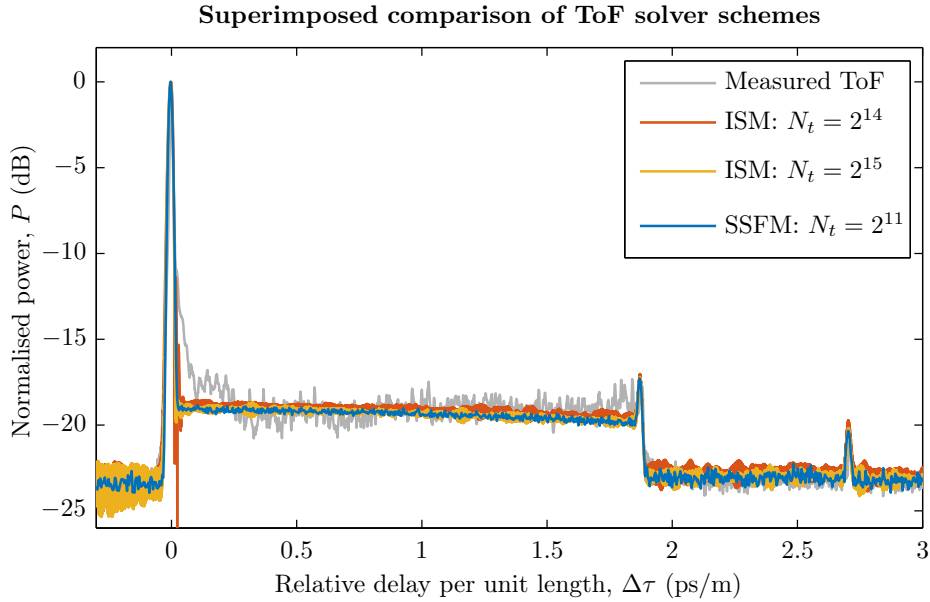


FIGURE 5.5: Superimposed comparison of numerical stability of ISM and SSFM on a 4MF for various  $N_t$ . Experimentally measured ToF of the corresponding fibre is shown in grey.

needs an  $N_t$  which is greater by at least 4 orders of magnitude than that of the SSFM to converge. For illustrative comparison, several of the simulated traces are superimposed on top of one another in Figure 5.5, together with the experimental measurement.

## Efficiency

Figure 5.6 shows how the computation times of the ISM and SSFM grow as the number of time steps  $N_t$  is sequentially doubled. The time of the ISM, using the second-order `ode23` routine, grows as  $\mathcal{O}(N_t^2)$  and quickly reaches tens of minutes to hours. This timing increase is much faster than that of the SSFM, which grows as  $\mathcal{O}(N_t \log_2 N_t)$  and remains on the order of seconds, even for  $N_t = 2^{15}$  which clocks  $\sim 41$  s; the SSFM growth can be seen more clearly in the magnified plot on the right of the figure. This, together with the lower requirement of  $N_t$  for convergence, makes the SSFM more computationally efficient than the ISM.

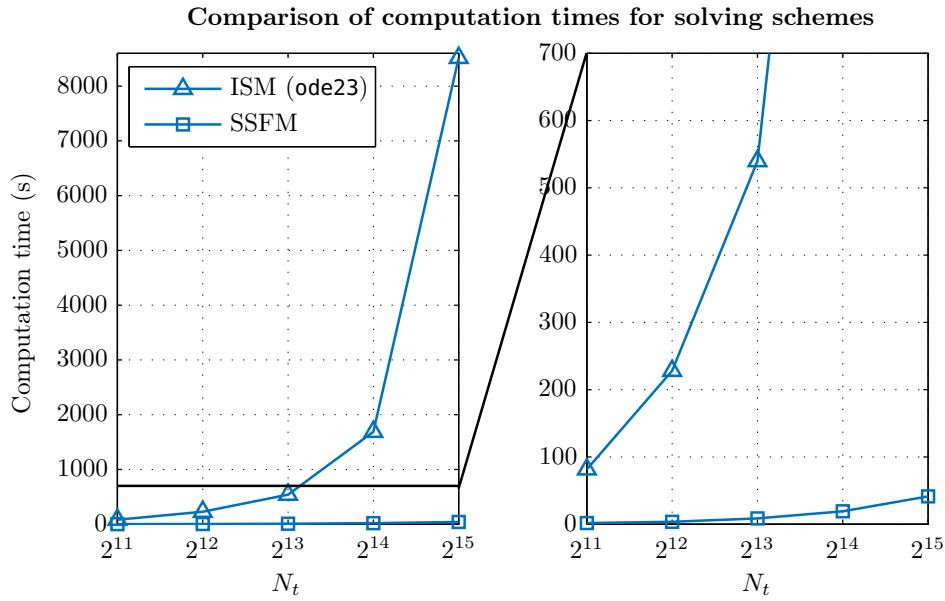


FIGURE 5.6: Comparison of computation time growths for ISM and SSFM with increasing  $N_t$  (i.e. decreasing  $\delta t$ ). Left: full picture. Right: magnified plot.

## 5.2 Analysis of Propagation

This section implements the propagation simulation, predominantly using the SSFM, and studies the evolution of the power profile as a signal travels through a multimode fibre, as well as the effects on the output ToF trace as the physical coefficients are varied.

### 5.2.1 Evolution of Power

In each repetition of the PFL, only a single pulse is incident at the fibre input, and so the power envelope looks like a single pulse peak. However, over the length of the fibre, the power undergoes attenuation and is split among various mode components travelling at different velocities, causing the envelope profile to evolve. Figure 5.7 depicts the simulation of an  $\text{LP}_{01}$  selective launch through an  $\ell = 10$  km 4MF with appreciable  $\mathcal{C}_{01 \leftrightarrow 11}$

coupling, showing how the power (with added noise) evolves through time (delay) and space (fibre length). From the input pulse, four peaks emanate outwards, corresponding to the launch-side discretely coupled components of the four guided modes in the fibre. As mentioned in Section 5.1.2, the initial relative strength of each component is set through the power scaling coefficient  $P_d$ . While not immediately obvious from the plot, the contribution from attenuation causes the power to gradually decrease. The attenuations of all modes have been set to be equal to 0.2 dB/km, and the total power has been normalised taking the peak power at the output as 0 dB. A distributed coupling plateau that forms between the  $LP_{01}$  and  $LP_{11}$  discrete peaks is also visible. The ToF trace that results at the fibre output is shown in the inset of Figure 5.7, whose delay has been normalised over the fibre length and shift-corrected to take the  $LP_{01}$  peak to be at  $\Delta\tau = 0$  ps/m. Because of the memory-saving change of variable in (5.2), the modal delays spread centrally, about the average relative delay  $\bar{\tau}$ , rather than forwardly in time, as contrasted in Figure 5.1. This spread is seen more clearly in the top-view plot in Figure 5.8.

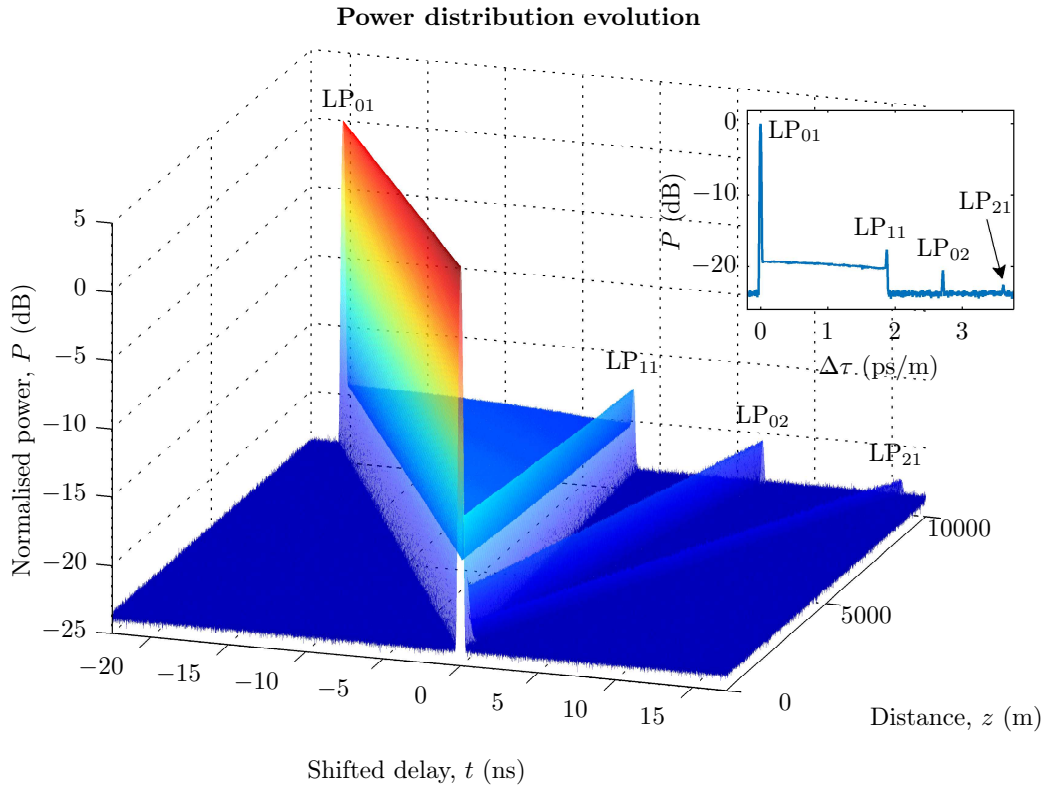


FIGURE 5.7: Simulated evolution of optical power in a 10 km 4MF with  $\mathcal{C}_{01 \leftrightarrow 11}$  coupling, after  $LP_{01}$  selective launch. The inset shows the resultant ToF trace at the fibre end.  $\Delta\tau$  = relative delay per unit length.

Figure 5.7 shows that over the fibre length, the main  $LP_{01}$  component maintains dominance, but continuously loses power to  $LP_{11}$ . It is key to remind ourselves again that this lost power does not add to the discrete  $LP_{11}$  peak, but rather the continuously forming plateau between  $LP_{01}$  and  $LP_{11}$ , as explained in Section 2.2.3 and Figure 2.3. Moreover,

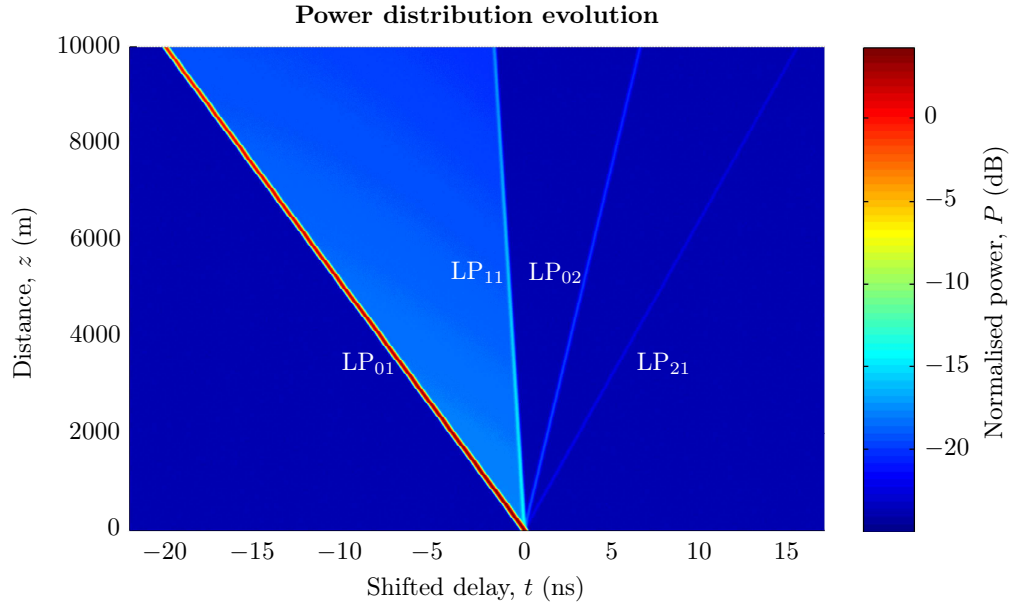


FIGURE 5.8: Modal delay spread in a 10 km 4MF with  $\mathcal{C}_{01 \leftrightarrow 11}$  coupling, after  $\text{LP}_{01}$  selective launch. The spread is centrally pivoted due to the change of variable in (5.2). Discrete mode peaks are labelled.

it is not only the power lost from the discrete  $\text{LP}_{01}$  peak that composes the plateau; there is also a (comparatively smaller, but nonzero) contribution from the discrete  $\text{LP}_{11}$  peak being coupled to  $\text{LP}_{01}$ , as well as power from plateau components that has been repeatedly coupled and recoupled between the two modes.

In the inset of Figure 5.7, the two extremes in the coupling plateau can be considered: the  $\text{LP}_{11}$  side (right, near  $\Delta\tau = 1.9 \text{ ps/m}$ ) and the  $\text{LP}_{01}$  side (left, near  $\Delta\tau = 0 \text{ ps/m}$ ). The former is composed of  $\text{LP}_{11}$  components arising from ‘early’ (meaning near  $z = 0 \text{ km}$ )  $\mathcal{C}_{01 \rightarrow 11}$  coupling events as well as  $\text{LP}_{01}$  components arising from ‘late’ (meaning near  $z = \ell$ )  $\mathcal{C}_{11 \rightarrow 01}$  coupling events, and vice versa for the latter. The  $\text{LP}_{01}$  side of the plateau has more power than the  $\text{LP}_{11}$  side. To see why this is so, it is helpful to decompose the total ToF trace into the contributions from individual modes. This is experimentally infeasible, but simple to do in the simulation, since the powers of each mode are represented by separate matrices.

Figure 5.9 plots the overall ToF trace (grey), as well as the components of power belonging only to  $\text{LP}_{01}$  (blue) and  $\text{LP}_{11}$  (orange); the grey ‘Total’ trace is the sum of the individual mode traces. For the sake of this analysis, the discretely coupled  $\text{LP}_{02}$  and  $\text{LP}_{21}$  components can be ignored. Considering first the orange pure  $\text{LP}_{11}$  trace, its coupling plateau is composed *only* of  $\text{LP}_{11}$  components that have been converted from the discrete  $\text{LP}_{01}$  peak over the fibre length and repeated back-and-forth coupling within the plateau that ends up as  $\text{LP}_{11}$  at the fibre end, i.e. only contributions from nett  $\mathcal{C}_{01 \rightarrow 11}$  events. The plateau is progressively formed from the RHS (the side closest to the discrete  $\text{LP}_{11}$  peak) in a leftwards manner, since the earlier  $\mathcal{C}_{01 \rightarrow 11}$  components, after branching off from the discrete  $\text{LP}_{01}$  peak, travel at the  $\text{LP}_{11}$  group velocity  $v_{11}$  over the

majority of the fibre length and so have large delays relative to  $LP_{01}$ , whereas the later coupled components have travelled for most of the fibre length at  $v_{01}$  and only travel at  $v_{11}$  for a short remaining distance, thereby ending up with small delays close to  $LP_{01}$  on the left-hand-side (LHS). In other words, the *direction of increasing distance* for  $\mathcal{C}_{01 \rightarrow 11}$  coupling is from right to left. Since the later (LHS)  $\mathcal{C}_{01 \rightarrow 11}$  components are produced from the discrete  $LP_{01}$  peak or plateau components that have been more attenuated after having travelled a further distance, they thus have less power than their earlier coupled counterparts (those near the  $LP_{11}$  peak/RHS). Conversely, the plateau of the blue pure  $LP_{01}$  trace is formed in the opposite direction from left to right. Early-coupled  $\mathcal{C}_{11 \rightarrow 01}$  components leaving the discrete  $LP_{11}$  peak end up near the discrete  $LP_{01}$  peak on the LHS, whereas late-coupled components end up on the RHS. Again, the later coupled components (this time on the RHS) have less power since they were coupled from the discrete  $LP_{11}$  peak having experienced nearly a fibre length's worth of attenuation. Thus, for  $\mathcal{C}_{11 \rightarrow 01}$  coupling, the direction of increasing distance is from left to right. These directions are indicated with arrows in Figure 5.9.

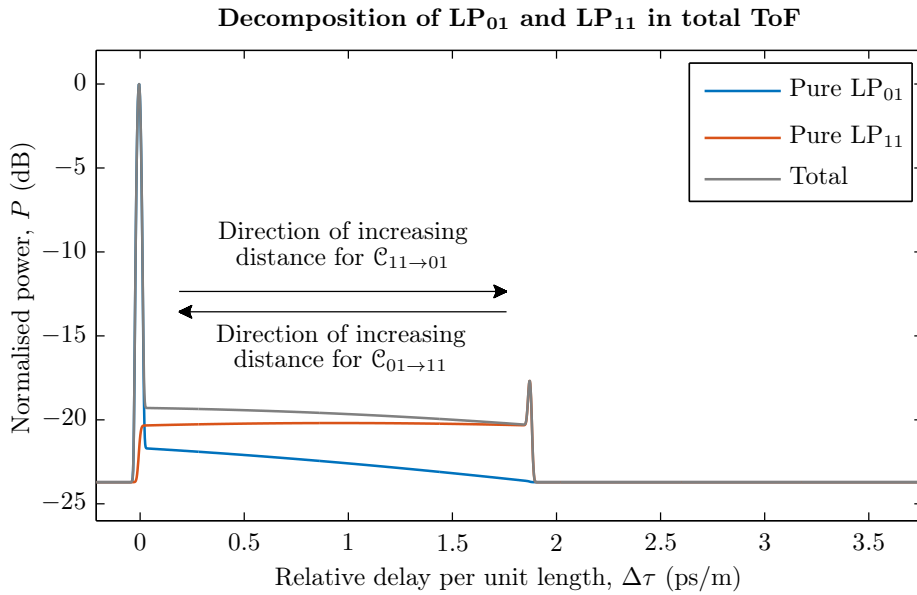


FIGURE 5.9: Total and decomposed ToF traces in a 10 km 4MF with  $\mathcal{C}_{01 \leftrightarrow 11}$  coupling, after  $LP_{01}$  selective launch. Only  $LP_{01}$  and  $LP_{11}$  are considered here.

Comparing the two pure-mode traces, it can be observed firstly that the blue  $LP_{01}$  plateau has a much more conspicuous tilt than the orange  $LP_{11}$  plateau, and secondly that the former has a lower power than the latter. These both result from  $LP_{01}$  having started with a great deal more discretely coupled power than  $LP_{11}$ . Because both modes' discrete peaks continuously lost power due to attenuation and had power coupled away over the fibre length, both plateaus have tilts that decrease in their respective coupling directions of increasing distance. However, the orange pure  $LP_{11}$  plateau has a much smaller tilt due to the fact that while power is continuously exchanged between the two modes,  $LP_{11}$  receives a nett gain in power because it was at a deficit relative to  $LP_{01}$ 's

initial power. That is, in the later stages of propagation (i.e. the LHS of the orange plateau) the plateau raising effect due to the nett positive gain in power of  $LP_{11}$  from coupling from  $LP_{01}$  counteracts the plateau suppressing effect due to the attenuation of the donor  $LP_{01}$ . On the other hand, this counteraction is absent from the blue  $LP_{01}$  trace, resulting in its plateau decreasing much more quickly. With regards to the relative plateau heights (powers), the orange  $LP_{11}$  plateau is taller, again because of the relative difference in initial mode powers causing  $LP_{11}$  to have a nett gain and  $LP_{01}$  to have a nett loss. Figure 5.10 illustrates this point with the total power evolution of each mode as a function of distance,<sup>6</sup> which shows the nett power gain and loss of  $LP_{11}$  and  $LP_{01}$ , respectively. Furthermore, this  $LP_{01}$  loss is greater than if  $LP_{01}$  had only undergone attenuation and no coupling. This is evidenced by the fact that the output power of  $LP_{01}$  is about 3.63 dB weaker than its input power, in contrast to the output powers of  $LP_{02}$  and  $LP_{21}$ , which are only 2 dB weaker than their respective input powers, as expected for modes that had only suffered the  $\alpha = 0.2$  dB/km attenuation. Although not seen in the graph, had the fibre been longer, the blue and orange power curves would eventually come together and then decrease linearly with a gradient equal to  $-\alpha$ .

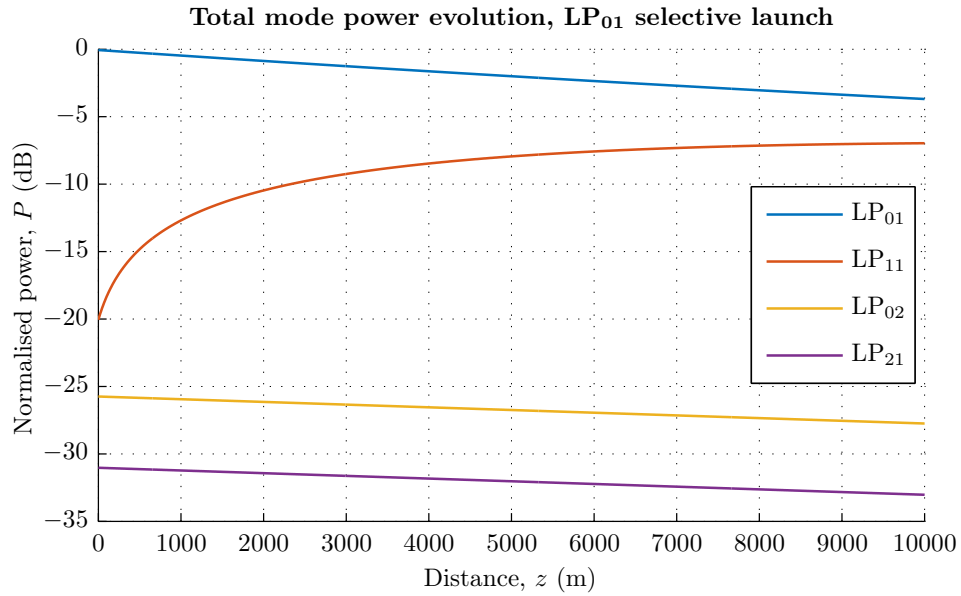


FIGURE 5.10: Total power evolution of individual modes in a 10 km 4MF with  $C_{01 \leftrightarrow 11}$  coupling, after  $LP_{01}$  selective launch.

For comparison with the  $LP_{01}$  selective launch case, Figure 5.11 shows the power evolution through the same fibre as in Figure 5.7, but with a dominant  $LP_{11}$  mode-selective launch instead. Again, the tilt of the overall  $C_{01 \leftrightarrow 11}$  plateau (as seen in the inset) is away from the dominant mode, i.e. pointing away from  $LP_{11}$ .

<sup>6</sup>Note that in this plot, the mode powers have been normalised relative to the summed total *initial* power across all modes.

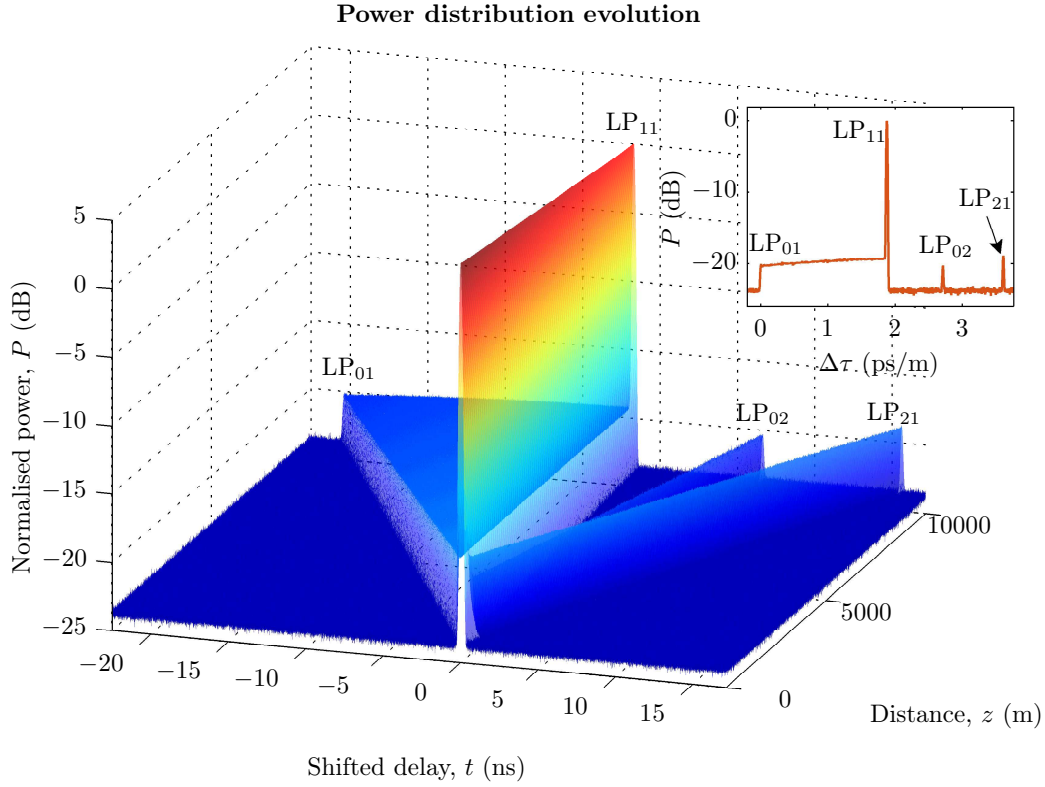


FIGURE 5.11: Simulated evolution of optical power in a 10 km 4MF with  $C_{01 \leftrightarrow 11}$  coupling, after  $LP_{11}$  selective launch. The inset shows the resultant ToF trace at the fibre end.  $\Delta\tau$  = relative delay per unit length.

### 5.2.2 Effects of Varying Coefficients

This subsection explores the effects that changing the various coefficients have on the ToF trace.

#### Attenuation

Figure 5.12 shows traces of simulated ToF on a 4MF, which guides  $\{LP_{01}, LP_{11}, LP_{02}, LP_{21}\}$ , with appreciable coupling only between the first two modes (i.e.  $LP_{01}$  and  $LP_{11}$ ). The launch is  $LP_{01}$ -dominant and the attenuation of this mode is varied; all other modes are set to zero attenuation. The powers of each trace have been normalised in relation to the peak power of the  $\alpha_{01} = 0$  dB/km case. A few observations can be made. Firstly, the powers of the discretely coupled components of  $\{LP_{11}, LP_{02}, LP_{21}\}$  do not change; they are not affected by the varying attenuation of  $LP_{01}$ . Secondly, the differences in peak output powers of the discretely launched  $LP_{01}$  mode match the variation of the attenuation; the peak powers are labelled in the plot. Thirdly and most importantly, the slope of the  $C_{01 \leftrightarrow 11}$  coupling plateau also changes according to the  $LP_{01}$  attenuation.

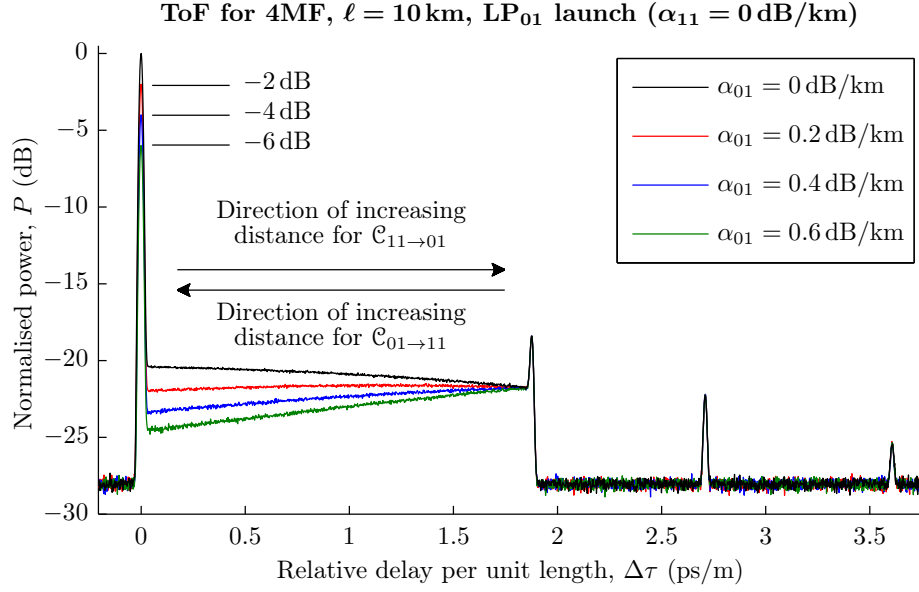


FIGURE 5.12: Simulated ToF with varying  $\alpha_{01}$  attenuation in a 10 km 4MF with  $\mathcal{C}_{01 \leftrightarrow 11}$  coupling, after  $\text{LP}_{01}$  selective launch.

Consider the lossless case where  $\alpha_{01} = 0 \text{ dB/km}$  (black trace). This scenario is akin to that addressed in Section 5.2.1, where all mode attenuations were equal, albeit with  $\alpha = 0 \text{ dB/km}$  now rather than  $\alpha = 0.2 \text{ dB/km}$  previously. The  $\mathcal{C}_{01 \leftrightarrow 11}$  plateau is ‘anchored’ on the more powerful discretely coupled  $\text{LP}_{01}$  (LHS) peak and tilts away from it.

On the other hand, when  $\alpha_{01} \neq \alpha_{11}$ , and in particular when  $\alpha_{01} > \alpha_{11}$ , the plateau tilts in the opposite direction, with the tilt becoming steeper as  $\alpha_{01}$ , or more specifically as  $(\alpha_{01} - \alpha_{11})$ , increases. This is shown by the red, blue, and green traces in the plot. To understand this, recall from Section 5.2.1 and Figure 5.9 that the total  $\mathcal{C}_{01 \leftrightarrow 11}$  plateau in the ToF trace is composed of the sum of the individual pure  $\text{LP}_{01}$  and  $\text{LP}_{11}$  plateaus. Figure 5.13 shows the same plot as Figure 5.9, but with  $\alpha_{01} = 0.4 \text{ dB/km} > \alpha_{11} = 0 \text{ dB/km}$ . The new tilt of the total plateau is largely influenced by the tilt of the pure  $\text{LP}_{11}$  (orange) plateau, which is composed of  $\mathcal{C}_{01 \rightarrow 11}$  components. Using the ‘early/late’ framework explained in the previous section, the direction of increasing distance for  $\mathcal{C}_{01 \rightarrow 11}$  coupling is from the RHS to the LHS, i.e. early  $\mathcal{C}_{01 \rightarrow 11}$  coupled components end up near the RHS and late  $\mathcal{C}_{01 \rightarrow 11}$  components end up near the LHS. Since the late LHS components had propagated as the now more lossy  $\text{LP}_{01}$  over a longer distance, their final powers eventually become significantly lower than that of their earlier components on the RHS, hence the much more conspicuous orange tilt, as compared to that in Figure 5.9, which ultimately changes the tilt direction of the total plateau.

The key point here is that it is the *difference* in attenuations between two modes that affects the profile of the coupling plateau between them. This is evident from Figure 5.14, which plots the ToF of the same fibre as in Figure 5.12, using the same  $\text{LP}_{01}$  selective launch, but instead with the attenuation of  $\text{LP}_{11}$  varying and that of  $\text{LP}_{01}$  (and also

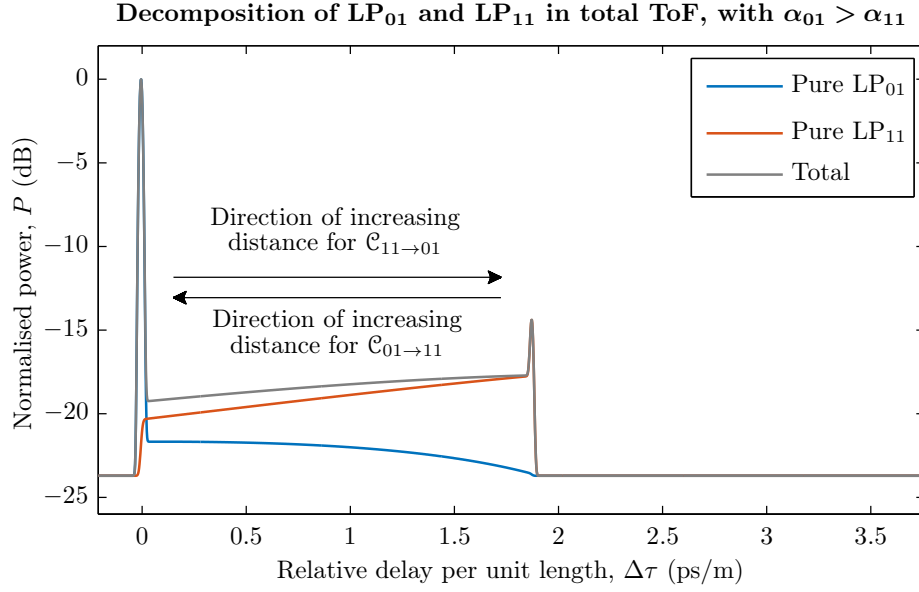


FIGURE 5.13: Total and decomposed ToF traces in a 10 km 4MF with  $\mathcal{C}_{01 \leftrightarrow 11}$  coupling, after  $\text{LP}_{01}$  selective launch, with  $\alpha_{01} = 0.4 \text{ dB/km} > \alpha_{11} = 0 \text{ dB/km}$ . Only  $\text{LP}_{01}$  and  $\text{LP}_{11}$  are considered here.

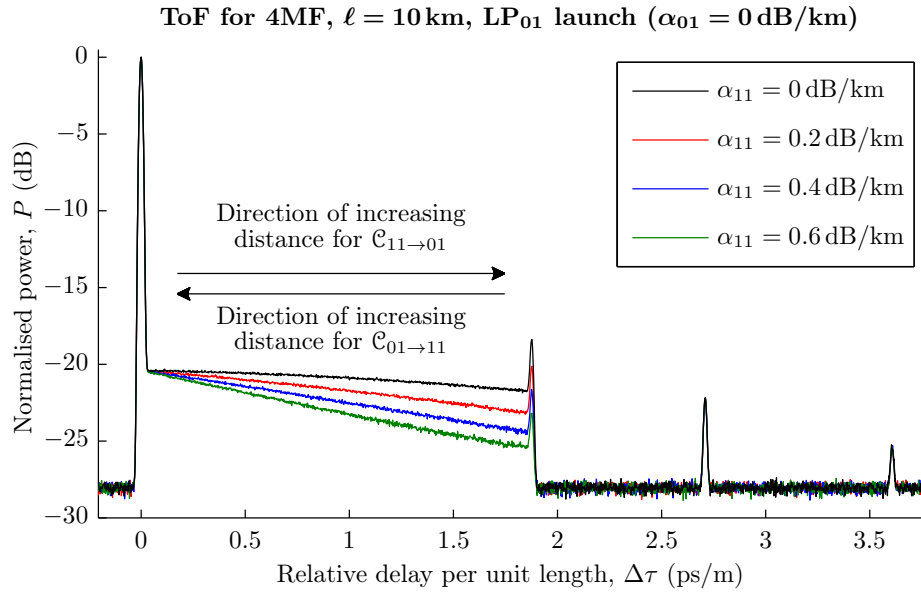


FIGURE 5.14: Simulated ToF with varying  $\alpha_{11}$  attenuation in a 10 km 4MF with  $\mathcal{C}_{01 \leftrightarrow 11}$  coupling, after  $\text{LP}_{01}$  selective launch.

$\text{LP}_{02}$  and  $\text{LP}_{21}$ ) kept constant and at 0 dB/km. The coupling plateau tilts away from the mode that is attenuated less.

## Coupling

The coupling coefficients also affect the profiles of ToF coupling plateaus. Figure 5.15 shows the simulated ToF trace after an  $\text{LP}_{01}$  selective launch in the same fibre as before.

The black trace is identical to that in the inset of Figure 5.7. In this study, the magnitude of the  $\mathcal{C}_{01 \leftrightarrow 11}$  coupling coefficients is varied as multiples of the original, and the coloured traces correspond to the various cases. The modal losses have all been set to  $\alpha = 0.2 \text{ dB/km}$ .

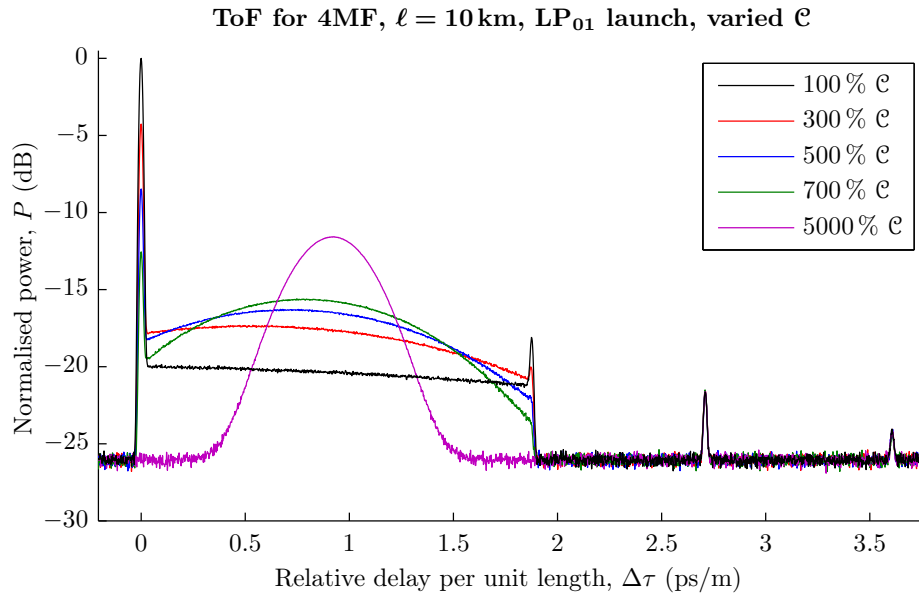


FIGURE 5.15: Simulated ToF with varying  $\mathcal{C}$  scalings in a 10 km 4MF with  $\mathcal{C}_{01 \leftrightarrow 11}$  coupling, after  $\text{LP}_{01}$  selective launch.

A feature of coupling plateaus that is seen in previous plots but not yet explicitly mentioned is that they are not exactly straight. There is always some amount of upwards curvature, centred at the average of the two modal delays which demarcate the plateau. The reason for this is that the continuous repeated coupling and back-coupling, or *cyclic coupling*, between  $\text{LP}_{01}$  and  $\text{LP}_{11}$  components over the length of the fibre cause the velocity of the optical signals to be evenly averaged between that of the two modes, leading to a concentration of power ending up with a delay that is equally separated between the two modal delays. When the coupling coefficients are relatively small, i.e. the black trace, the impact of cyclic coupling is not great, and the plateau profile is still mostly influenced by the ratios of the initial discretely coupled powers with the plateau curvature remaining comparatively tiny. However, as the coupling coefficients are magnified, the impact of cyclic coupling gets stronger and the plateau curvature increases, as the proportion of time that the power spends travelling as either  $\text{LP}_{01}$  and  $\text{LP}_{11}$  is more evenly distributed, resulting in most of the power propagating at the arithmetic mean of the two modal delays. When the coupling coefficients are very strong (magenta trace), the individual discretely coupled peaks of  $\text{LP}_{01}$  and  $\text{LP}_{11}$  disappear, since they had been entirely siphoned by the coupling plateau, and the plateau itself is now a single peak.

Figure 5.16 shows the evolution of power in each of  $\text{LP}_{01}$  and  $\text{LP}_{11}$  for weak (100 %  $\mathcal{C}$ ) and strong (700 %  $\mathcal{C}$ ) coupling. In the strong coupling case (dashed lines), power is

distributed evenly between the two modes much more quickly than in the weak coupling case. The two mode curves rapidly coalesce and subsequently decrease linearly according to the average modal attenuation.

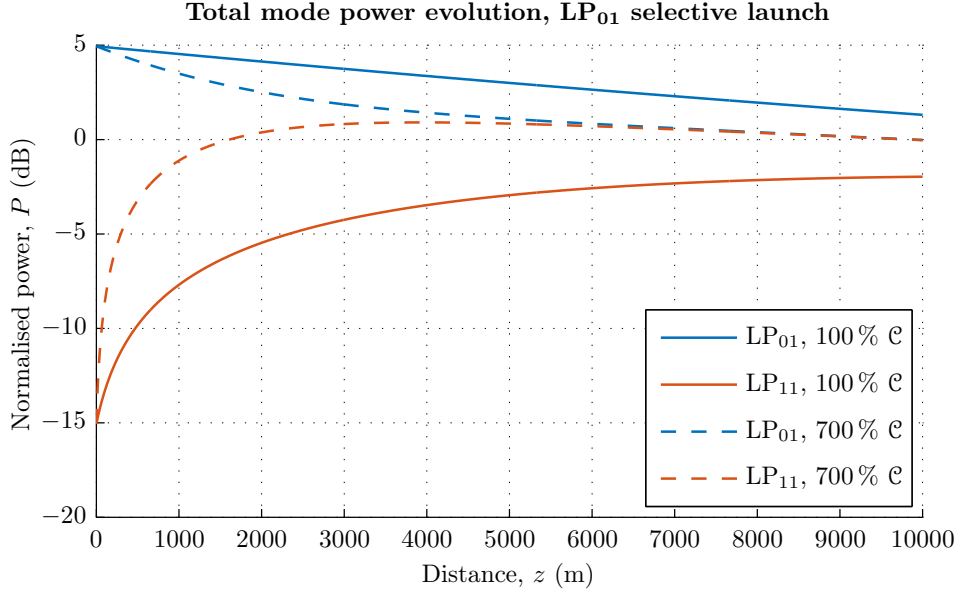


FIGURE 5.16: Total power evolution of  $LP_{01}$  and  $LP_{11}$  in a 10 km 4MF with  $C_{01 \leftrightarrow 11}$  coupling, after  $LP_{01}$  selective launch, for different  $C$  scaling cases.

This averaging effect caused by mode coupling has a practical benefit in real FMFs in terms of reducing mode-dependent loss (MDL). While the modes in FMFs generally suffer non-equal attenuations individually, in the presence of strong mode coupling, power propagating in such fibres is rapidly exchanged among the modes resulting in an averaging of the loss per mode and a reduction of the overall MDL [31]. This is akin to the polarisation-dependent loss (PDL) reduction effected in SMFs through the use of polarisation scrambling [31, 169].

Strong coupling also averages the delays of the two modes. This presents another practical advantage where the overall spread of delays is reduced, which is of benefit to MDM using MIMO DSP because it minimises the required signal processing complexity [52].

### 5.3 Fitting with Experimental Data

The pulse propagation model detailed in this chapter can be beneficially used in conjunction with experimentally measured ToF data in two ways. Firstly, although measured data can provide information about distributed coupling among modes propagating in optical fibres, it is challenging to quantitatively assess the relative coupling strengths purely by visual observation of the ToF trace profiles. The model can be applied to simulate ToF traces with various profiles via adjusting the physical coefficients as described

in Section 5.2.2. By tuning the parameters, the simulated traces can be fitted with the measured data to numerically ascertain the fitting coefficient values and thereby quantify the amounts of coupling between various modes.

Secondly, the model may be used to predict the propagation behaviour of fibres being manufactured. During the pre-fabrication stages, the coupling coefficients for a fibre can be calculated based on its designed structure and refractive index profile, using other finite element solver software. These coefficient values can then be inputted into the model for simulation to determine the fibre's predicted ToF behaviour. In an iterative manner, the fibre's structural design can be adjusted until a desired ToF simulation profile is achieved. After fabrication, measured ToF data of the fibre can be compared with simulation predictions for verification or possible diagnosis in events of mismatch.

The following parts in this section address these two directions.

### 5.3.1 Determination of Coupling Coefficients Through Fitting

From the oscilloscope traces of measured ToF data of MMFs, specifically the distributed coupling plateaus, the extent of mode coupling can be qualitatively assessed. However, it is difficult to accurately quantify the relative mode coupling coefficients from the measured data alone. The pulse propagation model can be used to aid in this regard, by fitting simulated traces onto the experimental results. This is achieved by an iterative process of varying the values of the coupling coefficients  $\mathcal{C}_{m,q}$  that specify the propagation equation (5.2) and then solving to produce traces that can be matched with the measured data until a good fit is found. An example is given here using the 10 km 4MSIF previously mentioned in Section 3.3.2. Figure 5.17 shows the measured ToF traces for this fibre, with blue, orange, purple, and green representing selective launching of LP<sub>01</sub>, LP<sub>11</sub>, LP<sub>02</sub>, and LP<sub>21</sub>, respectively. The DMDs, relative to LP<sub>01</sub>, of each mode are where their discrete peaks occur in time, as indicated by the labels in the top-right plot.

Prior to running the simulation, other variable coefficients (see Table 5.1) are first determined through measurement to reduce the number of free parameters. The modal attenuations  $\alpha_m$  can be measured via cutback or other methods. The modal delays  $\tau_m$  can be obtained directly from the temporal locations of the discretely coupled mode peaks in the measured ToF trace. The initial launch discretely coupled mode powers, represented by the scaling factors  $P_{dm}$ , can be estimated, to some extent, by the relative ToF output peak powers (though variations in coupling coefficients do have minimal effects on the output peak powers and so it might be necessary to fine-tune the  $P_{dm}$  during the iterative fitting process). This leaves the coupling coefficients as the main remaining tunable parameter for fitting. For a rigorous fitting procedure, several mode-selective launch cases are considered, and fits between measured and simulation traces need to be achieved simultaneously for all launch cases.

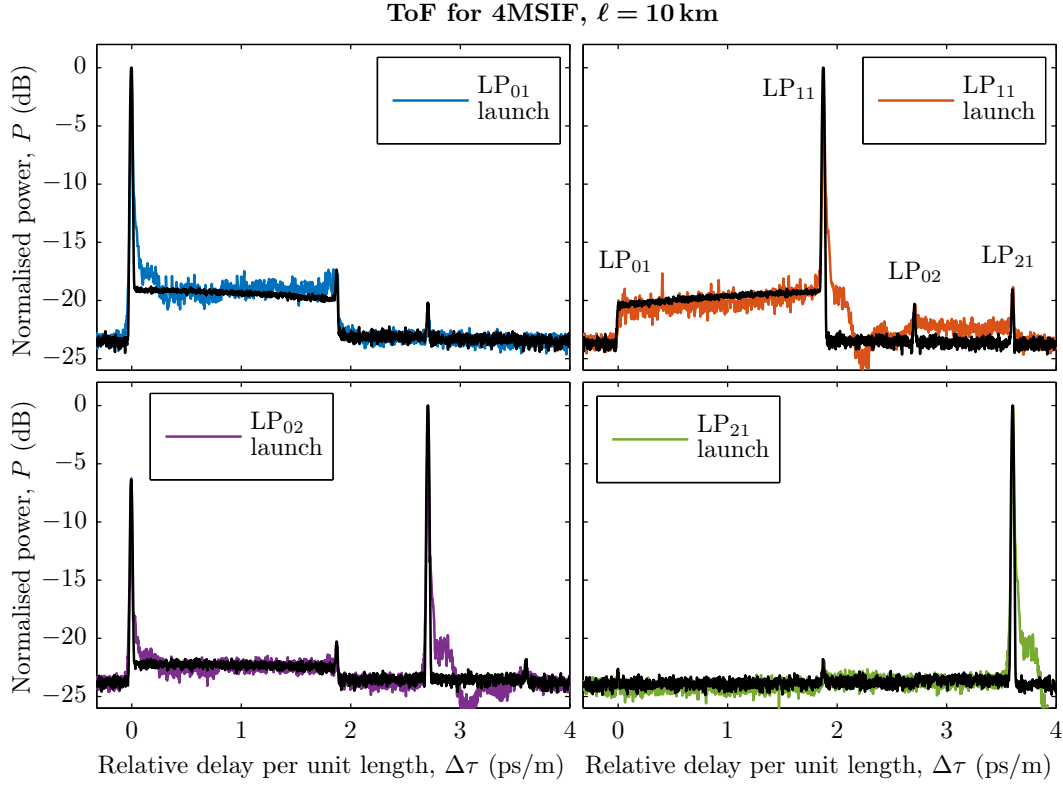


FIGURE 5.17: ToF data of a 10km 4MSIF for various mode-selective launch cases (coloured), with corresponding fitted simulated traces (black). Discrete launch-coupled mode peaks are labelled in top-right for reference.

In this work, the fitting was done using an iterative process of adjusting the coupling coefficients  $\mathcal{C}$  followed by visual inspection of the closeness between the simulated and measured ToF traces. For the 4MSIF example, there are  ${}^4C_2 = 6$  independent tunable coefficients, each of which quantify the coupling between two of the four guided modes.<sup>7</sup> For example,  $\mathcal{C}_{01,11}$  is the coefficient for coupling between  $LP_{01}$  and  $LP_{11}$ .

Coupling between adjacent nearest-neighbour modes (in terms of relative delay position) was considered first, since nearest neighbours have smaller propagation constant differences compared to non-adjacent modes (see Section 2.2.3) and so are most prone to cross-coupling. That is, the plateau between two mode peaks is most sensitive to changes in the coupling coefficient linking those two modes, compared to any other coupling coefficient linking either of the two modes to other modes. The coefficient  $\mathcal{C}_{01,11}$  was used as a starting point, since in Figure 5.17, the plateau between the  $LP_{01}$  and  $LP_{11}$  discrete peaks, i.e. the  $\mathcal{C}_{01 \leftrightarrow 11}$  plateau, is the most prominent (in all selective launch cases producing large output peaks of either  $LP_{01}$  or  $LP_{11}$ ). By adjusting this coefficient and observing the output each time, the  $\mathcal{C}_{01 \leftrightarrow 11}$  plateau was successively raised or lowered until a good fit was obtained simultaneously for all mode-launch cases. The adjustments were made such that successive changes were marginally less than previous adjustments,

<sup>7</sup>The notation  ${}^N C_p$  represents the number of  $p$ -combinations from a set of  $N$  elements.

until the simulation converged with the measurements. The idea is to progressively reduce the variability range of the coefficients. If the coupling coefficient was adjusted to a point where the mode output peak powers no longer aligned with their measurement counterparts, then the initial launch power scaling factors  $P_{dm}$  were tuned to correct the mismatch. For example, in the  $LP_{01}$  launch case (top-left), if increasing  $\mathcal{C}_{01,11}$  to raise the  $\mathcal{C}_{01 \leftrightarrow 11}$  plateau caused the  $LP_{01}$  discrete peak to drop due to more of its power being siphoned to the plateau (or rather if the other mode discrete peaks grew, since the plot is normalised to the peak power of the dominant mode), then  $P_{d01}$  would be increased to correct the mismatch. Although this might suggest that the adjustment procedure is now complicated with an additional free parameter, in practice, the coupling plateaus are finitely but not significantly influenced by the initial launched mode powers, and changing the  $P_{dm}$  does not drastically change the plateau heights such that the adjustment of the various  $\mathcal{C}_{m,q}$  needs to be redone. That is, unless a drastic change is made to the initial launched powers, on an order much larger than the adjustment sizes in each iteration, then any small change would produce no discernibly large change in the plateaus, and vice versa.

Once a (visually judged) reasonable fit was obtained for the  $\mathcal{C}_{01 \leftrightarrow 11}$  plateau, then the next plateau and the corresponding coupling coefficient linking the two modes demarcating that plateau was addressed, and so on for the rest of the plateaus (a total of three in this case). Where the adjustment of coefficients achieved fits for some plateaus but not others, then the affected plateaus were treated by first changing the coefficients linking the affected modes to their nearest neighbours once removed, e.g.  $\mathcal{C}_{01,02}$ , and possibly thereafter, neighbours even further removed, e.g.  $\mathcal{C}_{01,21}$ . Once the fitting was done, the corresponding coupling coefficient values were recorded. Figure 5.18 shows the strength of each coefficient relatively normalised with respect to the largest, in this case  $\mathcal{C}_{01,11}$  (as expected).

This iterative adjustment procedure is not perfect. For instance, although the fits in Figure 5.17 are somewhat decent, the plateau between the  $LP_{02}$  and  $LP_{21}$  peaks for  $LP_{11}$  launch (top-right) has not been matched, even after trying to readjust all six coupling coefficients without considerably disrupting the already established fits with the other plateaus. While it is likely the case, as mentioned in Section 3.3.2.2, that the elevation in the measured data was caused by a pulse ringing effect in the detector, rather than mode coupling, the answer cannot be certain with the current fitting method. This basic method of manually selecting coupling coefficients to adjust and basing fit quality on qualitative visual observation was intended to only be a starting point. It has served its purpose in demonstrating that it is possible, using a set of rules, to fit simulation outputs onto measured data to obtain a quantitative measure of the mode coupling in optical fibres.

For future work, the next step will be to develop these adjustment guidelines into a proper set of rules so that the fitting can be heuristically performed. Moreover, a more

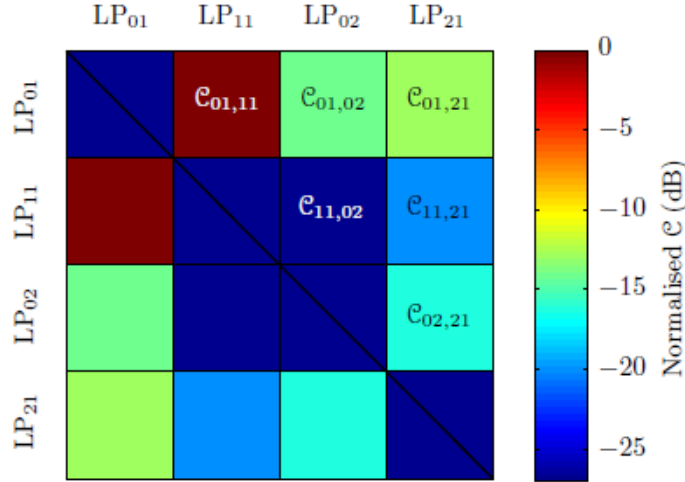


FIGURE 5.18: Coupling coefficients resulting from fitting ToF results of a 10 km 4MSIF. The six independent coefficients are labelled.

robust, quantitative method of determining fit quality needs to be applied. This could possibly take the form of using the data points to measure the consolidated Euclidean distance between the simulated and measured traces in each step. If these two can be implemented, then the fitting process can be automated and any human subjectivity can be avoided.

### 5.3.2 Comparing Calculated and Measured ToF

In the previous subsection, the coupling coefficients of a FUT were determined using the measured ToF traces and applying a fitting procedure to the model. In this part, the reverse is done, i.e. the known (calculated) coupling coefficients of a FUT are used to define the model's propagation equation and simulate the predicted ToF trace that is then compared with measured data.

The objective of this study was to validate a model that describes the origin of the coupling coefficients in real HC-PBGFs with irregular core boundaries, which was presented in [36] as part of our MODE-GAP project contributions. While the specifics of the coupling coefficient model and the method of calculation are outside the scope of this thesis, it suffices to note that the coefficients depend on three quantities [36]:

1. the materials used for the solid and hollow parts of the PBGF as characterised by their refractive indices,
2. the extent of overlap of the electric and magnetic fields of optical signals with the irregular core boundary, and

3. the power spectral density (PSD) of the core boundary distortion describing its spatial statistics.

Based on these parameters, the coupling coefficients in a fabricated  $\ell = 230$  m 19c HC-PBGF were calculated. For simplicity, only the two lowest-order mode groups  $\{\text{LP}_{01}, \text{LP}_{11}\}$  were considered, though the 2-fold and 4-fold mode degeneracies of the former and latter, respectively, were not assumed, making the study cover six individual modes. The coupling coefficients were inputted into (5.1) and the pulse propagation model was used to simulate the predicted ToF trace. The fibre was also subjected to a ToF experiment and the measured trace is plotted in Figure 5.19, with the simulated trace overlaid. The good agreement between the simulated and measured traces substantiates the coupling coefficient model.

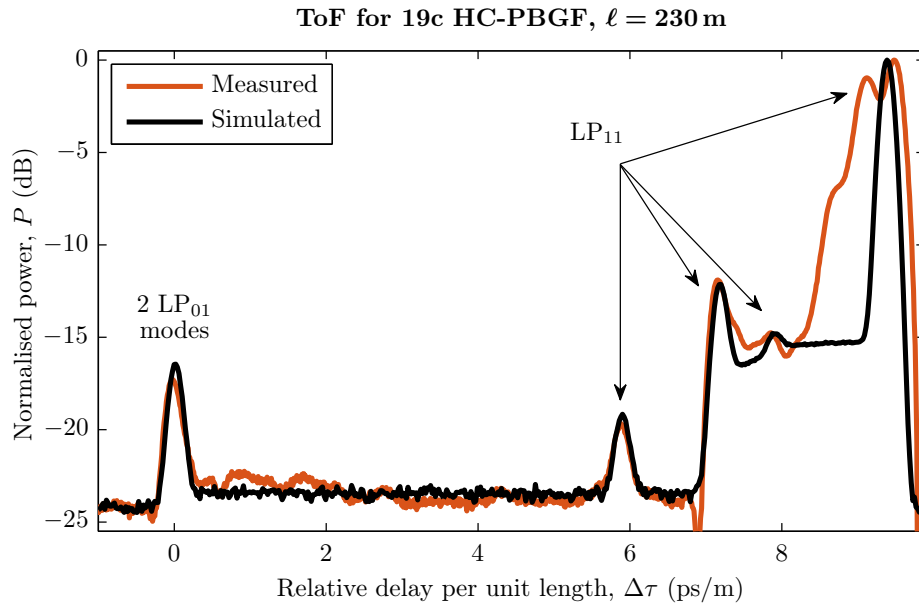


FIGURE 5.19: Measured (orange) and simulated (black) ToF for a 230 m 19c HC-PBGF, for  $\text{LP}_{11}$  dominant launch. Individual discrete launch-coupled mode peaks are labelled.

This coupling coefficient model, which was formulated by Numkam Fokoua [36], predicts that because fibre surface roughness scattering causes both loss and mode coupling in HC-PBGFs, efforts to reduce loss should result in simultaneous reductions in the coupling coefficients. The coupling coefficient between  $\text{LP}_{01}$  and  $\text{LP}_{11}$  in this fibre, calculated by the coefficient model, is  $\mathcal{C} = 2.76 \times 10^{-2} \text{ km}^{-1}$ , which is larger than those for solid-core FMFs. This is expected, as the fibre's measured loss (3.5 dB/km) is correspondingly greater than the  $\sim 0.2$  dB/km typical in SCFs. Calculations using the coefficient model show that HC-PBGFs exhibiting similar low-loss levels would have far lower coupling coefficients compared to those in SCFs [36].

For completeness, coupling coefficients for the 37c HC-PBGF 37c1 from Section 4.1 were calculated by Numkam Fokoua. These values were used to simulate mode propagation of

the  $LP_{01}$  (2 modes),  $LP_{11}$  (4 modes), and  $LP_{21}$  (4 modes) groups, from an  $LP_{11}$  dominant launch. Figure 5.20 shows the output trace compared with the measured ToF data from Figure 4.4b. Of note is the coupling between  $LP_{01}$  and  $LP_{11}$ . The  $C_{01 \leftrightarrow 11}$  coefficient for this 37c fibre is about 5 times greater than that for the 19c fibre in Figure 5.19. This is readily observed from the more elevated  $C_{01 \leftrightarrow 11}$  plateau in Figure 5.20. It should be noted however, that under ideal conditions, the coupling coefficients in 37c fibres are predicted to be lower than their 19c fibre counterparts, given the reduced field interaction with the rough microstructure boundaries in the former [36].

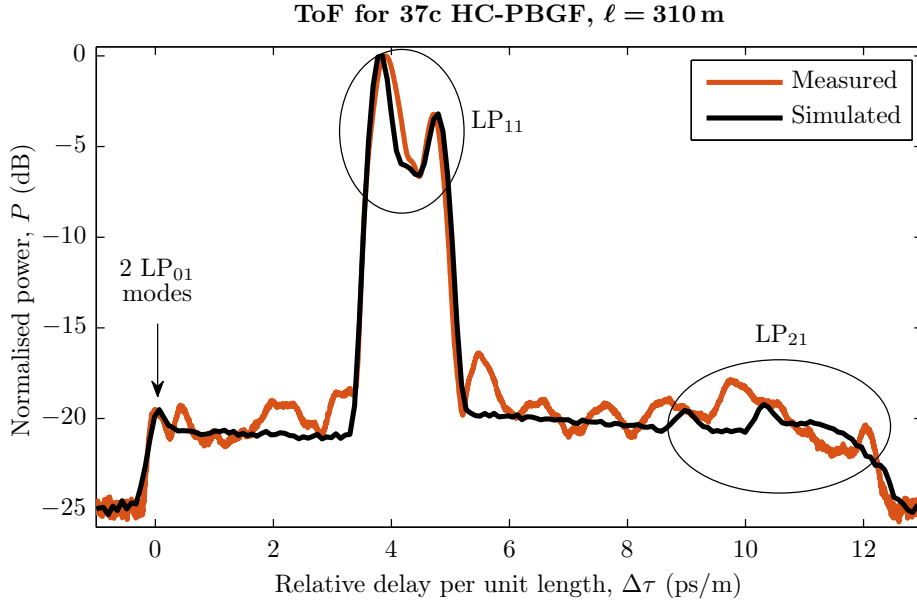


FIGURE 5.20: Measured (orange) and simulated (black) ToF for the 310 m 37c HC-PBGF 37c1, for  $LP_{11}$  dominant launch. Mode groups are labelled.

The coupling coefficient model has widened our understanding of mode coupling in HC-PBGFs, and the fact that it was validated by means of the propagation simulation model, as well as the ToF experimental method, demonstrates the usefulness of the latter two.

## 5.4 Conclusions and Future Work

This chapter has described the implementation of a mode propagation simulation model based on the coupled power equation (5.1). The heart of the model is the ability to solve this partial differential equation and two methods have been outlined, namely, the iterative stepping method (ISM) and the split-step Fourier method (SSFM). Given the more straightforward logic of its mathematics, the ISM was implemented first, for use as a reference. The SSFM was also implemented, and though the principles behind which the method is grounded are less trivial, it was shown, via a number of comparison tests, to be superior in this context to ISM both in terms of rate of convergence and computational efficiency. The ISM was therefore only used to check the correctness of

the SSFM implementation, and the latter was used predominantly in the actual fibre simulations.

Using the model, ToF in any fibre can be simulated. By glancing into the model, the power evolution of the various propagating modes in fibres can be visualised and understood. A key advantage of the simulation is that it is possible to access the propagation at any point along the transit, in contrast to experimental ToF which only produces output traces. The variability in the simulation stems from the independent parameters that encode the various physical phenomena, such as attenuation, DMD, and mode coupling. In particular, the effects of variations in attenuation and coupling coefficients on the shapes of the output ToF traces were explored, giving insight into how they are constituted. This will be reported in [119].<sup>8</sup>

Two practical uses of the simulation model in fibre characterisation were mentioned. Firstly, an attempt was made to use the model as a tool for quantitatively determining the coupling coefficients of FMs by performing an iterative fitting procedure on measured ToF traces, based on a set of fitting guidelines. A 4MSIF was used in the example and the fitting process managed to produce a rough agreement with the measured data, giving credence to the method. Nevertheless, it is acknowledged that the procedure needs to be made more rigorous in order to be truly useful. Several possibilities for future development include concretising the fitting rules into a set of proper heuristics, advancing the fit quality assessment procedure from subjective visual observation to robust deviation measurement, and ultimately automating the whole process so that a considerably larger number of modes, as is typical in HC-PBGFs, can be realistically considered.

Secondly, the propagation model was used as a validation tool for another model, namely, that of the origin and cause of mode coupling in HC-PBGFs. A fabricated 19c HC-PBGF was used as an example in this study. Its coupling coefficients were first calculated using the coefficient model, and then the propagation model was used to simulate the ToF in that fibre. The result was compared with the measured ToF of the fibre, and the good agreement demonstrated the soundness of the coefficient model. A similar comparison was made with the 37c HC-PBGF 37c1. This has implications on HC-PBGF design, as the coefficient model predicts reduced coupling coefficients as progress is made on loss reduction. This study has also verified the applicability of the coupled power equation and the associated propagation model to HC-PBGFs, in addition to solid-core fibres.

The utility of this propagation model and simulation environment goes beyond studying distributed mode coupling. Discrete mode coupling effects can also be simulated, and in the next chapter, the model is used in the development of a fibre defect inspection technique.

---

<sup>8</sup>At the time of writing, the mentioned article had been accepted for oral presentation at the CLEO, OECC & PGC mega conference in Singapore, occurring in early August 2017.

It is worth mentioning that I composed a brief non-technical write-up [27] about this simulation model and its utility to study mode coupling behaviour to address the issue of the predicted internet capacity crunch [22]. This was submitted to the 2016 Take-AIM competition, hosted by the *Smith Institute for Industrial Mathematics and System Engineering*, and eventually won the first prize [170]. The competition, which sought to publicise an appreciation that mathematics is a ubiquitous tool in everyday life, was judged by industrial and academic representatives from diverse sectors, including the EPSRC. This result underscores a general interest, not limited to the optics community, to tackle this 21<sup>st</sup> century issue.

## Chapter 6

# Inspection of Fibre Defects

In communications, optical fibre fabrication is just as important as the development of data transmission methods. Although current state-of-the-art fabrication techniques are generally robust, reliable, and reproducible in their performance, it is still possible—albeit however rare—that some fibres produced may contain longitudinal defects, particularly over multi-kilometre lengths. Understanding the origin and impact of these will be critical in fabricating long lengths of fibre [134]. The physical forms that such defects take come in a variety including structural irregularity, microfractures, and contamination. They can be anticipated to potentially cause transmission loss, undesirable mode coupling, mode dependent loss, and other ill effects. These are problematic, especially when long length ( $>km$ ) scales are considered. Thus, the detection and ultimate elimination of defects is a pertinent issue [136].

Conventionally, defects are detected and located in optical fibres via Optical Time-domain Reflectometry (OTDR). When an input optical pulse is launched into a fibre-under-test (FUT), light is continuously Rayleigh scattered. The backscattered light is detected by the OTDR apparatus and displayed as a lengthwise trace. An OTDR measurement of a defect-free fibre would produce a smoothly descending trace demarcated by large spikes corresponding to the launch and output sides of the FUT. If a local defect exists somewhere along the FUT, the backscattered light produced by the pulses encountering it will be significantly greater than that from the distributed Rayleigh scattering. The OTDR would then register an impulse peak against the otherwise continuous trace, and the location of the peak would correspond to the physical lengthwise position of the defect [143].

Whereas this method is robust for SMFs, the situation gets complicated with multimode fibres. HOMs experience unequal and often higher amounts of attenuation than the fundamental mode and travel at different group velocities. These obfuscate the OTDR traces and, together with dead zone issues [143, 171], raise doubts about the accuracy of OTDR in the multimode regime [172]. OTDR also does not provide much information

about how the defects affect individual mode propagation and coupling. For example, it might be the case that certain types or geometries of defects cause appreciable amounts of discrete mode coupling and others do not. In certain instances involving multimode fibres that may contain defects, and with only OTDR information, it is possible for fibre manufacturers, seeking to err on the side of caution, to disregard such fibres, even if they may not necessarily exhibit strong mode coupling and may still be usable for data transmission.

The ToF method, which is well-suited to study mode coupling effects, is considered to attempt to answer these questions. Of the many uses of ToF, yet another extension to its utility is demonstrated here by detecting longitudinal fibre defects, with the aim being to complement OTDR and enhance the information that it can provide, rather than to supplant it.

This chapter proceeds as follows. First, the principle of defect-induced mode coupling, in the context of the ToF framework, is outlined in Section 6.1. The relationship between the locations of defects and the temporal positions of their induced mode coupling features is explained through simulations, using the modelling tool described in Chapter 5, as well as experimental verification. Next, Section 6.2 illustrates the defect inspection method, which uses ToF complemented by measurements from OTDR and the recently developed infrared side-scattering capture technique. The method is used on a defective HC-PBGF in Section 6.3, to detect the defect locations and study the mode coupling behaviour therein. Section 6.4 then concludes the chapter and gives some suggestions for future work.

## 6.1 Defect-Induced Mode Coupling

The central premise for considering ToF in the analysis of longitudinal fibre defects is that it supposes that discrete mode coupling occurs at the defects and distorts the ToF trace from its defect-free version, producing defect features that can be resolved and identified. This section outlines the defect-induced mode coupling principles.

### 6.1.1 Concept

As the simplest case, consider a 2MF of length  $\ell$ , guiding  $\{LP_{01}, LP_{11}\}$ , with negligible distributed mode coupling (i.e. the coupling coefficients are zero), and having a single defect occurring halfway along the fibre. This can be analogised as two fibre segments, labelled S1 and S2 and of lengths  $\ell/2$  each, connected back-to-back at a discrete interface. For the sake of explanation, also consider the fictional but helpful scenario that the relative DMDs of  $LP_{11}$  in each segment are different, and  $\Delta\tau_{11,S1} < \Delta\tau_{11,S2}$ , where  $\Delta\tau_{11,Sx}$  is the DMD of  $LP_{11}$  relative to  $LP_{01}$  in segment Sx.

In reality, the two fibre segments can be joined and held in place by a commercial fibre splicer, with a transverse offset introduced at the joining interface to emulate a discrete defect. Figure 6.1 illustrates the pulse propagation in this composite two-segment 2MF. The grey peak at the origin represents a general pulsed launch that discretely excites both  $LP_{01}$  and  $LP_{11}$ , depicted in blue and orange, respectively. The two mode components propagate discretely at their respective group velocities in segment S1 until they reach the interface between the two segments. The coloured solid lines indicate their trajectories. The interface forms a defect in the continuity of the composite fibre and *discretely* couples portions of light from the two mode components into the alternate modes. That is, some power from the original  $LP_{01}$  component gets coupled to  $LP_{11}$  and vice versa for the original  $LP_{11}$  component. Note that the percentages of power coupled from either mode need not be equal. These new components, represented in the figure by the coloured dashed lines, branch off from their sources and now propagate at the S2 mode group velocities till the end of S2, to form peaks B ( $LP_{01}$ ) and C ( $LP_{11}$ ). The remaining power in the original mode components also continue to propagate in S2 and end up as peaks A ( $LP_{01}$ ) and D ( $LP_{11}$ ). In the time domain, the delay between peaks A and B, as well as that between C and D, is proportional to the DMD between  $LP_{01}$  and  $LP_{11}$  in S1 (i.e.  $\Delta\tau_{11,S1}$ ) and is equal to  $\Delta\tau_{11,S1} \times \ell/2$ . On the other hand, the delay between A and C, as well as between B and D, is proportional to the S2 DMD and equal to  $\Delta\tau_{11,S2} \times \ell/2$ .

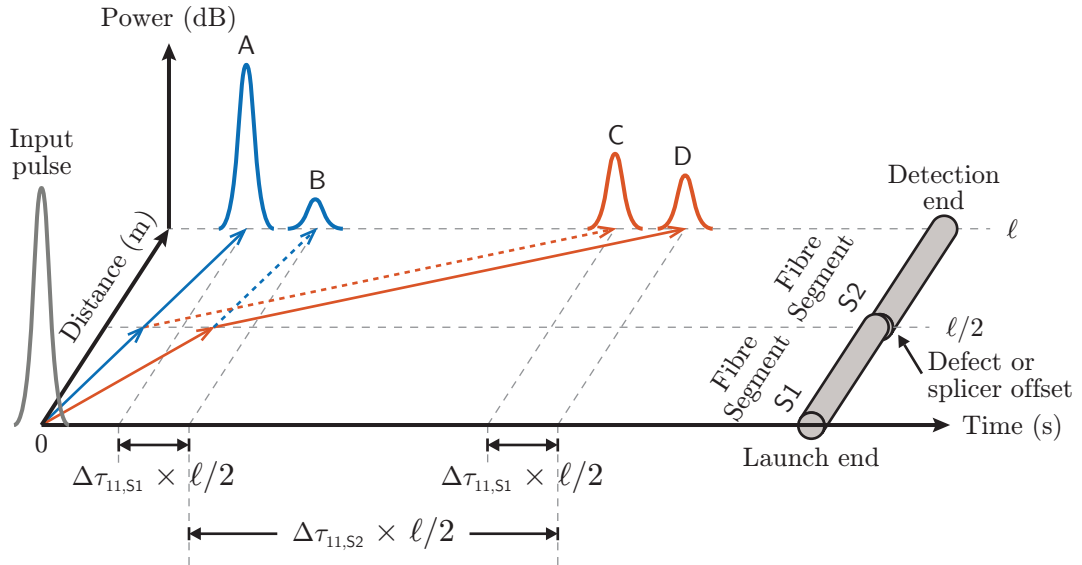


FIGURE 6.1: Pulse propagation and discrete mode coupling in a composite 2MF of length  $\ell$ , formed by joining two (unequal DMD) 2MF segments of lengths  $\ell/2$  each.  $\Delta\tau_{11,Sx}$  = DMD of  $LP_{11}$  in segment  $Sx$ .

### 6.1.2 Simulation

The propagation model described in Chapter 5 is employed to simulate the ToF of this scenario. In this example, the lengths of both segments are 10 km each, giving

the composite fibre a length of  $\ell = 20$  km. The DMDs in each segment are listed in Table 6.1. These values were chosen to match those in experimental fibres mentioned later in Section 6.1.3.

TABLE 6.1: DMDs of each segment in an example composite two-segment 2MF.

Segment	First (S1)		Second (S2)	
Mode	LP <sub>01</sub>	LP <sub>11</sub>	LP <sub>01</sub>	LP <sub>11</sub>
$\Delta\tau$ (ps/m)	0	0.08375	0	1.995

The model's split-step Fourier method routine is run once to propagate the signals down segment S1. At the interface between the end of S1 and the start of S2, the power in each mode is redistributed. Each mode gives a percentage of its power to, and receives some power from, the other mode. For example, the input powers of LP<sub>01</sub> and LP<sub>11</sub> at the start of S2 are respectively given by

$$P_{01,S2in} = \left(1 - P_r^{01 \rightarrow 11}\right) \cdot P_{01,S1out} + P_r^{11 \rightarrow 01} \cdot P_{11,S1out} \quad (6.1)$$

$$P_{11,S2in} = \left(1 - P_r^{11 \rightarrow 01}\right) \cdot P_{11,S1out} + P_r^{01 \rightarrow 11} \cdot P_{01,S1out}, \quad (6.2)$$

where  $P_{lm,S1out}$  is the power in mode LP<sub>lm</sub> at the output of S1, and the  $P_r$  are power redistribution factors that determine the proportions of power transferred between the two modes as indicated by the arrow directions in the superscripts.  $P_r$  is in units of % and note that it is possible for  $P_r^{01 \rightarrow 11} \neq P_r^{11 \rightarrow 01}$ .

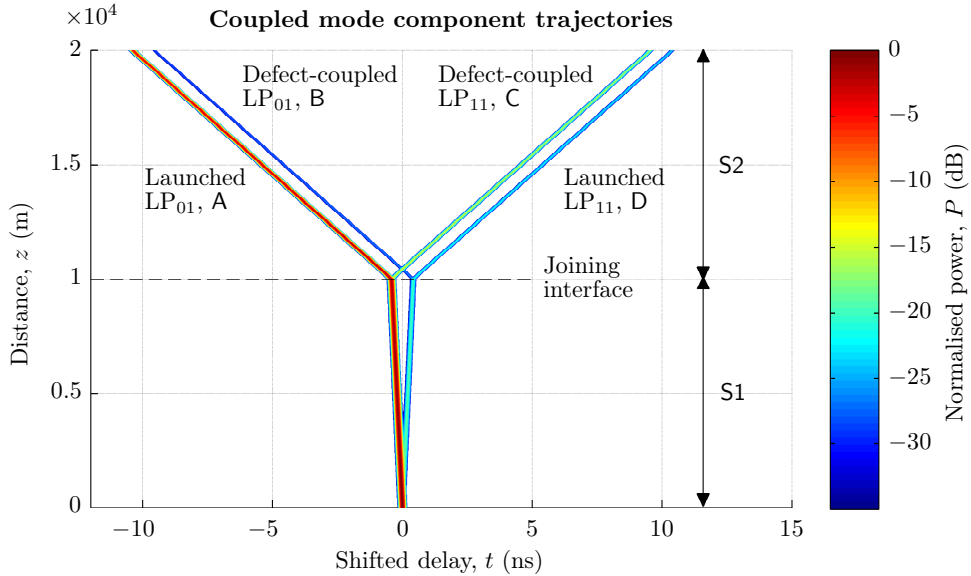


FIGURE 6.2: Mode component transit map in a simulated two-segment 2MF where each segment has a different LP<sub>11</sub> DMD. The delay spread is centrally pivoted due to the change of variable in (5.2).

Figure 6.2 shows the simulated transit of the launched and defect-coupled discrete mode power components. The lines branch outwards centrally in time because of the memory-saving simulation technique explained in Figure 5.1 in Section 5.1.1. The power redistribution factors were set as  $P_r^{01 \rightarrow 11} = 5\%$  and  $P_r^{11 \rightarrow 01} = 25\%$ .

Figure 6.3 plots the corresponding output ToF trace, showing the relative temporal delay positions of each discrete peak. The labelled discrete peaks relate to those in Figures 6.1 and 6.2. As expected, the launched  $LP_{11}$  component D arrives at a relative delay of  $(\Delta\tau_{11,S1} + \Delta\tau_{11,S2}) \cdot \ell/2 = 20.79$  ns from the launched  $LP_{01}$  component A. Furthermore, the delays between the defect-coupled components B ( $LP_{01}$ ) and C ( $LP_{11}$ ) and the respective launched components (i.e. between A and B, and between C and D) match  $\Delta\tau_{11,S1} \cdot \ell/2 = 837.5$  ps. Moreover, the relative delays between A and C and between B and D match  $\Delta\tau_{11,S2} \cdot \ell/2 = 19.95$  ns.

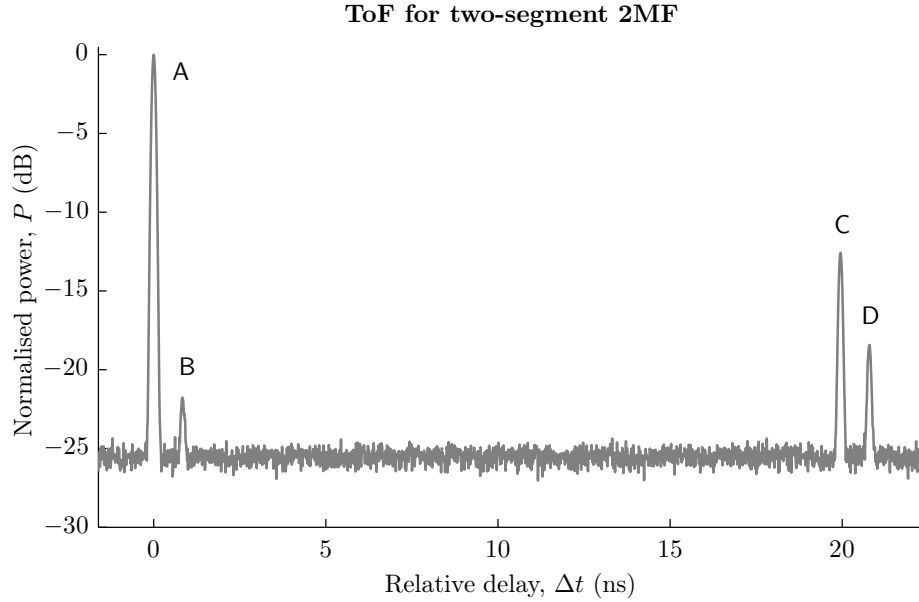


FIGURE 6.3: Simulated ToF for a two-segment 2MF where each segment has a different  $LP_{11}$  DMD. Labelled peaks correspond to components in Figure 6.2.

### 6.1.3 Experimental Verification

In order to verify the accuracy of the simulation, ToF measurements were carried out experimentally using two 10 km 2MF spools to form the composite fibre. The first spool S1 is a low-DMD 2-mode graded-index fibre (2MGRINF) and the second spool S2 is a 2-mode step-index fibre (2MSIF), the same one used in Section 3.3.1.<sup>1</sup> The DMDs of each fibre are the values of their simulation counterparts listed in Table 6.1. The measurement set-up is as Figure 3.3, with the only difference being that the FUT comprises the two spools butt coupled and held in place by a fibre splicer. By electronically controlling the

<sup>1</sup>These fibres were provided by *OFS* as part of earlier MODE-GAP collaborative work.

alignment of the splicer's translation mounts, a slight mechanical offset can be introduced at the interface between the two spools. The amount of misalignment offset affects the amount of power discretely coupled between the modes at the interface, and this effect can be seen in real-time by observing the live output trace changing on the oscilloscope. A photograph of the splicer used in this measurement, holding the two fibres in place, and a screenshot of the mechanical alignment, are shown in Figure 6.4.

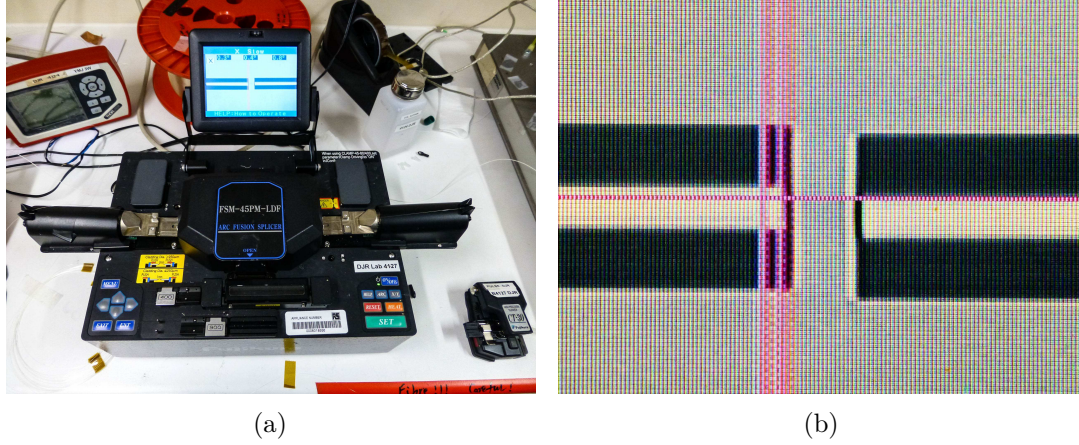


FIGURE 6.4: (a) Photograph of Fujikura Arc Fusion Splicer concatenating two fibre spools. (b) Screenshot of transverse mechanical alignment between both fibres.

Measurements were taken in four cases: selectively launching either  $LP_{01}$  or  $LP_{11}$  dominantly, and for each launch, introducing either a minor or major transverse mechanical alignment offset at the joining interface between both spools, by controlling the splicer. To preserve the launch conditions of each dominant mode case, the two cases of minor and major offsets were measured for an  $LP_{01}$  dominant launch first, before switching to the measurement of the two offset cases for an  $LP_{11}$  dominant launch. The ToF traces are shown in Figure 6.5, with the peaks labelled A, B, C, and D corresponding to the respective components in Figures 6.1, 6.2, and 6.3.

The following observations are made. Firstly, the presence of the discrete peaks B and C in the measurements shows that there is indeed discrete mode coupling occurring at the joining interface or ‘defect’. Secondly, comparison with Figure 6.3 shows that the relative delays between the peaks agree with their simulated counterparts and thus verifies the accuracy of the model. Finally, the relative powers of each peak provide information about the extent of the mode coupling.

For a dominant  $LP_{01}$  selective launch (blue traces) and with a minor alignment offset (top-left plot), majority of the optical power still resides in the original launched  $LP_{01}$  component A, while a small amount was launched in  $LP_{11}$  (D). The presence of peak C implies that some power was discretely coupled from the launched  $LP_{01}$  to  $LP_{11}$  at the defect. In fact, the relative powers of C and D indicate that the amount of power defect-coupled to  $LP_{11}$  is greater than the power initially launched into  $LP_{11}$  at the start

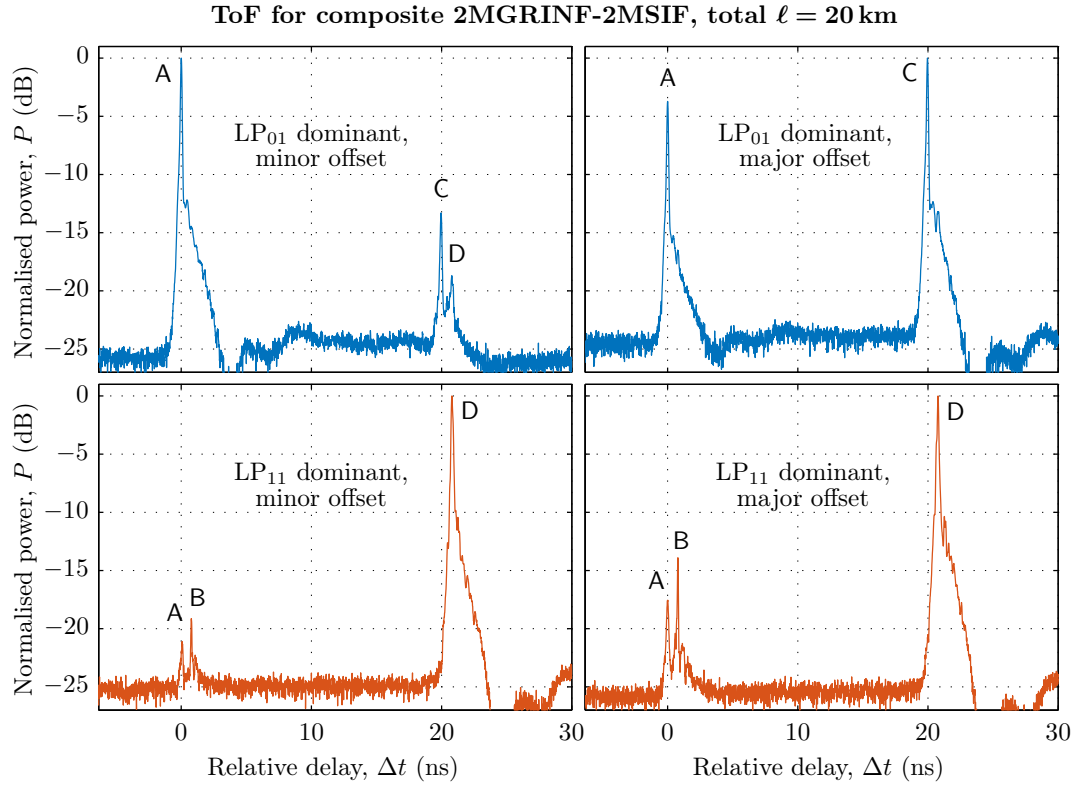


FIGURE 6.5: ToF measurements for a 10 km 2MGRINF butt coupled via splicer to a 10 km 2MSIF. Blue and orange traces result from dominant  $LP_{01}$  and  $LP_{11}$  launches, respectively, with minor and major interface alignment offsets introduced in each case.

of fibre S1. On the other hand, with a large alignment offset (top-right plot), a significant amount of power has been defect-coupled to  $LP_{11}$  and so peak C now dominates over A.

Looking at the dominant  $LP_{11}$  selective launch cases (orange traces), for a minor offset (bottom-left plot), the originally launched  $LP_{11}$  component D retains majority of the power at the end of S2. The little peak A comes from a small amount of power having been launched into  $LP_{01}$  at the input. Some power defect-coupled to  $LP_{01}$  forms peak B, with this component being larger than the launch-coupled A. With respect to modes, this scenario is the inverse of that in the top-left plot. With a bigger offset (bottom-right plot), more power has been defect-coupled to  $LP_{01}$  and so peak B becomes larger.

#### 6.1.4 A More Realistic Example

The previous subsections showed the conceptual demonstration of discrete mode coupling caused by a longitudinal fibre defect (in that scenario, it was a splice point between two fibres). Whereas the locations of fibre splice points are known, that of actual defects occurring within fibres are generally not, and it is of real interest to both find them as well as determine what kind of mode coupling (if any) could occur if light encounters them.

In certain MMFs, the degeneracies of HOMs are not preserved and the individual mode components composing each mode group can propagate at different velocities and spread out in time. For example, it is possible for the constituent modes in the  $LP_{11}$  group (see Table 2.1) to spread such that the ToF trace shows a multiple-peak profile, as was seen in Chapter 4 (e.g. Figure 4.2). This behaviour is not unusual in HC-PBGFs [36, 93, 95].

Consider a HC-PBGF (or any MMF in general) of length  $\ell = 500$  m supporting  $\{LP_{01}, LP_{11}\}$  with a single defect located at say, a quarter of the fibre length from the launch end. That is, the defect location is  $z_{\text{de}} = 0.25\ell$ . Suppose also that there is a finite spread between the constituent modes in the  $LP_{11}$  group. Figure 6.6 shows the simulated ToF of this fibre, where  $LP_{11}$  is dominantly launched.

**ToF for two-mode HC-PBGF with single defect,  $\ell = 500$  m,  $LP_{11}$  dominant launch**

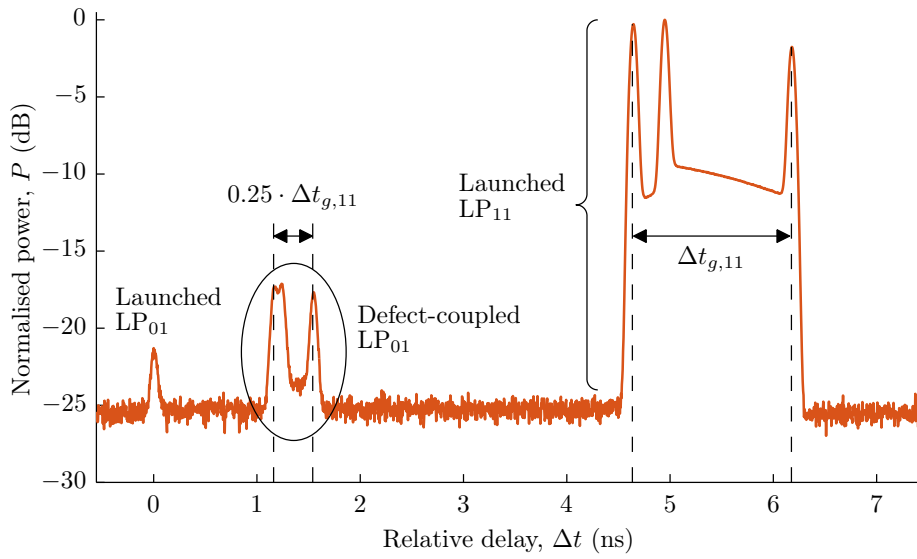


FIGURE 6.6: Simulated ToF for an  $\ell = 500$  m HC-PBGF with a longitudinal defect at  $\ell/4$ , after  $LP_{11}$  selective launching.

The launched  $LP_{11}$  mode group in this scenario comprises three discernible peaks separated in time in the output ToF trace, with the fastest peak at  $\Delta t \approx 4.623$  ns delay and the slowest peak at  $\Delta t \approx 6.159$  ns. There is also some power launched into  $LP_{01}$ , as shown by the peak at  $\Delta t = 0$  ns. After the launched  $LP_{11}$  group propagates through 25 % of the length of the fibre, it encounters the defect which causes some power to be coupled to  $LP_{01}$  (in this simulation,  $P_r^{11 \rightarrow 01} = 1\%$ ). The key observation for the defect-induced artefact is that since each component of the launched  $LP_{11}$  group travels at its respective velocity for a quarter of the fibre length and then, after mode conversion, at the  $LP_{01}$  velocity for the remainder of the fibre, their relative delays from the launched  $LP_{01}$  peak are all scaled by the same amount (a factor of  $\ell/z_{\text{de}} = 4$  in this case) compared to the relative delays of the  $LP_{11}$  components that make it to the end of the fibre unconverted. For instance, the ratio of the delays of the LHS peaks is  $4.635/1.161 \approx 4$ , as is the delay

ratio of the RHS peaks,  $6.175/1.540 \approx 4$ . This causes the general  $\text{LP}_{11}$  mode group profile shape to be preserved, albeit temporally scaled (compressed) by a factor of 4, after power has been coupled from  $\text{LP}_{11}$  to  $\text{LP}_{01}$  at the defect. That is, the temporal delay extent of the defect-coupled feature is compressed by a quarter of that of the launched  $\text{LP}_{11}$  group  $\Delta t_{g,11}$ . From this, it is possible to derive a relationship between the spatial location of the defect, and the temporal position of the mode coupling artefact that it induces. Viewing from the perspective of a dominant  $\text{LP}_{11}$  launch, where the power is coupled from  $\text{LP}_{11}$  to  $\text{LP}_{01}$  at the defect (i.e.  $\mathcal{C}_{11 \rightarrow 01}$  coupling), the relation is

$$z_{\text{de}} = \left( \frac{\Delta t_{\text{de}}}{\Delta t_{11,\text{la}}} \right) \ell, \quad (6.3)$$

where  $\Delta t_{\text{de}}$  and  $\Delta t_{11,\text{la}}$  are the relative delays of the defect-induced artefact and the launched  $\text{LP}_{11}$  component, respectively, and  $\ell$  is the fibre length.

On the contrary, if instead  $\text{LP}_{01}$  is launched, but we still wish to use the known relative delay of  $\text{LP}_{11}$  as a reference, then (6.3) would become

$$z_{\text{de}} = \left( 1 - \frac{\Delta t_{\text{de}}}{\Delta t_{11,\text{la}}} \right) \ell. \quad (6.4)$$

The physical basis for this is that  $\mathcal{C}_{01 \rightarrow 11}$  (for  $\text{LP}_{01}$  launch) and  $\mathcal{C}_{11 \rightarrow 01}$  (for  $\text{LP}_{11}$  launch) defect-coupling events cause slower and faster subsequent propagation, respectively, of the converted mode components, since  $\text{LP}_{11}$  travels slower than  $\text{LP}_{01}$ . For example,  $\mathcal{C}_{01 \rightarrow 11}$  events occurring near the output end of the FUT would cause ToF features at smaller delay deviations from the main launched  $\text{LP}_{01}$  peak, since the coupled mode components would propagate as the slower  $\text{LP}_{11}$  for only a short remaining fibre distance after having travelled as the faster  $\text{LP}_{01}$  for most of the fibre length. That is, a defect feature at a short  $\Delta t_{\text{de}}$  relative delay (and hence a small  $\Delta t_{\text{de}} : \Delta t_{11,\text{la}}$  ratio) occurs at a large  $z_{\text{de}}$  (i.e. close to the output). Vice versa for the case of  $\text{LP}_{11}$  launch and  $\mathcal{C}_{11 \rightarrow 01}$  events.

## 6.2 Defect Inspection Experimental Set-Up and Method

This section describes the experimental procedure for fibre defect inspection and uses the principles developed in the previous section.

### 6.2.1 Mode-Selective OTDR

The defect inspection procedure consists of a number of steps. First, OTDR measurements of the FUT are obtained, the purpose of which is to coarsely identify the longitudinal positions of any defects. The experimental set-up is identical to Figure 3.14.

Measurements are taken where individual modes are selectively launched via the phase plate arrangement, and for each mode, results of transmission and reflection through both directions of the FUT are acquired. For this, each end of the fibre is labelled as either “Start of Pull” (SoP) or “End of Pull” (EoP), following fabrication nomenclature.

### 6.2.2 Infrared Side-Scattering


It has been shown that longitudinal defects in optical fibres, particularly in HC-PBGFs, can occur within scales of a few millimetres, which is generally smaller than the minimum spatial resolution offered by OTDR measurements [134]; our device can resolve down to  $\sim 1$  m. This means that while an OTDR trace provides the capability to locate defects roughly, it is possible that the defect peaks could actually represent clusters of closely spaced individual defects or that some defects might be completely missed and not show up in the trace at all.

The infrared side-scattering (IRSS) procedure, which was developed by Sandoghchi and first demonstrated in [134], improves on the resolution provided by OTDR. The FUT must first be prepared by being wound on a bobbin such that each wind is evenly spaced between adjacent winds and that no winds are buried beneath subsequent winds, i.e. there is only a single layer of winds. This ensures that no part of the FUT is blocked from view, and also enables the determination of the lengthwise position of any spot on the fibre, since each successive wind around the bobbin circumference corresponds to a unit length of fibre. Depending on the length of the FUT, a larger bobbin may be necessary to accommodate the many winds. A bobbin whose rim flanges are short is also preferable so as not to obscure the visibility of the winds.

Figure 6.7a shows a the IRSS experimental set-up. The prepared FUT is illuminated using an infrared (IR) tunable laser source (TLS) that can emit light within the fibre’s transmission bandwidth. The light is launched into the FUT through a butt coupling arrangement with a feeder SMF pigtail connected to the TLS. Both the pigtail and the FUT input end are mounted on translation stages and the coupling alignment is done using the standard technique of maximising the power detected at the output end of the FUT on a power meter. Since only power is being measured, it is unnecessary to use a precise lens focusing launch set-up, and the butt coupling arrangement is sufficient.<sup>2</sup> A photograph of this is shown in Figure 6.7b.

When the IR light propagating in the fibre encounters a defect, power is scattered in all directions, with some being scattered to the visible side of the wound bobbin, as depicted in Figure 6.8a. This is captured by the IR camera, controlled by a computer, and imaged as a bright spot in greyscale, as in Figure 6.8b. The camera can be operated in video

---

<sup>2</sup>  For safety, the output end of the FUT is terminated within a bare fibre adapter and covered with a metal fibre cap. Plastic caps are unsuitable for termination because they are transparent at the operating wavelength of the TLS.

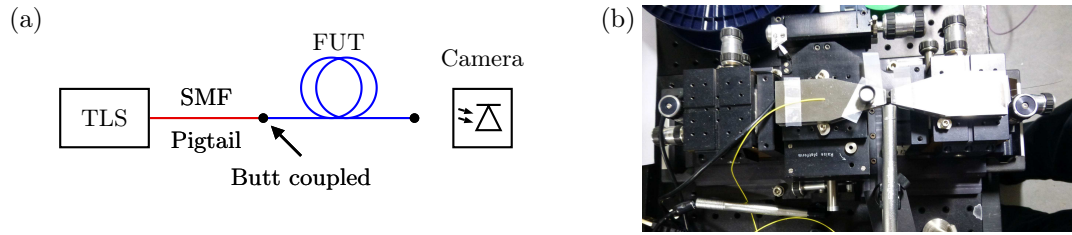


FIGURE 6.7: Infrared side-scattering (IRSS) capture set-up. (a) Schematic. (b) Top-view photograph of SMF pigtail to FUT butt coupling arrangement.

mode to display the feed on the computer. By using the live feed, the bright IR spots can be physically located on the the bobbin. The method used here is to look at the live feed while using one's hand to cover parts of the bobbin and create an IR shadow over the bright spots; the hand and hence the shadow is moved around to pin-point the defect positions. A felt tip marker is used to harmlessly mark the defect locations on the FUT. By counting the number of fibre winds from either the top or the bottom of the bobbin, the location (in metres from one of the ends) of each defect spot can be determined. The OTDR traces previously obtained are used as a reference to note those defects which register OTDR peaks, and these are singled out by using marked labels on adhesive tape affixed at their locations, as shown in Figures 6.8c and 6.8d.

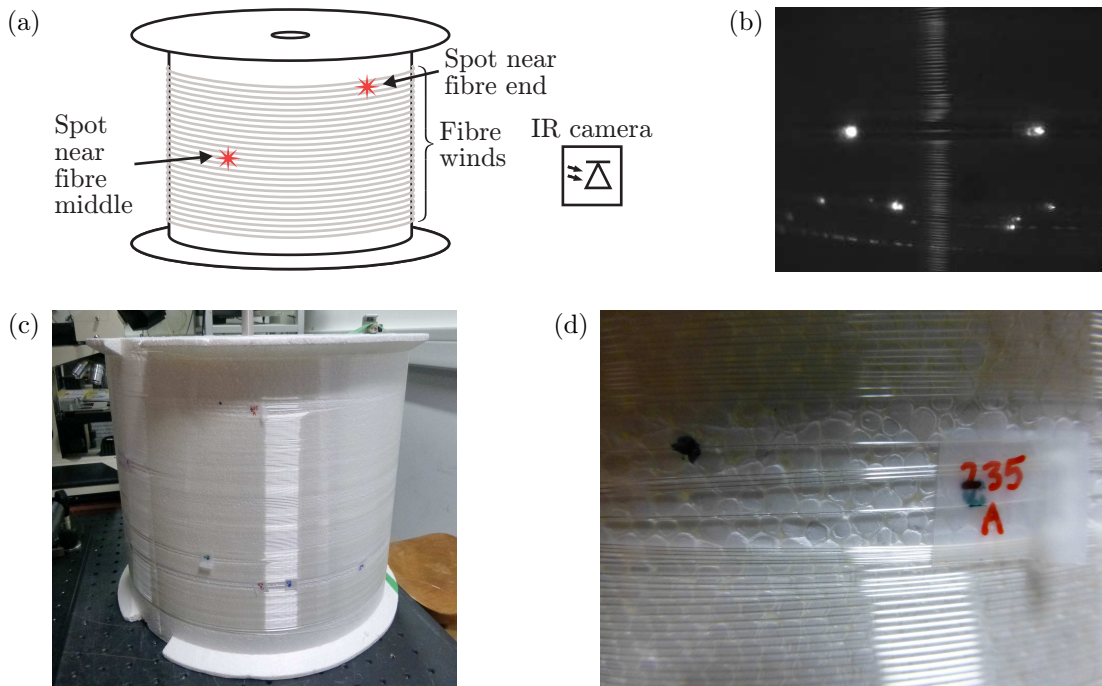


FIGURE 6.8: IR defect spot detection. (a) IR-illuminated FUT regularly wound (grey) on a white bobbin showing examples of IR-scattered bright spots. (b) IRSS capture of several defect bright spots in a real fibre. (c) Photograph of labelled spots on a FUT. (d) A single spot marked and labelled.

Figure 6.9 shows a photograph of the entire set-up. This IRSS procedure achieves two things. Firstly, it greatly enhances knowledge of the locations of defects because defects

within a metre (on the same wind) can be individually resolved. Secondly, it prepares the fibre for subsequent time-of-flight analysis since the defect locations are now marked and visible.

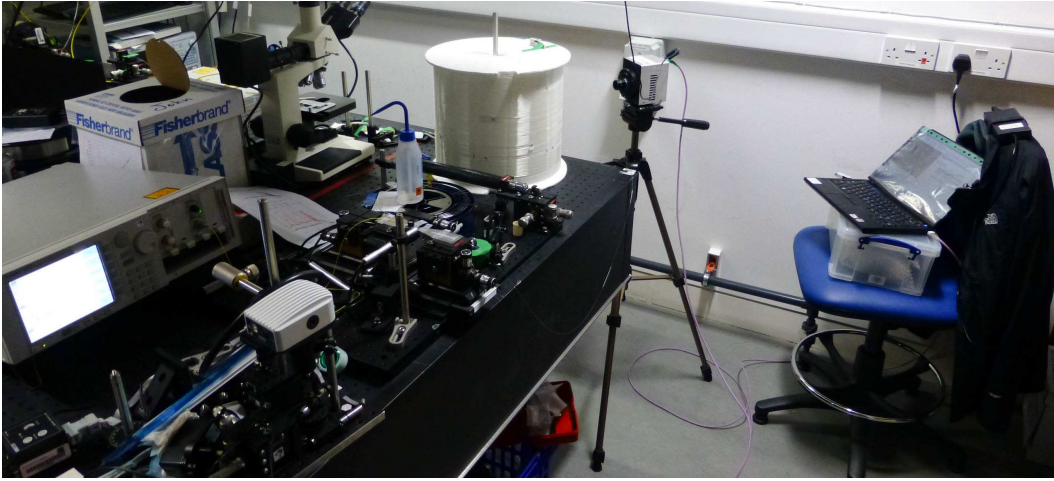


FIGURE 6.9: Laboratory equipment photograph showing the TLS, translation stages, FUT on the white bobbin, IR camera on the tripod, and computer.

### 6.2.3 Time-of-Flight

The time-of-flight (ToF) procedure follows the same set-up as in Figure 3.3. As with the mode-selective OTDR step, modes are dominantly excited in turn and in each case, the launch is done in both directions of the FUT, i.e. in both the  $\text{SoP} \rightarrow \text{EoP}$  and  $\text{EoP} \rightarrow \text{SoP}$  directions. This is to give added verification that defect features indeed correspond to their identified fibre locations. The temporal peak features in the ToF traces are correlated with the spatial features in the OTDR traces using the time-to-space relationship established in Section 6.1.4. For further verification that the ToF peaks belong to identified defects, light non-destructive mechanical force (finger tapping) is applied to the marked spots on the bobbin to introduce tactile perturbations. These perturbations can be seen in motion as the corresponding ToF peaks grow and shrink in real-time on the oscilloscope display.

Combining the ToF information with that from OTDR and IRSS, not only can the fibre defects be located, but the mode coupling behaviour at the defects can also be analysed. This is explained in more detail in the following section, which describes an example of using this defect inspection process on a HC-PBGF to locate its longitudinal defects as well as to study the induced mode coupling.

### 6.3 Inspection of Defects in HC-PBGFs

The method outlined in Section 6.2 was used to inspect some HC-PBGFs that were known to have longitudinal defects. These fibres were identified based on defect features observed in prior OTDR tests that are part of standard post-fabrication protocol.<sup>3</sup> This section describes the results of measurements on an  $\ell = 281$  m-long 19-cell (19c) HC-PBGF known to have several defects. Figure 6.10 shows an SEM image of the fibre's cross-section. The following study assumes a 2-mode  $\{LP_{01}, LP_{11}\}$  guidance scenario, based on the fact that HOMs are much lossier and therefore undetectable within the dynamic range of our ToF apparatus.

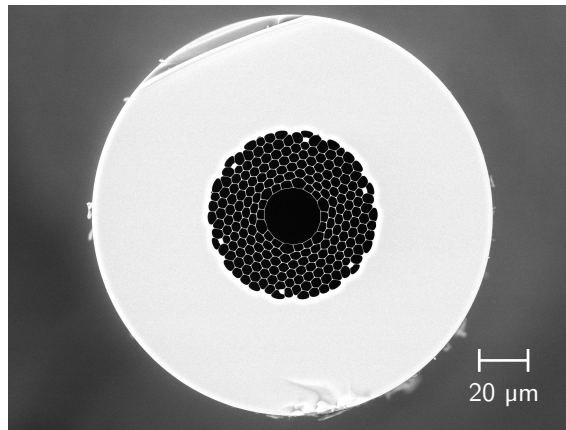


FIGURE 6.10: SEM cross-section of the 19c HC-PBGF used in defect analysis. *Courtesy of S.R. Sandoghchi [135].*

Mode-selective OTDR was first performed to obtain a general sensing of the mode-dependent effects at the major defects in the FUT. Figure 6.11 shows the OTDR traces obtained after  $LP_{01}$  and  $LP_{11}$  selective launches, each over both fibre directions. The measurements taken in the SoP→EoP direction have been reversed (hence their upward rather than downward trend as seen from left to right) so that the spatial observation perspective matches the EoP→SoP case and the defect features can be aligned. Prominent features are observed along the fibre, four of such are labelled A, B, C, and D. Bidirectional measurements are necessary because some smaller defects, e.g. A, might be too far from the input end in one direction and thus not show up in that direction's trace since the backscattered power would be too low. The traces show that the relative reflection amplitudes of the peaks are different for each mode launch and therefore imply mode-dependence. For example, the biggest reflection defect peaks are D for an  $LP_{01}$  launch and B for  $LP_{11}$ , two defects that are distinct and spatially separated. This hints at the possibility that the type of defects at different locations are varied, and that different types affect different modes. As per the concerns raised in [172], the OTDR traces

<sup>3</sup>It should be noted that such defective HC-PBGFs are rare, and that our fibre fabrication facility is capable of repeatedly drawing mostly defect-free fibres as long as a few kilometres [108, 111].

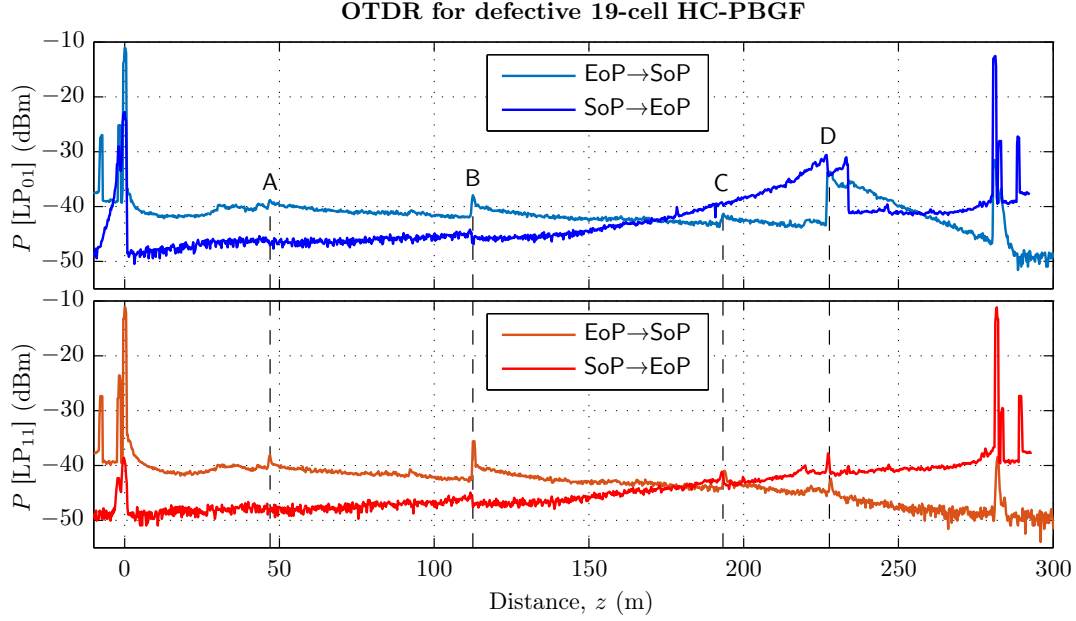


FIGURE 6.11: Mode-selective OTDR for an  $\ell = 281$  m 19c HC-PBGF with longitudinal defects, after selective  $LP_{01}$  (top) and  $LP_{11}$  (bottom) launches, taken over both fibre directions.  $SoP \rightarrow EoP$  traces are plotted in reverse to align with features in the  $EoP \rightarrow SoP$  direction. Prominent features are labelled; dashed black lines indicate their lengthwise positions.  $P$  = backscattered power.

do not provide a concrete way of measuring the mode-dependent loss, and are merely used for defect identification [136].

The measurements in Figure 6.11 were also used to correlate the defect locations with separate measurements on this fibre using the recently developed OSSR technique. The full details of the OSSR measurements can be found in [135].

The set-up in Figure 6.7 was used to illuminate, locate, and mark the IR bright spots at the defects.<sup>4</sup> Figure 6.12 shows the defect bright spots corresponding to each of the four labelled features. From the IR camera snapshots, it is evident that some defect features actually contain multiple closely spaced individual defects. For example, feature C comprises two defects that are within  $\sim 50$  cm from each other on the same wind. Such a separation is too small to be resolved in the OTDR measurements in Figure 6.11. Only OTDR features separated by at least 1 m or more can be distinguished from one another [134, 143]. This is the case for feature D in the (darker blue) OTDR trace for an  $LP_{01}$  launch (top plot) in the  $SoP \rightarrow EoP$  direction, which sports two main peaks separated by  $\sim 6$  m. The separation of the D bright spots in Figure 6.12, which are about 6 winds from each other (this FUT was wound on a bobbin with a circumference of  $\sim 1$  m), concurs with the OTDR results. This thus conveys the higher spatial resolution offered by IRSS as compared to OTDR.

<sup>4</sup>The IRSS measurement on this fibre was done primarily by Sandoghchi from the *ORC's* MOFG, with my assistance.

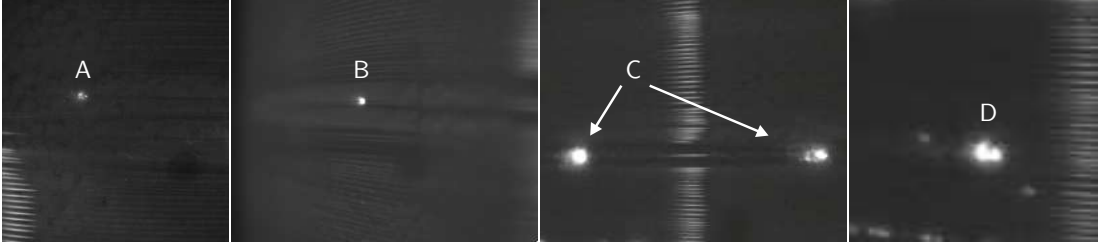


FIGURE 6.12: Snapshots of IR-illuminated bright spots at defects in the 19c HC-PBGF.

After the FUT defects were marked, ToF measurements were taken by selectively launching either  $LP_{01}$  or  $LP_{11}$ . Figure 6.13b depicts the measured ToF trace for an  $LP_{01}$  selective launch, with the  $LP_{01}$  main mode component at  $\Delta t_{01} = 0$  ns, and Figure 6.13c shows the ToF trace for an  $LP_{11}$  launch. Both launches were done in the EoP→SoP direction. The main  $LP_{11}$  mode group is composed of individual vector mode peaks which disperse due to the typical behaviour of HOMs in HC-PBGFs, as discussed in Section 4.1.2. Two  $LP_{11}$  peaks, labelled 1 and 2, are identified with relative delays of  $\Delta t_{11,1} = 2.6$  ns and  $\Delta t_{11,2} = 3.5$  ns, respectively. The large plateau within the  $LP_{11}$  mode group results from strong cross-coupling among its constituent vector modes. Although selective excitation of the much lossier HOMs beyond  $LP_{11}$ , e.g.  $LP_{21}$ , was attempted, no discernible ToF features were observed. For reference, Figure 6.13a replots the EoP→SoP OTDR traces from Figure 6.11, and they have been scaled to align with the ToF traces such that the time delay between  $\Delta t_{01}$  and  $\Delta t_{11,1}$  correspond to the total length of the fibre (black dashed lines). ToF features occurring between these delays are a result of defect-induced mode coupling because coupled mode components arising from defects have nett relative delays that are combinations of the main  $LP_{01}$  (faster) and  $LP_{11}$  (slower) mode delays. Defect features in Figure 6.13b are  $\mathcal{C}_{01 \rightarrow 11}$  events, whereas features in Figure 6.13c are  $\mathcal{C}_{11 \rightarrow 01}$  events. Furthermore, the vector mode spread in  $LP_{11}$  manifests such that the same defect produces multiple ToF peaks. For example, in Figure 6.13b, defect D (appearing as the largest  $LP_{01}$ -launch (blue trace) OTDR feature at  $z_D = 228$  m in Figure 6.13a) causes the  $\mathcal{C}_{01 \rightarrow 11}$  ToF feature group [D1; D2]. Their delays are calculated, using (6.4), as  $[\Delta t_{D1}; \Delta t_{D2}] = (1 - z_D/\ell) \times [\Delta t_{11,1}; \Delta t_{11,2}] \approx [0.5; 0.7]$  ns, which matches what is observed on the ToF trace. Similarly, the large OTDR defect B, at  $z_B = 113$  m in Figure 6.13a for  $LP_{11}$  launch (orange trace), produces the  $\mathcal{C}_{11 \rightarrow 01}$  ToF feature group [B1; B2] in Figure 6.13c, with  $[\Delta t_{B1}; \Delta t_{B2}] = (z_B/\ell) \times [\Delta t_{11,1}; \Delta t_{11,2}] \approx [1.0; 1.4]$  ns, using (6.3), again matching with the corresponding ToF trace. Note the difference between using  $(1 - z/\ell)$  as the scaling factor for the  $\mathcal{C}_{01 \rightarrow 11}$  calculation and  $(z/\ell)$  for  $\mathcal{C}_{11 \rightarrow 01}$ , as reasoned in Section 6.1.4. The delay spreads of each ToF feature group (e.g.  $|\Delta t_{D2} - \Delta t_{D1}|$  and  $|\Delta t_{B2} - \Delta t_{B1}|$ ) also scale correctly with these respective factors. Through manually applying light tactile perturbations at the defect marks on the FUT, B1 and B2 were both observed, on the oscilloscope, to grow and shrink in real-time simultaneously, thus confirming their origins from the same defect B. The same test was

performed to verify the grouping of D1 and D2 as coming from defect D. In the figure, peak B1, in the LP<sub>11</sub>-launch ToF trace (bottom), lines up with feature B in the OTDR traces (top), since the traces were aligned taking peak 1 of the LP<sub>11</sub> group as the reference for the full fibre length delay extent. Had the OTDR and ToF traces been aligned taking LP<sub>11</sub> peak 2 as the reference, then ToF defect peak B2 instead would line up with OTDR feature B.

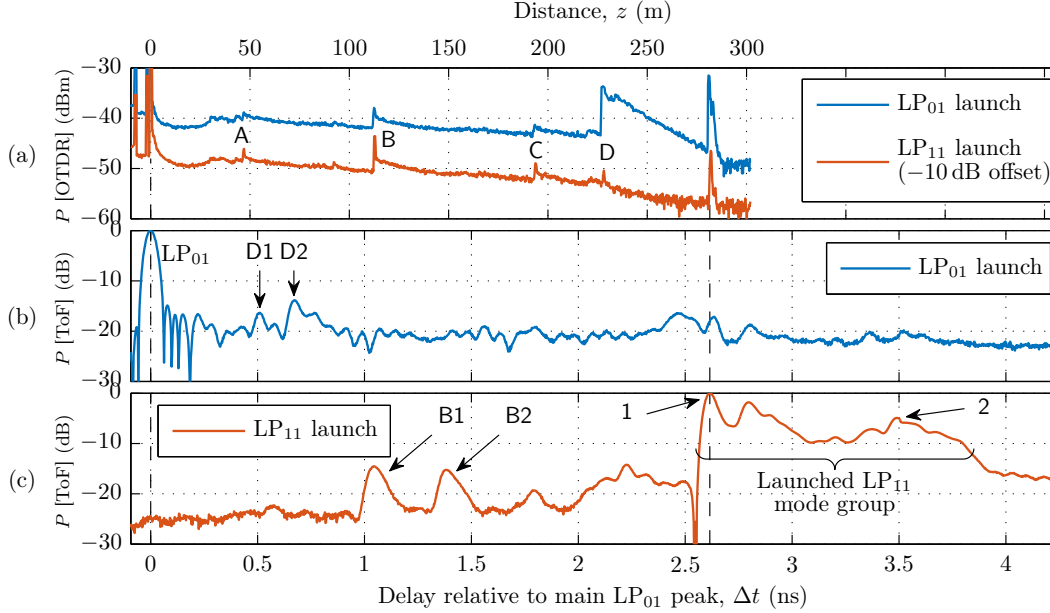


FIGURE 6.13: (a) OTDR and (b–c) ToF traces for selective LP<sub>01</sub> and LP<sub>11</sub> launches, in the EoP→SoP direction, in the  $\ell = 281$  m 19c HC-PBGF under test. The LP<sub>11</sub>-launch OTDR trace is offset  $-10$  dB downwards for clarity.  $P$  = power.

From these results, it is palpable that different defects produce ToF features for different mode launches and this thus implies some mode selectivity. For instance, defect D produces conspicuous  $\mathcal{C}_{01 \rightarrow 11}$  ToF features but no large  $\mathcal{C}_{11 \rightarrow 01}$  features. The converse is true for defect B. Certain defects, e.g. A, may not even produce significant coupling among modes under study. This notion is encouraging because it could mean that fibres, even with such defects, may not suffer from defect-induced mode coupling and could possibly still be data transmission-worthy for specific modes.

An observation of Figure 6.11 suggests that mode-selective OTDR is quite capable on its own to reveal defect features resulting from mode-dependent interactions, not to mention its higher dynamic range and spatial resolution compared to ToF. That being said, the modal information gained from ToF measurements is unique. For instance, defect features from OTDR traces primarily result from power from the same mode being backscattered. A slow decay—as opposed to a sharp impulse—after a backscattering event (e.g. defect D in the top plot of Figure 6.11) might (or might not) indicate some conversion to other modes, but it is difficult to be certain, much less to be able to identify the converted mode(s). On the other hand, defect features in ToF measurements are *all* caused by mode coupling events. Furthermore, the specific modes involved in these

conversions are identifiable due to the deliberate choice of mode-selective launching as well as the ability to correlate the temporal defect positions with known relative modal delays. This provides a level of additional information unobtainable purely from OTDR. It is emphasised again that this complementary usage of both OTDR and ToF (with IRSS) is what enables the collection of location *and* mode coupling information relating to longitudinal defects.

## 6.4 Conclusions and Future Work

In this chapter, it has been confirmed that longitudinal defects occurring in HC-PBGFs as well as multimode SCFs do cause discrete mode coupling. Based on this phenomenon, a procedure for inspecting longitudinal defects in multimode fibres has been outlined. I call this “Time-of-flight enabled defect inspection” (TEDI). Using a combination of ToF, IRSS and OTDR, defects in fibres, particularly HC-PBGFs, can be detected and information can be gained about the consequential mode coupling behavior. It was shown that there is a direct correlation between OTDR defect position and expected ToF feature delay. Applying the TEDI technique to a defective 19c HC-PBGF, it was discovered that certain defects can cause preferential mode coupling, whereas others may not induce any coupling that is detectable. Parts of this work have been published in [136].

There are of course limitations to using ToF. For example, the detectability of features is restricted by the dynamic range of the measurement equipment (detector and oscilloscope). The distinguishability of separate features depends on the input pulse width, the detector bandwidth, as well as how dispersive the FUT is. There is also a double-edged sword effect from using a long fibre to delay the modes enough to be temporally resolved, at the expense of not being able to detect the lossier HOMs after a long distance. Nevertheless, the ToF information does provide some level of understanding of defect-induced mode coupling that is not immediately discernible purely from OTDR.

Several directions are available for moving forward. Firstly, other tests can be performed to determine the cause of the mode selectivity in HC-PBGFs. At the time of writing, a plan was conceived to apply the X-ray computed tomography method in [133], using the facilities in the  *$\mu$ -VIS X-Ray Imaging Centre* at the *University of Southampton*, to image specific defects, e.g. B and D in the example of the previous section, and determine if there are any structural differences pertaining to defects and their possible impact on mode coupling and mode selectivity. However, unlike the centimetre-length samples scanned in [133], the hope is to scan a defective fibre without chopping out the defect regions. This will require a specialised rig to be designed so that the FUT can be mounted in its entirety and rotated during the scan process. If this materialises, it will provide

the capability to non-destructively and 3-dimensionally image the internal structure of HC-PBGFs and other fibres.

Secondly, the defect analysis using ToF principles can be extended beyond the 2-mode case. As more modes are considered, the trajectories of each propagating mode component can become complex and a concrete delay analysis framework needs to be formulated in order to be applied to make sense of the information provided in experimentally measured ToF traces.

Thirdly, and in the same spirit as the previous point, improvements can be explored for the ToF experimental set-up, in areas such as dynamic range and resolution. These could enhance the detection capabilities of the set-up and extend the coverage to more HOMs, as well as generally improve measurement accuracy.

## Chapter 7

# Conclusions

The work in this thesis has largely been in support of the (now ended) FP7 project MODE-GAP, which sought to address the impending internet capacity crunch by developing low-loss, low-latency HC-PBGFs and the relevant SDM technologies. It has also contributed, to a smaller extent, to another FP7 project called COSIGN, which explores advances in optical communications for data centre applications. These are summarised in Section 7.1 and proposed future work is discussed in Section 7.2. Some concluding remarks are then given in Section 7.3.

### 7.1 Summary of Main Chapters

This thesis has covered the characterisation of MMFs and HC-PBGFs in the telecommunications waveband, through a number of experiments using, chiefly, the time-of-flight (ToF) technique and other methods.

Chapter 3 introduced the ToF method as a tool for modal characterisation. It works by exploiting DMD to spread different mode components in time. The measurement procedure was detailed, followed by experimental proofs of concept using available 2-mode and 4-mode SIFs. With the help of experimental data, the processes of discrete and distributed mode coupling, as well as DMD, were explained. Additionally, I used the technique to characterise a novel 9-mode fibre from our MODE-GAP project collaborators. The tests, together with my mode-dependent OTDR measurements, revealed that the modes are clustered into five temporally spaced families, each of which exhibits low loss at  $\sim 0.2$  dB/km. This spurred the fabrication, by our collaborator, of a 22.8 km MMF supporting 30 spatial and polarisation modes, based on the same fibre design, which was demonstrated in a high spectral efficiency transmission experiment. The chapter concluded with a comparison between ToF and the complementary spectral characterisation method  $S^2$ , and discussed the benefits of each.

In Chapter 4, I applied the ToF method to characterise the modal content of recently produced 19c HC-PBGFs as well as the first ever fabricated 37c HC-PBGFs. The DGDs were measured and confirmed theoretical predictions of larger core sized PBGFs having lower DGDs. DGD measurements also showed chromatic dispersion to be present in both 19c and 37c cases, with the latter suffering less. Furthermore, the lack of crossings in the DGD curves corroborated earlier wide-bandwidth measurements. ToF tests also showed that distributed mode coupling does occur in these fibres and that vector effects manifest more strongly than in SCFs, due to the larger refractive index contrast between the core and cladding in PBGFs, as well as possible ellipticity-induced birefringence. Nevertheless, good mode extinction ratio measurements indicated the possibility for reliable single-mode data transmission. I conducted 10 Gbit/s NRZ OOK tests on the two 19c HC-PBGFs to compare them, and attempts to relate relative eye diagram performance suggested distributed mode coupling to have an effect. 40 Gbit/s NRZ OOK transmission was performed for the first time, by myself and group members, on one of the 37c PBGFs, which showed good single-mode performance. This prompted a subsequent MDM trial by our MODE-GAP collaborators, using MIMO DSP to undo the distributed coupling. A record 73.7 Tbit/s capacity was achieved. We also attempted MDM transmission using direct detection on the other 37c PBGF as ToF results showed little vector mode spreading. Unfortunately, the HOM peaks were not narrow enough and eye diagram results were subsequently poor, though this does not preclude a future direct detection attempt should a PBGF with even lower amounts of vector effects ever become available. Other of my single-mode transmission tests were mentioned, particularly one to check the transmission ability of another 19c PBGF that would be used as low-latency interconnects in data centre network experiments, under the collaboration with partners from the COSIGN project.

The chapter also described my use of ToF to diagnose unexpected poor transmission performance of a sectioned 11 km 19c HC-PBGF, the longest ever fabricated. The three sectioned bands were systematically tested and eventually, distributed mode coupling was observed to be present and was determined to be the culprit. The coupling was found to have come from mechanical issues pertaining to the spooling of the bands. Respooling efforts showed reduced mode coupling in subsequent ToF tests, and corresponding improvements in transmission trials. These bands were later used by MODE-GAP collaborators in a record 74.8 km recirculating loop test that paved the way for entry of HC-PBGFs into longer-reach metropolitan network communications. Finally, a short discussion on ToF measurements in the 2  $\mu$ m waveband was given.

To gain further understanding into the behaviour of mode propagation and coupling in optical fibres, a simulation model that I developed was outlined in Chapter 5, based on representing pulse propagation as a coupled power partial differential equation. The mathematical formulation was laid out and two solver schemes, ISM and SSFM, were described and compared, with SSFM being shown to have better convergence and

computational efficiency. The model was then used to simulate pulse propagation in various 2-mode and 4-mode configurations, and the physical parameters, such as the attenuation and coupling coefficients, were varied to study their effects on practical ToF measurements. This provided insight into the interpretation of ToF results. A method for determining coupling coefficients by fitting simulation curves onto ToF measurements was described, and I used a 4MSIF as an example. Finally, the model was used to support the *ORC's* PBGF fabrication work. Using a 19c HC-PBGF sample, the values of the coupling coefficients calculated from a recently developed coupling model were fed into the simulation and the resulting time-domain trace obtained matched with measured ToF data. This validated the coupling model, which predicts that reductions in loss should bring about simultaneous reductions in coupling coefficients, potentially to levels even lower than in SCFs. It also confirms that the coupled power framework is not only applicable to SCFs, but to HC-PBGFs as well, and promotes the utility of the mode propagation model and simulation as a tool to assist in fibre design.

Lastly, Chapter 6 detailed a method that I developed to use ToF to inspect longitudinal defects in fibres. This method relies on the (now verified) assumption that fibre defects cause discrete mode coupling. Again, the temporal spreading behaviour of propagating modes is exploited to resolve defect-induced ToF features. The behaviour of defect-induced discrete coupling was first studied and understood through simulations using the aforementioned propagation model. Experiments using a 2MSIF and 2MGRINF combination, concatenated via adjustable translation stages in a fibre splicer, validated the simulation predictions. The technique, which I call “ToF enabled defect inspection” (TEDI), uses ToF results, complemented by mode-dependent OTDR (the results of which contributed to a separate new defect analysis technique called OSSR) as well as the recently developed IRSS method, to detect and locate fibre defects and reveal any discrete mode coupling behaviour occurring there. I applied it for the first time to inspect a defective 19c HC-PBGF, demonstrating its applicability with hollow-core fibres. This provides a valuable tool to aid the fibre production process, as efforts are geared towards improving fibre uniformity.

My work in this thesis has contributed to technological advances reported in the [List of Publications](#), with significant contributions made in [27, 36, 93–95, 119, 135, 136, 138, 173].

## 7.2 Future Work

Several avenues for future work can be identified. Firstly, while the ToF set-up as it stands has proven considerably useful in fibre characterisation, it does have limitations, one of which is the dynamic range. The dynamic range of 30 dB offered by our oscilloscope’s photodetector may be insufficient in some cases to observe weak HOM content.

A recently published technique, that uses a vector network analyser set-up to measure impulse response, exhibits at least a 40 dB dynamic range and has prompted interest to explore its use for our own characterisation work.

Secondly, ToF and transmission test results hinted at the possibility for using direct detection in MDM experiments on HC-PBGFs that exhibit minimal vector mode spreading. Further work can be done to look for ways to reduce such spreading in PBGFs, and to design fibres that could potentially be used in this MDM regime.

Thirdly, the manual fitting method for quantifying coupling coefficients through the use of the mode propagation model, described in Chapter 5, can be made more robust. Moving forward from a series of pseudo-rules, it may be possible to develop a set of heuristics to formally describe the fitting procedure. Work can also be done to explore ways to objectively determine fitting quality, and to subsequently automate the fitting process once the heuristics have been defined.

Finally, the TEDI technique can be improved. Currently, the principle works for the 2-mode case, which is usually sufficient for fibres whose HOMs are very lossy. However, it may be possible to extend its applicability for cases with more than two modes, as well as many more defects. The discrete coupling behaviour becomes more complex once more modes and defects are considered, and a rigorous study based on simulations and experimental tests on known fibres is needed to understand what ToF results could be expected. Moreover, improvements in dynamic range as mentioned above will be helpful to increase the resolvability of defects against the noise floor, as will be improvements in temporal resolution.

### 7.3 Concluding Remarks

Progress has been made towards the grand endeavour to avoid the capacity crunch. The characterisation methods and tools described have been greatly useful for the work in this thesis, as well as the corresponding collaborative projects in which the *ORC* is involved. Particularly, it is hoped that the reader has developed an appreciation for the utility and diversity of the time-of-flight method, which is simple to implement, and is capable of revealing a wealth of information, perhaps some of which remain to be discovered and recognised.

## Appendix A

# Calculation of Focal Lengths For Free-Space Set-Up

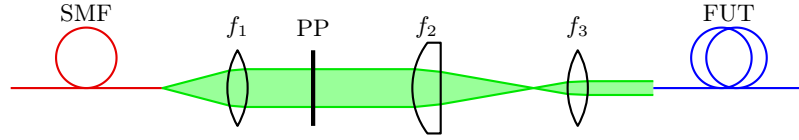


FIGURE A.1: Free-space lens setup used in ToF experiments.

Figure A.1 shows the free-space arrangement used in the ToF measurements, with exaggerated beam sizes. In order to use the phase plate (PP), the incident beam diameter must be on the order of 0.1 mm to 1 mm. For the beam that exits the SMF and is collimated by lens  $f_1$ , its beam radius is given by [174]

$$w_{\text{collimated}} \approx f_1 \cdot \frac{\lambda}{\pi w_{\text{SMF}}}, \quad (\text{A.1})$$

where  $\lambda = 1550 \text{ nm}$  is the wavelength of light and  $w_{\text{SMF}}$  is the beam radius (i.e. half the MFD) of the SMF used. Here, standard SMF-28 fibre was used, so  $w_{\text{SMF}} = 5.2 \mu\text{m}$  [175]. Using a focal length of  $f_1 = 4.5 \text{ mm}$  would produce a collimated beam with a waist radius of  $w_{\text{collimated}} = 0.43 \text{ mm}$  (i.e. a beam diameter of 0.86 mm), which is suitable for the PP. Similarly,  $f_1 = 3.1 \text{ mm}$  gives a beam diameter of  $2 \times 0.29 = 0.58 \text{ mm}$ , which is also suitable.<sup>1</sup> The choice then comes down to practicality. In practice, the collimation offered by these lenses is not perfect and there is a small but finite divergence associated with each. The divergence is inversely proportional to the focal length. Thus, choosing the larger focal length lens will be preferable.

---

<sup>1</sup>The rationale for consideration of these specific focal lengths is that these lenses are readily available in the laboratory.

As for the telecentric system formed by lenses  $f_2$  and  $f_3$ , the magnification factor is given by

$$\mathcal{M} = \frac{f_2}{f_3}. \quad (\text{A.2})$$

In order to achieve optimal coupling of the free-space beam into the FUT, the beam diameter must not exceed the FUT's MFD. The MFD of the 19c and 37c HC-PBGFs are  $16\text{ }\mu\text{m}$  [13] and  $\sim 22\text{ }\mu\text{m}$  [94]<sup>2</sup>, respectively. Comparing these numbers with the beam diameter of  $0.86\text{ mm}$ , a demagnification factor of about  $\mathcal{M}^{-1} = 40$  is needed. Using  $f_2 = 125\text{ mm}$  and  $f_3 = 3.1\text{ mm}$  achieves this.

In summary, the following values are chosen:

- 19c HC-PBGF:  $f_1 = f_3 = 3.1\text{ mm}$ ,  $f_2 = 125\text{ mm}$
- 37c HC-PBGF:  $f_1 = 4.5\text{ mm}$ ,  $f_2 = 125\text{ mm}$ ,  $f_3 = 3.1\text{ mm}$

---

<sup>2</sup>Although the actual MFD has not been measured, the authors in the reference estimate the MFD to be approximately 60% of the core diameter, which is  $37\text{ }\mu\text{m}$  in this case.

## Appendix B

# MATLAB Code For Pulse Propagation With Mode Coupling

### B.1 Main Program: **Coupling.m**

```
%% Coupling.m
% Model pulse propagation and mode power coupling in multimode fibres
%
% Copyright Nicholas Heng Loong WONG, 2017

clear all
close all
clc

%% Initialisations

global NM NT dt tau tau_ave L

% Define colours for plots
ColOrd = [0 0.4470 0.7410;... % LP01 blue
          0.8500 0.3250 0.0980;... % LP11 orange
          0.9290 0.6940 0.1250;... % LP31 yellow
          0.4940 0.1840 0.5560;... % LP02 purple
          0.4660 0.6740 0.1880;... % LP21 green
          0.6350 0.0780 0.1840;... % LP41 maroon
          0.5000 0.5000 0.5000;... % All grey
          0.8000 0.8000 0.8000... % Light grey
          1;
```

```

% Run script to set parameters for specific fibre
SetParameters_4MF;

c = physconst('LightSpeed');           % Speed of light; m/s
dt = t(2)-t(1);                         % Time-step; ps
NT = numel(t);                          % No. of time frames
Delta_tau_scale = t/L;                  % Calculate delay scale (used later); ps/m
tau01 = (10^12)*n01/c;                  % Absolute group delay per unit length
                                         % of LP01; ps/m
tau = Delta_tau+tau01;                  % Absolute modal delays; ps/m
tau_ave = mean(tau);                    % Average of absolute modal delays; ps/m

noiseFlr = -23.7;                       % Noise floor; dB
flrLim = -30;                           % Floor limit; dB

tPlotStep = 5;                          % Time skip-step for plotting
zPlotStep = 10;                         % Distance skip-step for plotting

%% Input pulse
A_pu = 1.0;                             % Input magnitude
Amp_pu = A_pu*exp(-t.^2/(tau_w^2));      % Input pulse amplitude
P_pu = Amp_pu.^2;                       % Input pulse power

P_pu = P_pu/trapz(t,P_pu); % Normalise so that total pulse power
                           % is 1 W

%% Propagation

tstart = tic;

% P is NZ-by-NT*NM
P_in = P_pu*P_disc(1:NМ).';

% The following code uses the ISM solver. Uncomment as necessary
% options = odeset('RelTol',1e-10);      % Set an error
% zSpan = [0:7.8125:L];                  % Distance span
% [z,P] = ode23(@powerCouplingISM,zSpan,P_in,options); % Call ode23
% NZ = numel(z);

```

```

% P = reshape(P,NZ,NT,NM);          % Reshape to NZ-by-Nt-by-NM

% The following code uses the SSFM solver. Uncomment as necessary
dz = 7.8125;                        % Distance-step; m
z = 0:dz:L;
NZ = numel(z);
P = powerCouplingSSFM(NZ,dz,P_in);   % Call SSFM solver

% Measure solver time taken
telapsed = toc(tstart)

%% Combining

P_ToF = sum(P,3);                   % Combine the traces

% Add noise floor
noise = (10^(noiseFlr/10))*max(P_ToF(end,:)).*...
        (ones(NZ,NT)+(0.5*10^-1).*randn([NZ,NT])));
P_ToF = P_ToF + noise;

P_ToF_norm = P_ToF./max(P_ToF(end,:)); % Normalise power
P_ToF_norm_dB = real(10*log10(P_ToF_norm)); % Calculate dB
P_ToF_norm_dB(P_ToF_norm_dB<flrLim) = flrLim; % Limit floor

%% Plots

% Plot combined power evolution (3-D)
figure3D = figure;
hSurf = surf(t(1:tPlotStep:NT)/(10^3),z(1:zPlotStep:numel(z)),...
            P_ToF_norm_dB(1:zPlotStep:numel(z),1:tPlotStep:NT),...
            'EdgeColor','none','MeshStyle','row');
alpha(0.55) % Set transparency
xlabel('Shifted delay, t (ns)')
ylabel('Distance, z (m)')
zlabel('Normalised power, P (dB)')
title('Power distribution evolution')
view(18,24); % Set view angle
axis([t(1)/(10^3) t(end)/(10^3) 0 L -25 5])

```

```

% Plot combined power evolution (2-D top)
figure2D = figure;
set(figure2D, 'units', 'centimeters');    % Needs to be before next line
Coord=get(figure2D, 'Position');
NewLength=Coord(3)*1;
NewHeight=Coord(4)*0.75;
set(figure2D, 'Position', [Coord(1), Coord(2), ... % Resize figure
    NewLength, NewHeight]);
hTop = surf(t/(10^3), z, P_ToF_norm_dB);
set(hTop, 'edgecolor', 'none')
view(0, 90);
cbar = colorbar;
set(get(cbar, 'ylabel'), 'string', 'Normalised power, P (dB)');
locate = get(cbar, 'ylabel');
cbarPos = get(locate, 'position');
cbarPos(1,1) = cbarPos(1,1)+1.00;
set(locate, 'pos', cbarPos);
xlabel('Shifted delay, t (ns)')
ylabel('Distance, z (m)')
title('Power distribution evolution')
axis([t(1)/(10^3) t(end)/(10^3) 0 L])

% Plot final ToF
figure
plot(Delta_tau_scale+offset, P_ToF_norm_dB(end, :));
xlabel('Relative delay (ps/m)')
ylabel('Normalised power (dB)')
title('Time-of-flight at Fibre End')

%% Total power evolution

figure1 = figure;
set(figure1, 'units', 'centimeters');    % Needs to be before next line
Coord=get(figure1, 'Position');
NewLength=Coord(3)*1;
NewHeight=Coord(4)*0.75;
set(figure1, 'Position', [Coord(1), Coord(2), ... % Resize figure
    NewLength, NewHeight]);

% Plot each mode's total power over distance

```

```
hold on
for mm = 1:NM
    plot(z,10*log10(sum(P(:,:,mm),2)./sum(sum(P(end,:,:),:))),...
        'color',ColOrd(mm,:), 'linewidth',1.0,...
        'DisplayName',char(modes(mm)));
end
grid on
xlabel('Distance, z (m)')
ylabel('Normalised Power, P (dB)')
title('Total mode power evolution, LP_{01} selective launch')
legend(gca,'show','location','northeast');
hold off

%% Clear memory of large variables
clear P_ToF P_ToF_norm
```

## B.2 Parameter Initialisations:

### SetParameter\_4MF.m

```

%% SetParameters_4MF.m
% Set parameters for 4MF

% Copyright Nicholas Heng Loong WONG, 2017

global C alpha_dB

NM = 4; % Total number of modes
modes = cellstr(['LP_{01} ' ;... % Array of mode names
                'LP_{11} ' ;...
                'LP_{02} ' ;...
                'LP_{21} ' ]);

L = 10000; % Length of fibre; m
tau_w = 150; % Temporal pulse width; ps

% Relative modal delays; ps/m
Delta_tau = [0; 1.878; 2.71; 3.608];

t = linspace(... % Temporal frame vector
    -mean(Delta_tau)*L*1.1,...
    (Delta_tau(end)-mean(Delta_tau))*L*1.1,...
    2^11).';

n01 = 1.447; % Group index of LP01

% Coupling matrix; m^-1
C = 1e-3*[0.0,0.05,0.002,0.0025;...
          0.05,0.0,0.0001,0.0005;...
          0.002,0.0001,0.0,0.0012;...
          0.0025,0.0005,0.0012,0.0];

% Coupling matrix scaling factor
CFac = 1;
C = C.*(eye(size(C))+CFac*(1-eye(size(C))));

% Loss vector

```

```
alpha_dB = [0.2; 0.2; 0.2; 0.2].*(10^-3);    % Loss (dB/m)

% Power matrix initial conditions; W
P_in = zeros(NM,NM);                        % Dimensions: time, mode
P_disc = [1.0; 0.01; 0.0027; 0.0008];        % Power scaling factors,
                                              % LP01 launch

t_lim = [-0.5 4];                           % Temporal limit at output

offset = 2.0435;                             % LP01 temporal offset
```

### B.3 Propagation Solver Function Using ISM:

#### **powerCouplingISM.m**

```

function [dP_dz] = powerCouplingISM(~,P_in)
%POWERCOUPLINGISM Coupled propagation.
% dP_dz = POWERCOUPLINGISM(~,P) solves the coupled mode power
% propagation equation, where P is an NM*NT-by-1-long array, where
% NM is the number of modes and NT is the number of time samples.
%
% dP_dz is the lengthwise propagation derivative of power in an
% optical fibre.
%
% POWERCOUPLINGISM defines the ODEFUN to be used with an ODE solver.
%
% See also ODE23.

% Copyright Nicholas Heng Loong WONG, 2017

global NM NT dt tau tau_ave C alpha_dB

alpha = alpha_dB/4.343;      % Loss (/km) (linear)
                             % Ref: page#55 eqn#2.5.3
                             % Agrawal, Fiber-optic Communications

P_rs = reshape(P_in,NT,NM); % Reshape into NT-by-NM

dP_dz = zeros(NT,NM);      % Pre-allocate memory

% Loop over time
for jj = 2:1:(NT-1)

    % Loop over all modes
    for mm = 1:1:NM

        % Ref: page#2
        % Yevick & Stoltz, 1983
        dP_dz(jj,mm) = - (tau(mm)-tau_ave)*(1/(2*dt))* ...
            (P_rs(jj+1,mm)-P_rs(jj-1,mm)) - ...
            alpha(mm)*P_rs(jj,mm) + ...
            sum(C(mm,1:NM).*(P_rs(jj,:)-P_rs(jj,mm)));
    end
end

```

```
        end
    end

    dP_dz = reshape(dP_dz,NT*NM,1);

    return
```

## B.4 Propagation Solver Function Using SSFM:

### **powerCouplingSSFM.m**

```

function [P] = powerCouplingSSFM(NZ,dz,P_in)
%POWERCOUPLINGSSFM Coupled propagation.
% [P] = POWERCOUPLINGSSFM(NZ,dz,P_in) solves the coupled mode power
% propagation equation, using the fast Fourier transform approximation
% method, where P_in is an NT-by-NM matrix of initial powers, where NM
% is the number of modes and NT is the number of time samples. NZ is
% number of length steps. dz is the length step size.
%
% This function avoids the use of the ODE23 or ODE45 functions in order
% to speed up processing time.
%
% See also POWERCOUPLINGISM.

% Copyright Nicholas Heng Loong WONG, 2017

global NM NT dt tau tau_ave C alpha_dB

alpha = alpha_dB/4.343;      % Loss (/km) (linear)
                             % Ref: page#55 eqn#2.5.3
                             % Agrawal, Fiber-optic Communications

domega = 2*pi/(NT*dt);
omega = ((-NT/2:NT/2-1)*domega).';

P = zeros(NZ,NT,NM);
P(1, :, :) = P_in;

% Form the zeroth-order differential's coefficient
Cmat = C - diag(C*ones(NM,1) + alpha);

% Loop over length
for ii = 2:1:NZ

    % Extract the NT-by-NM slice for this z step
    Pz = squeeze(P(ii-1, :, :));

    % Loss and coupling terms: Update each time slot for
    % P(z+dz) = P(z) + dz*P(z)*Cmat

```

```
Pz = Pz + dz*Pz*Cmat;

% DMD term (first-order differential)
Pz = fft(Pz);
Pz = exp(dz*fftshift(1i*omega)*(tau_ave-tau.')).*Pz;
Pz = ifft(Pz);
P(ii, :, :) = Pz;
end

P = real(P);

return
```



## Appendix C

# Derivation of Fourier Transform Representation of The Derivative

The **Fourier transform** of a time-domain function  $f(t)$  maps it to the frequency-domain as  $\hat{f}(\omega)$  and is defined as [14, 176]

$$\hat{f}(\omega) = \mathcal{F}\{f(t)\} := \int_{-\infty}^{\infty} f(t) e^{-j\omega t} dt, \quad (\text{C.1})$$

where  $\omega$  is the angular frequency,  $e = 2.71828\dots$  is Euler's number, and  $j = \sqrt{-1}$  is the imaginary unit. The **inverse Fourier transform**, which maps the function  $\hat{f}(\omega)$  to the time-domain, is defined as

$$f(t) = \mathcal{F}^{-1}\{\hat{f}(\omega)\} := \frac{1}{2\pi} \int_{-\infty}^{\infty} \hat{f}(\omega) e^{j\omega t} d\omega. \quad (\text{C.2})$$

Using this definition, the Fourier transform of the  $p$ th derivative of  $f(t)$  can be worked out as

$$\begin{aligned} \mathcal{F}\left\{\frac{d^p}{dt^p}(f(t))\right\} &= \mathcal{F}\left\{\frac{d^p}{dt^p}\left(\frac{1}{2\pi} \int_{-\infty}^{\infty} \hat{f}(\omega) e^{j\omega t} d\omega\right)\right\} \\ &= \mathcal{F}\left\{(j\omega)^p \left[\frac{1}{2\pi} \int_{-\infty}^{\infty} \hat{f}(\omega) e^{j\omega t} d\omega\right]\right\} \\ &= (j\omega)^p \mathcal{F}\left\{\left(\frac{1}{2\pi} \int_{-\infty}^{\infty} \hat{f}(\omega) e^{j\omega t} d\omega\right)\right\} \\ &= (j\omega)^p \mathcal{F}\{f(t)\}. \end{aligned} \quad (\text{C.3})$$

From this, the following relation [142] comes about

$$\frac{d^p}{dt^p}(f(t)) = \mathcal{F}^{-1}\{(j\omega)^p \mathcal{F}\{f(t)\}\}. \quad (\text{C.4})$$



## Appendix D

# Other Collaborative Work

This chapter gives a brief overview of work done where I played supporting role. The work was done together with various researchers from the *ORC*. While the descriptions may not encompass the experiments in their entirety, they mostly cover the specific aspects where I was directly involved. Most of the following experiments involve the ToF technique and demonstrates its usefulness as a diverse enabling tool.

### D.1 Enabling Fibre Measurements Through ToF

In addition to the information it is able to give in the time-domain, the ToF technique is also useful as a tool for other experimental work. Most notably, its response provides a good qualitative real-time gauge when the suppression of HOMs is required, or when ERs need to be assessed for possible single-mode-transmission. Indeed, the ToF methodology has been used in larger MODE-GAP project activities over the past few years, e.g. characterisation of photonic lanterns and MDM in HC-PBGFs at *Coriant* (previously *NSN*). The following sections describe some of our work where ToF played an important role in several MODE-GAP research efforts.

#### D.1.1 Accurate Mode-Dependent Loss Measurements on HC-PBGFs

See [93]. Collaboration with Y. Jung and N.K. Baddela. Contribution: I built the ToF set-up and helped with mode launch optimisation.

Cutback measurements are performed to measure the amount of loss in HC-PBGFs. In order to characterise MDL, we need to selectively excite individual LP modes in the fibres. We use the phase plate method in the free-space optical set-up as in Figure 3.3, utilising the ToF method to selectively launch each mode at  $\lambda = 1550$  nm. Once the optics are aligned for a particular mode, cutback measurements are taken. This was

performed on fibre **37c1** to measure the MDL of  $LP_{01}$  and  $LP_{11}$ , which are shown in Figure D.1.<sup>1</sup> Also superimposed is the loss spectrum for an unoptimised launch (i.e. no selective excitation) that was priorly measured. While the specific shape and features of the loss curves are outside the scope of this discussion, we focus on the general loss levels. From the graph (within the low-loss region and also particularly at  $\lambda = 1550$  nm), we see not only that the loss is dependent on which mode is excited, but also that the loss measurements for optimised mode launch and unoptimised cases produce considerably different results, on the order of a few dBs/km. Whereas unoptimised launch measurements give only general loss information, mode-dependent loss characterisation provides losses for individual modes. This highlights the need for MDL characterisation in HC-PBGFs if they are to be used for data communications, in both the single-mode and MDM regimes, and emphasises the usefulness of the ToF method in fulfilling this need.

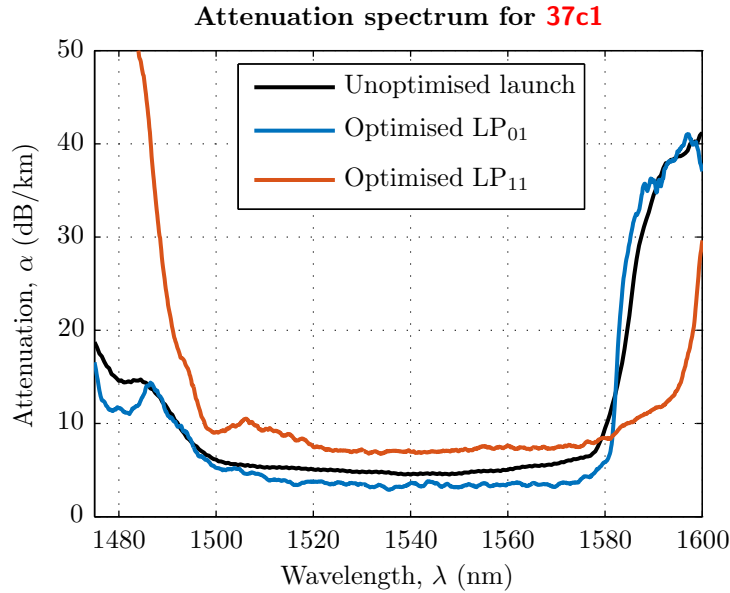


FIGURE D.1: Unoptimised and optimised mode loss measurements for **37c1**. *Actual cutback and loss calculations performed by Y. Jung and N.K.. Baddela; used with permission.*

### D.1.2 Low Crosstalk Splicing of HC-PBGF with SMF

Contribution: Collaboration with J.P. Wooler. I assembled the ToF set-up and assisted with mode launch optimisation.

The splicing of HC-PBGF to SMF is a key but non-trivial aspect of single-mode communication over PBGF [131]. Ideal splices ought not to excite any HOMs at the splice interface, so that low-crosstalk communication can be permitted. ToF measurements can be used to check for HOM content propagating in the fibre due to discrete scattering

<sup>1</sup>Note, the loss values at 1550 nm on the blue and orange curves in Figure D.1 are the measurements of 3.3 dB/km and 7.4 dB/km for  $LP_{01}$  and  $LP_{11}$ , respectively, in Table 4.1.

induced mode coupling at the splice. We performed a ToF test<sup>2</sup> at 1550 nm on a 19c HC-PBGF<sup>3</sup> spliced with SMF at the input and checked for HOMs. As shown in Figure D.2, most of the optical energy resides in the fundamental mode, centred at  $\Delta\tau = 0$  ps/m. There is distinct discrete scattering to a HOM at  $\sim 8.3$  ps/m (this DGD corresponds to that of  $LP_{11}$  in typical 19c PBGFs). The ER of  $\sim 16.05$  dB between this peak and the peak power of  $LP_{01}$  is indicative that a HOM has been discretely excited at the splice interface, though this level could still allow low crosstalk transmission.

This demonstrates the diagnostic ability of ToF to assess splice quality.

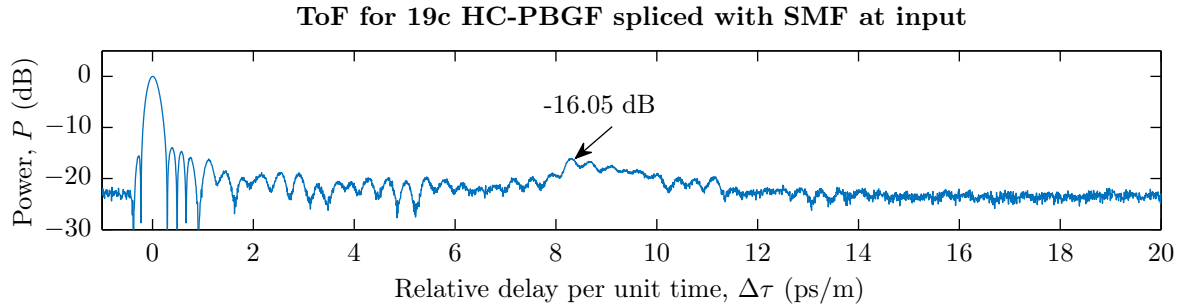


FIGURE D.2: ToF measurement showing low crosstalk in a 19c HC-PBGF spliced at the input with SMF.

## D.2 Enabling Amplifier Development Through ToF – Cladding Pumped Few-Moded EDFA

See [49, 177]. Collaboration with E.E. Lim and Y. Jung. Contribution: I helped to build the mode multiplexer and used ToF to optimise the optical alignment.

A cladding pumped 4-mode group EDFA was built and demonstrated for the first time. A major component of the experimental set-up is the mode multiplexer. This was assembled using free-space optics, where four input beams from individual tunable lasers were multiplexed via a combination of beam splitters. Each beam was optimised to carry one of the  $\{LP_{01}, LP_{11}, LP_{02}, LP_{21}\}$  modes supported by the 4-moded fibre used as the passive element. This was achieved with the phase plate method described in Section 3.2. ToF measurements were taken at 1550 nm (on a  $\sim 1550$  m spool of the same fibre) to optimise the extinction ratios in real-time. CCD camera images of the mode profiles were taken to complement the measurements. We achieved  $\sim 10$  dB of extinction for all four modes simultaneously. Overall, the amplifier modal gain was measured to be  $> 20$  dB over the 1540 nm to 1570 nm range and the differential modal gain was  $\sim 4$  dB.

<sup>2</sup>Note, there was no free-space launching arrangement in this case as the FUT was connectorised, and the input SMF was connected directly to the EDFA.

<sup>3</sup>The sample is part of a 19c HC-PBGF that was fabricated in our cleanroom facility, and is being explored by *CERN* for fast data delivery in high energy particle physics experiments.

### D.3 Spatial Mode Switchable Erbium-doped Fibre Laser

See [178]. Collaboration with Y. Jung. Contribution: I assisted with the coupling lens selection.

We developed a 2-mode switchable and wavelength tunable erbium-doped fibre laser using a spatial light modulator (SLM) as the mode switching component. Within the laser cavity, there are two important collimating/coupling lenses; one to couple light from one end of the 2-mode fibre to the SLM (and back),  $f_1$ , and the other to couple light from the other end of the 2-mode fibre to a 100% reflective silver mirror (and back). The lens choices are made according to the best focal length necessary to ensure a high mode extinction ratio. For lens  $f_2$ , we tested various commercially available focal lengths by imaging the output beam with a CCD camera and assessing the mode profile. We found that  $f_2 = 4.5$  mm produced the best ER. With regards to  $f_1$ , there is the added requirement that the collimated beam size is large enough so that it covers a large area of the SLM. This is needed to obtain a high resolution in the produced phase pattern since the SLM panel is digitally composed of finite-sized pixels. This would suggest that we use a lens with a large focal length and corresponding numerical aperture. However, we observed that the mode ERs begin to deteriorate as the focal length is increased beyond the optimum of 4.5 mm. Hence, a trade-off was made and we selected  $f_1 = 13.8$  mm, which afforded a high resolution phase pattern while maintaining a decent ER. In this setup,  $> 10$  dB ER was achieved.

# List of Publications

## Thesis-Related Publications

The following publications include work and results described in this thesis.

### Journal Articles

1. Y. Yan, G.M. Saridis, Y. Shu, B.R. Rofoee, S. Yan, M. Arslan, T. Bradley, N.V. Wheeler, **N.H.L. Wong**, F. Poletti, M.N. Petrovich, D.J. Richardson, S. Poole, G. Zervas, and D. Simeonidou, “All-optical programmable disaggregated data centre network realized by FPGA-based switch and interface card,” *J. Lightw. Technol.*, **34**(8):1925–1932, Apr. 2016.
2. S.R. Sandoghchi, M.N. Petrovich, D.R. Gray, Y. Chen, N.V. Wheeler, T.D. Bradley, **N.H.L. Wong**, G.T. Jasion, J.R. Hayes, E. Numkam Fokoua, M.B. Alonso, S.M. Mousavi, D.J. Richardson, and F. Poletti, “Optical side scattering radiometry for high resolution, wide dynamic range longitudinal assessment of optical fibers,” *Opt. Express*, **23**(21):27960–27974, Oct. 2015.
3. Y. Jung, E.L. Lim, Q. Kang, T.C. May-Smith, **N.H.L. Wong**, R. Standish, F. Poletti, J.K. Sahu, S.U. Alam, and D.J. Richardson, “Cladding pumped few-mode EDFA for mode division multiplexed transmission,” *Opt. Express*, **22**(23):29008–29013, Nov. 2014.
4. V.A.J.M. Sleiffer, Y. Jung, N.K. Baddela, J. Surof, M. Kushnerov, V. Veljanovski, J.R. Hayes, N.V. Wheeler, E.R.N. Fokoua, J.P. Wooler, D.R. Gray, **N.H.L. Wong**, F.R. Parmigiani, S. Alam, M.N. Petrovich, F. Poletti, D.J. Richardson, and H. de Waardt, “High capacity mode-division multiplexed optical transmission in a novel 37-cell hollow-core photonic bandgap fiber,” *J. Lightw. Technol.*, **32**(4):854–863, Feb. 2014.

## Conference Papers

1. **N.H.L. Wong**, Y. Jung, S.U. Alam, P. Petropoulos, and D.J. Richardson, “**Numerical analysis of mode propagation and coupling in multimode fibers,**” in *Proc. Conf. Lasers Electro-Opt. Pacific Rim (CLEO-PR)/Opto-Electron. Commun. Conf. (OECC)/Photon. Global Conf. (PGC)*, Singapore, Aug. 2017. (*Accepted*).
2. E. Numkam Fokoua, **N. Wong**, D.J. Richardson, and F. Poletti, “**Analysis and comparison of intermodal coupling coefficient of standard and hollow core few moded fibres,**” in *Proc. 41st Eur. Conf. Opt. Commun. (ECOC)*, Valencia, Spain, Oct. 2015, paper 0664.
3. D.J. Richardson, Y. Chen, N.V. Wheeler, J.R. Hayes, T. Bradley, Z. Liu, S.R. Sandoghchi, G.T. Jasion, E. Numkam Fokoua, D.R. Gray, R. Slavík, Y. Jung, **N.H.L. Wong**, F. Poletti, and M.N. Petrovich, “**Photonic bandgap fibres for low-latency data transmission,**” in *Proc. 41st ECOC*, Valencia, Spain, Oct. 2015, paper 0890. (*Invited*).
4. M. Kuschnerov, V.A.J.M. Sleiffer, Y. Chen, E. de Man, Y. Chen, Z. Liu, S.R. Sandoghchi, G.T. Jasion, T. Bradley, E. Numkam Fokoua, J.R. Hayes, N.V. Wheeler, D.R. Gray, R. Slavík, Y. Jung, **N.H.L. Wong**, B.J. Mangan, F. Poletti, M.N. Petrovich, and D.J. Richardson, “**Data transmission through up to 74.8 km of hollow-core fiber with coherent and direct-detect transceivers,**” in *Proc. 41st ECOC*, Valencia, Spain, Sep. 2015, paper 0049.
5. G.M. Saridis, Y. Yan, Y. Shu, S. Yan, M. Arslan, T. Bradley, N.V. Wheeler, **N.H.L. Wong**, F. Poletti, M.N. Petrovich, D.J. Richardson, S. Poole, G. Zervas, and D. Simeonidou, “**EVROS: All-optical programmable disaggregated data centre interconnect utilizing hollow-core bandgap fibre,**” in *Proc. 41st ECOC*, Valencia, Spain, Oct. 2015, paper 0021.
6. **N.H.L. Wong**, S.R. Sandoghchi, Y. Jung, T. Bradley, N.V. Wheeler, N.K. Badela, J.R. Hayes, F. Poletti, M.N. Petrovich, S.U. Alam, P. Petropoulos, and D.J. Richardson, “**Inspection of defect-induced mode coupling in hollow-core photonic bandgap fibers using time-of-flight,**” in *Proc. Conf. Lasers Electro-Opt. (CLEO)*, San Jose, CA, USA, May 2015, paper STu1N.6.
7. R.V. Jensen, L. Grüner-Nielsen, **N.H.L. Wong**, Y. Sun, Y. Jung, and D.J. Richardson, “**Demonstration of a 9 LP-mode transmission fiber with low DMD and loss,**” in *Proc. Opt. Fiber Commun. Conf. Expo. (OFC)*, Los Angeles, CA, USA, Mar. 2015, paper W2A.34. (*Poster*).
8. Y. Jung, Z. Li, **N.H.L. Wong**, J.M.O. Daniel, J.K. Sahu, S.U. Alam, and D.J. Richardson, “**Spatial mode switchable, wavelength tunable erbium doped fiber laser**”

- incorporating a spatial light modulator,” in *Proc. OFC*, San Francisco, CA, USA, Mar. 2014, paper Tu3D.4.
9. E.L. Lim, Y. Jung, Q. Kang, T.M. Smith, **N.H.L. Wong**, R. Standish, F. Poletti, J.K. Sahu, and D.J. Richardson, “First demonstration of cladding pumped few-moded EDFA for mode division multiplexed transmission,” in *Proc. OFC*, San Francisco, CA, USA, Mar. 2014, paper M2J.2.
  10. N.K. Baddela, M.N. Petrovich, Y. Jung, J.R. Hayes, N.V. Wheeler, D.R. Gray, **N. Wong**, F. Parmigiani, E. Numkam, J.P. Wooller, F. Poletti, D.J. Richardson, “First demonstration of a low loss 37-cell hollow core photonic bandgap fiber and its use for data transmission,” in *Proc. CLEO*, San Jose, CA, USA, Jun. 2013, paper CTu2K.3.
  11. Y. Jung, V.A.J.M. Sleiffer, N.K. Baddela, M.N. Petrovich, J.R. Hayes, N.V. Wheeler, D.R. Gray, E.R. Numkam Fokoua, J.P. Wooller, **N.H.L. Wong**, F. Parmigiani, S.U. Alam, J. Surof, M. Kushnerov, V. Veljanovski, H. de Waardt, F. Poletti, and D.J. Richardson, “First demonstration of a broadband 37-cell hollow core photonic bandgap fiber and its application to high capacity mode division multiplexing,” in *Proc. OFC/Nat. Fiber Opt. Engineers Conf. (NFOEC)*, Anaheim, CA, USA, Mar. 2013, paper PDP5A.3. (*Postdeadline*).

## Posters

1. **N.H.L. Wong**, “Differential equations to prevent the internet capacity crunch,” in *TakeAIM*, Oxford, UK, Nov. 2016.
  - Won First Prize in *TakeAIM 2016* competition.
2. **N.H.L. Wong**, Y. Jung, S.R. Sandoghchi, T. Bradley, N.K. Baddela, N.V. Wheeler, J.R. Hayes, M.N. Petrovich, F. Poletti, S.U. Alam, P. Petropoulos, and D.J. Richardson, “Modal Characterization of Hollow-core Photonic Bandgap Fibers in the Time-domain,” in *Siegman Int. School Lasers*, Amberg, Germany, Aug. 2015.
  - First presented at *Siegman International School on Lasers* in Amberg, Germany, Aug. 2015. Won Honorable Mention in poster competition.
  - Subsequently presented at *The Future Photonics Hub Industry Day* in Southampton, UK, Sep. 2016. Won Second Prize in student poster competition.

## Other Publications

The following publications include both technical and non-technical work carried out during this PhD, but were not included in the main body of this thesis.

## Conference Papers

1. **N.H.L. Wong**, A.S.K. Tong, M.T. Posner, and A. Ravagli, “**Modular and extensible lesson on fiber optics for youths**,” in *Proc. SPIE, Edu. Training Opt. Photon. (ETOP)*, Hangzhou, China, May 2017. (*To be published*).
2. M.T. Posner, A. Jantzen, L.D. van Putten, A. Ravagli, A.L. Donko, N. Soper, **N.H.L. Wong**, and P.V. John, “**Cathedral outreach: student-led workshops for school curriculum enhancement in non-traditional environments**,” in *Proc. SPIE, ETOP*, Hangzhou, China, May 2017. (*To be published*).
3. **N.H.L. Wong**, M.T. Posner, V. Mittal, D.R. Gray, and P.V. John, “**Taking local optics outreach abroad for IYL 2015: administrative and logistical challenges and strategies**,” in *Proc. SPIE 9946, Opt. Edu. Outreach IV*, San Diego, CA, USA, Aug. 2016, paper 99460F.
4. M.T. Posner, P.V. John, **N.H.L. Wong**, V. Mittal, and M.M. Nunez-Velazquez, “**From school classes to UNESCO: IYL-enabled environments for tackling the STEM skills shortage through student-led outreach**,” in *Proc. SPIE 9946, Opt. Edu. Outreach IV*, San Diego, CA, USA, Aug. 2016, paper 994607.
5. M.T. Posner, P.V. John, D. Standen, N.V. Wheeler, L.D. van Putten, N. Soper, T.L. Parsonage, **N.H.L. Wong**, and G. Brambilla, “**Reflecting Photonics: Reaching new audiences through new partnerships – IYL 2015 and the Royal Horticultural Society Flower Show**,” in *Proc. SPIE 9946, Opt. Edu. Outreach IV*, San Diego, CA, USA, Aug. 2016, paper 994603.
6. **N.H.L. Wong**, M.T. Posner, and P.V. John, “**The Lightwave programme and roadshow: an overview and update**,” in *Proc. SPIE 9793, ETOP*, Bordeaux, France, Jun. 2015, paper 97932V.

## Poster

1. **N.H.L. Wong**, “**The University of Southampton Optics and Photonics Society**,” in *Opt. Soc. (OSA) Student Leadership Conf.*, San Jose, CA, USA, Oct. 2015.

### Magazine and Newsletter Articles

1. K. Buchwald, **N.H.L. Wong**, S. Kumar, and E.H. Chen, “Write the Future,” *Opt. Photon. News*, **27**(11):44–47, Nov. 2016.
  - Won Honorable Mention in the OSA Centennial (OSA100) “Write the Future Story Contest”.
2. **N. Wong**, “Photonics Society Members Attend IEEE Young Entrepreneurs Open Day 2016,” *Inst. Elect. Electron. Eng. (IEEE) Photon. Soc. Newslett.*, **30**(4):44, Aug. 2016.

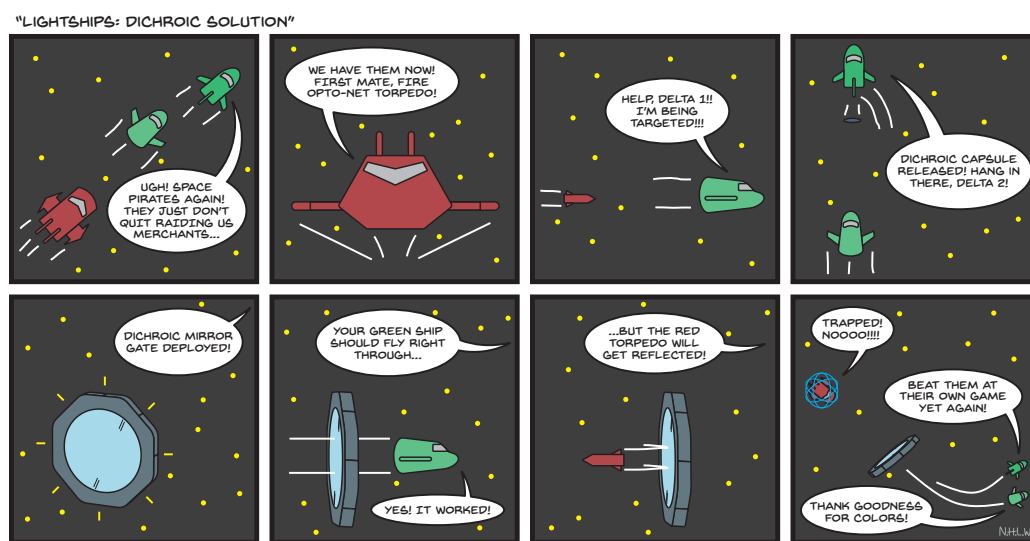


## Other Artistic Creations

The following lists works of art that I created during this PhD for various events. Many of them showcase elements of my work in this thesis.

1. **N.H.L. Wong**, “Lightships: Dichroic Solution,” May 2017.

This comic strip was created for the 2017 OSA Chapter/Section Poster Competition, with the objective of illustrating an optics and photonics phenomenon through a comic. The theme in this particular comic is dichroism and dichroic mirrors.



NICHOLAS H. L. WONG, UNIVERSITY OF SOUTHAMPTON OSA STUDENT CHAPTER, 2017

2. N. Wong, “My PhD in Emojis,” May 2017.

This is a representation of aspects of my PhD using emojis and was a result of the **Emoji Thesis** workshop, held during the *University of Southampton's Festival of Doctoral Research 2017*. This was also showcased at the festival's closing ceremony.

- Motivation: Global internet capacity is running out in conventional optical fibres. We need to investigate new fibres to avoid the “capacity crunch”.



- Thesis: Characterisation of Hollow-Core Photonic Bandgap Fibres and Other Multimode Fibres for Optical Communications



• Journey: 🧑🏻‍🔬 📖 🖥️ 🧪 📝 ⏳ 📄 😊 🎓 🌈

3. A. Tong and N. **Wong**, “Layer Cake Ring Laser & Hollow-Core Photonic Bandgap Roll,” in *Bake Your PhD Showcase*, Southampton, UK, Apr. 2017.

These two cakes, containing combinations of vanilla sponge cake, red velvet cake, pandan cake, and cream cheese, were creations by Amy Tong and myself for the [Bake Your PhD Showcase](#) of the *University of Southampton’s Festival of Doctoral Research 2017*.



4. Logo of the [University of Southampton Optics and Photonics Society](#) (OPSoc).

During my term in 2015 as president of OPSoc (a society that incorporates our university’s student chapters of OSA, SPIE, and the IEEE Photonics Society), I designed a new logo for the society. This was part of a larger effort to rebrand the society and to tie in with the festivities of the International Year of Light and Light-based Technologies (IYL 2015). The logo features various laboratory warning signs, a nod to the technical and experimental nature of our research work. The twin discharge arrows from the “High Voltage” warning ⚡ and the the magnet from the “Strong Magnetic Field” warning ⚠️ represent electricity and magnetism, respectively. These combine to produce light, which is represented by the beam from the “Laser” warning 🔦. The entire arrangement forms the shape of a lightbulb, signifying the disciplines of optics and photonics. Both a ‘central-word’ and a ‘side-word’ version were created.



5. **N.H.L. Wong** and S. Dawson, “A Luminous Quest,” in *Poetry and Science: The Litmus Project*, Southampton, UK, Mar. 2014. (Poster).

This is a poem written by Sophie Dawson, then a student in the *Department of English*, and myself capturing the use of MDM in HC-PBGFs to address the capacity crunch. It was produced as part of the *Poetry and Science: The Litmus Project* event, held during the *University of Southampton’s* Interdisciplinary Research Week in 2014.



# References

- [1] K.C. Kao and G.A. Hockham, “Dielectric-fibre surface waveguides for optical frequencies,” *Proc. Institution Elect. Engineers (IEE)*, **113**(7):1151–1158, Jul. 1966.
- [2] P.J. Winzer, “Modulation and multiplexing in optical communications,” in *Proc. CLEO/Conf. Quantum Electron. Laser Sci. (QELS)*, Baltimore, MD, USA, Jun. 2009, paper CTuL3.
- [3] C. Jeffcoat, J. Jackson, and J. Ewald, “Considerations in design and laying a new undersea fiber optic cable,” in *Proc. OCEANS ‘84 Conf. Expo.*, pp. 662–667, Washington, DC, USA, Sep. 1984.
- [4] P.J. Winzer, “Making spatial multiplexing a reality,” *Nat. Photon.*, **8**(5):345–348, May 2014.
- [5] S. Abbott, “Review of 20 years of undersea optical fiber transmission system development and deployment since TAT-8,” in *Proc. 34th ECOC*, Brussels, Belgium, Sep. 2008, paper Mo.4.E.1.
- [6] G.P. Agrawal. *Fiber-Optic Communication Systems*. Wiley, 3rd ed., 2002.
- [7] R.J. Mears, L. Reekie, I.M. Jauncey, and D.N. Payne, “Low-noise erbium-doped fibre amplifier operating at 1.54  $\mu\text{m}$ ,” *Electron. Lett.*, **23**(19):1026–1028, Sep. 1987.
- [8] F. Poletti, N.V. Wheeler, M.N. Petrovich, N. Baddela, E. Numkam Fokoua, J.R. Hayes, D.R. Gray, Z. Li, R. Slavík, and D.J. Richardson, “Towards high-capacity fibre-optic communications at the speed of light in vacuum,” *Nature Photon.*, **7**(4):279–284, Mar. 2013.
- [9] C.M. Smith, N. Venkataraman, M.T. Gallagher, D. Muller, J.A. West, N.F. Borrelli, D.C. Allan, and K.W. Koch, “Low-loss hollow-core silica/air photonic band-gap fibre,” *Nature*, **424**(6949):657–659, Aug. 2003.
- [10] P. Roberts, F. Couny, H. Sabert, B. Mangan, D. Williams, L. Farr, M. Mason, A. Tomlinson, T. Birks, J. Knight, and P.St.J. Russell, “Ultimate low loss of hollow-core photonic crystal fibres,” *Opt. Express*, **13**(1):236–244, Jan. 2005.

- [11] M.N. Petrovich, F. Poletti, A. van Brakel, and D.J. Richardson, “Robustly single mode hollow core photonic bandgap fiber,” *Opt. Express*, **16**(6):4337–4346, Mar. 2008.
- [12] F. Poletti, E.R. Numkam Fokoua, M.N. Petrovich, N.V. Wheeler, N.K. Baddela, J.R. Hayes, and D.J. Richardson, “Hollow core photonic bandgap fibers for telecommunications: Opportunities and potential issues,” in *Proc. OFC/NFOEC*, Los Angeles, CA, USA, Mar. 2012, paper OTh1H.3. (Invited).
- [13] N.V. Wheeler, M.N. Petrovich, R. Slavík, N. Baddela, E. Numkam, J.R. Hayes, D.R. Gray, F. Poletti, and D.R. Richardson, “Wide-bandwidth low-loss 19-cell hollow core photonic band gap fiber and its potential for low latency data transmission,” in *Proc. OFC/NFOEC*, Los Angeles, CA, USA, Mar. 2012, paper PDP5A.2. (Postdeadline).
- [14] B.E.A. Saleh and M.C. Teich. *Fundamentals of photonics*. Wiley, 2nd ed., 2007.
- [15] E.B. Desurvire, “Capacity demand and technology challenges for lightwave systems in the next two decades,” *J. Lightw. Technol.*, **24**(12):4697–4710, Dec. 2006.
- [16] D.J. Richardson, “Filling the light pipe,” *Sci.*, **330**(6002):327–328, Oct. 2010.
- [17] R.W. Tkach, “Scaling optical communications for the next decade and beyond,” *Bell Labs Tech. J.*, **14**(4):3–9, Feb. 2010.
- [18] “ICT Facts and Figures 2016,” report, International Telecommunication Union (ITU), Geneva, Switzerland, Jun. 2016.
- [19] C.E. Shannon, “A mathematical theory of communication,” *Bell Syst. Tech. J.*, **27**(3):379–423, Jul. 1948.
- [20] P.P. Mitra and J.B. Stark, “Nonlinear limits to the information capacity of optical fibre communications,” *Nature*, **411**(6841):1027–1030, Jun. 2001.
- [21] R. Essiambre, G. Kramer, P.J. Winzer, G.J. Foschini, and B. Goebel, “Capacity limits of optical fiber networks,” *J. Lightw. Technol.*, **28**(4):662–701, Feb. 2010.
- [22] E. Desurvire, C. Kazmierski, F. Lelarge, X. Marcadet, A. Scavennec, F.A. Kish, D.F. Welch, R. Nagarajan, C.H. Joyner, R.P. Schneider, S.W. Corzine, M. Kato, P.W. Evans, M. Ziari, A.G. Dentai, J.L. Pleumeekers, R. Muthiah, S. Bigo, M. Nakazawa, D.J. Richardson, F. Poletti, M.N. Petrovich, S.U. Alam, W.H. Loh, and D.N. Payne, “Science and technology challenges in XXIst century optical communications,” *Comptes Rendus Physique*, **12**(4):387–416, May 2011.
- [23] N.H.L. Wong, M.T. Posner, and P.V. John, “The lightwave programme and roadshow: an overview and update,” in *Proc. SPIE 9793, ETOP*, Bordeaux, France, Jun. 2015, paper 97932V.

- [24] M.T. Posner, P.V. John, D. Standen, N.V. Wheeler, L.D. van Putten, N. Soper, T.L. Parsonage, N.H.L. Wong, and G. Brambilla, “**Reflecting photonics: Reaching new audiences through new partnerships – IYL 2015 and the Royal Horticultural Society Flower Show,**” in *Proc. SPIE 9946, Opt. Edu. Outreach IV*, San Diego, CA, USA, Aug. 2016, paper 994603.
- [25] M.T. Posner, P.V. John, N.H.L. Wong, V. Mittal, and M.M. Nunez-Velazquez, “**From school classes to UNESCO: IYL-enabled environments for tackling the STEM skills shortage through student-led outreach,**” in *Proc. SPIE 9946, Opt. Edu. Outreach IV*, San Diego, CA, USA, Aug. 2016, paper 994607.
- [26] N.H.L. Wong, M.T. Posner, V. Mittal, D.R. Gray, and P.V. John, “**Taking local optics outreach abroad for IYL 2015: administrative and logistical challenges and strategies,**” in *Proc. SPIE 9946, Opt. Edu. Outreach IV*, San Diego, CA, USA, Aug. 2016, paper 99460F.
- [27] N.H.L. Wong, “**Differential equations to prevent the internet capacity crunch,**” in *TakeAIM*, Oxford, UK, Nov. 2016. (*Poster*).
- [28] P.J. Winzer, “**Spatial multiplexing in fiber optics: The 10X scaling of metro/core capacities,**” *Bell Labs Tech. J.*, **19**:22–30, Sep. 2014.
- [29] P.M. Hill, R. Olshansky, and W.K. Burns, “**Optical polarization division multiplexing at 4 Gb/s,**” *IEEE Photon. Technol. Lett.*, **4**(5):500–502, May 1992.
- [30] P. J. Winzer, “**Spatial multiplexing: The next frontier in network capacity scaling,**” in *Proc. 39th ECOC*, London, UK, Sep. 2013, paper We.1.D.1.
- [31] A. Lobato, F. Ferreira, M. Kushnerov, D. van den Borne, S.L. Jansen, A. Napoli, B. Spinnler, and B. Lankl, “**Impact of mode coupling on the mode-dependent loss tolerance in few-mode fiber transmission,**” *Opt. Express*, **20**(28):29776–29783, Dec. 2012.
- [32] K. Imamura, K. Mukasa, and T. Yagi, “**Effective space division multiplexing by multi-core fibers,**” in *Proc. 36th ECOC*, Torino, Italy, Sep. 2010, paper P1.09.
- [33] E. Numkam Fokoua, G.T. Jasion, Y. Chen, S.R. Sandoghchi, T.D. Bradley, D.R. Gray, N.V. Wheeler, J.R. Hayes, M.N. Petrovich, D.J. Richardson, and F. Poletti, “**Recent advances in hollow fiber technology for telecoms applications,**” in *Proc. IEEE Photon. Soc. Summer Topical Meeting Series (SUM)*, p. 186, Newport Beach, CA, USA, Jul. 2016, paper TuE4.2. (*Invited*).
- [34] V.A.J.M. Sleiffer, Y. Jung, P. Leoni, M. Kushnerov, N.V. Wheeler, N. Baddela, R.G.H. van Uden, C.M. Okonkwo, J.R. Hayes, J. Wooler, E.R. Numkam Fokoua, R. Slavík, F. Poletti, M.N. Petrovich, V. Veljanovski, S.U. Alam, D.J. Richardson, and H. de Waardt, “**30.7 Tb/s ( $96 \times 320$  Gb/s) DP-32QAM transmission over 19-cell**

- photonic band gap fiber,” in *Proc. OFC/NFOEC*, Anaheim, CA, USA, Mar. 2013, paper OW11.5.
- [35] K. Nagayama, M. Kakui, M. Matsui, T. Saitoh, and Y. Chigusa, “Ultra-low-loss (0.1484 dB/km) pure silica core fibre and extension of transmission distance,” *Electron. Lett.*, **38**(20):1168–1169, Sep. 2002.
- [36] E. Numkam Fokoua, N. Wong, D.J. Richardson, and F. Poletti, “Analysis and comparison of intermodal coupling coefficient of standard and hollow core few moded fibres,” in *Proc. 41st ECOC*, Valencia, Spain, Oct. 2015, paper 0664.
- [37] “First periodic report 1<sup>st</sup> October 2010 to 30<sup>th</sup> September 2011,” white paper, MODE-GAP, 2011.
- [38] E.R. Numkam Fokoua. *Ultralow loss and wide bandwidth hollow-core photonic bandgap fibres for telecom applications*. PhD thesis, University of Southampton, Oct. 2014.
- [39] H. Takara, A. Sano, T. Kobayashi, H. Kubota, H. Kawakami, A. Matsuura, Y. Miyamoto, Y. Abe, H. Ono, K. Shikama, Y. Goto, K. Tsujikawa, Y. Sasaki, I. Ishida, K. Takenaga, S. Matsuo, K. Saitoh, M. Koshihara, and T. Morioka, “1.01-Pb/s (12 SDM/222 WDM/456 Gb/s) crosstalk-managed transmission with 91.4-b/s/Hz aggregate spectral efficiency,” in *Proc. 38th ECOC*, Amsterdam, The Netherlands, Sep. 2012, paper Th.3.C. (*Postdeadline*).
- [40] D. Qian, E. Ip, M.-F. Huang, M.-J. Li, A. Dogariu, S. Zhang, Y. Shao, Y.-K. Huang, Y. Zhang, X. Cheng, Y. Tian, P. Ji, A. Collier, Y. Geng, J. Liñares, C. Montero, V. Moreno, X. Prieto, and T. Wang, “1.05 Pb/s transmission with 109 b/s/Hz spectral efficiency using hybrid single- and few-mode cores,” in *Proc. Frontiers Opt. 2012/Laser Sci. XXVIII*, Rochester, NY, USA, Oct. 2012, paper FW6C.3. (*Postdeadline*).
- [41] W. Rosenkranz and S. Schödlmann, “Optical MIMO-processing and mode-multiplexing: Experimental achievements and future perspectives,” in *Proc. 15th OECC*, pp. 44–45, Sapporo, Japan, Jul. 2010, paper 6B2-3. (*Invited*).
- [42] N. Hanzawa, K. Saitoh, T. Sakamoto, T. Matsui, S. Tomita, and M. Koshihara, “Demonstration of mode-division multiplexing transmission over 10 km two-mode fiber with mode coupler,” in *Proc. OFC/NFOEC*, Los Angeles, CA, USA, Mar. 2011, paper OWA4.
- [43] A. Al Amin, A. Li, X. Chen, and W. Shieh, “Spatial mode division multiplexing for overcoming capacity barrier of optical fibers,” in *Proc. 16th OECC*, pp. 415–416, Kaohsiung, Taiwan, Jul. 2011.

- [44] H.S. Chen, H.P.A. van den Boom, and A.M.J. Koonen, “30 Gbit/s  $3 \times 3$  optical mode group division multiplexing system with mode-selective spatial filtering,” in *Proc. OFC/NFOEC*, Los Angeles, CA, USA, Mar. 2011, paper OWB1.
- [45] R. Ryf, S. Randel, A.H. Gnauck, C. Bolle, A. Sierra, S. Mumtaz, M. Esmaeelpour, E.C. Burrows, R. Essiambre, P.J. Winzer, D.W. Peckham, A.H. McCurdy, and R. Lingle, “Mode-division multiplexing over 96 km of few-mode fiber using coherent  $6 \times 6$  mimo processing,” *J. Lightw. Technol.*, **30**(4):521–531, Feb. 2012.
- [46] Y. Jung, S. Alam, Z. Li, A. Dhar, D. Giles, I.P. Giles, J.K. Sahu, F. Poletti, L. Grüner-Nielsen, and D.J. Richardson, “First demonstration and detailed characterization of a multimode amplifier for space division multiplexed transmission systems,” *Opt. Express*, **19**(26):B952–B957, Dec. 2011.
- [47] Q. Kang, E.L. Lim, Y. Jung, F. Poletti, S. Alam, and D.J. Richardson, “Design of four-mode erbium doped fiber amplifier with low differential modal gain for modal division multiplexed transmissions,” in *Proc. OFC/NFOEC*, Anaheim, CA, USA, Mar. 2013, paper OTu3G.3.
- [48] Y. Jung, Q. Kang, J.K. Sahu, B. Corbett, R. Winfield, F. Poletti, S.U. Alam, and D.J. Richardson, “Few-mode EDFA supporting 5 spatial modes with reconfigurable differential modal gain control,” in *Proc. 39th ECOC*, London, UK, Sep. 2013, paper We.4.A.2.
- [49] E.L. Lim, Y. Jung, Q. Kang, T.C. May-Smith, N.H.L. Wong, R. Standish, F. Poletti, J.K. Sahu, S. Alam, and D.J. Richardson, “First demonstration of cladding pumped few-moded EDFA for mode division multiplexed transmission,” in *Proc. OFC*, San Francisco, CA, USA, Mar. 2014, paper M2J.2.
- [50] V.A.J.M. Sleiffer, Y. Jung, V. Veljanovski, R.G.H. van Uden, M. Kuschnerov, H. Chen, B. Inan, L. Grüner Nielsen, Y. Sun, D.J. Richardson, S.U. Alam, F. Poletti, J.K. Sahu, A. Dhar, A.M.J. Koonen, B. Corbett, R. Winfield, A.D. Ellis, and H. de Waardt, “73.7 Tb/s ( $96 \times 3 \times 256$ -Gb/s) mode-division-multiplexed DP-16QAM transmission with inline MM-EDFA,” *Opt. Express*, **20**(26):B428–B438, Dec. 2012.
- [51] S. Randel, R. Ryf, A. Sierra, P.J. Winzer, A.H. Gnauck, C.A. Bolle, R.-J. Essiambre, D.W. Peckham, A. McCurdy, and R. Lingle, “ $6 \times 56$ -Gb/s mode-division multiplexed transmission over 33-km few-mode fiber enabled by  $6 \times 6$  MIMO equalization,” *Opt. Express*, **19**(17):16697–16707, Aug. 2011.
- [52] J.M. Kahn, K.-P. Ho, and M.B. Shemirani, “Mode coupling effects in multi-mode fibers,” in *Proc. OFC*, Los Angeles, CA, USA, Mar. 2012, paper OW3D.3.
- [53] F. Zolla, G. Renversez, A. Nicolet, B. Kuhlmei, S. Guenneau, and D. Felbacq. *Foundations of photonic crystal fibres*. World Scientific, London, UK, 2005.

- [54] R.F. Cregan, B.J. Mangan, J.C. Knight, T.A. Birks, P.St.J. Russell, P.J. Roberts, and D.C. Allan, “Single-mode photonic band gap guidance of light in air,” *Sci.*, **285**(5433):1537–1539, Sep. 1999.
- [55] P.St.J. Russell, “Photonic band gaps,” *Physics World*, **5**(8):37–42, Aug. 1992.
- [56] M. Tur, “Optical fibers – basics,” in *Advanced Fiber Optics* (L. Thévenaz, ed.), pp. 1–27, Lausanne, Switzerland: EPFL Press, 2011.
- [57] Y.Z. Ma, Y. Sych, G. Onishchukov, S. Ramachandran, U. Peschel, B. Schmauss, and G. Leuchs, “Fiber-modes and fiber-anisotropy characterization using low-coherence interferometry,” *Appl. Physics B*, **96**(2–3):345–353, May 2009.
- [58] E. Hecht. *Optics*. Pearson, Essex, UK, 2014.
- [59] M.N.O. Sadiku. *Optical and wireless communications: Next generation networks*. CRC Press, Boca Raton, FL, USA, 2002.
- [60] D. Gloge, “Weakly guiding fibers,” *Appl. Opt.*, **10**(10):2252–2258, Oct. 1971.
- [61] E. Snitzer, “Cylindrical dielectric waveguide modes,” *J. Opt. Soc. Am.*, **51**(5):491–498, May 1961.
- [62] A.W. Snyder and W.R. Young, “Modes of optical waveguides,” *J. Opt. Soc. Am.*, **68**(3):297–309, Mar. 1978.
- [63] C.D. Poole, J.M. Wiesenfeld, D.J. DiGiovanni, and A.M. Vengsarkar, “Optical fiber-based dispersion compensation using higher order modes near cutoff,” *J. Lightw. Technol.*, **12**(10):1746–1758, Oct. 1994.
- [64] T.R. Woliński, “Polarization in optical fibers,” *ACTA PHYSICA POLONICA A*, **95**(5):749–760, May 1999.
- [65] T. Grosjean, A. Sabac, and D. Courjon, “A versatile and stable device allowing the efficient generation of beams with radial, azimuthal or hybrid polarizations,” *Opt. Commun.*, **252**(1–3):12–21, Aug. 2005.
- [66] S. Ramachandran, P. Kristensen, and M.F. Yan, “Generation and propagation of radially polarized beams in optical fibers,” *Opt. Lett.*, **34**(16):2525–2527, Aug. 2009.
- [67] K.Z. Aghaie, V. Dangui, M.J.F. Digonnet, S. Fan, and G.S. Kino, “Classification of the core modes of hollow-core photonic-bandgap fibers,” *IEEE J. Quantum Electron.*, **45**(9):1192–1200, Sep. 2009.
- [68] N. Bai, E. Ip, T. Wang, and G. Li, “Multimode fiber amplifier with tunable modal gain using a reconfigurable multimode pump,” *Opt. Express*, **19**(17):16601–16611, Aug. 2011.

- [69] N. Bai, E. Ip, Y.K. Huang, E. Mateo, F. Yaman, M.J. Li, S. Bickham, S. Ten, J. Liñares, C. Montero, V. Moreno, X. Prieto, V. Tse, K.M. Chung, A.P.T. Lau, H.Y. Tam, C. Lu, Y. Luo, G.D. Peng, G. Li, and T. Wang, “Mode-division multiplexed transmission with inline few-mode fiber amplifier,” *Opt. Express*, **20**(3): 2668–2680, Jan. 2012.
- [70] J. Han and J. Zhang, “Polarization-dependent principal modes of two degenerate LP<sub>11</sub> modes transmission in few-mode fibers,” *Opt. Lett.*, **37**(17):3546–3548, Sep. 2012.
- [71] J.W. Nicholson, A.D. Yablon, J.M. Fini, and M.D. Mermelstein, “Measuring the modal content of large-mode-area fibers,” *IEEE J. Sel. Topics Quantum Electron.*, **15**(1):61–70, Jan. 2009. (Invited).
- [72] S. Ramachandran, S. Ghalmi, J. Bromage, S. Chandrasekhar, and L.L. Buhl, “Evolution and systems impact of coherent distributed multipath interference,” *IEEE Photon. Technol. Lett.*, **17**(1):238–240, Jan. 2005.
- [73] J.W. Nicholson, A.D. Yablon, S. Ramachandran, and S. Ghalmi, “Spatially and spectrally resolved imaging of modal content in large-mode-area fibers,” *Opt. Express*, **16**(10):7233–7243, May 2008.
- [74] J.W. Nicholson, M. Mermelstein, and A.D. Yablon, “Characterizing discrete and distributed scattering of higher-order-modes in large-mode-area fibres,” in *Proc. 34th ECOC*, Brussels, Belgium, Sep. 2008, paper Mo.4.B.5.
- [75] D.R. Gray, Z. Li, F. Poletti, R. Slavík, N.V. Wheeler, N.K. Baddela, M.N. Petrovich, A. Obeysekara, and D.J. Richardson, “Complementary analysis of modal content and properties in a 19-cell hollow core photonic band gap fiber using time-of-flight and S<sup>2</sup> techniques,” in *Proc. 38th ECOC*, Amsterdam, The Netherlands, Sep. 2012, paper Mo.2.F.1.
- [76] R. Olshansky, “Mode coupling effects in graded-index optical fibers,” *Appl. Opt.*, **14**(4):935–945, Apr. 1975.
- [77] K. Balemarthy, A. Polley, and S.E. Ralph, “Electronic equalization of multikilometer 10-Gb/s multimode fiber links: Mode-coupling effects,” *J. Lightw. Technol.*, **24**(12):4885–4894, Dec. 2006.
- [78] D. Marcuse. *Theory of dielectric optical waveguides*. Academic Press, 1991.
- [79] Telecommunications Industry Association, *FOTP-220 Differential mode delay measurement of multimode fiber in the time domain*, **Standard TIA-455-220-A**, Jan. 2003.
- [80] T.-J. Ahn and D.Y. Kim, “High-resolution differential mode delay measurement for a multimode optical fiber using a modified optical frequency domain reflectometer,” *Opt. Express*, **13**(20):8256–8262, Oct. 2005.

- [81] J.Y. Lee and D.Y. Kim, “Determination of the differential mode delay of a multimode fiber using fourier-domain intermodal interference analysis,” *Opt. Express*, **14**(20):9016–9021, Oct. 2006.
- [82] J. Cheng, M.E.V. Pedersen, K. Wang, C. Xu, L. Grüner-Nielsen, and D. Jakobsen, “Time-domain multimode dispersion measurement in a higher-order-mode fiber,” *Opt. Lett.*, **37**(3):347–349, Feb. 2012.
- [83] D. Yevick and B. Stoltz, “Effect of mode coupling on the total pulse response of perturbed optical fibers,” *Appl. Opt.*, **22**(7):1010–1015, Apr. 1983.
- [84] J.D. Joannopoulos, S.G. Johnson, J.N. Winn, and R.D. Meade. *Photonic crystals: Molding the flow of light*. Princeton University Press, Princeton, NJ, USA, 2nd ed., 2008.
- [85] P.St.J. Russell, T.A. Birks, and F.D. Lloyd-Lucas, “Photonic bloch waves and photonic band gaps,” in *Confined Electrons and Photons: New Physics and Applications* (E. Burstein and C. Weisbuch, eds.), pp. 585–633, Boston, MA, USA: Springer, 1995.
- [86] F. Poletti, M.N. Petrovich, and D.J. Richardson, “Hollow-core photonic bandgap fibers: technology and applications,” *Nanophoton.*, **2**(5-6):315–340, Nov. 2013. (*Invited*).
- [87] T.A. Birks, P.J. Roberts, P.St.J. Russell, D.M. Atkin, and T.J. Shepherd, “Full 2-D photonic bandgaps in silica/air structures,” *Electron. Lett.*, **31**:1941–1943, Oct. 1995.
- [88] M.J.F. Digonnet, H.K. Kim, G.S. Kino, and S. Fan, “Understanding air-core photonic-bandgap fibers: analogy to conventional fibers,” *J. Lightw. Technol.*, **23**(12):4169–4177, Dec. 2005.
- [89] J.A. Buck. *Fundamentals of optical fibers*. Wiley, Hoboken, NJ, USA, 2004.
- [90] T.A. Birks, D.M. Bird, T.D. Hedley, J.M. Pottage, and P.St.J. Russell, “Scaling laws and vector effects in bandgap-guiding fibres,” *Opt. Express*, **12**(1):69–74, Jan. 2004.
- [91] P.St.J. Russell, “Photonic-crystal fibers,” *J. Lightw. Technol.*, **24**(12):4729–4749, Dec. 2006.
- [92] E. Numkam Fokoua, M.N. Petrovich, N.K. Baddela, N.V. Wheeler, J.R. Hayes, F. Poletti, and D.J. Richardson, “Real-time prediction of structural and optical properties of hollow-core photonic bandgap fibers during fabrication,” *Opt. Lett.*, **38**(9):1382–1384, May 2013.

- [93] Y. Jung, V.A.J.M. Sleiffer, N.K. Baddela, M.N. Petrovich, J.R. Hayes, N.V. Wheeler, D.R. Gray, E.R. Numkam Fokoua, J.P. Wooler, N.H.L. Wong, F. Parmigiani, S.U. Alam, J. Surof, M. Kushnerov, V. Veljanovski, H. de Waardt, F. Poletti, and D.J. Richardson, “First demonstration of a broadband 37-cell hollow core photonic bandgap fiber and its application to high capacity mode division multiplexing,” in *Proc. OFC/NFOEC*, Anaheim, CA, USA, Mar. 2013, paper PDP5A.3. (Postdeadline).
- [94] N.K. Baddela, M.N. Petrovich, Y. Jung, J.R. Hayes, N.V. Wheeler, D.R. Gray, N. Wong, F. Parmigiani, E. Numkam, J.P. Wooler, F. Poletti, and D.J. Richardson, “First demonstration of a low loss 37-cell hollow core photonic bandgap fiber and its use for data transmission,” in *Proc. CLEO*, San Jose, CA, USA, Jun. 2013, paper CTu2K.3.
- [95] V.A.J.M. Sleiffer, Y. Jung, N.K. Baddela, J. Surof, M. Kushnerov, V. Veljanovski, J.R. Hayes, N.V. Wheeler, E.R.N. Fokoua, J.P. Wooler, D.R. Gray, N.H.L. Wong, F.R. Parmigiani, S. Alam, M.N. Petrovich, F. Poletti, D.J. Richardson, and H. de Waardt, “High capacity mode-division multiplexed optical transmission in a novel 37-cell hollow-core photonic bandgap fiber,” *J. Lightw. Technol.*, **32**(4): 854–863, Feb. 2014.
- [96] M.N. Petrovich, N.V. Wheeler, N.K. Baddela, F. Poletti, E. Numkam Fokoua, J.R. Hayes, D.R. Gray, and D.J. Richardson, “Development of low loss, wide bandwidth hollow core photonic bandgap fibres for telecom applications,” in *Proc. 14th International Conference on Transparent Optical Networks (ICTON)*, Coventry, UK, Jul. 2012, paper We.B6.3. (Invited).
- [97] J. Xu and C. Peucheret, “Two-mode multiplexing at  $2 \times 10.7$  Gbps over 7-cell hollow-core photonic band gap fiber,” in *Proc. 37th ECOC*, Geneva, Switzerland, Sep. 2011, paper We.10.P1.66. (Poster).
- [98] J. Carpenter, J. Xu, C. Peucheret, and T. Wilkinson, “Mode multiplexing at  $2 \times 20$  Gbps over 19-cell hollow-core photonic band gap fibre,” in *Proc. OFC/NFOEC*, Los Angeles, CA, USA, Mar. 2012, paper JW2A.41. (Poster).
- [99] R. Slavík, M.N. Petrovich, N.V. Wheeler, J.R. Hayes, N.K. Baddela, D.R. Gray, F. Poletti, and D.J. Richardson, “1.45 Tbit/s, low latency data transmission through a 19-cell hollow core photonic band gap fibre,” in *Proc. 38th ECOC*, Amsterdam, The Netherlands, Sep. 2012, paper Mo.2.F.2.
- [100] H. Chen, R.G.H. van Uden, C.M. Okonkwo, Y. Jung, N.V. Wheeler, E.N. Fokoua, N. Baddela, M.N. Petrovich, F. Poletti, D.J. Richardson, Raz O., H. de Waardt, and A.M.J. Koonen, “Mode division multiplexing over 19-cell hollow-core photonic bandgap fibre by employing integrated mode multiplexer,” *Electron. Lett.*, **50**:1227–1229, Aug. 2014.

- [101] L. Olanterä, C. Sigaud, J. Troska, F. Vasey, M.N. Petrovich, F. Poletti, N.V. Wheeler, J.P. Wooley, and D.J. Richardson, “**Gamma irradiation of minimal latency hollow-core photonic bandgap fibres,**” *J. Instrum.*, **8**(12):C12010, Dec. 2013.
- [102] G.M. Saridis, Y. Yan, Y. Shu, S. Yan, M. Arslan, T. Bradley, N.V. Wheeler, N.H.L. Wong, F. Poletti, M.N. Petrovich, D.J. Richardson, S. Poole, G. Zervas, and D. Simeonidou, “**EVROS: All-optical programmable disaggregated data centre interconnect utilizing hollow-core bandgap fibre,**” in *Proc. 41st ECOC*, Valencia, Spain, Oct. 2015, paper 0021.
- [103] Y. Yan, G.M. Saridis, Y. Shu, B.R. Rofoee, S. Yan, M. Arslan, T. Bradley, N.V. Wheeler, N.H.L. Wong, F. Poletti, M.N. Petrovich, D.J. Richardson, S. Poole, G. Zervas, and D. Simeonidou, “**All-optical programmable disaggregated data centre network realized by FPGA-based switch and interface card,**” *J. Lightw. Technol.*, **34**(8):1925–1932, Apr. 2016.
- [104] M.N. Petrovich, F. Poletti, J.P. Wooley, A.M. Heidt, N.K. Baddela, Z. Li, D.R. Gray, R. Slavík, F. Parmigiani, N.V. Wheeler, J.R. Hayes, E. Numkam Fokoua, L. Grüner-Nielsen, B. Pálsdóttir, R. Phelan, B. Kelly, M. Becker, N. MacSuihbne, J. Zhao, F.C. Garcia Gunning, A.D. Ellis, P. Petropoulos, S.U. Alam, and D.J. Richardson, “**First demonstration of 2 $\mu$ m data transmission in a low-loss hollow core photonic bandgap fiber,**” in *Proc. 38th ECOC*, Amsterdam, The Netherlands, Sep. 2012, paper Th.3.A.5. (*Postdeadline*).
- [105] N. Mac Suihbne, Z. Li, B. Baeuerle, J. Zhao, J.P. Wooley, S.U. Alam, F. Poletti, M.N. Petrovich, A.M. Heidt, N.V. Wheeler, N.K. Baddela, E.R. Numkam Fokoua, I.P. Giles, D.J. Giles, R. Phelan, J. O’Carroll, B. Kelly, D. Murphy, B. Corbett, A.D. Ellis, D.J. Richardson, and F.C. Garcia Gunning, “**WDM transmission at 2 $\mu$ m over low-loss hollow core photonic bandgap fiber,**” in *Proc. OFC/NFOEC*, Anaheim, CA, USA, Mar. 2013, paper OW1I.6.
- [106] Z. Li, A.M. Heidt, J.M.O. Daniel, Y. Jung, S.U. Alam, and D.J. Richardson, “**Thulium-doped fiber amplifier for optical communications at 2  $\mu$ m,**” *Opt. Express*, **21**(8):9289–9297, Apr. 2013.
- [107] Y. Chen, N.V. Wheeler, N.K. Baddela, J.R. Hayes, S.R. Sandoghchi, E. Numkam Fokoua, M. Li, F. Poletti, M.N. Petrovich, and D.J. Richardson, “**Understanding wavelength scaling in 19-cell core hollow-core photonic bandgap fibers,**” in *Proc. OFC*, San Francisco, CA, USA, Mar. 2014, paper M2F.4.
- [108] Y. Chen, Z. Liu, S.R. Sandoghchi, G. Jasion, T.D. Bradley, E. Numkam, J.R. Hayes, N.V. Wheeler, D.R. Gray, B.J. Mangan, R. Slavík, F. Poletti, M.N. Petrovich, and D.J. Richardson, “**Demonstration of an 11km hollow core photonic bandgap fiber for broadband low-latency data transmission,**” in *Proc. OFC Post Deadline Papers*, Los Angeles, CA, USA, Mar. 2015, paper Th5A.1. (*Postdeadline*).

- [109] M. Kuschnerov, V.A.J.M. Sleiffer, Y. Chen, E. de Man, Y. Chen, Z. Liu, S.R. Sandoghchi, G.T. Jasion, T. Bradley, E. Numkam Fokoua, J.R. Hayes, N.V. Wheeler, D.R. Gray, R. Slavík, Y. Jung, N.H.L. Wong, B.J. Mangan, F. Poletti, M.N. Petrovich, and D.J. Richardson, “Data transmission through up to 74.8 km of hollow-core fiber with coherent and direct-detect transceivers,” in *Proc. 41st ECOC*, Valencia, Spain, Sep. 2015, paper 0049.
- [110] Y. Chen, S.R. Sandoghchi, E. Numkam, T.D. Bradley, J.R. Hayes, N.V. Wheeler, G. Jasion, D.R. Gray, F. Poletti, M.N. Petrovich, and D.J. Richardson, “Detailed study of macrobending effects in a wide transmission bandwidth hollow-core photonic bandgap fiber,” in *Proc. SPIE 9886, Micro-Structured Specialty Opt. Fibres IV*, Brussels, Belgium, Apr. 2016, paper 98860X.
- [111] Y. Chen, Z. Liu, S.R. Sandoghchi, G.T. Jasion, T.D. Bradley, E. Numkam Fokoua, J.R. Hayes, N.V. Wheeler, D.R. Gray, B.J. Mangan, R. Slavík, F. Poletti, M.N. Petrovich, and D.J. Richardson, “Multi-kilometer long, longitudinally uniform hollow core photonic bandgap fibers for broadband low latency data transmission,” *J. Lightw. Technol.*, **34**(1):104–113, Jan. 2016.
- [112] Z. Liu, Y. Chen, Z. Li, B. Kelly, R. Phelan, J. O’Carroll, T. Bradley, J.P. Wooler, N.V. Wheeler, A.M. Heidt, T. Richter, C. Schubert, M. Becker, F. Poletti, M.N. Petrovich, S.u. Alam, D.J. Richardson, and R. Slavík, “High-capacity directly modulated optical transmitter for 2- $\mu$ m spectral region,” *J. Lightw. Technol.*, **33**(7):1373–1379, Apr. 2015.
- [113] E. Numkam, F. Poletti, and D.J. Richardson, “Dipole radiation model for surface roughness scattering in hollow-core fibers,” in *Proc. OFC/NFOEC*, Los Angeles, CA, USA, Mar. 2012, paper JW2A.18. (Poster).
- [114] E. Numkam Fokoua, F. Poletti, and D.J. Richardson, “Analysis of light scattering from surface roughness in hollow-core photonic bandgap fibers,” *Opt. Express*, **20**(19):20980–20991, Sep. 2012.
- [115] F. Poletti and E. Numkam Fokoua, “Understanding the physical origin of surface modes and practical rules for their suppression,” in *Proc. 39th ECOC*, London, UK, Sep. 2013, paper Tu.3.A.4.
- [116] E. Numkam Fokoua, D.J. Richardson, and F. Poletti, “Impact of structural distortions on the performance of hollow-core photonic bandgap fibers,” *Opt. Express*, **22**(3):2735–2744, Feb. 2014.
- [117] E. Numkam Fokoua, Y. Chen, D.J. Richardson, and F. Poletti, “Microbending effects in hollow-core photonic bandgap fibers,” in *Proc. 42nd ECOC*, Düsseldorf, Germany, Sep. 2016, paper Tu.2.F.3.

- [118] E. Numkam Fokoua, S.R. Sandoghchi, Y. Chen, G.T. Jasion, N.V. Wheeler, N.K. Baddela, J.R. Hayes, M.N. Petrovich, D.J. Richardson, and F. Poletti, “**Accurate modelling of fabricated hollow-core photonic bandgap fibers,**” *Opt. Express*, **23**(18):23117–23132, Sep. 2015.
- [119] N.H.L. Wong, Y. Jung, S.U. Alam, P. Petropoulos, and D.J. Richardson, “**Numerical analysis of mode propagation and coupling in multimode fibers,**” in *Proc. CLEO-PR/OECC/PGC*, Singapore, Aug. 2017. (*Accepted*).
- [120] G.T. Jasion, S.R. Sandoghchi, Y. Chen, N.V. Wheeler, T. Bradley, N. Baddela, J. Hayes, M.N. Petrovich, D.J. Richardson, J.S. Shrimpton, and F. Poletti, “**Novel fluid dynamics model to predict draw of hollow core photonic band-gap fibres,**” in *Proc. 40th ECOC*, Cannes, France, Sep. 2014, paper Th.2.4.3.
- [121] G.T. Jasion, J.S. Shrimpton, Y. Chen, T. Bradley, D.J. Richardson, and F. Poletti, “**MicroStructure Element Method (MSEM): viscous flow model for the virtual draw of microstructured optical fibers,**” *Opt. Express*, **23**(1):312–329, Jan. 2015.
- [122] G.T. Jasion, E.R. Numkam Fokoua, J.S. Shrimpton, D.J. Richardson, and F. Poletti, “**Combined structural and optical modelling tool to optimise design and fabrication of hollow core photonic band gap fibres,**” in *Proc. 41st ECOC*, Valencia, Spain, Sep. 2015, paper 0395. (*Poster*).
- [123] G.T. Jasion, E. Numkam Fokoua, J.S. Shrimpton, D.J. Richardson, and F. Poletti, “**Studying the limits of production rate and yield for the volume manufacturing of hollow core photonic band gap fibers,**” *Opt. Express*, **23**(25):32179–32190, Dec. 2015.
- [124] D.R. Gray, S.R. Sandoghchi, N.V. Wheeler, G.T. Jasion, J.P. Wooler, M.N. Petrovich, F. Poletti, and D.J. Richardson, “**Towards real-time mode content characterization of multimode fibers,**” in *Proc. 40th ECOC*, Cannes, France, Sep. 2014, paper Th.1.4.3.
- [125] D.R. Gray, S.R. Sandoghchi, N.V. Wheeler, N.K. Baddela, G.T. Jasion, M.N. Petrovich, F. Poletti, and D.J. Richardson, “**Mitigating spectral leakage and sampling errors in spatial and spectral ( $S^2$ ) imaging,**” in *Proc. OFC*, Los Angeles, CA, USA, Mar. 2015, paper W4I.6.
- [126] D.R. Gray, M.N. Petrovich, S.R. Sandoghchi, N.V. Wheeler, N.K. Baddela, G.T. Jasion, T. Bradley, D.J. Richardson, and F. Poletti, “**Real-time modal analysis via wavelength-swept spatial and spectral ( $S^2$ ) imaging,**” *IEEE Photon. Technol. Lett.*, **28**(9):1034–1037, May 2016.
- [127] D.R. Gray, S.R. Sandoghchi, N.V. Wheeler, N.K. Baddela, G.T. Jasion, M.N. Petrovich, F. Poletti, and D.J. Richardson, “**Accurate calibration of  $S^2$  and interferometry based multimode fiber characterization techniques,**” *Opt. Express*, **23**(8):10540–10552, Apr. 2015.

- [128] G.M. Ponzo, M.N. Petrovich, X. Feng, P. Horak, F. Poletti, P. Petropoulos, and D.J. Richardson, “Fast and broadband fiber dispersion measurement with dense wavelength sampling,” *Opt. Express*, **22**(1):943–953, Jan. 2014.
- [129] T.D. Bradley, X. Wang, E. Numkam Fokoua, N.V. Wheeler, F. Poletti, M.N. Petrovich, and D.J. Richardson, “Measuring the group velocity dispersion of higher order modes in hollow core photonic bandgap fibre,” in *Proc. 41st ECOC*, Valencia, Spain, Sep. 2015, paper 0446. (Poster).
- [130] J.P. Wooller, D. Gray, Poletti F., M.N. Petrovich, N.V. Wheeler, F. Parmigiani, and D.J. Richardson, “Robust low loss splicing of hollow core photonic bandgap fiber to itself,” in *Proc. OFC/NFOEC*, Anaheim, CA, USA, Mar. 2013, paper OM3I.5.
- [131] J.P. Wooller, S.R. Sandoghchi, D. Gray, F. Poletti, M.N. Petrovich, N.V. Wheeler, N.K. Baddela, and D.J. Richardson, “Overcoming the challenges of splicing dissimilar diameter solid-core and hollow-core photonic band gap fibers,” in *Proc. Workshop Specialty Opt. Fibers their Appl. (WSOF)*, Sigtuna, Sweden, Aug. 2013, paper W3.26. (Poster).
- [132] J.P. Wooller, F. Parmigiani, S.R. Sandoghchi, N.V. Wheeler, D.R. Gray, F. Poletti, M.N. Petrovich, and D.J. Richardson, “Data transmission over 1km HC-PBGF arranged with microstructured fiber spliced to both itself and SMF,” in *Proc. 39th ECOC*, London, UK, Sep. 2013, paper Tu.3.A.3.
- [133] S.R. Sandoghchi, G.T. Jasion, N.V. Wheeler, S. Jain, Z. Lian, J.P. Wooller, R.P. Boardman, N. Baddela, Y. Chen, J. Hayes, E. Numkam Fokoua, T. Bradley, D.R. Gray, S.M. Mousavi, M. Petrovich, F. Poletti, and D.J. Richardson, “X-ray tomography for structural analysis of microstructured and multimaterial optical fibers and preforms,” *Opt. Express*, **22**(21):26181–26192, Oct. 2014.
- [134] S.R. Sandoghchi, T. Zhang, J.P. Wooller, N.K. Baddela, N.V. Wheeler, Y. Chen, G.T. Jasion, D.R. Gray, E. Numkam Fokoua, J.R. Hayes, M.N. Petrovich, F. Poletti, and D.J. Richardson, “First investigation of longitudinal defects in hollow core photonic bandgap fibers,” in *Proc. OFC*, San Francisco, CA, USA, Mar. 2014, paper M2F.6.
- [135] S.R. Sandoghchi, M.N. Petrovich, D.R. Gray, Y. Chen, N.V. Wheeler, T.D. Bradley, N.H.L. Wong, G.T. Jasion, J.R. Hayes, E. Numkam Fokoua, M.B. Alonso, S.M. Mousavi, D.J. Richardson, and F. Poletti, “Optical side scattering radiometry for high resolution, wide dynamic range longitudinal assessment of optical fibers,” *Opt. Express*, **23**(21):27960–27974, Oct. 2015.
- [136] N.H.L. Wong, S.R. Sandoghchi, Y. Jung, T. Bradley, N.V. Wheeler, N.K. Baddela, J.R. Hayes, F. Poletti, M.N. Petrovich, S.U. Alam, P. Petropoulos, and D.J. Richardson, “Inspection of defect-induced mode coupling in hollow-core photonic

- bandgap fibers using time-of-flight,” in *CLEO*, San Jose, CA, USA, May 2015, paper STu1N.6.
- [137] M.J. Hackert, “Development of chromatic dispersion measurement on multimode fiber using the relative time of flight measurement technique,” *IEEE Photon. Technol. Lett.*, **4**(2):198–200, Feb. 1992.
- [138] R.V. Jensen, L. Grüner-Nielsen, N.H.L. Wong, Y. Sun, Y. Jung, and D.J. Richardson, “Demonstration of a 9 LP-mode transmission fiber with low DMD and loss,” in *Proc. OFC*, Los Angeles, CA, USA, Mar. 2015, paper W2A.34. (Poster).
- [139] K. Jespersen, Z. Li, L. Grüner-Nielsen, B. Pálsdóttir, F. Poletti, and J.W. Nicholson, “Measuring distributed mode scattering in long, few-moded fibers,” in *Proc. OFC*, Los Angeles, CA, USA, Mar. 2012, paper OTh3I.4.
- [140] I.M. Avram, I.G. Tarnovan, and B. Tebrean, “Analysis of linearly polarized modes,” in *Proc. COMSOL Conf.*, Stuttgart, Germany, Oct. 2011.
- [141] W.Q. Thornburg, B.J. Corrado, and X.D. Zhu, “Selective launching of higher-order modes into an optical fiber with an optical phase shifter,” *Opt. Lett.*, **19**(7):454–456, Apr. 1994.
- [142] G.P. Agrawal. *Nonlinear Fiber Optics*. Academic Press, Boston, MA, USA, 2013.
- [143] M. Wuilpart, “Rayleigh scattering in optical fibers,” in *Advanced Fiber Optics* (L. Thévenaz, ed.), pp. 207–262, Lausanne, Switzerland: EPFL Press, 2011.
- [144] N.K. Fontaine, R. Ryf, H. Chen, A.V. Benitez, J.E. Antonio Lopez, R. Amezcua Correa, B. Guan, B. Ercan, R.P. Scott, S.J.B. Yoo, L. Grüner-Nielsen, Y. Sun, and R.J. Lingle, “30×30 MIMO transmission over 15 spatial modes,” in *Proc. OFC Post Deadline Papers*, Los Angeles, CA, USA, Mar. 2015, paper Th5C.1. (Postdeadline).
- [145] R. Maruyama, N. Kuwaki, S. Matsuo, and M. Ohashi, “Experimental investigation of relation between mode-coupling and fiber characteristics in few-mode fibers,” in *Proc. OFC*, Los Angeles, CA, USA, Mar. 2015, paper M2C.1.
- [146] D.J. Richardson, J.M. Fini, and L.E. Nelson, “Space-division multiplexing in optical fibres,” *Nature Photon.*, **7**(5):354–362, Apr. 2013.
- [147] J. Xu, C. Peucheret, J. Kristian Lyngsø, and L. Leick, “Two-mode multiplexing at  $2 \times 10.7$  gbps over a 7-cell hollow-core photonic bandgap fiber,” *Opt. Express*, **20**(11):12449–12456, May 2012.
- [148] M.N. Petrovich, N.K. Baddela, N.V. Wheeler, E. Numkam, R. Slavík, D.R. Gray, J.R. Hayes, J.P. Wooler, F. Poletti, and D.J. Richardson, “Development of low loss, wide bandwidth hollow core photonic bandgap fibers,” in *Proc. OFC/NFOEC*, Anaheim, CA, USA, Mar. 2013, paper OTh1J.3. (Invited).

- [149] S.S. Haykin and M. Moher. *An Introduction to Analog and Digital Communications*. Wiley, 2nd ed., 2007.
- [150] “Deliverable D1.1 – Requirements for Next Generation intra-Data Centre Networks Design,” report, COSIGN, 2014.
- [151] B.J. Mangan, L. Farr, A. Langford, P.J. Roberts, D.P. Williams, F. Couny, M. Lawman, M. Mason, S. Coupland, R. Flea, H. Sabert, T.A. Birks, J.C. Knight, and P.St.J. Russell, “Low loss (1.7 dB/km) hollow core photonic bandgap fiber,” in *Proc. OFC*, Los Angeles, CA, USA, Feb. 2004, paper PDP24. (Postdeadline).
- [152] F. Poletti and P. Horak, “Description of ultrashort pulse propagation in multimode optical fibers,” *J. Opt. Soc. Am. B*, **25**(10):1645–1654, Oct. 2008.
- [153] J.M. Dudley, G. Genty, and S. Coen, “Supercontinuum generation in photonic crystal fiber,” *Rev. Mod. Phys.*, **78**:1135–1184, Oct. 2006.
- [154] P. Fischer and J.D. Stegeman, “Fractional hadamard powers of positive semidefinite matrices,” *Linear Algebra its Applicat.*, **371**:53–74, Sep. 2003.
- [155] E. Desurvire. *Erbium-doped Fiber Amplifiers: Principles and Applications*. Wiley, Hoboken, NJ, USA, 1994.
- [156] L.N. Binh, “Matlab simulink simulation platform for photonic transmission systems,” *Int. J. Commun., Netw. and Syst. Sci.*, **2**(2):97–117, May 2009.
- [157] L.N. Binh. *Optical Fiber Communication Systems with MATLAB® and Simulink® Models*. CRC Press, Boca Raton, FL, USA, 2nd ed., 2014.
- [158] D. Marcuse, “Derivation of coupled power equations,” *Bell Syst. Tech. J.*, **51**(1): 229–237, Jan. 1972.
- [159] J.D. Hoffman. *Numerical Methods for Engineers and Scientists*. CRC Press, New York, NY, USA, 2nd ed., 2001.
- [160] S.C. Chapra and R.P. Canale. *Numerical Methods for Engineers*. McGraw-Hill Education, New York, NY, USA, 7th ed., 2014.
- [161] J.N. Kutz, “AMATH 581: Practical Scientific Computing,” *Course Notes* [Online], Jan. 2005. Available: <http://courses.washington.edu/amath581/581.pdf>.
- [162] W.E. Schiesser. *The Numerical Method of Lines: Integration of Partial Differential Equations*. Academic Press, San Diego, CA, USA, 1991.
- [163] H.J. Lee and W.E. Schiesser. *Ordinary and Partial Differential Equation Routines in C, C++, Fortran, Java®, Maple®, and MATLAB®*. Chapman and Hall/CRC, 2003.

- [164] J.H. Mathews and K.D. Fink. *Numerical Methods Using MATLAB*. Pearson, Upper Saddle River, NJ, USA, 4th ed., 2004.
- [165] R.H. Hardin and F.D. Tappert, “Applications of the split-step Fourier method to the numerical solution of nonlinear and variable coefficient wave equations,” *Soc. Ind. Appl. Math. (SIAM) Rev.*, **15**(2):423, Apr. 1973.
- [166] R.A. Fisher and W.K. Bischel, “Numerical studies of the interplay between self-phase modulation and dispersion for intense plane-wave laser pulses,” *J. Appl. Phys.*, **46**(11):4921–4934, Nov. 1975.
- [167] A. Hasegawa and F. Tappert, “Transmission of stationary nonlinear optical pulses in dispersive dielectric fibers. I. Anomalous dispersion,” *Appl. Phys. Lett.*, **23**(3):142–144, Aug. 1973.
- [168] P.J. Roache, “Perspective: A method for uniform reporting of grid refinement studies,” *J. Fluids Eng.*, **116**(3):405–413, Sep. 1994.
- [169] M. Kushnerov, M. Chouayakh, K. Piyawanno, B. Spinnler, M.S. Alfiad, A. Napoli, and B. Lankl, “On the performance of coherent systems in the presence of polarization-dependent loss for linear and maximum likelihood receivers,” *IEEE Photon. Technol. Lett.*, **22**(12):920–922, Jun. 2010.
- [170] J. Reynolds, “Cancer research and internet capacity win TakeAIM 2016,” Smith Institute, [Online], Nov. 2016. Available: <http://www.smithinst.co.uk/blog/cancer-research-internet-capacity-crunch-equations-among-mathematical-innovations-tipped-transform-world/>. [Accessed Dec. 30, 2016].
- [171] T.V. Mai, J.A. Molnar, and L.H. Tran, “Fiber optic test equipment – evaluation of OTDR dead zones and ORLM return loss,” in *Proc. AUTOTESTCON*, pp. 94–98, San Antonio, TX, USA, Sep. 2004.
- [172] M. Belal, M. Petrovich, N. Wheeler, J. Wooler, A. Masoudi, F. Poletti, S. Alam, D. Richardson, and T. Newson, “First demonstration of a 2- $\mu\text{m}$  OTDR and its use in photonic bandgap  $\text{CO}_2$  sensing fiber,” *IEEE Photon. Technol. Lett.*, **26**(9):889–892, May 2014.
- [173] N.H.L. Wong, Y. Jung, S.R. Sandoghchi, T. Bradley, N.K. Baddela, N.V. Wheeler, J.R. Hayes, M.N. Petrovich, F. Poletti, S.U. Alam, P. Petropoulos, and D.J. Richardson, “Modal characterization of hollow-core photonic bandgap fibers in the time-domain,” in *Siegman Int. School Lasers*, Amberg, Germany, Aug. 2015. (Poster).
- [174] R. Paschotta, “Fiber collimators,” [Online]. Available: [http://www.rp-photonics.com/fiber\\_collimators.html](http://www.rp-photonics.com/fiber_collimators.html). [Accessed Jan. 23, 2014].

- 
- [175] R. Paschotta, “Single-mode fibers,” [Online]. Available: [http://www.rp-photonics.com/single\\_mode\\_fibers.html](http://www.rp-photonics.com/single_mode_fibers.html). [Accessed Jan. 23, 2014].
- [176] L.C. Andrews and R.L. Phillips. *Mathematical Techniques for Engineers and Scientists*. SPIE Press, Bellingham, WA, USA, 2003.
- [177] Y. Jung, E.L. Lim, Q. Kang, T.C. May-Smith, N.H.L. Wong, R. Standish, F. Polletti, J.K. Sahu, S.U. Alam, and D.J. Richardson, “Cladding pumped few-mode EDFA for mode division multiplexed transmission,” *Opt. Express*, **22**(23):29008–29013, Nov. 2014.
- [178] Y. Jung, Z. Li, N.H.L. Wong, J.M.O. Daniel, J.K. Sahu, S. Alam, and D.J. Richardson, “Spatial mode switchable, wavelength tunable erbium doped fiber laser incorporating a spatial light modulator,” in *Proc. OFC*, San Francisco, CA, USA, Mar. 2014, paper Tu3D.4.